

**Origin and variability of the late Precambrian-
Cambrian Athel Silicilyte, South Oman Salt Basin**

A thesis submitted to The University of Manchester for the degree of
Doctor of Philosophy in the Faculty of Engineering and Physical
Sciences

2011

Ibrahim Mohamed Amur Al Rajaibi

**School of Earth, Atmospheric and Environmental
Sciences**

List of contents

<i>List of contents</i>	2
<i>List of figures</i>	5
<i>List of tables</i>	8
<i>List of appendices</i>	9
<i>Abstract</i>	10
<i>Declaration</i>	11
<i>Copyright statement</i>	12
<i>Acknowledgments</i>	13
<i>Dedication</i>	14
<i>Preface</i>	15
Chapter 1. Introduction.	16
1.1 Context of the research.....	17
1.2 Aims and objectives	18
1.3 Thesis layout	21
Chapter 2. Methodology	24
2.1 Introduction.....	25
2.2 Core description and sample collection	26
2.3 Petrographic techniques	30
2.3.1 Thin section preparation and scanning.....	30
2.3.2 Optical microscope	30
2.3.3 Scanning electron microscope (SEM).....	31
2.3.4 Pyrite framboid size-distributions	31
2.4 Geochemical techniques.....	32
2.4.1 X-ray diffraction (XRD)	33
2.4.2 X-ray fluorescence (XRF).....	34
2.4.3 Laser ablation-inductively coupled plasma-mass spectroscopy (LA- ICP-MS)	36
2.4.4 Total organic carbon (TOC).....	38
2.5 Wireline log interpretation	39
2.6 Reaction-path modelling	42
2.7 Constituents abundance and lithofacies nomenclature.....	42

Chapter 3. Regional geology.....	44
3.1 Introduction.....	45
3.2 The Huqf Supergroup: an overview.....	45
3.3 Ara Group tectonism and palaeogeography.....	50
3.4 Ara Group lithostratigraphy in the South Oman Salt Basin.....	53
3.5 Ara basin reconstruction.....	55
3.5.1 Phase one.....	55
3.5.2 Phase two.....	55
3.5.3 Phase three.....	56
3.6 Ara Group chronostratigraphy.....	58
3.7 Ara Group chemostratigraphy.....	58
3.8 Dating the Precambrian-Cambrian boundary.....	60
Chapter 4. Chert accumulation and distribution.....	62
4.1 Introduction.....	63
4.2 Silica Geochemistry.....	63
4.2.1 Silica polymorphs and diagenesis.....	63
4.2.2 Silica Solubility.....	65
4.3 Chert accumulation.....	67
4.3.1 Modern.....	67
4.3.2 Phanerozoic.....	69
4.3.3 Precambrian.....	72
4.4 Secular change in chert distribution.....	76
4.4.1 Precambrian.....	77
4.4.2 Phanerozoic.....	78
Chapter 5. Lithofacies analysis and distribution.....	80
5.1 Introduction.....	81
5.2 Lithofacies.....	81
5.2.1 Silica-rich facies.....	89
5.2.2 Silt-rich facies.....	103
5.2.3 Evaporite lithofacies.....	107
5.2.4 Post-depositionally modified lithofacies.....	112
5.3 Pyrite framboid size-distribution.....	120
5.4 Temporal and spatial variability of the Athel Silicilyte.....	124
5.5 Summary.....	130
Chapter 6. Inorganic geochemistry.....	132
6.1 Introduction.....	133
6.2 Background.....	133
6.2.1 Detrital monitor.....	133
6.2.2 Hydrothermal signature.....	134

6.2.3	Seawater signature	134
6.2.4	Redox monitor	135
6.3	Results.....	137
6.3.1	Data presentation and normalisation.....	137
6.3.2	Major and trace elements	142
6.3.3	Rare Earth Elements	148
6.4	Origin of rock components.....	152
6.4.1	Detrital inputs	152
6.4.2	Detrital contamination to REE.....	154
6.4.3	Hydrothermal source.....	156
6.4.4	Seawater source	156
6.5	Redox conditions.....	158
6.6	Summary	165
Chapter 7. Origin of the Athel Silicilyte.....		167
7.1	Introduction.....	168
7.2	Silica source	168
7.2.1	Mass-balance calculations	171
7.2.2	Required vs. available seawater mass	176
7.2.3	Seawater renewal time	179
7.3	Precipitation mechanism	183
7.3.1	Silica polymerisation	186
7.3.2	Hydrogen bonding	187
7.3.3	Athel Silicilyte precipitation and distribution	190
7.4	Locus of primary chert precipitation during the Precambrian.....	194
7.5	Summary	196
Chapter 8. Conclusions.		197
<i>References.....</i>		<i>202</i>
<i>Appendices.....</i>		<i>228</i>

Number of words = 70,505

List of figures

Figure 1.1. Simplified geological map of Oman.....	19
Figure 1.2. Seismic section of an entrapped slab of the Athel Silicilyte within Ara Salt domes in South Oman Salt Basin.....	20
Figure 2.1. A map of the South Oman Salt Basin and Athel Basin showing location of wells	27
Figure 2.2. Stratigraphic distribution of obtained samples for this study from in the Athel Basin	29
Figure 2.3. Schematic illustration of the major components in the XRD and the XRF analysis	35
Figure 2.4. Schematic illustration of the components in laser ablation system ...	37
Figure 2.5. A graph showing mutual element concentrations from the XRF and the LA-IC-MS analysis from 21 samples used to correct the results obtained from LA-ICP-MS	38
Figure 3.1. Restored map of NW Gondwana reconstruction at the end of the Neoproterozoic.	47
Figure 3.2. A simplified stratigraphic log of the Huqf Supergroup.....	49
Figure 3.3. A map of the South Oman Salt Basin and Athel Basin.....	52
Figure 3.4. A geological cross section of the South Oman Salt Basin between the Western Margin and the Eastern Flank.	53
Figure 3.5. Schematic diagram illustrating a reconstruction of the Ara basin and evolution of the Ara Group cycles	57
Figure 4.1. XRD patterns of silica polymorphs: opal-A, opal-CT and quartz.....	64
Figure 4.2. Quartz and amorphous silica solubility as a function of pH.....	66
Figure 4.3. Amorphous silica solubility as a function of temperature.	66
Figure 4.4. Outcrop pictures of Phanarazoic bedded cherts.....	70
Figure 4.5. Outcrop and optical microscope photograph of Phanerozoic nodular chert.....	72
Figure 4.6. Outcrop and optical microscope photograph of Proterozoic nodular chert.....	75
Figure 4.7. An outcrop picture of chert layers in Banded Iron Formation.....	76

Figure 4.8 A diagram shows direct and early diagenetic chert distribution from Late Archean to the present day.....	79
Figure 5.1. A map of the South Oman Salt Basin and the Athel Basin showing well location	82
Figure 5.2. Wells correlation and lithofacies variability from the Birba Platform through the Athel Basin (margins and centre)	83
Figure 5.3. Wireline log data of well ALNR-2	85
Figure 5.4. Photomicrographs of laminated microcrystalline quartz-rich mudstones (LF1)	90
Figure 5.5. An XRD plot of LF1.....	91
Figure 5.6. Photomicrographs of laminated microcrystalline quartz-dominated mudstones (LF2).. ..	93
Figure 5.7. An XRD plot of LF2.....	94
Figure 5.8. Photomicrographs of laminated microcrystalline quartz-rich, detritus-bearing mudstones (LF3)	96
Figure 5.9. An XRD plot of LF3.....	97
Figure 5.10. A plot showing spectral GR of well ALNR-2	98
Figure 5.11. A graph shows the relation between clay minerals and pyrite contents in the silica-rich facies	102
Figure 5.12. Photomicrographs of laminated silt-rich, clay-mineral bearing mudstones (LF4)	104
Figure 5.13. Photomicrographs illustrate the ripple lamination in LF4.....	105
Figure 5.14. An XRD plot of LF4.....	106
Figure 5.15. Photomicrographs of anhydrite- and detritus-bearing mudstones (LF5).....	109
Figure 5.16. An XRD plot of LF5.....	110
Figure 5.17. An XRD plot of halite-dominated mudstones (LF6).....	111
Figure 5.18. Photomicrographs of slumped mudstones (LF7).....	113
Figure 5.19. Photomicrographs of brecciated mudstones (LF8).....	115
Figure 5.20. Photomicrographs of microcrystalline quartz-, carbonate- and detritus- bearing mudstones (LF9)	118
Figure 5.21. An XRD plot of LF9	119
Figure 5.22. Back scattered electron images of pyrites.	122
Figure 5.23. Pyrite framboid size distributions.....	124

Figure 5.24. A summary logs of lithofacies vertical and lateral variability in the Athel Basin	127
Figure 5.25. Paleotopographical map of the Athel Basin	129
Figure 6.1. Plots of Al ₂ O ₃ vs. K ₂ O, Fe ₂ O ₃ , TiO ₂ and Zr.....	143
Figure 6.2. A plot showing SiO ₂ vs. Al ₂ O ₃ concentration.. ..	143
Figure 6.3. A stratigraphic plot of SiO ₂ and selected detrital parameters (Al ₂ O ₃ , TiO ₂ and Zr) from well ALNR-2	144
Figure 6.4. A plot shows Al ₂ O ₃ /(Al ₂ O ₃ +Fe ₂ O ₃ + MnO) vs. Fe ₂ O ₃ /TiO ₂	145
Figure 6.5. Cross plots of redox-sensitive element concentrations.....	146
Figure 6.6. Cross plots of redox-sensitive element enrichment factor.....	147
Figure 6.7. A stratigraphic plot of redox-sensitive element enrichment factor from well ALNR-2	148
Figure 6.8. Plots of TiO ₂ concentrations vs. ΣREE and Y/Ho ratios.....	149
Figure 6.9. Rare Earth Element PAAS-normalised patterns.....	151
Figure 6.10. Rare Earth Element anomalies from this study	152
Figure 6.11. Rare Earth Element anomalies from this study compare to modern oxic/anoxic seawater and hydrothermal fluids.....	158
Figure 6.12. Rare Earth Element PAAS-normalised patterns from this study and from modern oxic/anoxic seawater and hydrothermal fluids.....	158
Figure 7.1. Paleotopographical map of the Athel Basin	174
Figure 7.2. Sediment Mo/TOC ratios vs. average renewal times of modern restricted basins (Saanich Inlet, Cariaco Basin, Framvaren Fjord and Black Sea)	182
Figure 7.3. Secondary electron images of microcrystalline quartz textures from the Athel Silicilyte and a representation showing development of spherical silica polymers.	184
Figure 7.4. Illustration hydrogen bonding (between dissolved silica and microbial layer), polymerisation and aggregation process	189
Figure 7.5. Reaction path modelling results show that as HS ⁻ concentration increases pH drops.	191
Figure 7.6. Depositional model for the Athel Silicilyte.....	194

List of tables

Table 2.1. Number of collected samples from each well.....	28
Table 2.2. Comparison between measured major oxide concentrations by XRF and certified concentration of a reference material.....	35
Table 2.3. Comparison between measured trace element concentrations by XRF and certified concentration of a reference material.....	35
Table 5.1. A summary of the lithofacies identified in this study.	86
Table 6.1. Average concentrations of the major and selected trace elements....	140
Table 6.2. Average REE concentrations and calculated anomalies.	141
Table 7.1. Parameters used in the mass-balance calculations.....	176
Table 7.2. Summaries required water masses, available water masses and their ratios at various concentrations and depths.....	178

List of appendices

Appendix I. Wireline log interpretation	2288
Appendix II. Core and thin-section photographs	229
Appendix III: mineralogical composition and elemental concentrations of each studied sample.....	283
Appendix IV: Reaction-path modelling.....	301

Abstract

The Precambrian-Cambrian Athel Silicilyte is an enigmatic chert unit of up to 390 m thick found as slabs (each slab typically 2 × 6 km across) entrapped within salt domes at a depth of 4-5 km in the South Oman Salt Basin. This formation is a prolific self-charged reservoir with high porosity (up to 34 %) and high oil saturation (80 %). Despite its economic value, the origin and the variability of this formation are not fully understood. This study therefore aims to investigate the variability and the origin (silica source and precipitation mechanism) of the Athel Silicilyte. Data obtained from core, wireline log and petrographical analysis were employed to establish the vertical and the lateral variability and, with the assistance of geochemical data, the likely source and precipitation mechanism of silica was determined.

The Athel Silicilyte is only present in the deepest parts of the South Oman Salt Basin within the fault-bounded Athel Basin, bounded by two silt-rich mudstone units. Six lithofacies were recognised in the Athel Silicilyte that reflect variability in detrital material contents (three silica-rich facies), sediment remobilisation (slumped and brecciated lithofacies) and diagenetic modification (carbonate-bearing lithofacies), with the silica-rich facies being the most abundant (> 97 % of the total thickness). The Athel Silicilyte exhibits wavy discontinuous lamination and it is predominately (silica-rich facies average = 80 wt. %) composed of connected-networks of microcrystalline quartz (1-5 µm). Other constituent components are detrital quartz (3 wt. %), illite (10 wt. %), pyrite (4 wt. %) and organic carbon (TOC = 3 wt. %). The detrital contents increase towards the Upper Athel Silicilyte and towards the basin margins (ranging from 3 to 30 wt. %). The wavy laminations are interpreted to have a microbial origin. The homogeneity, loose packing of detrital grains and preservation of 390 m thick laminated fabric suggest that the Athel Silicilyte precipitated syndepositionally in microbial layers during low detrital input. The intense detrital input during bounding mudstones sedimentation inhibited Athel Silicilyte precipitation as a result of the rapid burial of microbial layers. The Athel Silicilyte shows strong enrichments of redox-sensitive elements (U, V and Mo), Mn-depletion, positive Ce anomalies, and small framboidal pyrites (3.6-4.0 µm), suggesting that the water column was euxinic during precipitation.

Based on the petrographical evidence for the Athel Silicilyte forming as a syndepositional precipitate alongside seawater-like rare earth element (REE) characteristics, silica is interpreted to have been sourced directly from seawater. Mass balance calculations support this interpretation, indicating that silica-rich Precambrian seawater provided the significant silica mass in the Athel Silicilyte. The ability of dissolved silica to form hydrogen bonds with the functional groups (e.g. carboxyl and hydroxyl) in microbial layers was the key for Athel Silicilyte precipitation. The formation of hydrogen bonds was made possible under euxinic conditions, where the pH values were probably lower (< 7) than for the normal seawater as a result of HS⁻ and H⁺ production by sulphate reducing bacteria and HS⁻ oxidation at the redox boundary by sulphur oxidising bacteria. Consequently, dissolved silica was concentrated in microbial layer microenvironments, resulting in silica nucleation and polymerisation.

Declaration

The author declares that no portion of the work referred to in the thesis has been submitted in support of an application for another degree or qualification of this or any other university or other institute of learning.

Copyright statement

- i.** The author of this thesis (including any appendices and/or schedules to this thesis) owns any copyright in it (the “Copyright”) and he has given The University of Manchester the right to use such Copyright for any administrative, promotional, educational and/or teaching purposes.
- ii.** Copies of this thesis, either in full or in extracts, may be made **only** in accordance with the regulations of the John Rylands University Library of Manchester. Details of these regulations may be obtained from the Librarian. This page must form part of any such copies made.
- iii.** The ownership of any patents, designs, trade marks and any and all other intellectual property rights except for the Copyright (the “Intellectual Property Rights”) and any reproductions of copyright works, for example graphs and tables (“Reproductions”), which may be described in this thesis, may not be owned by the author and may be owned by third parties. Such Intellectual Property Rights and Reproductions cannot and must not be made available for use without the prior written permission of the owner(s) of the relevant Intellectual Property Rights and/or Reproductions.
- iv.** Further information on the conditions under which disclosure, publication and exploitation of this thesis, the Copyright and any Intellectual Property Rights and/or Reproductions described in it may take place is in the University IP Policy (see <http://documents.manchester.ac.uk/DocuInfo.aspx?DocID=487>), in any relevant Thesis restriction declarations deposited in the University Library, The University Library’s regulations (see <http://www.manchester.ac.uk/library/aboutus/regulations>) and in The University’s policy on Presentation of Theses.

Acknowledgments

First and foremost I offer my sincerest gratitude to my supervisors, Dr. Cathy Hollis and Dr. Joe MacQuaker, who have supported me throughout my thesis with their expertise, understanding, patience, excellent supervision and constructive criticism. I would also like to express my appreciation to Prof. David Polya for his useful suggestions and advices in mass balance calculations and Dr. Mike Lawson for his help in reaction-path modelling.

I am also thankful to Dr. John Waters for his help in the XRD analysis, Mr. Paul Lythgoe for his help in the XRF and the REE analysis, Mr. Steve Caldwell and Mr. David Plant for assistance in using the SEM, Mr. Harry William and Mr. Steve Stockley for thin-section preparation. I am also very grateful to Prof. Kevin Taylor and Mr. David McKendry from the Manchester Metropolitan University for their help in the TOC analysis.

I would also like to thank Petroleum Development of Oman (PDO) for the logistic and the financial support, and for allowing access to the subsurface core data, wireline logs and internal reports. Lastly, but not least, I offer my regards to all of those who supported me in any respect during the completion of this project.

Dedication

To my brother, Omar. May Allah bless his soul and grant him heaven.

Preface

The author has a BSc in geological sciences from the University of Leeds (2002-2005) and an MSc in petroleum geosciences from the University of Manchester (2005-2006). Since September 2006, the author has been undertaking research for this PhD at the University of Manchester.

Chapter 1.

Introduction

1.1 Context of the research

The Precambrian-Cambrian Athel Silicilyte is a chert unit bounded by two silt-rich mudstones (below by the U Shale and above by the Thuleilat Shale). The Athel Silicilyte is found as packages or slabs entrapped within salt domes at a depth of 4 km in the South Oman Salt Basin; a restricted marine-fed intracratonic basin (Figs. 1.1 & 1.2). The Athel Silicilyte is a self-charged reservoir of up to 390 m thick and each slab is several kilometres wide (2×6 km across; Fig. 1.2) characterised by high porosity (up to 34 %), very low permeability (0.02 mD), organic carbon-rich (average TOC = 3 wt. %) and high oil saturation (80 %; Amthor et al. 1998; Amthor et al. 2005). Estimated oil-in-place in this formation is around 292×10^6 m³ (Amthor et al. 1998).

The Athel Silicilyte has been dated at the Precambrian-Cambrian boundary (\approx 541 Ma; Amthor et al. 2003; Bowring et al. 2007), which represents a major turning-point in Earth's history, marking the "Cambrian explosion" (e.g. Brasier 1992; Knoll and Walter 1992; Grotzinger et al. 1995; Knoll and Carroll 1999; Halverson et al. 2009). Global geochemical and biological changes are thought to have occurred at this boundary, including a global negative carbon excursion (e.g. Banerjee et al. 1997; Knoll and Carroll 1999; Amthor et al. 2003) and a global extinction of early marine organisms (e.g. Brasier 1989; Amthor et al. 2003). These global events have been interpreted as a result of a global anoxia development at the Precambrian-Cambrian boundary (e.g. Kimura and Watanabe 2001; Schröder and Grotzinger 2007).

Despite the economic and the scientific significance of the Athel Silicilyte, its origin, areal distribution and variability are not fully understood, and therefore it is often described as an enigmatic or an unusual formation (Amthor et al. 2005; Schröder and Grotzinger 2007). Previous work on the Athel Silicilyte has suggested that the Athel Silicilyte was deposited in the deepest parts of the Athel Basin (called "mini-basins": faulted-bounded basins) during relative sea level rise, whilst carbonate precipitation was taking place proximally, on shallow water platforms (Mattes and Morris 1990; Amthor et al. 2005; Schröder et al. 2005). During basin restriction and relative sea level fall, evaporites were

deposited on the top of the platforms and in the deepest parts of the basin (Mattes and Morris 1990; Schröder et al. 2003). Repeated basin restriction and flooding resulted in at least six 3rd Order evaporite-carbonate cycles (termed A0/A1-A6; Mattes and Morris 1990; Amthor et al. 2003; Schröder et al. 2003; Al-Siyabi 2005; Amthor et al. 2005; Schröder et al. 2005), in which the Athel Silicilyte is only present in the A4 cycle. The main unresolved questions concerning this enigmatic formation are:

- 1) Why is it only present in one cycle?
- 2) How does it vary vertically and laterally?
- 3) What is the origin of the large volume of silica present?
- 4) What is the mechanism responsible for silica precipitation?
- 5) Why is it a localised precipitate in the mini-basins?

1.2 Aims and objectives

Based on the above, this study aims to provide a better understanding of the Athel Silicilyte by investigating the vertical and the lateral variability, the origin of the large volumes of silica, the mechanism responsible for silica precipitation, and the controls on areal distribution. Several potential origins of the Athel Silicilyte were identified at the project start-up, specifically: biological accumulation of radiolaria and early sponges, hydrothermal precipitation, and/or chemically/biochemically mediated precipitation. In order to test these hypotheses, this study utilises various techniques, including core description, high resolution petrographical (optical and electronic) analysis and whole-rock geochemical (X-ray diffraction [XRD], X-ray fluoresce [XRF], laser ablation-inductively coupled plasma-mass spectroscopy [LA-ICP-MS] and total organic carbon [TOC]) analysis, mass balance calculations and reaction-path modelling. In addition, wireline logs (gamma ray, sonic, neutron, density, porosity) from 12 wells were employed to investigate the variability of the Athel Silicilyte at the basin scale. Understanding the origin of this formation, the control on its distribution and its likely occurrence away from the Athel Basin, will have relevance for future exploration strategies. Understanding its variability will also help to predict reservoir heterogeneity across the basin.

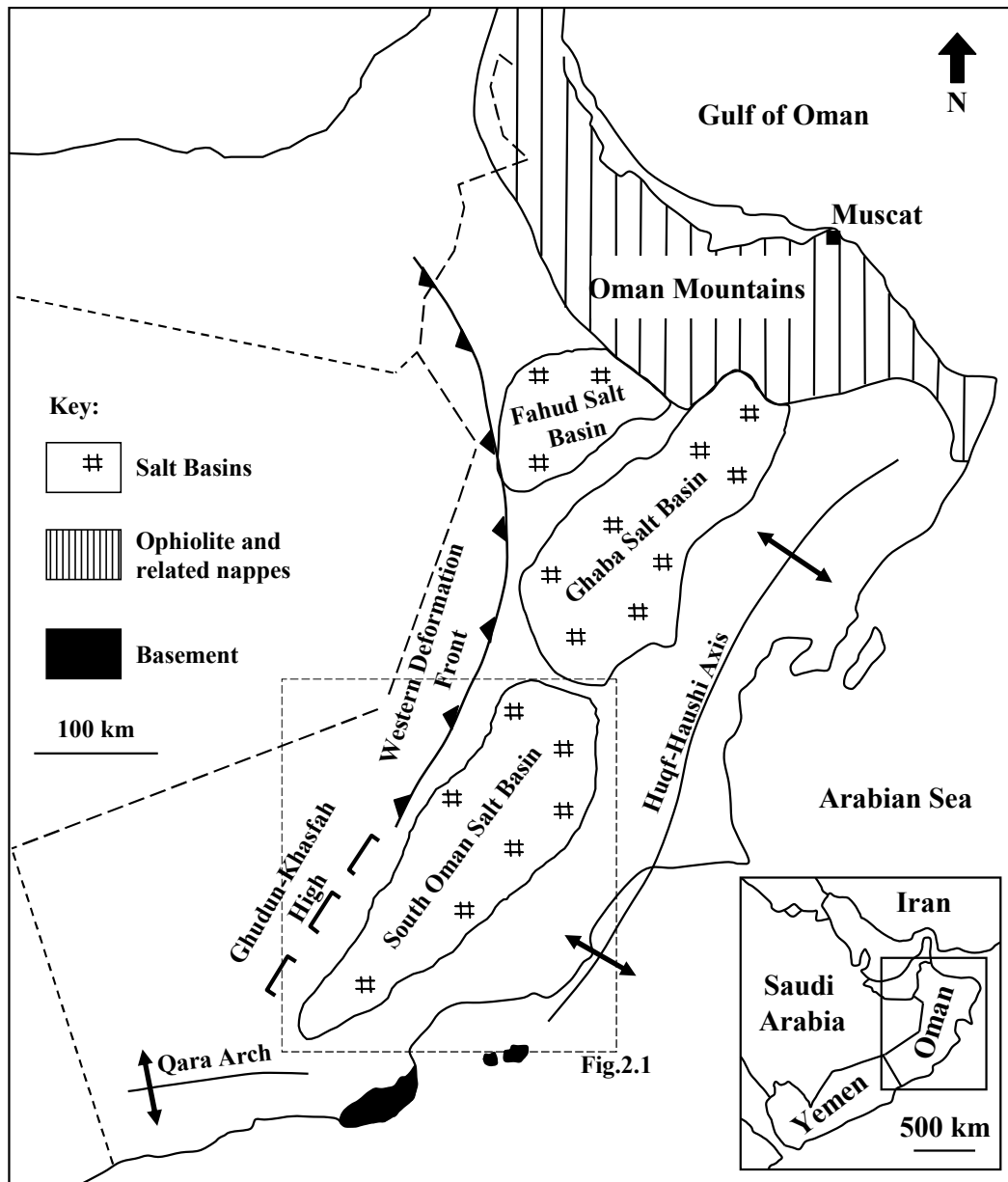


Figure 1.1. Simplified geological map of Oman showing the three salt basins occupying most of the Oman Interior. Oman Mountains of ophiolite and related nappes located to the north of the salt basins. The Athel Silicilyte is only found in the South Oman Salt Basin. Modified after Loosveld et al. (1996) and Schröder et al. (2004).

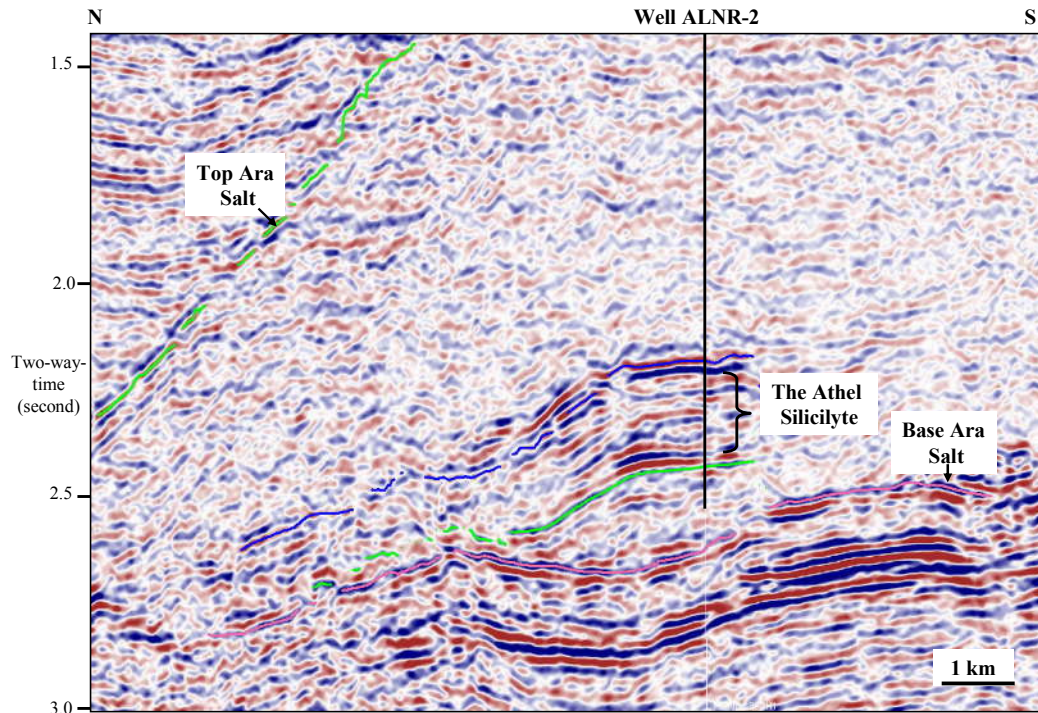


Figure 1.2. Seismic section showing an entrapped slab of the Athel Silicilyte within Ara Salt domes in South Oman Salt Basin. The total thickness of the Athel Silicilyte encountered from well ALNR-2 is 390 m. This well location is shown in Fig. 2.1 and wireline logs are presented in Chapter 5 (Fig. 5.2 & 5.3). Modified after Amthor et al. (2005).

In order to meet the aims above, the objectives of this project are to:

- 1) Review the regional geology, specifically, the geological setting of the Ara Group and its stratigraphy, geochronology and chemostratigraphy. In addition, silica geochemistry and controls on chert precipitation and distribution from the Precambrian to the present day are reviewed.
- 2) Describe available cores of the Athel Silicilyte. In particular, cores were described from six wells, including ALNR-2, ALNR-3, ALNR-4, ASH-2, ASH-4 and MKZ-1. Only well ALNR-2 was fully cored, providing a complete stratigraphic section of the Athel Silicilyte, whilst core data from other wells only cover small intervals (<10% of the total Athel Silicilyte thickness).
- 3) Sample cores for petrographical (optical and electron microscopy) and whole-rock geochemical analyses (XRD, XRF, LA-ICP-MS and TOC). Core, petrographical and XRD data were then used to describe

microstructures present and constituent components in order to classify different lithofacies present.

- 4) Calibrate wireline log responses using core- and petrographic-defined lithofacies to identify a characteristic log response for each lithofacies in order to facilitate the interpretation of uncored wells/intervals. The vertical and the lateral variability were then investigated.
- 5) Determine silica source using data derived from core investigation, petrographical analysis, statistical analysis of elemental concentrations (major, trace and rare earth element), TOC analysis and mass-balance calculations.
- 6) Determine silica precipitation mechanism by using a) petrographical observations, b) elemental concentrations to assess redox conditions and c) reaction-path modelling to investigate how bacterial diagenetic reactions might influence silica precipitation.

1.3 Thesis layout

The thesis is divided into eight chapters as follows:

- **Chapter 1 (Introduction):** This chapter describes the research context, provides the basic background information of the Athel Silicilyte and outlines the research problem. It also outlines the specific aims and objectives of this study.
- **Chapter 2 (Methodology):** This chapter describes all the techniques employed to achieve the aims and the objectives of this study. These techniques are described in terms of the rationale for using them, their basic principles, operation conditions and sample preparation. It also describes sampling strategies, the method used to estimate different components abundance and nomenclature used to describe the lithofacies.

- **Chapter 3 (Regional geology):** This chapter provides a general review of the geological setting and stratigraphy of the Huqf Supergroup, and a detailed description of the Ara Group in terms of basin development, palaeogeography, lithostratigraphy, Ara cycle evolution and lithofacies distribution, chemostratigraphy and chronostratigraphy.
- **Chapter 4 (Chert precipitation and distribution):** This chapter provides a description of silica geochemistry (diagenesis and solubility). It also provides a brief description of different types of cherts found in the sedimentary strata from the Precambrian to the present day. Cherts found in the geological record are described in terms of the controls on their precipitation and distribution. The secular change in chert distribution is also discussed in this chapter.
- **Chapter 5 (Lithofacies analysis and distribution):** This chapter describes and interprets the different lithofacies identified from this study within the Athel Silicilyte and bounding mudstones. It also discusses the vertical and the lateral variability of the Athel Silicilyte in the Athel Basin.
- **Chapter 6 (Inorganic geochemistry):** This chapter outlines the elemental concentrations including major, trace and rare earth elements of the Athel Silicilyte and bounding mudstones. These elements are described in order to provide a confirmation of the mineralogical concentrations identified from petrographical data, and lead on to a discussion of the likely silica source for the Athel Silicilyte and the redox conditions during precipitation.
- **Chapter 7 (Origin of the Athel Silicilyte):** This chapter brings the findings from the previous chapters (5 and 6) together to interpret the possible sources of silica in the Athel silicilyte and the likely mechanisms responsible for silica precipitation. This chapter also includes mass-balance calculations to estimate the mass of silica required to further constrain the silica source. Results from the reaction-path modelling are also included in this chapter to

test how diagenetic reactions might influence silica precipitation. The likely controls on the Athel Silicilyte distribution are discussed in this chapter.

- **Chapter 8 (Conclusions):** This chapter provides a full summary of the main findings from this study.
- **Appendices:** At the end of the thesis, three appendices are provided. Appendix I provides all available wireline logs and shows detailed lithofacies interpretation from each investigated well. Appendix II provide core and thin-section photographs from all sampled wells. Appendix III includes mineralogical composition, elemental concentrations and TOC of each analysed samples. Appendix IV shows the medium composition used in reaction-path modelling.

Chapter 2.

Methodology

2.1 Introduction

An extensive array of analytical methods was employed throughout this study; including core description, optical microscope, electronic microscope, framboidal pyrite size-distributions, X-ray diffraction (XRD), X-ray fluorescence (XRF), laser ablation-inductively coupled plasma-mass spectroscopy (LA-ICP-MS), total organic carbon (TOC), wireline logs interpretation/correlation and reaction-path modelling. This chapter briefly describes these techniques, their basic principles, the rationale for employing them, and provides a detailed description of sample preparation methods and specific instrument parameters. It also discusses the method employed to estimate different components abundance and nomenclature used to describe the lithofacies of the Athel Silicilyte.

The key data for this project were obtained from Petroleum Development of Oman (PDO), which are core samples and wireline logs, as well as porosity and spectral gamma ray data from core analysis reports. Core description and sampling were carried out at the core shed of PDO (Mina Al Fahel, Muscat), while the rest of analytical techniques and interpretations were carried out at the University of Manchester.

In order to interpret the Athel Silicilyte origin and lithofacies variability, different combinations of analysis were used. A combination of core description with the petrographic and geochemical techniques enabled different textures and mineralogy to be determined and imaged for each sample (e.g. Macquaker and Keller 2005; MacQuaker et al. 2007; Al Balushi et al. in press) and then lithofacies to be classified. The wireline log signature for each lithofacies was then determined in order to interpret lithological composition in uncored wells/intervals. Interpreting uncored wells/intervals facilitates the investigation of vertical and lateral variability at a basin scale. In addition, elemental concentrations (major, trace and rare earth elements) obtained from XRF and LA-ICP-MS analysis were employed to interpret silica source and redox conditions during Athel Silicilyte precipitation. Such techniques are widely used to determine sediment source and redox conditions during precipitation of fine grained rocks (e.g. Elderfield 1988; Emerson and Husted 1991; Murray 1994;

Zhang and Nozaki 1996; Morford et al. 2001; Sugitani et al. 2002; McLennan et al. 2003; Hofmann and Harris 2008).

2.2 Core description and sample collection

The Athel Silicilyte has been cored in six exploration wells in the South Oman Salt Basin (Fig. 2.1) over a range of stratigraphic intervals. In order to investigate the vertical and lateral variability of the Athel Silicilyte, cores were selected from different wells at different locations (basin centre and basin margin, Fig. 2.1) and from various stratigraphic intervals (Table 2.1 and Fig. 2.2). However, due to the limited availability of cores from the basin margin, the Athel Silicilyte is mostly sampled from Al Noor and Al Shomou fields in the basin centre (Fig. 2.1). From the basin margin, samples were only obtained from well MKZ-1 (Figs. 2.1 & 2.2), although the Athel Silicilyte was cored from another well (MMNW-7) at the basin margin but this core was not available. A complete stratigraphic section of the Athel Silicilyte Formation was fully cored from well ALNR-2 encountering a total thickness of 390 m from which the vertical variability is well investigated in this study. In other wells, however, only small intervals (few meters to 10s of meters; <10% of the total thickness of the Athel Silicilyte) were cored allowing mainly lateral variability to be investigated.

To ensure a detailed core description of the Athel Silicilyte, cores were cleaned to remove dust and then the surface was wetted to bring out textures. The cores were described and photographed using a digital camera (either Nikon D50 or Sony Cyber-shot cameras). In order to gain maximum details on textural and mineralogical information using petrographical and geochemical techniques, a total of 107 hand-specimens were collected from the Athel Silicilyte cores (Table 2.1). For comparison, between the Athel Silicilyte and the bounding silt-rich mudstones (from the bottom by the U Shale and from the top by Thuleilat Shale), a total of 10 hand-specimens were collected from U-Shale cores (Table 2.1). However, no samples from the Thuleilat Shale were analysed because when the core was requested for sampling, the wrong core was provided. The petrographical investigations reveal that the core provided was the Athel

Silicilyte core. In any case, the Thuleilat Shale is mineralogically and texturally similar to the U-Shale (Amthor et al. 2005; Schröder and Grotzinger 2007), and hence no further attempt was carried out to sample the Thuleilat Shale.

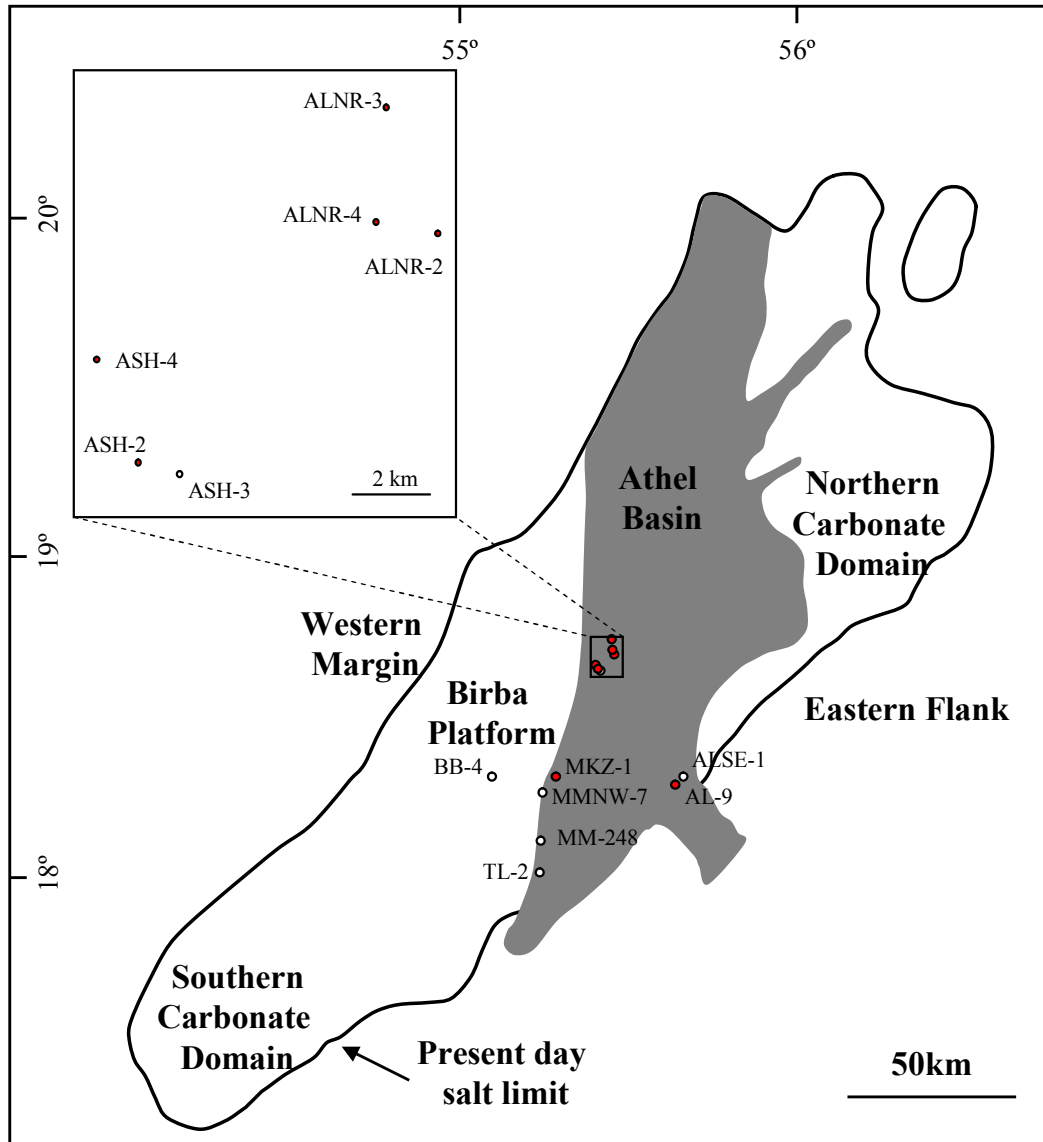


Figure 2.1. A map of the South Oman Salt Basin showing the Athel Basin (grey) and the carbonate platforms (white). Upper left rectangular shows enlarged map of wells in Al Noor and Al Shomou field. Wells in red color are the sampled wells and wells in white color are wells from which the wireline data were obtained in addition to the sampled wells. Modified after Amthor et al. (2005) and Schröder and Grotzinger (2007).

The initial sampling strategy was based on 1 sample every 25 cm, however, after laboratory analyses of the initial samples, insufficient heterogeneity was observed. In order to generate a detailed lithofacies description, three criteria were taken into account during sampling: (1) taking samples wherever textural or lithological changes were observed; (2) obtaining

samples at various depths that cover the full stratigraphic thickness; (3) capturing all lithofacies described by Amthor et al. (2005) and in the PDO core analysis report. Subsequently, the following samples were taken at wider ranges. The well names and the depths for each hand-specimen were recorded during sampling. The samples were then shipped to the University of Manchester for detailed analyses using petrographic and geochemical techniques. Core photographs from each sampled well are presented in Appendix II.

Table 2.1. Shows intervals and number of the samples collected from each well. Core photographs from each well are presented in Appendix II accompanied by a representative selections of thin-section microphotographs.

Well	Formation	Interval depth/ m measure depth(MD)	No. of samples
ALNR-2	Athel Silicilyte	3967- 4374	48
ALNR-3	Athel Silicilyte	3861- 3683, 4750-4786 and 4812-4832	16
ALNR-4	Athel Silicilyte	4220-4230	8
ASH-2	Athel Silicilyte	3810- 3811 and 3867-3876	8
ASH-4	Athel Silicilyte	4438-4444, 4543-4547 and 4645-4652	20
MKZ-1	Athel Silicilyte	2768.5 - 2774.7	7
AL-9	U-Shale	5676.5- 5706.8	10
Total			117

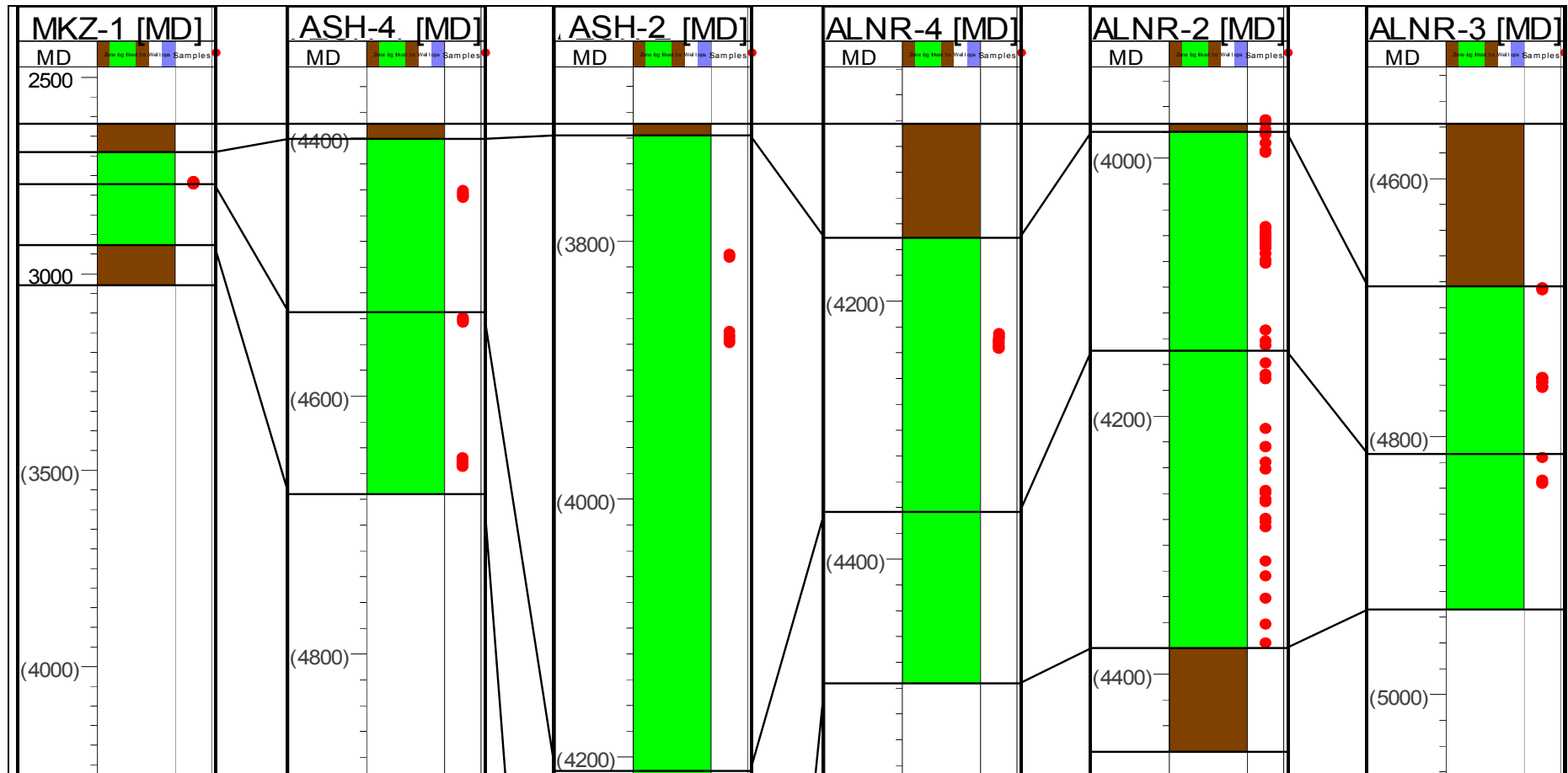


Figure 2.2. Shows the wells from which the Athel Silicilyte (green) was sampled. Red circles show sampled intervals (number of samples from each interval is shown in Table 2.1 above). Most samples are obtained from well ALNR-2 (48 samples) since it was fully cored. Well ASH-2 only shows the upper Athel Silicilyte and the lower Athel is truncated for the purpose of scale. Bounding silt-rich mudstones are shown in brown. Full stratigraphic thickness and interpretation of each well are presented in Appendix I and core photographs are presented in Appendix II. Note, distance between well is not to scale (well location is shown in Fig. 2.1).

2.3 Petrographic techniques

Three petrographical techniques were employed to characterise textures and mineral contents for the Athel Silicilyte including thin section scanning, optical and electron microscopic analyses. Thin section preparation and petrographical analyses were carried out at the Williamson Research Centre for Molecular Environmental Science, University of Manchester. Description of the petrographical techniques and operating conditions are outlined in the following subsections.

2.3.1 *Thin section preparation and scanning*

In preparation for petrographic analyses, polished thin sections of typically 20-25 μm thick were made from each hand-specimen on either a small (26 mm by 48 mm) or a large (50 mm by 70 mm) format glass slide. An oil (Castrol Ilocut 430) media was used to minimise sample damage caused by hydration of clays during sample preparation (e.g. Macquaker and Adams 2003; Adams et al. 2006). The thin sections were prepared in this way to enhance textural resolution during petrographic analyses.

Prepared thin sections were then scanned at low resolution in an Epson Perfection 4490 Photo flatbed scanner to obtain full images of the textures in each thin section. This technique enables determination of laminae continuity, type and their stacking pattern that are not always possible to image using microscopic analyses (e.g. Macquaker and Keller 2005; Al Balushi and Macquaker in press).

2.3.2 *Optical microscope*

In order to obtain more textural and mineralogical information, the thin sections were analysed optically at low to intermediate power in an optical microscope under both plane-polarised light (PPL) and cross-polarised light (XPL). The analysis was carried out using a Nikon Optiphot 2.0-POL microscope equipped by a Proges C10 Plus digital Camera. Pairs (PPL and XPL)

of photographs at different magnifications (2X, 4X, 10X and 20X) were recorded using a Progres Capture Pro. 2.0 software.

2.3.3 *Scanning electron microscope (SEM)*

Following thin section description, samples were described and analysed at high resolution in a SEM. The SEM analysis is extremely useful to analyse very fine grained rock, which enables high magnification images to be captured that show detailed textural and mineralogical information. Prior to the SEM analysis, the thin sections were carbon coated to increase electronic conductivity across analysed samples and prevent sample charging. The SEM analysis was performed on a JEOL 6400 scanning electron microscope equipped with a Link four-quadrant backscattered electron detector and Princeton Gamma-Tech (PGT) energy-dispersive spectrometer. The microscope was operated at 15 mm working distance at 20 kV and 1.5 nA. Both backscattered electron images (BSEI) and secondary electron images (SEI) of different magnification (ranging from X20 to X2500) were recorded digitally using Semafore software. Individual minerals present in each sample were identified on the basis of their different backscattered coefficients (η) and/or by elemental results from the energy dispersive spectrometer. A backscattered coefficient (η) is a value describing the efficiency of a solid to backscatter incident electrons and is a strong function of electron density (Lewis and McConchie 1994).

The photographs obtained from all petrographical techniques were then scaled and annotated using a software package of Adobe Illustrator or in Power Point. Colour and brightness correction to bring out textural and mineralogical details were carried out using a software package of either Adobe Photoshop CS2 or Microsoft Office Picture Manager.

2.3.4 *Pyrite framboid size-distributions*

Pyrite framboid size-distribution could indicate the redox-conditions during sediment accumulation (e.g. Wilkin and Barnes 1996; Wilkin et al. 1996; Wignall et al. 2005) and thus it was carried out to interpret redox conditions

during deposition of the Athel Silicilyte and the U Shale. In total, eight samples were analysed for pyrite framboid size-distributions, six from the Athel Silicilyte and two from the U Shale.

Pyrite framboids were measured from the prepared thin sections using a scanning electron microscope; sample preparation and operation conditions were the same as in subsection 2.3.3. The SEM was set in backscattered electron mode, which easily enabled identification of pyrite framboids based on their high backscattering coefficients (η) and morphology (e.g. Wignall and Newton 1998; Zhou and Jiang 2009; Wignall et al. 2010). Each sample was analysed over 5-10 closely spaced vertical transects across the sample (15-25 mm). Framboid size was measured directly from the SEM screen to the nearest 0.1 μm (e.g. Wilkin and Barnes 1996; Wilkin and Barnes 1997; Wilkin and Arthur 2001; Bond and Wignall 2010). At least 100 pyrite framboids were measured from each sample to ensure a maximum accuracy of pyrite framboid size-distributions. The measured size from the SEM screen is smaller than the true size in median section, but calculation shows that the deviation from the true framboid diameter is unlikely to exceed 10 % (Wilkin et al. 1996). The size-frequency distribution was used to calculate mean and maximum framboid diameters and standard deviation.

2.4 Geochemical techniques

Various geochemical techniques including X-ray diffraction (XRD), X-ray fluorescence (XRF), solid laser ablation-inductively coupled plasma-mass spectroscopy (LA-ICP-MS) and total organic carbon (TOC) analyses were conducted to quantify the mineralogical, elemental and organic carbon composition of the Athel Silicilyte. In preparation for the XRD, XRF and TOC analysis, a powder (50-100 g) from each hand-specimen (from which a thin section had been prepared) was obtained by machine-crushing to produce a homogeneous powder.

The XRD, XRF and LA-ICP-MS analyses were carried out at Manchester Geochemical Unit, University of Manchester, while the TOC analysis was

performed at the Department of Environmental and Geographical Sciences, Manchester Metropolitan University. The following subsections provide a detailed description of each technique, sample preparation and instrument operating conditions.

2.4.1 X-ray diffraction (XRD)

To identify as well as to confirm bulk-rock mineralogy (from the petrographic analyses), XRD analysis was undertaken on all samples. This analysis is widely used to identify minerals with crystalline or semi-crystalline structure if they are present in sufficient abundance (> 3-4%). An X-ray beam is diffracted differently by each mineral, dependent upon the atoms making up the crystal lattice and their arrangement (Fig. 2.3). Atomic layer spacing (*d*-spacing) of each mineral can be calculated by applying Bragg's Law ($n\lambda = 2d\sin\theta$) and consequently each mineral present in the sample will produce a unique set of diffraction peaks corresponding to *d*-spacings characteristic of its crystal structure (Lewis and McConchie 1994).

In preparation for the XRD analysis, 4-5 g of powder from each sample was dissolved in amyl acetate acid, then smeared on a piece of glass and allowed to air dry. After that, the samples were loaded and analysed on a Bruker Axs D8 Advance diffractometer operating at 40 kV and 40 mA. Each sample was scanned from 5° to 70° 2-theta at 0.02° per second. The patterns produced by X-ray diffraction were collected and analysed using software (Eva version 5.0), which calculates *d*-spacing and consequently identifies each mineral present by comparison to a standard database (ICDD: International Centre for Diffraction Data).

Mineral quantification was carried out using Siroquant software (version 2.0). This is a Rietveld based software that quantifies minerals by generating a scan with a known mineralogy and match it to collected XRD pattern of the sample (Taylor 1991). Consequently, Siroquant software quantifies mineralogical content (in weight percentage) of the collected scan by XRD analysis. In total 13 samples were analysed in this software out of 117 samples

that were analysed by XRD. This software showed very small errors, average error of the 13 analysed samples is 0.8 % (ranges 0.29 % to 1.48 %). The mineral quantification for the rest of samples was estimated semiquantitatively by comparing the XRD peak intensities from each sample to those quantified by Siroquant software in addition to estimation derived from petrographical data (see subsection 2.7 below).

2.4.2 *X-ray fluorescence (XRF)*

In order to determine the concentrations of major and trace elements, XRF analysis was applied to all samples. This analysis is a non-destructive analytical technique that is widely used to identify and quantify elements present in minerals and rocks (Fig. 2.3). The XRF analysis can detect elements at very low concentration (sub ppm), as long as they are included in the used machine standard. The XRF spectrometer produces X-rays targeting the sample; elements present in the sample will emit fluorescent X-ray radiation with discrete energies that are characteristic for each element. These energies are revealed as characteristic peaks. The different elements present in the sample are identified by the energy of the peaks (qualitative analysis), while the peak intensity of each element provides the elemental concentration (quantitative analysis; Brouwer 2003).

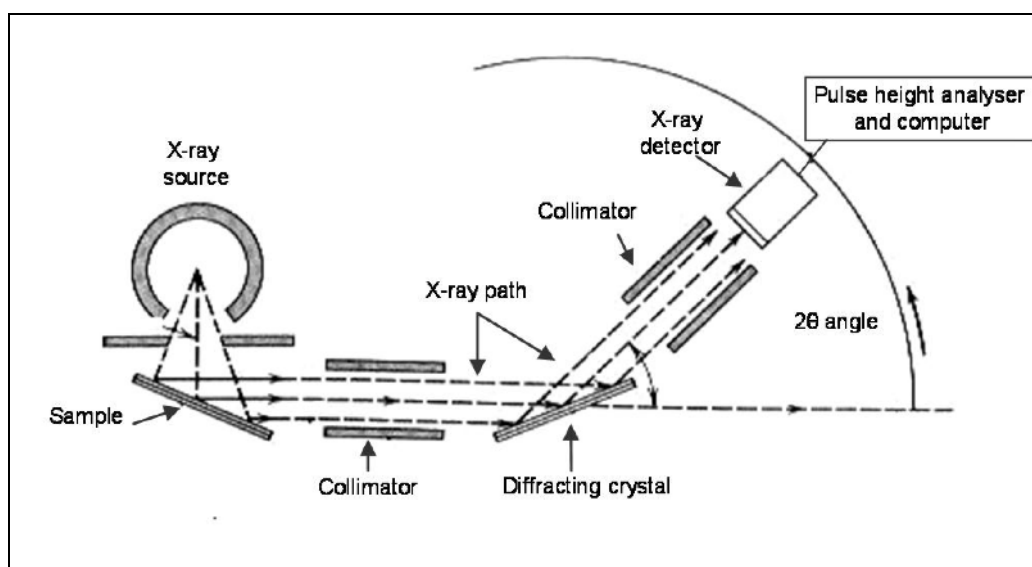
In preparation for the XRF analysis, a powder of 12 g from each sample was mixed with 3 g of Hoechst Wax C. The mixture was formed into a pellet by pressing it under high pressure. The prepared pellet was then analysed in an Axios Sequential XRF Spectrometer operating under normal conditions (voltage and current were varied depending on elements to be identified). Results acquired from the XRF machine were analysed in SuperQ and ProTrace softwares for major and trace element concentrations, respectively. This machine is calibrated by running internal standard, e.g. National Institute of Standards and Technology (NIST 2711 and NIST1880a), during analysis. The machine has a very small error (average for the major oxides and trace elements is 1.8 % and 4.5 %, respectively; Table 2.2 & 2.3).

Table 2.2. Shows comparison between measured major oxide concentrations by XRF and certified concentration of a reference material (sample AGV-1)

Element	Na ₂ O	MgO	Al ₂ O ₃	SiO ₂	K ₂ O	CaO	Fe ₂ O ₃	TiO ₂
Measured concentration (%)	4.26	1.49	16.59	58.3	2.98	4.88	6.66	1.08
Certified concentration (%)	4.26	1.53	17.15	58.84	2.92	4.94	6.77	1.05
Error (%)	0.0	2.6	3.3	0.9	2.0	1.2	1.6	2.9

Table 2.3. Shows comparison between measured trace element concentrations by XRF and certified concentration of a reference material (sample GBW07405). Error presented are only for interpreted trace element in this study

Element	V	Mn	Y	Zr	Mo	La	Ce	Nd	U
Measured concentration (ppm)	156.4	1370	23.5	283.4	4.6	36.2	97.5	22.2	6.6
Certified concentration (ppm)	166	1360	21	272	4.6	35.7	91	24	6.5
Error (%)	5.8	0.8	11.9	4.2	0.0	1.4	7.1	7.5	1.5

**Figure 2.3.** Schematic illustration of the major components in the XRD and the XRF analysis. Although the same principles applied for both analyses, a different detector is used in each analysis. The detector used in the XRD analysis detects diffracted X-rays by minerals, while in the XRF analysis fluorescent X-rays emitted by elements present in analysed sample are detected. Modified after Klein et al. (1993).

2.4.3 *Laser ablation-inductively coupled plasma-mass spectroscopy (LA-ICP-MS)*

LA-ICP-MS analysis was employed to identify concentration of rare earth elements (REEs) that were not included in the XRF standard, only four REEs (La, Ce, Nd and Y) identified by XRF analysis. The LA-ICP-MS analysis works by focusing a pulsed laser beam on to a sample surface targeting either a defined spot or a line along the sample (Fig. 2.4). Pulses of the laser beam cause very rapid heating, which in turn, causes the matrix to be volatilised or ablated, creating a laser-induced aerosol. The aerosol is then transported to the ICP in an argon carrier gas stream where it is decomposed, atomised and then ionised by removing one electron from each atom. These ions are separated and collected according to their mass and charge ratios in the mass spectrometer (MS) creating a mass spectrum. The magnitude of each peak in the spectrum is directly proportional to the concentration of an element in a sample which then measured by comparing signal intensities to those generated by calibration standards.

Prior to the LA-ICP-MS analyses, pieces (around 20 by 15 mm and thickness of 5 mm) from 21 selected hand-specimens (17 from the Athel Silicilyte and five from the U Shale) were taken from the same area where thin sections were previously made (to ensure a precise ablation of the required minerals identified previously from the petrographic analyses). Each piece was then fitted in a rounded disk made of resin and the samples upper surface was exposed. To ensure a clear view of textures and minerals present in the sample, the upper surface was polished and then cleaned using acetone [(CH₃)₂CO] to remove any dust that might affect elemental concentrations during analysis. The LA-ICP-MS analysis was performed on a New Wave Research-Merchantek Product Up 213 laser ablation connected to a Agilent 7500 Series ICP-MS.

Each disk was then uploaded to the ablation chamber, which was purged with argon gas and connected to a high magnification video camera, enabling a high-resolution image of the sample to be viewed on the ICP-MS monitor directly. Since the Athel Silicilyte is predominately composed of very small silica crystals (1-5 µm) and available laser diameter is 100 µm, the samples were

ablated along a line defined from the ICP-MS monitor for 17 seconds at a speed of 10 μm per second. The line was defined along silica-rich layers to ensure that measured REE concentrations were only from silica crystals and to minimise REE detection from terrigenous material. Results were collected using ICP-MS Top Mass Hunter software that is calibrated by a standard (NIST: National Institute of Standards and Technology 610 Standard Glass Reference).

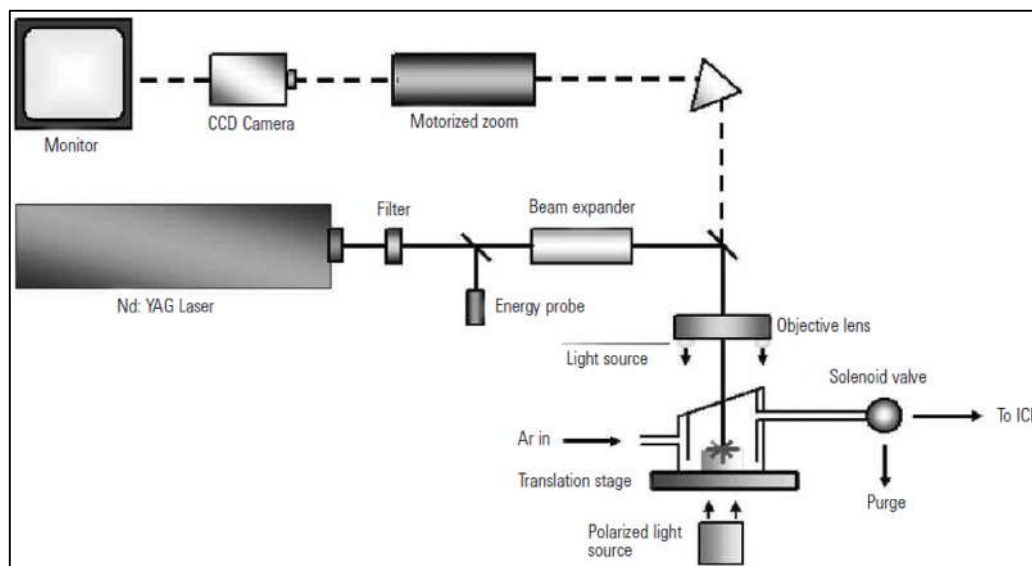


Figure 2.4. Schematic illustration of the components in a laser ablation system. The analysed sample is ablated using Nd:YAG (neodymium doped yttrium aluminium garnet crystal) laser in the laser chamber purged with argon gas. The laser-induced aerosol in the ablation chamber is then transported to an ICP-MS for element concentration calculation (from Agilent 2005).

In order to check the accuracy of the results, the four REEs (La, Ce, Nd and Y) with a concentration that had been previously determined by the XRF analyses were analysed again using the LA-ICP-MS technique. The concentrations of these elements were consistently 5.0 times higher than their concentration from the XRF analysis (Fig. 2.5; Appendix III). This higher concentration measured by the LA-ICP-MS technique is attributed to the higher amount of sample material picked by the laser compared to the standard used since the sample are softer than the standard. To correct those results obtained from the LA-ICP-MS analysis, concentration of the four REEs determined from the XRF analysis were used. The machine used for the XRF analysis shows very small error for trace element concentration between measured and certified values of a reference material (average error $\approx 4.5\%$; Table 2.3 above). To

further test the XRF machine accuracy, element (K, Th, and U) concentrations of selected samples from the XRF analysis was compared to their concentrations from spectral gamma ray data. A good correlation between XRF and spectral gamma ray results was found from samples at the same depth. The XRF results are therefore confidently used to correct LA-ICP-MS results by dividing them by a factor of 5.0. In addition, the REE results are interpreted in this study using REE ratios from the same sample, and thus absolute concentration of REEs from this technique should not affect REE ratios.

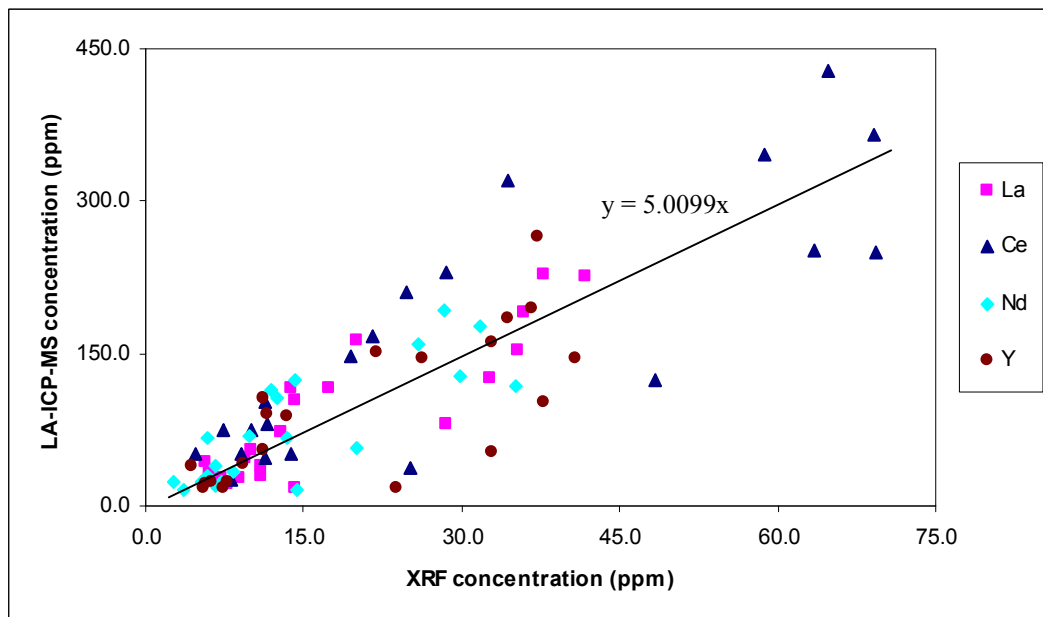


Figure 2.5. Element concentrations from the XRF and the LA-IC-MS analysis from 21 samples. The LA-ICP-MS results were corrected according to mutual element concentrations from XRF analysis. Element concentrations from the LA-ICP-MS analysis are 5.0 times higher.

2.4.4 Total organic carbon (TOC)

In order to measure the volume of organic carbon within the Athel Silicilyte and the U Shale, TOC analysis was performed on 50 selected samples. Around 0.1-0.2 g of powder from each sample was digested by adding a few drops of 1 molar hydrochloric acid (HCl) until no more CO₂ bubbles were observed. The digested powder was then dried in an oven at 45 °C for 2 hours. Combustion followed in a Leco TruSpec-CN machine at 950 °C and the evolved CO₂ was measured and considered to be representative of the TOC, assuming all carbonate carbon was removed by the acid digestion. The machine was calibrated

by running a standard with known TOC value three times prior to sample combustion.

2.5 Wireline log interpretation

Due to the limited number of cores covering the full stratigraphic thickness of the Athel Silicilyte, as well as to generate a better understanding of lateral and vertical variability of the Athel Silicilyte across the basin, subsurface wireline log data were obtained for this study. Different wells were selected on the basis of their paleogeographic location in the basin (.e.g. platforms, basin margins and basin centre, Fig. 2.1) covering the full stratigraphic thickness of the Athel Silicilyte as well as bounding silt-rich mudstones. In total 12 wells were chosen including wells from which the cores were sampled. The wells selected for correlation were ALNR-2, ALNR-3, ALNR-4, ASH-2, ASH-3, ASH-4, AMSE-1, MKZ-1, BB-4, MMNW-7, MM-248 and TL-2 (Fig. 2.1). Wireline log data for all wells were supplied by PDO, and were loaded in Petrel Well Correlation software at the Basin Studies computer station, University of Manchester.

The log loaded to Petrel are:

- 1) Gamma-ray (GR): the GR log measures natural radioactivity of formations. The main radioactive element in rocks is potassium (K), uranium (U) and thorium (Th), which are normally abundant in clay mineral and organic-matter rich facies (e.g. shale), whilst they are relatively less abundant in clean sandstone and carbonate rock. Thus, GR is a very important tool for identifying lithology. The radioactivity of the formation is measured in American Petroleum Institute units (API; standard calibrated units to a reference with known level of radioactivity). GR logs are displayed here in a scale from 0-150 API.
- 2) Sonic: the sonic log measures formation sonic transit time (DT) by sending compressional wave from the tool through the formation and measures the wave first arrival time at two receivers. The travel time will depend on the formation mineralogy and porosity. This log can

be used in combination with other logs to characterise the formation mineralogy and porosity. Sonic logs in this study are displayed in a scale from 40-200 $\mu\text{s/m}$.

- 3) Density: this log measures formation bulk density by emitting gamma radiation into the formation and records the amount of gamma radiation returning from the formation. Emitted gamma ray loses its energy as it collides with the electrons in the formation. Therefore, the drop in returning energy level is a function of electron density of the atoms in the formation, which is, in turn, directly related to the bulk density of the formation. Density logs are displayed here in a scale from 1.95-2.95 g/cm^3 .
- 4) Neutron: the neutron log is produced by bombarding the formation with high energy neutrons from a radioactive source. Decline in neutron energy levels in the formation is primarily caused by collisions with hydrogen atoms. Hence, the decline in neutron energy levels is directly proportional to hydrogen content. Hydrogen is found in gas, oil and water (occupying pore spaces) but not in minerals. Therefore, the response of the neutron log is essentially correlative with the formation porosity. Because clay minerals contain bonded water, the neutron log is reading higher porosity than actually exist in clay-rich facies. The neutron log is measured in either sandstone or limestone porosity unit (SPUs and LPU, respectively). These units should give the correct porosity of the formation providing the matrix is pure quartz (SPUs) or calcite (LPU) and the pores are filled with fresh waters. Neutron logs are displayed in this study in a reverse scale from 0.45 to -0.15 LPU.
- 5) Porosity: the porosity logs in this study are calculated using the density log since the density log shows close porosity values to the measured porosity (from core plugs) compared with the neutron log. The bulk density from the density log represents the sum of the density of the matrix (P_{ma}) and the density of the fluid (P_{f}). Porosity was calculated using the following equation (e.g. Selley 1998):

$$\text{Porosity (\%)} = P_{\text{ma}} - P_{\text{b}} / (P_{\text{ma}} - P_{\text{f}})$$

Where P_{ma} and P_f are calculated to be 2.58 g/cm^3 1.16 g/cm^3 , respectively (densities measured in PDO).

Log shift data to match core data were provided by PDO. However, MKZ-1 log shift data were not available and therefore elemental concentrations of U, Th, and K from both the spectra gamma ray and the XRF analysis were used to determine how far the core data should be shifted to match wireline log data.

The ALNR-3 well shows two slabs of the Athel Silicilyte separated by salt (Appendix I). The upper slab is inverted as a result of salt movement and hence, the Athel Silicilyte GR trend is different from other wells. Generally, GR values increase from the Lower to Upper Athel Silicilyte. MKZ-1 well also shows a GR trend similar to the ALNR-3 upper slab and therefore it is also interpreted to be inverted.

Five major surfaces were interpreted from each well (from top to bottom): (1) Salt base/Thuleilat Shale top; (2) Thuleilat-Shale base/Athel Silicilyte top; (3) Upper/Lower Athel Silicilyte; (4) Athel Silicilyte base/U-Shale top; (5) and U-Shale base. All major surfaces indicate changes lithology (from top to bottom; salt-mudstone-chert-mudstone) apart from the upper/lower Athel Silicilyte surface, which is marked by an increase in GR response. Major surfaces were mainly interpreted by the change in GR response with the aid of PDO stratigraphic interpretation from well completion logs. All wells were hung on the Salt base/Thuleilat Shale top surface and major surfaces were then correlated to investigate thickness variation of Athel Silicilyte and bounding silt-rich mudstones across the basin. After that, the wireline log signature was determined for each lithofacies, which are identified from core data, petrographic and geochemical analyses. Different lithofacies log signatures were then used to facilitate interpretation of the uncored intervals/wells. After interpreting different lithofacies from each well, their distribution, abundance and thickness variation in each well were investigated to interpret their vertical and lateral variability across the basin. No attempt was made to correlate minor lithofacies between

wells as they are very thin or show unsystematic alternation. Detailed interpretation of each well is provided in Appendix I.

2.6 Reaction-path modelling

In order to understand the controls on the precipitation of silica in the Athel Silicilyte, reaction-path modelling was carried out using the React tool in Geochemist's Workbench Standard 6.0 software. The reaction-path modelling was proceeded by theoretically creating an aqueous medium (1kg of water) under defined pressure and temperature, adding a dissolved species concentration (i.e. seawater composition) and using 1 mg of acetate as a reactant (i.e. organic matter). The reaction was then run at a scale from 0 (start) to 1 (end) and its effect on species concentration, mineral saturation and pH can be plotted against the reaction path variable.

By modifying seawater composition, e.g. dissolved species concentration (oxygen, silica, sulphate, iron), different diagenetic reactions will take place (e.g. iron-reduction and sulphate-reduction). The effect of different diagenetic reactions on silica precipitation therefore can be tested. Initial parameters used in the modelling to represent seawater composition are shown in Appendix IV.

2.7 Constituents abundance and lithofacies nomenclature

The combination of microscopic analyses and geochemical analyses (XRD and XRF) enabled textures and individual minerals to be determined. After different minerals were identified, their abundance in each sample was estimated in order to generate a detailed description of the lithofacies variability. Abundance of each constituent was estimated semiquantitatively using a percentage estimation chart (e.g. Toker 2003, p. 33) by comparing optical and electron microscopic images, ranging from X2 to X2500, with help from the XRD, XRF and TOC results. The abundance of the constituents in each sample is reported in Appendix III (Table 1).

The nomenclature used to describe the lithofacies in this study was selected in order to be representative of the textures and mineralogical composition of each lithofacies. The nomenclature used in this study was proposed by Macquaker and Adams (2003) to describe mudstone (sedimentary rock containing >50 % grains <63.5 μm) based on the presence of sedimentary structures and abundance of all constituents forming more than 10 % of rock volume. A lithofacies composed of a material that represents more than 90 % of the rock volume is described as “dominated” by that component, “rich” if it represents 50-90 % of the rock volume, and “bearing” by the component if it only represents 10-50 % of the rock volume. Sedimentary features present in a certain lithofacies are added into this nomenclature by prefixing the rock name with the name of sedimentary features (Macquaker and Adams 2003).

Due to the low abundance (< 10 %) of individual detrital minerals (e.g. clays, quartz, feldspar) in the Athel Silicilyte, they are considered together as one component and termed as “detritus”. For example, a laminated lithofacies that is composed of 87 % of microcrystalline quartz, 5 % quartz grains and 8 % clay minerals will be described as “laminated microcrystalline quartz-rich, detritus-bearing mudstones”. Using this nomenclature enables more precise description of the lithofacies in terms of the compositions and textures and it helps to identify and to interpret the variability of the Athel Silicilyte.

Chapter 3.

Regional geology

3.1 Introduction

In order to understand the South Oman Salt Basin development and its spatial and temporal facies distribution, it is important to review the regional geology of the Huqf Supergroup. This will help in interpreting the origin and lithofacies variability of the Athel Silicilyte. This chapter therefore briefly describes the geological setting and stratigraphy of the Huqf Supergroup, and provides a detailed description of the Ara Group basin development, palaeogeography, lithostratigraphy, Ara cycles evolution, lithofacies distribution, chemostratigraphy and chronostratigraphy. At the end of this chapter, the sediments associated with the Precambrian-Cambrian boundary will be interpreted based on available published data.

3.2 The Huqf Supergroup: an overview

The Huqf Supergroup is one of the best preserved and most continuous sections of Late Neoproterozoic to Early Cambrian strata (Schröder et al. 2004; Amthor et al. 2005; Fike and Grotzinger 2008). Within these rocks, many key biogeochemical and biological changes are recorded, associated with the early evolution of life (e.g. Mattes and Morris 1990; Grotzinger et al. 1995; Knoll and Carroll 1999; Amthor et al. 2003; Schröder et al. 2004; Fike et al. 2006; Schröder and Grotzinger 2007; Fike and Grotzinger 2008; Wille et al. 2008). Furthermore, the Huqf Supergroup has a high hydrocarbon potential, especially the upper part of the Ara Group, which is the main exploration target in the South Oman Salt Basin (Figs. 1.1 & 3.3; Schröder et al. 2003; Al-Siyabi 2005; Amthor et al. 2005). The Huqf Supergroup, therefore, has been extensively studied for its scientific and economic importance (e.g. Nicholas and Brasier 2000; Al-Siyabi 2005; Amthor et al. 2005; Fike et al. 2006; Allen 2007; Schröder and Grotzinger 2007; Schoenherr et al. 2009; Gold 2010).

During the late Precambrian to Cambrian, Oman was located to the southeast of the Arabian Peninsula. Sediments were deposited in basins that form part of a northeast-southwest trending system of restricted, marine-fed intracratonic basins (Fig. 3.1; Mattes and Morris 1990; Loosveld et al. 1996;

Amthor et al. 2005; Allen 2007). The structural alignment of these basins suggests that this system stretched from the Indian Craton across the Arabian Shield (Fig. 3.1; Mattes and Morris 1990; Grotzinger et al. 2002; Amthor et al. 2005; Allen 2007). In the Oman Interior, the lower interval of these basins are filled with sedimentary strata of the Huqf Supergroup (Neoproterozoic to Early Cambrian in age) and overlie an early Neoproterozoic crystalline basement (Gorin et al. 1982; Brasier et al. 2000; Allen 2007). The Huqf Supergroup comprises three main groups (from base to top): 1) Abu Mahara; 2) Nafun and; 3) Ara. Fig. 3.2 shows the Huqf Supergroup stratigraphic, lithologic, geochronologic, biostratigraphic and chemostratigraphic constraints. The Abu Mahara and Nafun groups are defined from outcrop and subsurface data, whereas the stratigraphy of the Ara Group is well constructed from subsurface data (Al-Siyabi 2005; Amthor et al. 2005). Time and lithostratigraphic equivalent outcrops of the Ara Group are also found in the Huqf area and in the Oman Mountains (Fig. 1.1) overlying the upper Nafun Group sediments (Brasier et al. 2000; Nicholas and Brasier 2000; Gold 2010).

The Abu Mahara Group consists of two intervals of glacially-derived clastic sediments separated by non-glacial deep to shallow-marine clastic and volcanic rocks (Loosveld et al. 1996; Leather et al. 2002; Allen 2007; Bowring et al. 2007). Seismic images indicate the presence of large, N-S oriented basins of a rift origin during deposition of the Abu Mahara Group. The formation of these basins was probably related to regional extension, possibly due to large-scale strike-slip tectonics, associated with subsidence and volcanism (Loosveld et al. 1996; Leather et al. 2002; Le Guerroue et al. 2005; Worthing 2005; Allen 2007).

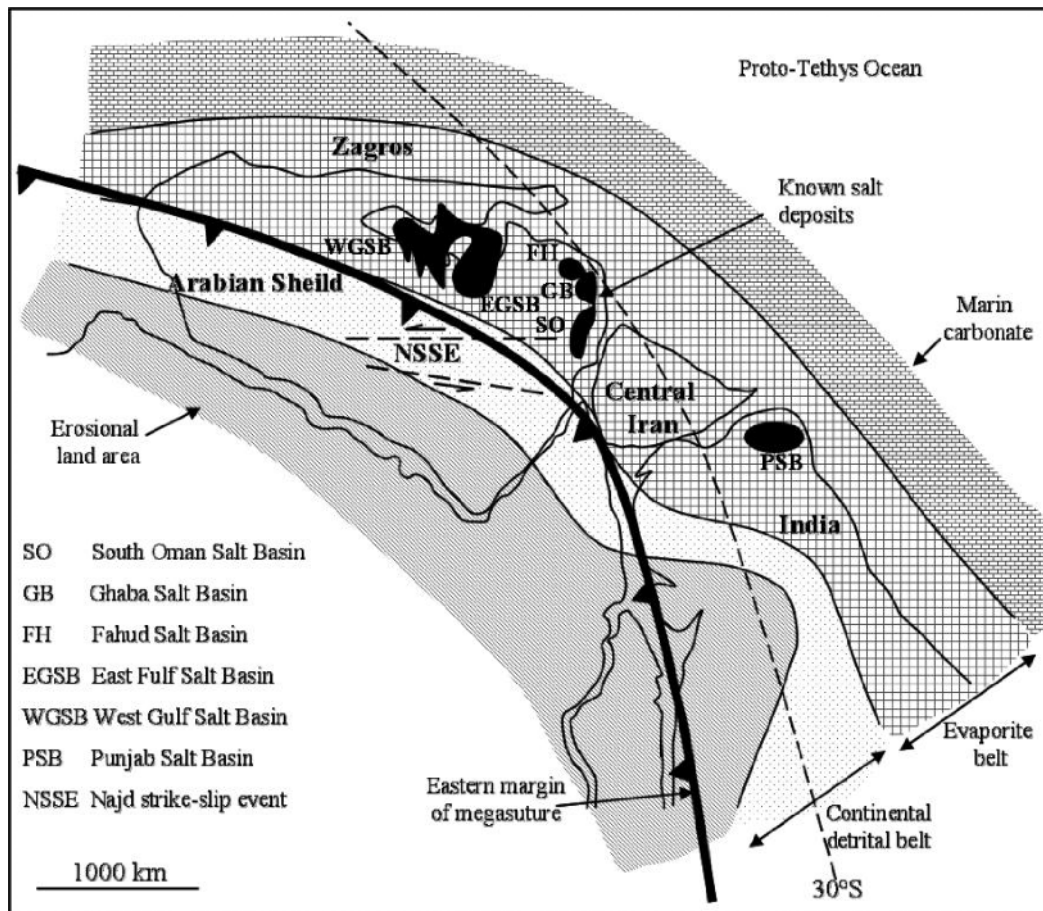


Figure 3.1. Restored map of NW Gondwana reconstruction at the end of the Neoproterozoic showing an evaporite belt extending along 30°S palaeolatitude. Oman was bounded to the south by the Arabian Shield detrital belt and to the west by Central Iran Craton. The open ocean of Proto-Tethys Ocean was located to the north of Oman. It also shows the Najd strike-slip tectonic event (dated 600-540 Ma; Husseini and Husseini 1990; Loosveld et al. 1996), which is linked to the development of NE-SW trending system of restricted basins in the Oman Interior. Modified after Allen (2007).

The Nafun Group comprises a 1 km thick succession that can be subdivided into two cycles of siliciclastic to carbonate sediments (Le Guerroue et al. 2006a; Le Guerroue et al. 2006b; Allen 2007). The lower cycle consists of marine mudstones, siltstones and tidal-wave sandstones of the Masirah Bay Formation that pass gradationally into the progradational carbonate ramp of the Khufai Formation (Allen and Leather 2006; Allen 2007). A similar lithological order is repeated in the upper cycle from the gradational Shuram Formation siliciclastics into the progradational Buah Formation limestones (Cozzi et al. 2004a; Cozzi et al. 2004b; Allen 2007). On regional seismic lines, the Nafun Group appears as an extensive sheet above the structurally confined Abu Mahara Group (Loosveld et al. 1996; Allen 2007). Therefore, the Nafun Group deposits represent extensive regional subsidence, which enhanced the accumulation of

open- to shallow-marine sediments (Loosveld et al. 1996; Cozzi et al. 2004a; Allen 2007). In the absence of any intrabasinal magmatism within the Nafun Group deposits, the Nafun basin subsidence could be explained by thermal relaxation of the lithosphere following the Abu Mahara rifting (Loosveld et al. 1996; Allen 2007; Bowring et al. 2007). Alternatively, it could be linked to dynamic subsidence in a retro-arc setting, related to westward subduction of an oceanic slab beneath the Arabian Plate from the north-eastern margin of Gondwanaland (eastern Oman; Grotzinger et al. 2002; Cozzi et al. 2004b).

Renewed tectonism, volcanism and rapid basin subsidence marked the end of Nafun Group and the beginning of Ara Group accumulation (Amthor et al. 2005; Allen 2007; Bowring et al. 2007). Rapid Ara basin subsidence suggests a shift from extensive regional subsidence in the Nafun basin to sedimentation in a more active tectonic setting (Loosveld et al. 1996; Immerz et al. 2000; Allen 2007; Bowring et al. 2007), possibly related to the Najd NW-SE strike-slip tectonic event in western Saudi Arabia (Fig. 3.1; Hussein and Hussein 1990; Loosveld et al. 1996) and subduction of the ocean floor beneath the Arabian Plate (Allen 2007). Thick sequences of felsic volcanic rocks overlying the Buah Formation of the upper Nafun Group are found in both North Oman (as the lower part of the Fara Formation) and South Oman (Abu Butabul; Nicholas and Brasier 2000). The presence of such felsic rocks and deep-water facies in the lower Ara Group are consistent with the interpretation of a transition from the Nafun Basin to the Ara Basin that was associated with volcanism and fault-related subsidence (Amthor et al. 2003; Amthor et al. 2005; Allen 2007; Bowring et al. 2007).

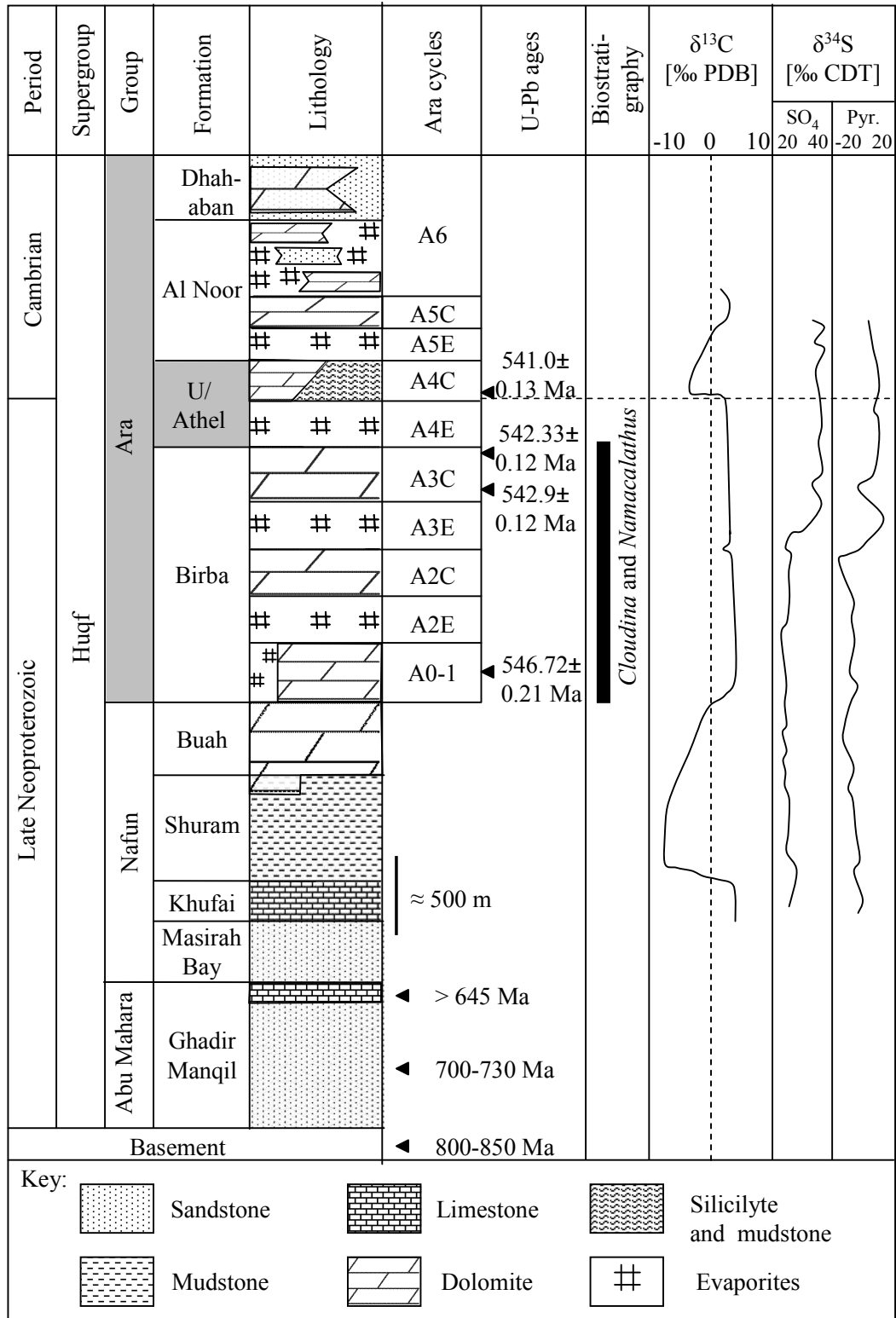


Figure 3.2. Simplified stratigraphic log of the Huqf Supergroup showing its main groups, formations and lithologies (Mattes and Morris 1990; Loosveld et al. 1996; Schröder et al. 2004). The Ara Group is highlighted in grey. The A4 cycle comprises evaporites at the base, overlain by carbonates, mudstones and a chert unit of the Athel Silicilyte. The lower A4C cycle straddles the Precambrian-Cambrian boundary, constrained by U-Pb age-dating of 541 Ma (Bowring et al. 2007), which coincides with a negative $\delta^{13}\text{C}$ excursion and extinction of *Cloudina* and *Namacalathus* fossils (Amthor et al. 2003). Sulphur isotopes in sulphate and pyrite show parallel enrichment during Ara time (Fike and Grotzinger 2008).

The tectonic style of deformation of the Nafun-Ara transition is characterised by uplift of large basement blocks that compartmentalised the broader Nafun basin into three fault-bounded smaller-scale basins: South Oman Salt Basin, Ghaba Salt Basin and Fahud Salt Basin (Fig. 1.1; Immerz et al. 2000; Amthor et al. 2005; Allen 2007). The western margin of these salt basins is delineated by complex transpressional deformation fronts (Western Deformation Front and Ghudun-Khasfah High; Fig. 1.1), which acted as a clastic-sediment source in the upper strata of the Ara Group (Loosveld et al. 1996; Immerz et al. 2000; Amthor et al. 2005.). In contrast, the eastern margin of these basins is characterised by onlap and thinning of the basin strata onto a structural high of the Huqf-Haushi Axis (Fig. 1.1; Amthor et al. 2005).

Sedimentation during deposition of the Ara Group was characterised by cyclic alternation of evaporites and carbonates (Fig. 3.2), suggesting a repeated restriction and flooding from the open seaway, associated with a shift to a more arid climate during this period (Mattes and Morris 1990; Schröder et al. 2003; Amthor et al. 2005). Basin restriction from the open ocean was probably caused by construction of new topography in the subduction zone or by the uplifted blocks that compartmentalised the broader basin (Allen 2007). Each flooding event replenished the water mass of the salt basins through short-lived connectivity with the open ocean. At this time, the Proto-Tethys Ocean was located towards the north of Oman (Fig. 3.1; see Allen 2007 for more detailed discussion on the Gondwana assemblage). Evidence for the open seaway connection with the South Oman Salt Basin includes high bromine concentrations (45 to 110 ppm) in halite, which is consistent with a marine origin of the halite-precipitating brine (Schröder et al. 2003). Furthermore, the presence of *Cloudina* and *Namacalathus* fossils, which are found exclusively in marine facies (Germis 1972; Mattes and Morris 1990), in the Ara carbonates suggests periodic connectivity with the open ocean (Amthor et al. 2003).

3.3 Ara Group tectonism and palaeogeography

During the deposition of the Ara Group, the South Oman Salt Basin (Fig. 3.3) was also further segmented by localised subsidence, related to basement

block faulting (Immerz et al. 2000; Grotzinger et al. 2002; Allen 2007). Consequently, the South Oman Salt Basin was subdivided into three palaeogeographical domains. These domains include two carbonate platforms (Eastern Flank and Birba Platform) separated by a deep, sediment-starved basin of the Athel Basin (Figs. 3.3-3.5; Amthor et al. 2005; Schröder and Grotzinger 2007). There are several lines of evidence to suggest differential and repeated subsidence of these domains, which controlled the pattern of sediment accumulation, in particular:

1. Precipitation of thick evaporites on top of the Birba Platform (Fig. 3.5) required a high level of subsidence that led to significant creation of accommodation for evaporites to precipitate (Schröder et al. 2003; Amthor et al. 2005; Schröder et al. 2005; Bowring et al. 2007).
2. On the Eastern Flank Platform, evaporite-free carbonate sediments are encountered (Fig.3.5), suggesting reduced accommodation due to lower subsidence rates (Schröder et al. 2003; Amthor et al. 2005).
3. The Athel Basin contains both shallow-shelf and basinal facies separated by a shelf edge (Fig. 3.5; Mattes and Morris 1990; Amthor et al. 2005).

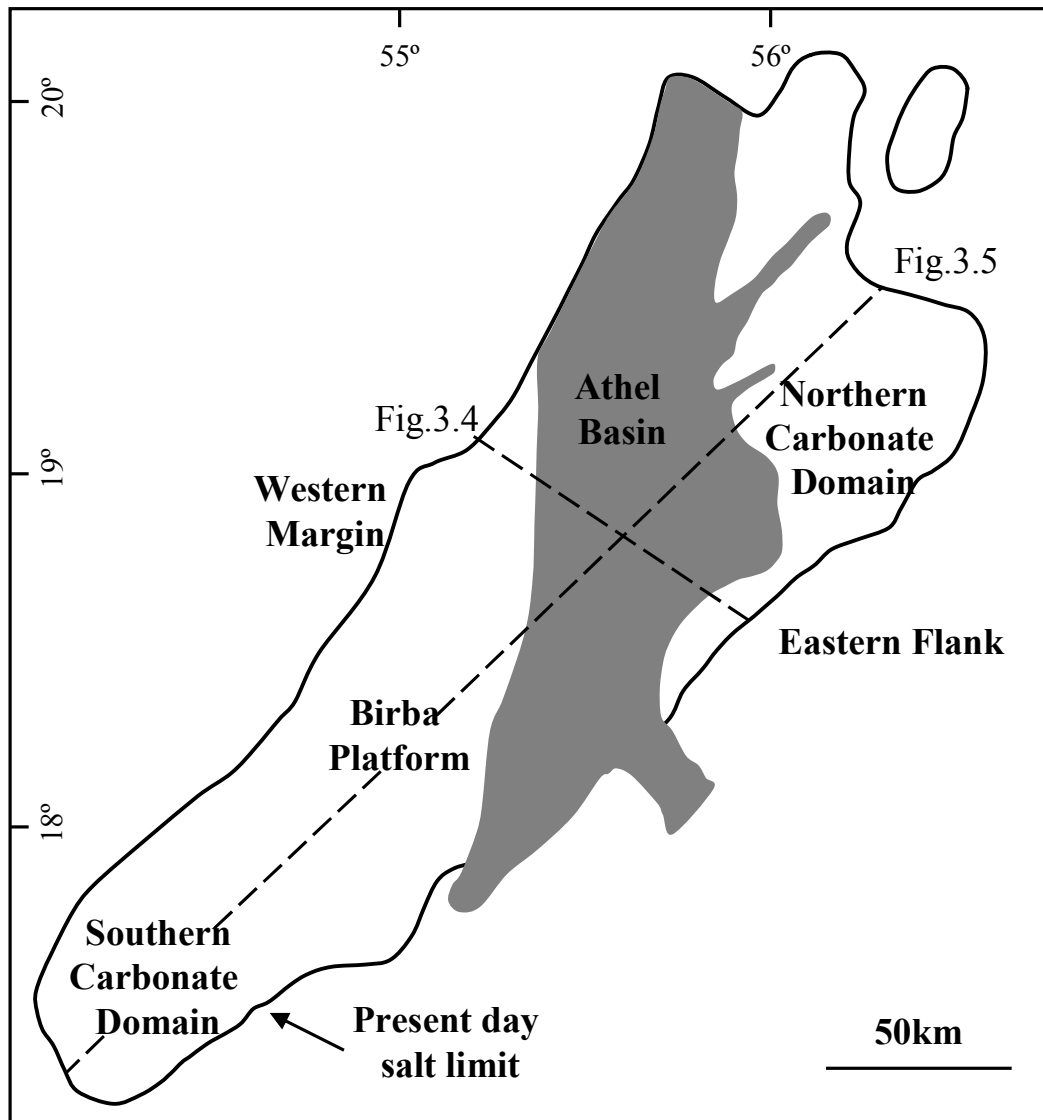


Figure 3.3. Enlargement map of the South Oman Salt Basin showing the two carbonate platforms of Birba and Eastern Flank and between them the Athel Basin. The Athel Silicilyte and mudstones of the A4C cycle precipitated only in the Athel Basin, while the time-equivalent carbonate rocks precipitated on the platforms. Modified after Amthor et al. (2005) and Schröder and Grotzinger (2007).

Platform areas became sites for carbonate deposition, while organic-rich mudstones and cherts of the Athel Silicilyte accumulated in the Athel Basin during transgressive and highstand conditions. Evaporites accumulated on platform areas and in the Athel Basin during lowstand conditions. Repeated subsidence, restriction and flooding of the South Oman Salt Basin result in at least six third-order shallowing-upward carbonate-evaporite cycles termed A0/A1 to A6, from bottom to top (Fig. 3.2; Amthor et al. 2005). The basal Ara carbonate unit (A0) appears to have been precipitated prior to basin restriction as it contains no evaporites. Each subsequent cycle contains carbonates (A1C-A6C,

C stands for carbonate) and evaporites (A1E-A6E, E stands for evaporite). Hence, each carbonate unit is enclosed between two evaporite units, one from the same cycle and one from the overlying cycle. Ara Group lithostratigraphy and basin reconstruction are discussed in detail in subsections 3.4 and 3.5.

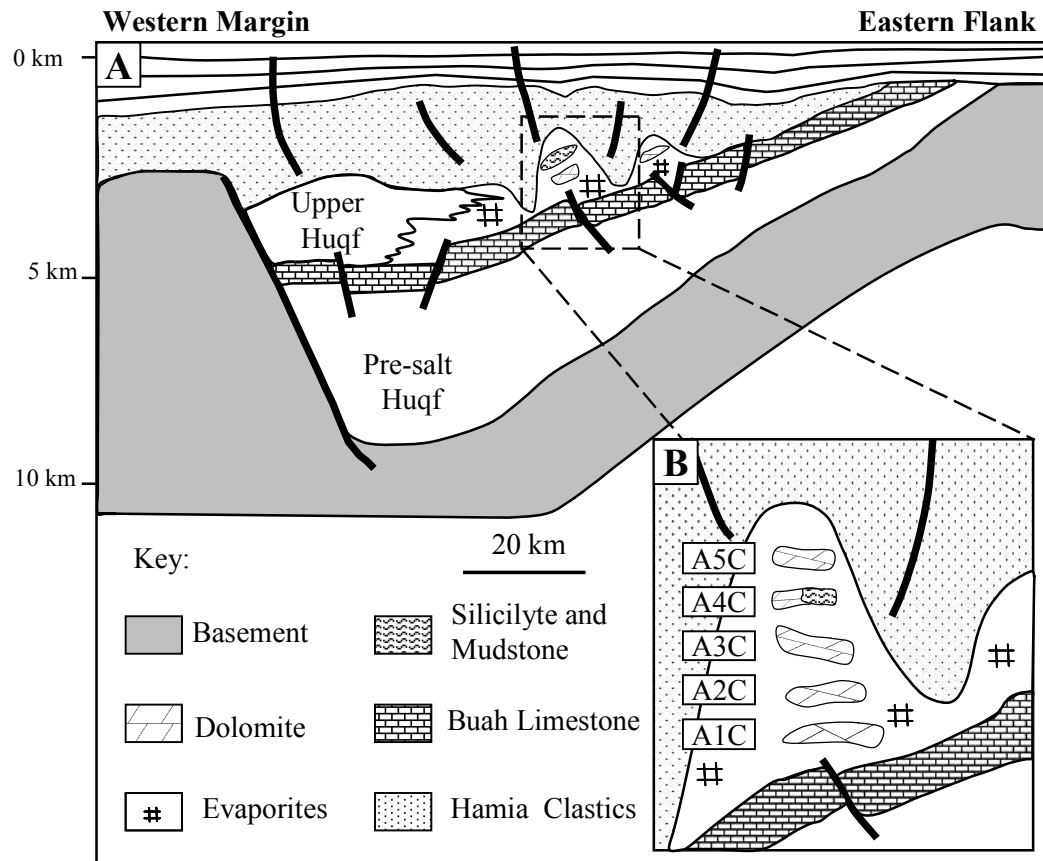


Figure 3.4. (A) A geological cross section showing the South Oman Salt Basin between the Western Margin and the Eastern Flank (see Fig. 3.2 for cross-section line). The Ara Group evaporite-carbonate units overly the faulted Buah limestone rocks of the upper Nafun Group. Buah faulting is related to the tectonic-style deformation and subsidence. Faulting on the Western Margin shifted the South Oman Salt Basin depocenter to the west. (B) Ara salt geometry caused by strong diapirism and salt down-building triggered by 2-km thick accumulation of the Haima clastics. Carbonates, clastics and the Athel Silicilyte of the Ara Group are entrapped within salt domes and fragmented as a result of salt movement. (A) modified after Loosveld et al. (1996) and (B) after Schoenherr et al. (2009).

3.4 Ara Group lithostratigraphy in the South Oman Salt Basin

The Ara Group is subdivided into four main formations, from bottom to top: Birba, ‘U’, Athel, Al Noor and Dhahaban. The Ara Group lithostratigraphy is summarised in Fig. 3.2.

The Birba Formation consists of carbonate and evaporite units of A0-A3 cycles (Amthor et al. 2005). The carbonate units range in thickness from 50-200 m and are mainly composed of dolomites with minor limestones (Amthor et al. 2005). The evaporite units generally comprise 10-20 m thick anhydrite layers at the base and top of each evaporite unit, with 50-200 m thick halite and potash salt layers between the anhydrite layers (Schröder et al. 2003; Amthor et al. 2005).

The “U” and Athel formations were deposited during the A4 cycle. The “U” Formation comprises up to 1000 m thick evaporites (anhydrite and salt; Schröder et al. 2003), 50-150 m thick dolomites (Schröder et al. 2005) and 80 m thick organic-rich mudstones of the U Shale (Amthor et al. 2005; Schröder and Grotzinger 2007). The Athel Formation consists of up to 390 m thick Athel Silicilyte (Amthor et al. 2005), 120 m thick organic-rich mudstone of the Thuleilat Shale and 50-150 m thick Athel dolomites (Amthor et al. 2005; Schröder and Grotzinger 2007). Stratigraphically, the Athel Silicilyte is bounded by the U-Shale and the Thuleilat Shale, which are all enclosed between A4 and A5 evaporites (Fig. 3.2).

The Al Noor Formation, which was deposited during the A5 and lower A6 cycles, consists of evaporites, carbonates and siliciclastics. The evaporite unit comprises more than 1,000 m thick anhydrites, halites and potash salts (Amthor et al. 2005). The carbonates (10-50 m thick) comprise both thrombolite pinnacle reefs of shallow-water and deep-water environments. Siliciclastic rocks (ranging from a few metres to up to 230 m thick) are found at the bottom of A6 cycle intercalated with evaporites (Amthor et al. 2005).

The Dhahaban Formation, which forms the upper part of the A6 cycle, consists of shallow- to deep-water carbonates. These carbonates interfinger with red-brown siliciclastic mudstones towards the west of the South Oman Salt Basin (Amthor et al. 2005). Siliciclastic material was probably derived from topographically high areas of the Western Deformation Front and Ghudun-Khasfah High (Fig. 1.1; Amthor et al. 2005).

3.5 Ara basin reconstruction

A geological model to illustrate the tectonostratigraphic evolution of the Ara Group (Fig. 3.5) was developed by Amthor et al. (2005) based on stratigraphic and seismic reconstructions using the extensive subsurface data from the South Oman Salt Basin. This model is summarised and grouped into three main phases: Birba platform growth, “U”/Athel depositional cycle and Al Noor/Dhahaban depositional cycle.

3.5.1 Phase one

The growth of the Birba platform was initiated by a major tectonic event that restructured the depositional basin. Volcanic ash beds found at the A0 cycle, at the base of Birba Formation, are consistent with an active deformational setting. The Birba platform rim developed into a steep shelf-edge with a vertical relief of at least 400 m. Towards the southwest of the Birba Platform, an intra-platform shelf developed (i.e. Southern Carbonate Domain, Fig. 3.5). In front of the Birba Platform, to the northeast, a starved basin developed, which was segmented into structural highs and lows with a vertical relief of more than 200 m. During transgressive and highstand conditions, carbonates (A0/1C-A3C) were precipitated in the intra-platform margin and in the Eastern Flank. In the starved basin, only argillaceous limestones and minor amounts of mudstones (condensed sections) were deposited. During lowstand conditions, the Birba Platform acted as a barrier resulting in restricted conditions in the intra-platform shelf. Hence, evaporite deposits are only found to the southwest of the Birba Platform (Fig. 3.5).

3.5.2 Phase two

The second phase representing the “U”/Athel depositional cycle (A4) was marked by a major drop in relative sea level, and tectonically controlled basin subsidence. Consequently, high areas, i.e. carbonate platforms, became subaerially exposed. The maximum relief between basin floor and basin margin could have been as high as 200 metres. As a result, a thick evaporite unit (A4E)

accumulated on the basin floor, onlapping the exposed basin margins. Following the onset of the next relative sea level rise, carbonates of the “U” and Athel formations developed on depositional highs, whilst the U Shale was deposited in the basinal areas. The Athel Silicilyte was deposited only in the deepest parts of the basin, within a series of fault-bounded mini-basins (Fig. 3.5), which were developed as a result of strong differential subsidence in the starved basin. With the onset of the next relative sea level fall, deposition of the Athel Silicilyte gave way to the deposition of the Thuleilat Shale and Athel carbonates.

3.5.3 Phase three

The Al Noor and Dhahaban formation (A5 and A6 cycles) deposition was initiated by a combination of strong basin subsidence and transient flooding, resulting in the deposition of evaporites both in basinal areas and on carbonate platforms that were formed during the previous A4 cycle (Schröder et al. 2003). The strong tectonic subsidence created enough accommodation for the lowstand evaporites to blanket the highstand carbonates (Amthor et al. 2005; Schröder et al. 2005). The Western Deformation Front was undergoing differential subsidence, which created high-relief areas of a westerly-sourced clastic material that was deposited interbedded with evaporites. Additionally, the distribution of the carbonate facies and their geometries, and the presence of isolated carbonate build-ups and deep-water mudstones within the A5 and A6 cycles all suggest a significant accommodation differentiation during deposition of these cycles.

Finally, the sedimentation of the Ara Group evaporite-carbonate depositional cycles was terminated by the deposition of continental Haima Supergroup clastics (Millson et al. 1996; Amthor et al. 2005). The differential loading of up to 2 km thick of Haima clastics above the Ara salt resulted in strong diapirism and down-building of salt (Fig. 3.4B; Heward 1990; Loosveld et al. 1996; Schoenherr et al. 2009).

The different Ara Group facies of shallow-water carbonates (reservoir rock) and basinal organic-rich mudstones (source rock) that are enclosed by evaporites (seal) created an ideal geological setting for hydrocarbon

accumulation and preservation (Schröder et al. 2003; Al-Siyabi 2005; Amthor et al. 2005; Schröder et al. 2005).

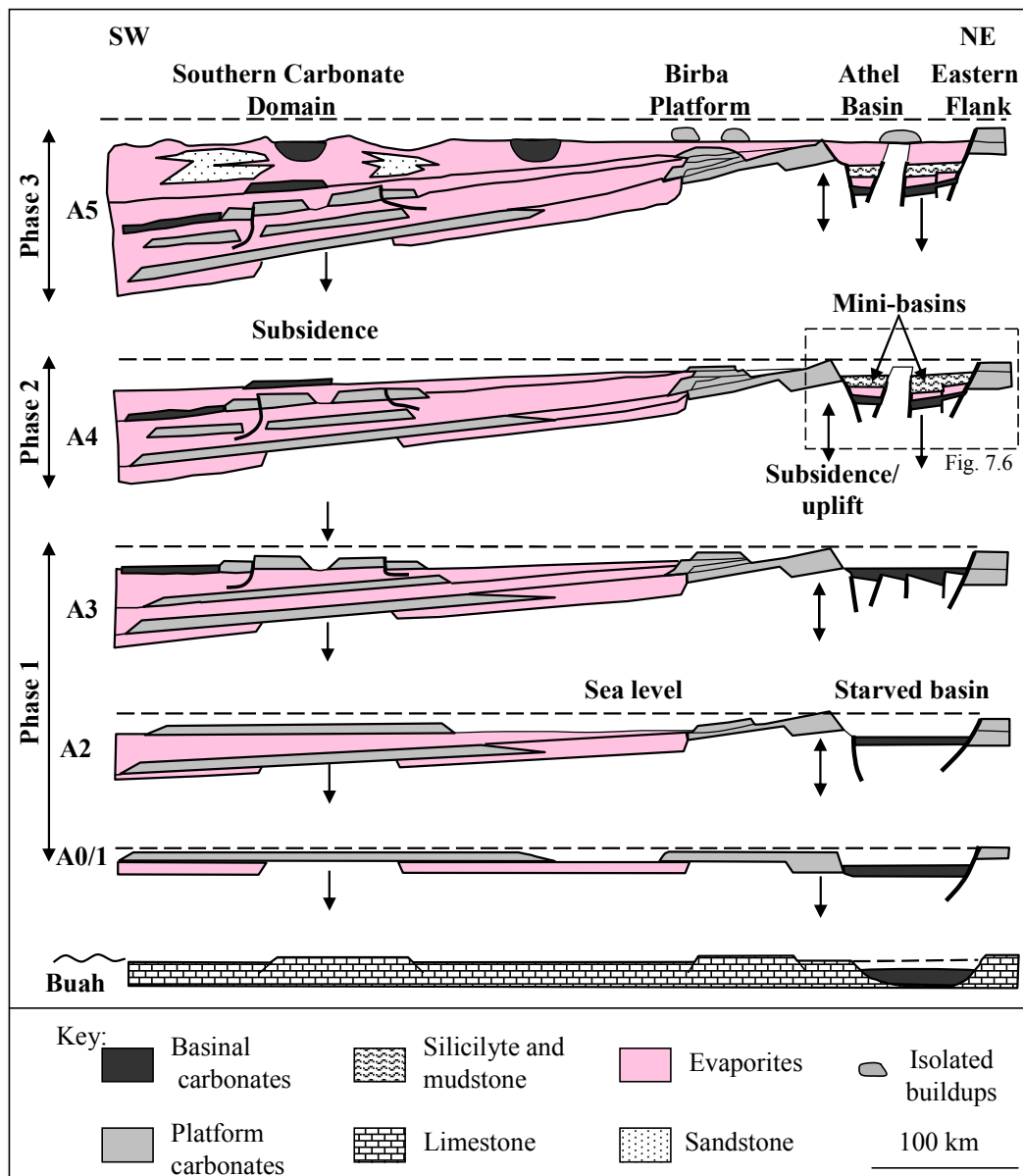


Figure 3.5. Schematic diagram illustrating a reconstruction of the Ara basin and the evolution of the Ara Group cycles. Ara cycles and basin evolution comprise three phases. Phase 1: carbonates of the A0/A1–A3 (Birba carbonates) deposited during transgressive and highstand conditions, and evaporites precipitated during lowstand conditions recording basin restriction. Phase 2: strong subsidence that segmented the starved basin into palaeogeographic highs and lows, resulting in the precipitation of the Athel Silicilyte in the basin centre during highstand conditions bounded by transgressive mudstones (U Shale and Thuleilat Shale). Contemporaneous, carbonate units precipitated on the adjacent platforms. Phase 3: strong subsidence and complete restriction of the basin, which resulted in evaporite accumulation on deep basin floors and shallow carbonate platforms. The interbedding of clastics and evaporites are to the result of tectonism on the Western Deformation Front, which created a westerly clastic source. Modified after Amthor et al. (2005).

3.6 Ara Group chronostratigraphy

The Ara Group contains multiple ash beds that have been used for U/Pb dating in order to constrain the duration of the Ara Group cycles, as well as global correlation for the Ara Group stratigraphy (e.g. Amthor et al. 2003; Bowring et al. 2007). Recently, Bowring et al. (2007) have constructed the timing of the Ara Group deposition using U/Pb zircon dating from four ash beds within the Ara cycles (Fig. 3.2). The first ash bed occurs in the middle part of the A0 cycle, which was dated at 546.72 ± 0.21 Ma. The second and third ash beds occur at the base and top of the A3C cycle, dated at 542.90 ± 0.12 Ma and 542.33 ± 0.11 Ma, respectively. The fourth ash bed occurs at the base of the A4C and dates at 541 ± 0.13 Ma. Based on this, deposition of the Ara group is estimated to have occurred between 547 Ma to 540 Ma.

The duration of each evaporite-carbonate cycle can be estimated according to the age of the ash beds found within the Ara cycles. The age difference between middle A0 and base A3C (three and a half cycles) ranges from 4.1 to 4.7 million years, which yields an average of 1.2 to 1.3 million years per cycle. The duration of the A3C half cycle is calculated from the age difference between its base and top (approximately 0.3 to 0.8 million years). The age difference between the top A3C and base A4C suggests a duration of 1.1 to 1.6 million years for the A4E (evaporite) half cycle (Bowring et al. 2007).

3.7 Ara Group chemostratigraphy

The base of A4C shows an abrupt decrease in $\delta^{13}\text{C}_{\text{carb}}$ from +2 ‰ PDB (Pee Dee Belemnite) to -7 ‰, and then gradually increasing to -2 ‰ through the rest of the A4 cycle (Amthor et al. 2003). All carbonate units (A0-A3 and A5) show positive values of $\delta^{13}\text{C}_{\text{carb}}$ from 2.5 ‰ to 3.5 ‰ (Fig. 3.2). The negative $\delta^{13}\text{C}_{\text{carb}}$ excursion (lasted for ≈ 1 Ma) recorded in A4C is interpreted to reflect seawater composition that was enriched by isotopically light carbon (^{12}C). Light carbon can be derived from organic-matter degradation (e.g. by sulphate-reducing bacteria in the anoxic deep water), increase in mantle-derived carbon and a crash in basin primary productivity (e.g. Hsü and McKenzie 1985; Knoll et

al. 1986; Knoll et al. 1996; Walter et al. 2000). Expansion or overturn of the anoxic deep water had been invoked to explain the negative excursion recorded in A4C carbonated (Schröder and Grotzinger 2007, see also Kimura et al. 1997; Strauss 1997; Bartley et al. 1998). This interpretation is supported by sulphur and molybdenum isotopic data (below), which suggest development of anoxia as a result of dominate process of sulphate reduction in the South Oman Salt Basin deep water.

Sulphur isotope data show parallel enrichment of paired sulphate ($\delta^{34}\text{S}_{\text{SO}_4}$) and pyrite ($\delta^{34}\text{S}_{\text{pyr}}$) throughout the Ara Group (Fig.3.2; Fike and Grotzinger 2008). An increase in $\delta^{34}\text{S}_{\text{SO}_4}$ from around 20 ‰ CDT (Canyon Diablo Troilite) to 42 ‰ is observed, which is associated with an increase in $\delta^{34}\text{S}_{\text{pyr}}$ from around -15 ‰ to 10 ‰. Schroder et al. (2004) carried out a detailed sulphur isotopic study on the A4C cycle, which shows sulphur isotope average values of 37.7 ‰ and 0.81 ‰ for $\delta^{34}\text{S}_{\text{SO}_4}$ and $\delta^{34}\text{S}_{\text{pyr}}$, respectively. Whereas, the typical values of $\delta^{34}\text{S}_{\text{SO}_4}$ during the Late Neoproterozoic-Cambrian time are in the range from 15 to 25 ‰ (Strauss 1993; Canfield 1998; Fike et al. 2006; Kaufman et al. 2007; McFadden et al. 2008). This segregation in the sulphur isotope values between sulphate and pyrite during the A4C cycle is interpreted to have been influenced by the activity of sulphate-reducing bacteria that reduce SO_4^{-2} to HS^- (Schröder et al. 2004). The produced HS^- is enriched in light sulphur isotope (^{32}S) and may ultimately be incorporated into pyrites and/or organic-matter, whereas the residual SO_4^{-2} is enriched in heavy sulphur isotope (^{34}S) that is incorporated into evaporite minerals, reflecting the isotopic composition of seawater (Claypool et al. 1980; Strauss 1993; Strauss 1997; Canfield 1998).

Molybdenum isotope ($^{98/95}\text{Mo}$) data of the mudstones and Athel Silicilyte of the A4 cycle show a positive transit signal, with an overall value of $\delta 1.2^{98/95}\text{Mo}$ relative to J&M Mo standard (Wille et al. 2008). At the base of the U-Shale, the $\delta^{98/95}\text{Mo}_{\text{J\&M standard}}$ values spike from 0.79 to 1.30 (J&M Mo standard) and then decrease through the upper Athel Silicilyte until they reach a value of 1.01 (J&M Mo standard), recorded in the Thuleilat Shale. A similar overall Mo isotopic composition of $\delta 1.1^{98/95}\text{Mo}_{\text{J\&M standard}}$ is found in the Precambrian-Cambrian Chinese sulphide marker bed, leading to the interpretation of seawater

being the main source of the Mo signal (Wille et al. 2008). Mo is redox-sensitive and it is removed from the water column without fractionation in sediments accumulated under euxinic conditions, and hence it should reflect the seawater value of 2.3 ± 0.2 (Arnold et al. 2004). Whereas, in oxic conditions, sediments preferentially adsorb isotopically light Mo (e.g. Mn-oxide has an average $\delta^{98/95}\text{Mo}$ value of -0.7; Barling et al. 2001; Arnold et al. 2004). The $\delta^{98/95}\text{Mo}$ signal observed in the Athel Silicilyte is therefore interpreted to record intense upwelling of hydrogen sulphide-rich deep waters (Wille et al. 2008), consistent with the disappearance of shallow-marine fossils of *Cloudina* and *Namacalathus* in the basin (Amthor et al. 2003). The significance of these data to this study will be evaluated in Chapter 6 (section 6.5) and consequently linked to the findings.

3.8 Dating the Precambrian-Cambrian boundary

The Precambrian-Cambrian boundary has been interpreted globally based on biogeochemical, geological and biological characteristics (e.g. Brasier 1989; Bowring et al. 1993; Strauss 1993; Grotzinger et al. 1995; Knoll et al. 1995; Strauss 1997; Kimura and Watanabe 2001; Amthor et al. 2003; Bowring et al. 2007; Wille et al. 2008). The A4C unit records changes in biogeochemical cycles, including negative excursions of marine $\delta^{13}\text{C}$ (Amthor et al. 2003), segregation between light and heavy sulphur isotopes (Schröder et al. 2004; Fike and Grotzinger 2008) and a transit signal of $\delta^{98/95}\text{Mo}$ (Wille et al. 2008). Furthermore, the A4C is marked by the disappearance of the Ediacaran *Cloudina* and *Namacalathus* body fossils, which are common in A0 to A3 carbonate units (Amthor et al. 2003). Therefore, the Precambrian-Cambrian boundary is placed at the base of A4C. This boundary is constrained by an absolute U-Pb age of 541 ± 0.13 Ma (Bowring et al. 2007; previously dated at 542 ± 0.3 Ma by Amthor et al. 2003). Negative $\delta^{13}\text{C}_{\text{carb}}$ excursions of similar magnitude and duration to the A4C and the extinction of *Cloudina* and *Namacalathus* are recorded at the Precambrian-Cambrian boundary in some stratigraphic sections globally (e.g. Brasier 1989; Brasier et al. 1990; Bowring et al. 1993; Grotzinger et al. 1995; Knoll and Carroll 1999; Grotzinger et al. 2000; Hofmann and Mointjoy 2001; Kimura and Watanabe 2001). This interpretation also supports the conclusion

that the Precambrian-Cambrian transition occurred during the A4C (Amthor et al. 2003; Bowring et al. 2007; Schröder and Grotzinger 2007).

Chapter 4.

Chert accumulation and distribution

4.1 Introduction

This chapter provides a description of silica geochemistry (diagenesis and solubility) and provides a brief description of the different types of cherts found in the sedimentary strata from the Precambrian to the present day. In particular, chert depositional environments and controls on precipitation and distribution are discussed. At the end of this chapter, secular changes in chert distribution throughout the Precambrian and the Phanerozoic is reviewed.

4.2 Silica Geochemistry

The geochemistry of silica has been reviewed in detail by Iller (1979), Astor (1983), Williams and Crerar (1985), and Williams et al. (1985). Here, silica polymorphs, diagenesis and solubility are briefly reviewed.

4.2.1 *Silica polymorphs and diagenesis*

Silica principally has three polymorphs, including opal-A (amorphous silica), opal-CT (mixed phase of cristobalite and tridymite) and quartz (Iller 1979; Williams et al. 1985). Opal-A is a hydrous form of silica ($\text{SiO}_2 \cdot n\text{H}_2\text{O}$) with a water content varying from 2 to 13 wt% and it has no crystal structure. Amorphous silica is a major constituent of tests and skeletons of diatoms, silicoflagellates, radiolaria and silicisponges, and it is also found in dissolved silica-rich settings, e.g. hydrothermal and evaporitic settings (Hein et al. 1978; Williams et al. 1985; Greensmith 1988; Eversull and Ferrell 2008). Opal-CT is also a hydrous form of silica, but with a more ordered crystalline structure and comprising alternating layers of cristobalite and tridymite (Williams and Crerar 1985; Eversull and Ferrell 2008). Quartz is an anhydrous stable form of silica (SiO_2) with a crystalline structure. These different polymorphs of silica are principally identified by X-ray diffraction (XRD) analysis on the basis of their structure and crystallinity (e.g. Hein et al. 1978; Helz et al. 1996). The XRD typical pattern of each silica polymorph is shown in Fig. 4.1. Generally, opal-A shows a broad peak, and the peak narrows as opal-A is converted to opal-CT and then to quartz (e.g. Elzea and Rice 1996; Eversull and Ferrell 2008).

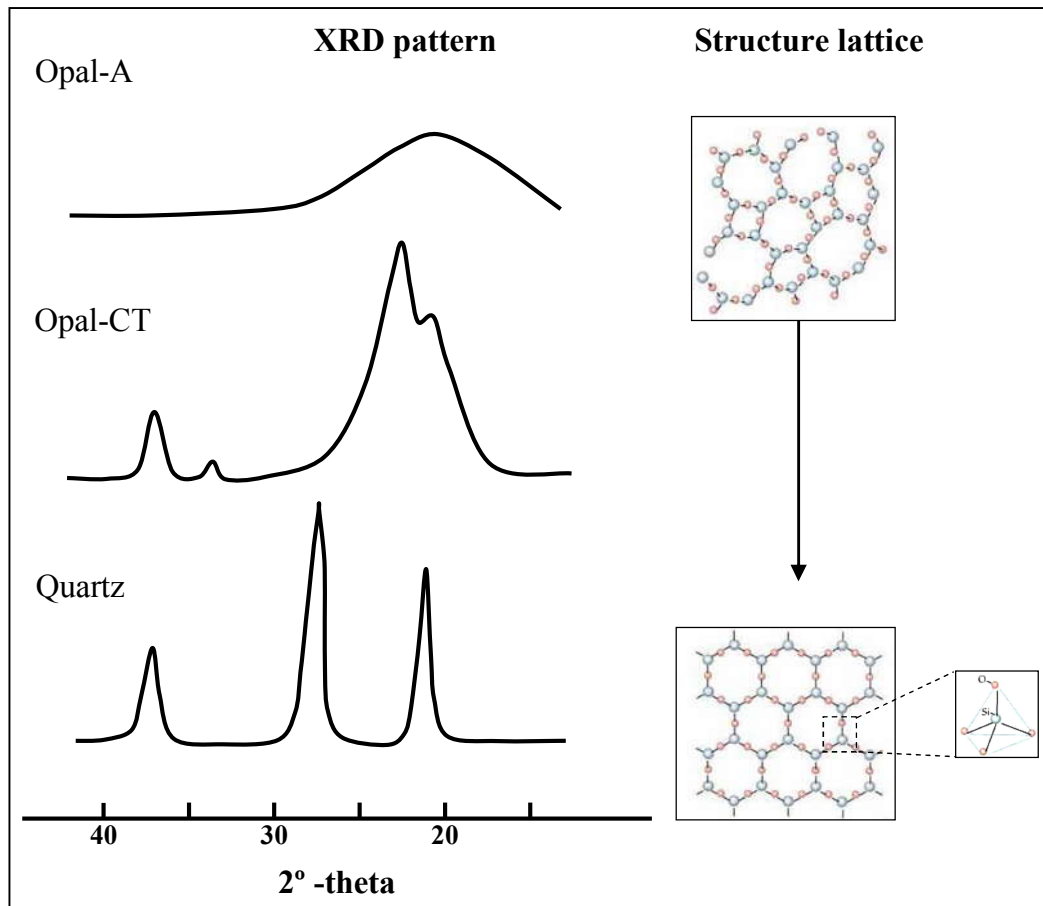


Figure 4.1. XRD patterns of silica polymorphs: opal-A, opal-CT and Quartz. Opal-A shows a broad peak and the peak narrows as it is transformed to quartz. It also shows structure of the two end-members; amorphous silica and quartz. Amorphous silica shows no crystalline structure, whilst quartz has well-defined crystalline structure. These structures shown here are two dimensional and each silicon atom is actually attached to three oxygen atoms (not two atoms as shown), three dimensional building block is shown next to the quartz structure. XRD patterns are modified after Pisciotto (1981) and structure lattice modified after Brown et al. (2000).

In sedimentary systems, under ambient temperatures and pressures, silica usually precipitates inorganically from a medium that is supersaturated with respect to all silica polymorphs (Williams et al. 1985). Precipitation of opal-A is kinetically favoured over precipitation of the thermodynamically more stable phase of quartz (Williams and Crerar 1985; Williams et al. 1985; Hinman 1998). Biogenic or inorganic Opal-A can then be transformed to crystalline quartz through a series of dissolution-reprecipitation reactions; opal A to opal-CT and opal-CT to quartz (e.g. Keller and Isaacs 1985; Williams and Crerar 1985; Hinman 1998). Transformation of silica phases is mainly controlled by temperature and time (Hein et al. 1978; Kastner and Siever 1983; Keller and Isaacs 1985; Williams et al. 1985), and hence the burial depth. Studies of diatom ooze cores from Deep Sea Drilling Project (DSDP) sites suggest that the opal-A

to opal-CT conversion occurs at an average temperature (35-50 °C), typically between 300 to 1000 m burial depth, which can take up to a few million years, while conversion of the opal-CT to quartz may take more than 50 million years under similar conditions (Hein et al. 1978).

4.2.2 *Silica Solubility*

The most important factors affecting silica solubility in waters are pH and temperature (Fig. 4.2 & 4.3), whilst the affect of pressure is not significant (e.g. Iller 1979; Williams et al. 1985). At 25 °C, the solubility of opal-A is 120-140 ppm, opal-CT is 25-60 ppm and quartz is 6-10 ppm (Kastner and Siever 1983; Williams et al. 1985). An increase in pH and/or temperature will increase the solubility of different silica phases and vice versa (Fig. 4.2 & 4.3; e.g. Iller 1979; Williams et al. 1985). The threshold of pH for silica solubility is around pH 9; silica solubility dramatically increases above 9, whilst it hardly changes below 9 (Fig. 4.2; Krauskopf 1967; Iller 1979). Correspondingly, high concentrations of dissolved silica are generally found in high temperature hydrothermal fluids (e.g. Williams et al. 1985; Konhauser and Ferris 1996; Konhauser et al. 2001), high pH evaporitic and hyperalkaline environments (e.g. Peterson and von der Borch 1965; Jones et al. 1967). A drop in temperature and/or pH will initiate silica precipitation. For example, emplacement of hydrothermal fluids in near surface settings, mixing with less saline waters that are characterised by lower pH, and/or organic matter degradation (related to pH drop as a result of H^+ , HS^- and CO_2 production) will lower silica solubility, and hence silica will precipitate from solution.

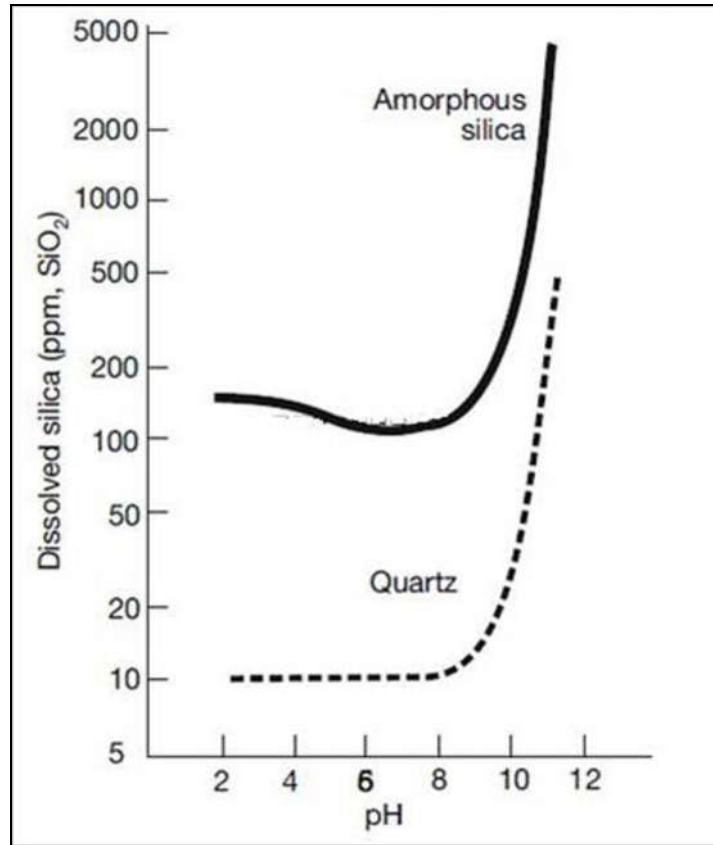


Figure 4.2. Quartz and amorphous silica (opal-A) solubility at 25 °C as a function of pH. Solubility of quartz and amorphous silica dramatically increases above pH 9, whilst it hardly changes below pH 9. Modified after Krauskopf (1967) and Warren (2006).

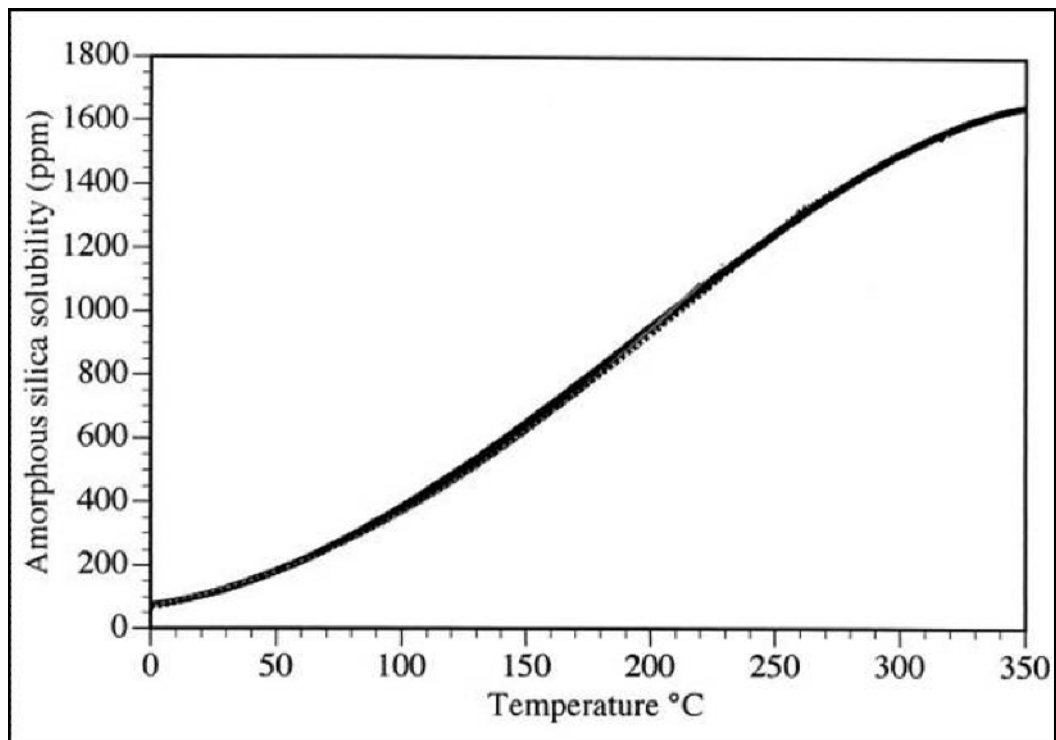


Figure 4.3. Amorphous silica solubility (ppm) as a function of temperature (°C). Amorphous silica solubility increases as temperature increases from 0 to 350 °C. Modified after Gunnarsson and Arnórsson (2000).

4.3 Chert accumulation

Chert is a generic term for siliceous sedimentary rocks that have a chemical, biochemical (microbially mediated) or biogenic origin. Cherts are chiefly composed of quartz that has different forms, including micro, mega, fibrous and chalcedonic quartz (Maliva and Siever 1989a; Knauth 1994). These forms are originally precipitated as amorphous silica from an aqueous solution and then transformed to quartz during diagenesis (section 4.2.1).

Cherts in sedimentary strata are preserved in various forms, the most common being bedded and nodular (e.g. Maliva and Siever 1988b; Maliva and Siever 1989b; Siever 1992; Maliva et al. 2005). Bedded chert is principally found interbedded with other sedimentary rocks, such as mudstone, carbonate and iron (in Banded Iron Formations [BIFs]). Nodular cherts occur as a cement filling voids and cavities, replacing pre-existing minerals, such as carbonate and evaporite minerals, or a permineralising organic layer (e.g. Knoll 1985; Simonson 1985; Maliva et al. 1989; Maliva and Siever 1989b; Knauth 1994; Maliva et al. 2005). Various forms of chert are found throughout the geological record. The following sections briefly review cherts found in sedimentary strata from the Precambrian to the present day.

4.3.1 *Modern*

Modern day primary (i.e. non-diagenetic) chert deposition is mainly controlled by productivity of siliceous organisms dominated by diatoms, with a minor contribution from radiolarians and siliceous sponges (Maliva et al. 1989; Siever 1989; Siever 1991; Kidder and Erwin 2001; Maliva et al. 2005). Chert deposition in modern settings is principally restricted to marine environments, while a small amount of silica is precipitated in hydrothermal and hyperalkaline environments.

Marine environments

Silica deposition on the modern sea floor is mainly biologically controlled by silica-secreting organisms that are located within areas of high

primary organic productivity, especially regions of extensive nutrient upwelling (Maliva et al. 1989). Silica deposition takes place primarily by pelagic sedimentation in two principal oceanic environments. The first is the open ocean pelagic realm where silica accumulates as layers of siliceous organisms (siliceous ooze) with little dilution by terrigenous input. These siliceous oozes might mix or interlayer with pelagic clay and carbonate nannofossil oozes (Hein et al. 1978; Maliva et al. 1989). The second environment accounting for biological silica accumulation is the active continental margin basin, typically fore- and back-arc basins and deep troughs created by transforms of spreading centres (Maliva et al. 1989). The Gulf of California is a typical example of such an environment, where high nutrient upwelling triggers high diatom productivity in the surface waters and the water circulation from the open Pacific ocean ensure the supply of nutrients and dissolved silica to maintain diatom productivity (Maliva et al. 1989). Large volumes of diatomaceous ooze accumulate on the Gulf floor, where they are mixed with terrigenous material and phosphorites (Maliva et al. 1989). Siliceous ooze accumulation in shallow subtidal shelf and platforms environments is not common as the water is typically dissolved silica poor, thus limiting siliceous organism productivity and/or there is a high terrigenous input that dilutes accumulated silica (Maliva et al. 1989).

Hyperalkaline environments

Hyperalkaline environments show small volumes of abiotic (i.e. inorganic) silica precipitation. For example, the Coorong Lagoon (Mg-rich carbonate lake) of South Australia is rich in dissolved silica (up to 400-500 ppm; Peterson and von der Borch 1965). High silica concentrations are linked to high pH values (9.5-10.2; Fig. 4.2) as a result of CO₂ consumption by photosynthesis during humid seasons. In such high pH environments, detrital silicate minerals coming to the lake by weathering are dissolved leading to high silica concentrations. In the dry season, the lake dries-up as a result of high evaporation, and hence dissolved silica is concentrated in porewaters. Below the sediment-water interface, there is a zone of vegetation decomposition in which the pH of porewaters is as low as 6.5 as a result of released CO₂ from vegetation

decomposition. Eventually, silica precipitates form very thin discontinuous layers (1 cm thick and 10 cm long; Peterson and von der Borch 1965).

Other examples of hyperalkaline environments are Lake Magadi in Kenya and Albert Lake basin in the USA, both showing high silica concentrations (up to 2700 ppm; Jones et al. 1967). Inorganic precipitation of silica in these hyperalkaline environments is linked to fresh water input, which lowers the pH (Jones et al. 1967; Eugster 1969). In Lake Magadi a hydrous sodium silicate mineral (magadiite; $\text{NaSi}_7\text{O}_{13}(\text{OH})_3 \cdot 3\text{H}_2\text{O}$) precipitates. Subsequent leaching of sodium by ground waters results in a pure silica precipitate (Eugster 1969; Schubel and Simonson 1990).

Hydrothermal environments

Silica precipitation is encountered in hot spring environments (siliceous sinters), such as the Icelandic hot springs (Konhauser and Ferris 1996; Konhauser et al. 2001; Konhauser et al. 2002) and Yellowstone National Park, USA (Ferris et al. 1986; Hinman and Lindstrom 1996; Cady and Farmer 1996). Hydrothermal fluids are rich in dissolved silica (400 ppm at 100 °C) and upon rising to the surface, they become supersaturated with respect to amorphous silica as a result of rapid cooling, steam loss and evaporation, mixing and changing in fluid pH (e.g. Konhauser et al. 2004). Consequently, silica inorganically precipitates filling void spaces and cavities in sinters, and/or on organic surfaces (microbial mats, leaves and woods; Renaut et al. 1998; Konhauser et al. 2004; Konhauser et al. 2008).

4.3.2 Phanerozoic

Phanerozoic bedded and nodular cherts were deposited mainly by recrystallisation of siliceous oozes and replacement of carbonate and evaporite minerals (Maliva et al. 2005). Dissolution of buried siliceous organisms has been supplied as the principal source for the silica in nodular cherts (Maliva and Siever 1989a; Maliva and Siever 1989b; Kidder and Erwin 2001). Generally, radiolaria and sponges played an important role from the Cambrian to the Late Cretaceous in removing dissolved silica from seawater and precipitating it as

sediments, whilst diatoms have dominated since the mid Cretaceous (Maliva et al. 1989).

Bedded cherts

Bedded cherts are typically found in basinal settings interbedded with terrigenous material (e.g. clay and silt-sized quartz), carbonates and volcanic ash, producing rhythmic alternations (ribbon cherts); each bed is typically millimetres to centimetres thick (Fig. 4.4). Bedded cherts have an origin comparable to that of present day siliceous oozes produced from pelagic settling of siliceous organisms under high productivity as a result of high nutrient upwelling in these settings (section 4.3.1; Maliva et al. 1989; Maliva et al. 2005). Subsequent burial and diagenesis recrystallised these siliceous oozes to form cherts (section 4.2.1; Hein et al. 1978; Maliva et al. 1989; Knauth 1994). The alternation between chert and terrigenous beds are interpreted as a result of seasonal changes in productivity and/or change in terrigenous supply (Iijima et al. 1983; Maliva and Siever 1989a).

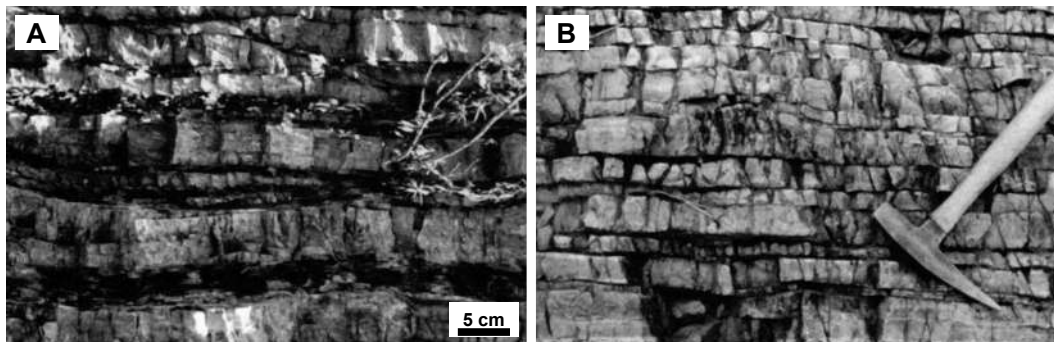


Figure 4.4. Outcrops pictures showing bedded cherts. (A) a diatomite chert of the Monterey Formation (Miocene), Berkeley, California, USA. (B) a radiolarian chert of the Hida River (Triassic-Jurassic), Kamiaso, Japan. Modified after Maliva et al. (1989).

Nodular cherts

Nodular cherts typically occur as discrete replacive bodies mostly within limestone and dolomite formations (Maliva and Siever 1989b). They range in size from a few centimetres to meter-sized lenses; the majority are smaller than half a meter (Fig. 4.5 A; Maliva and Siever 1989b; Knauth 1994). Authigenic quartz might be finely disseminated throughout the host rock matrix or concentrated along bedding planes (Gao and Land 1991; Knauth 1994). In some cases, silica selectively replaces carbonate skeletons, burrows and stromatolitic

or microbial layers in calcareous sediments (Maliva and Siever 1989b; Gao and Land 1991; Kidder and Erwin 2001). Preservation of precursor original textures and microbial layer structures are often evident for these types of chert replacement.

The mode of nodular chert replacement could suggest that the intraformational distribution of nodular cherts was controlled by permeability and organic matter contents (Knauth 1979; Knoll 1985). Fluid transport in permeable beds could have allowed dissolved silica to concentrate in porewaters above amorphous silica solubility, and hence trigger chert precipitation. Whilst organic matter availability could play a role by changing the local pH during diagenesis (related to the production of acidic CO_2 , H^+ and HS^-), which would lead to carbonate dissolution and silica precipitation (Clayton 1986; Knauth 1994). The preservation of uncompact precursor grains (Fig. 4.5 B) and the presence of draped laminae around nodular cherts in some example suggest that silica precipitation took place during early diagenesis below the sediment-water interface, before significant compaction (Maliva and Siever 1989a; Maliva and Siever 1989b; Gao and Land 1991; Knauth 1994).

The source of silica in nodular cherts is interpreted to be principally derived from the dissolution of siliceous organisms (Maliva and Siever 1988a; Maliva and Siever 1989b; Maliva et al. 2005). Consequently, the distribution of nodular cherts between different depositional environments reflects evolution and activity of silica-secreting organisms in the water column (Maliva et al. 1989; Kidder and Erwin 2001; Kidder and Mumma 2003) and this is discussed in section 4.4. Generally, nodular cherts are common in low energy subtidal and basinal settings. However, they are also found in early Cambrian to mid-Ordovician shallow platforms and high energy settings, in addition to low energy subtidal and basinal settings (Maliva et al. 1989).

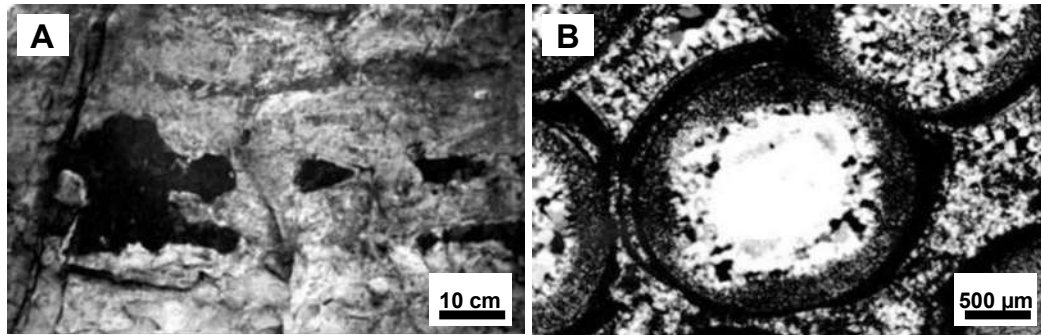


Figure 4.5. (A) Outcrop picture of nodular chert (dark) in limestone of the Onondaga Limestone (Middle Devonian), near Nedrow, New York, USA. (B) Optical microscope image showing chert nodule replacing oolite prior to significant compaction in the Mines and Gatesburg Formations (Upper Cambrian), Pennsylvania, USA. Modified after Maliva et al. (1989).

Cherts replacing evaporite minerals

Nodular cherts are also found to have replaced anhydrite and gypsum minerals in Phanerozoic strata that were deposited in hypersaline environments, e.g. geode cherts in the Lower Mississippian strata of southern Kentucky and northern Tennessee, USA (Milliken 1979; Maliva 1987). The presence of anhydrite and gypsum minerals and their pseudomorphs within quartz crystals supports an evaporite-replacement origin (Milliken 1979; Maliva 1987; Maliva et al. 2005). Silicification of evaporite minerals normally begins from the outer part of the evaporite mineral and then proceeds inwards towards the centre (Milliken 1979; Henchiri and Slim-S'Himi 2006). High concentrations of dissolved silica in these evaporitic environments result from water volume reduction and high pH values, which permit dissolved silica to build up (e.g. Hesse 1989; Schubel and Simonson 1990; Dove 1994). Silica precipitation is linked to a change in porewater pH, possibly induced by mixing with less saline water (phreatic fluids), which are characterised by lower pH values, thereby reduce silica solubility (Fig. 4.2; Milliken 1979; Warren 2006). Consequently, this less saline water leads to dissolution of evaporite mineral and their replacement with silica (Eugster 1969; Milliken 1979).

4.3.3 Precambrian

The Precambrian predates the major evolution of silica-secreting organisms. Although siliceous sponge spicules have recently been found in some Ediacaran deposits in south Australia (Gehling and Rigby 1996) and in southwest

Mongolia (Brasier et al. 1997), their low abundance in these localities suggests that they did not play a major role in silica precipitation during the Precambrian. Therefore, Precambrian seawater must have been rich in dissolved silica than the Phanerozoic in the absence of any effective biogenic mechanism for its removal (Siever 1992; Saylor et al. 1998; Maliva et al. 2005; Perry and Lefticariu 2007). The oceanic silica concentrations might have reached opal-CT saturation (60 ppm) or amorphous silica saturation (120-140 ppm; Holland 1984; Siever 1992; Morris 1993). In order to balance silica input from continental weathering and hydrothermal fluids, silica removal during the Precambrian must have been controlled by chemical (inorganic) and/or biochemical processes. These processes include reactions with clay minerals and zeolites, replacement of carbonate and evaporite minerals, permineralisation of organic matter, and coprecipitation with iron minerals in BIFs (Melnik 1982; Ewers 1983; Birnbaum and Wireman 1984; Siever 1992; Knauth 1994; Simonson and Hassler 1996; Simonson 2003; Fischer and Knoll 2009).

Cherts throughout the Precambrian are found in shallow water peritidal settings and in basinal settings. In particular, basinal cherts are only found in Archean and Paleoproterozoic strata (> 1.8 Ga) interbedded with BIFs, whereas shallow water peritidal cherts are common throughout the Precambrian (Knoll 1985; Maliva et al. 2005). Therefore, basinal bedded cherts in the Phanerozoic do not have an analogue in the Upper Precambrian (< 1.8 Ga; Mesoproterozoic and Neoproterozoic; Maliva et al. 2005). The cherts found in these two settings are described below.

Peritidal cherts

Precambrian primary and early diagenetic cherts mostly occur in shallow peritidal and subtidal carbonate. They mainly precipitated by replacing carbonate and evaporite minerals, as well as silicifying organic laminae (Knoll 1982; Knoll et al. 1991; Maliva 2001; Maliva et al. 2005). Different modes of silicification can be found within some formations and even within some individual samples (e.g. Knoll 1985; Maliva et al. 1989; Maliva et al. 2005). Their textures and paragenesis are similar to Phanerozoic carbonate replacement cherts (e.g. Maliva

2001). For example, shallow water facies of the Draken Formation of the Akademikerbreen Group (700-800 Ma from Spitsbergen) show early diagenetic chert that formed as ellipsoidal to irregular nodules (Fig. 4.6A), individually silicified carbonate minerals and conglomerate void-cementation. Individually silicified organic laminae are present as well (Fig. 4.6 B), which are interpreted to indicate a microbial mat and stromatolitic origin (Knoll 1982; Maliva et al. 1989; Fairchild et al. 1991; Knoll et al. 1991; Maliva et al. 2005). Microtextures of these cherts suggest early diagenetic replacement of carbonates prior to significant compaction, while silicification of organic laminae and void space cementation in conglomerates is interpreted to be a direct precipitation from seawater (Knoll 1985; Maliva et al. 1989; Knoll et al. 1991; Maliva et al. 2005). Silicification of the precursor carbonate is evident by the presence of dolomite inclusions, while the preservation of tightly interwoven microbial filaments is evidence of a microbial mat origin (Maliva et al. 1989; Knoll et al. 1991; Maliva et al. 2005).

Chert distributions in Upper Precambrian strata largely correlate with organic-rich facies. Relative permeability is also important, but permeability alone cannot explain chert distribution (Knoll 1985). The major role played by organic matter appears to have been to change porewater chemistry during diagenesis (by dropping pH) causing silica precipitation (Fig. 4.2). In addition, the high affinity of dissolved silica to nucleate on organic matter contributes to silica precipitation (Knoll 1985; Amores and Warren 2007; Konhauser et al. 2008; Orange et al. 2009), particularly in environments of pH less than 9 where silica solubility is insensitive to the change in pH (Fig. 4.2). The affinity of dissolved silica to precipitate on organic matter is likely the result of hydrogen bonding between the functional groups in organic matter (hydroxyl and carboxyl) and dissolved silica (e.g. Leo and Barghoorn 1976; Knoll 1985; Konhauser et al. 2004). This mechanism is explored in more detail in Chapter 7 (section 7.3.2).

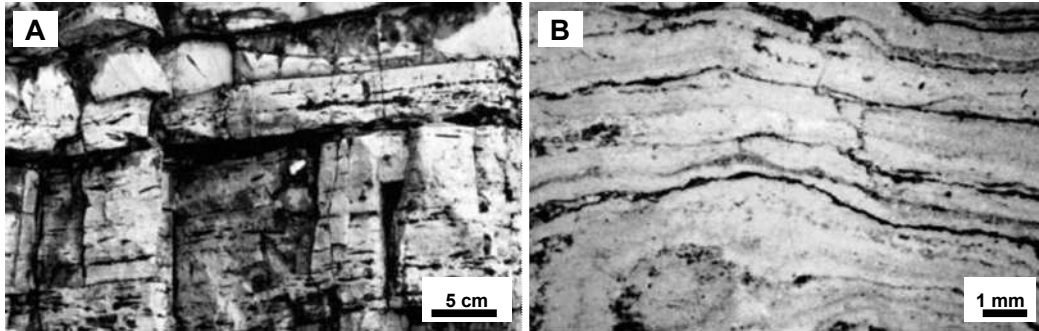


Figure 4.6. (A) Outcrop picture showing individually silicified clasts (dark) in the Draken Formation, Spitsbergen (700-800 Ma). (B) Optical microscope image showing chert layers (dark) within stromatolite (dolomite-rich) from the Draken Formation. (A) modified after Maliva et al. (1989) and (B) after Knoll et al. (1991).

Cherts in BIFs

Archean and Paleoproterozoic BIFs contain more than 15 wt. % iron (on average 30 wt. %) and commonly comprise 35–50 wt. % silica (James 1954; James and Trendall 1982; Hamade et al. 2003; Klein 2005; Fischer and Knoll 2009). The banding in BIFs is generally defined by alternation between silica-rich layers and iron-rich layers, which can have thicknesses ranging from a few micrometers to a few meters (Fig. 4.7; Trendall and Blockley 1970; Morris 1993; Perry and Lefticariu 2007; Fischer and Knoll 2009). Cherts in BIFs are mainly cementing pore spaces (depositional porosity $\leq 95\%$) and sometimes replacing precursor minerals (iron and carbonate; Simonson 2003; Maliva et al. 2005). Therefore, silica precipitation is believed to represent early diagenesis of precursor sediments close to the sediment-water interface (e.g. Trendall and Blockley 1970; Simonson 1987; Simonson 2003; Perry and Lefticariu 2007; Fischer and Knoll 2009).

Banded Iron Formations are interpreted to have been deposited in deep, semi-isolated basinal marine settings (James 1954; Trendall 1972; James and Trendall 1982; Morris 1993). The banding between silica-rich layers and iron-rich layers suggest switching between silica precipitation and iron precipitation. The presence of geochemical hydrothermal signatures (positive Eu anomalies, light REE enrichment and mantle-like Nd isotopic values) in iron-rich layers suggests that iron precipitation took place during episodic hydrothermal activity (e.g. Klein and Beukes 1992; Morris 1993). Whereas, silica-rich layers likely represent continuous background silica precipitation from silica-rich

Precambrian seawater, possibly aided by high evaporation (Trendall and Blockley 1970; Drever 1974; Hamade et al. 2003) and/or coprecipitated with iron minerals (e.g. Ewers 1983). There is good geochemical data to support a seawater source for the silica in BIFs from Ge/Si ratios, which show silica-rich layers having Ge/Si ratios similar to modern seawater and iron-rich layers having values similar to metalliferous sediments (Hamade et al. 2003). This suggests that most of the silica present in BIFs entered the ocean via continental weathering, whilst iron was sourced from hydrothermal fluids (Hamade et al. 2003). Iron-rich layer precipitation therefore took place during periods of intense hydrothermal activity and silica-rich layers precipitated during periods of relative hydrothermal quiescence (e.g. Morris 1993; Hamade et al. 2003).



Figure 4.7. Outcrop picture showing chert layers (grey) of various thickness interbedded with iron-rich layers (red) from the ca. 2.5 Ga Brockman Iron Formation, Dales Gorge, Western Australia. Modified after Fischer and Knoll (2009).

4.4 Secular change in chert distribution

The principal locus of primary and early diagenetic chert accumulation found throughout the geological record (from Precambrian to present) appears to have a secular pattern that changed at least three times. The locus of chert accumulation changed at least once during the Precambrian and twice during the Phanerozoic (Maliva et al. 1989; Maliva et al. 2005). These secular changes are most likely controlled by dissolved silica concentrations in seawater, and hence the evolution of silica-secreting organisms. The secular change in chert distribution during the Precambrian was discussed by Maliva et al. (2005) and

during the Phanerozoic by Maliva *et al.* (1989). The following subsection briefly describes each secular change and the causes invoked for each change during the Precambrian and the Phanerozoic.

4.4.1 Precambrian

During the Archean and the Paleoproterozoic, peritidal and basinal cherts were abundant. The end of widespread chert precipitation in basinal marine environments, found in banded iron formations, marks the first shift towards the end of the Paleoproterozoic (approx. 1.8 Ga; Fig. 4.8). During the Mesoproterozoic and Neoproterozoic, primary and early diagenetic chert precipitation was restricted to peritidal and shallow subtidal platforms. This shift might suggest higher dissolved-silica concentrations in seawater during the Archean and the Paleoproterozoic, which allowed cherts to precipitate in deep basinal water. High silica concentrations have been attributed to higher hydrothermal fluxes before ca. 1.8 Ga. This interpretation is supported by the hydrothermal patterns of REE data and mantle-like Nd isotopic signatures of the iron formations (e.g. Beukes and Klein 1990; Derry and Jacobsen 1990; Beukes and Klein 1992; Sugitani 1992). These same data suggest that there was a sharp decline in the hydrothermal fluxes at or later than ca. 1.8 Ga (Beukes and Klein 1992).

Based on Ge/Si ratios, Hamade *et al.* (2003), suggested that silica in BIFs from the ca. 2.5 Ga Dales Gorge Member (Western Australia), was mainly precipitated from silica-rich Precambrian seawater. In this scenario, the drop in silica concentrations after ca. 1.8 Ga might be attributed to a secular decrease in continental weathering. However, Fischer and Knoll (2009) have recently shown that dissolved silica can bind with iron hydroxides at the seawater surface and then be transported to basinal water and sediments, where silica then precipitated as early diagenetic cherts along with iron. If this were the case, then dissolved silica concentration might not have changed considerably throughout the Precambrian. Therefore, the presence of basinal cherts during the Archean and the Paleoproterozoic would be linked to iron precipitation. After all dissolved iron was precipitated as a result of Paleoproterozoic oceans becoming more

oxidising, basinal silica precipitation was terminated (Fischer and Knoll 2009). Consequently, chert precipitation was shifted to peritidal and subtidal settings during the Mesoproterozoic and the Neoproterozoic.

4.4.2 *Phanerozoic*

The removal of dissolved silica from seawater primarily by diatoms, with lesser contributions from radiolarians and sponges, maintains modern oceanic dissolved silica concentrations at a very low level (Maliva and Siever 1989a; Siever 1992). In the modern ocean, silica concentration is < 1 ppm at the surface and up to 10–15 ppm in some bottom waters (Maliva et al. 1989; Siever 1992; Perry and Lefticariu 2007; Fischer and Knoll 2009). Therefore, the distribution of cherts during the Phanerozoic is predominantly linked to the activity of silica-secreting organisms. Throughout the Phanerozoic, the principle loci of chert accumulation has changed twice (Maliva et al. 1989). These changes are interpreted to reflect the radiation of different siliceous organisms during the Phanerozoic (Maliva et al. 1989; Kidder and Erwin 2001; Kidder and Mumma 2003).

The first secular change occurred during the Early Palaeozoic (Late Ordovician; Fig. 4.8) which is marked by a decline of early diagenetic cherts in high energy tidal settings, with a concomitant increase in abundance in low-energy subtidal and deep water settings. The second secular change occurred during the Late Cretaceous, which is marked by a widespread disappearance of early diagenetic cherts from low energy subtidal settings whilst they remain abundant in deep water settings. The first secular change during the Early Palaeozoic is interpreted to reflect the dominance of siliceous sponges and radiolaria (Fig. 4.8) in silica deposition in subtidal environments and pelagic water columns, respectively. The second secular change is believed to correlate broadly with a major radiation of diatoms (Fig. 4.8) that shifted silica deposition to deep water environments and reduced oceanic silica concentrations to a low level. After the radiation of diatoms, siliceous sponges and radiolaria became less important to silica deposition, and hence there is an absence of early diagenetic

chert in subtidal and peritidal environments from the Late Cretaceous onwards (Fig. 4.8).

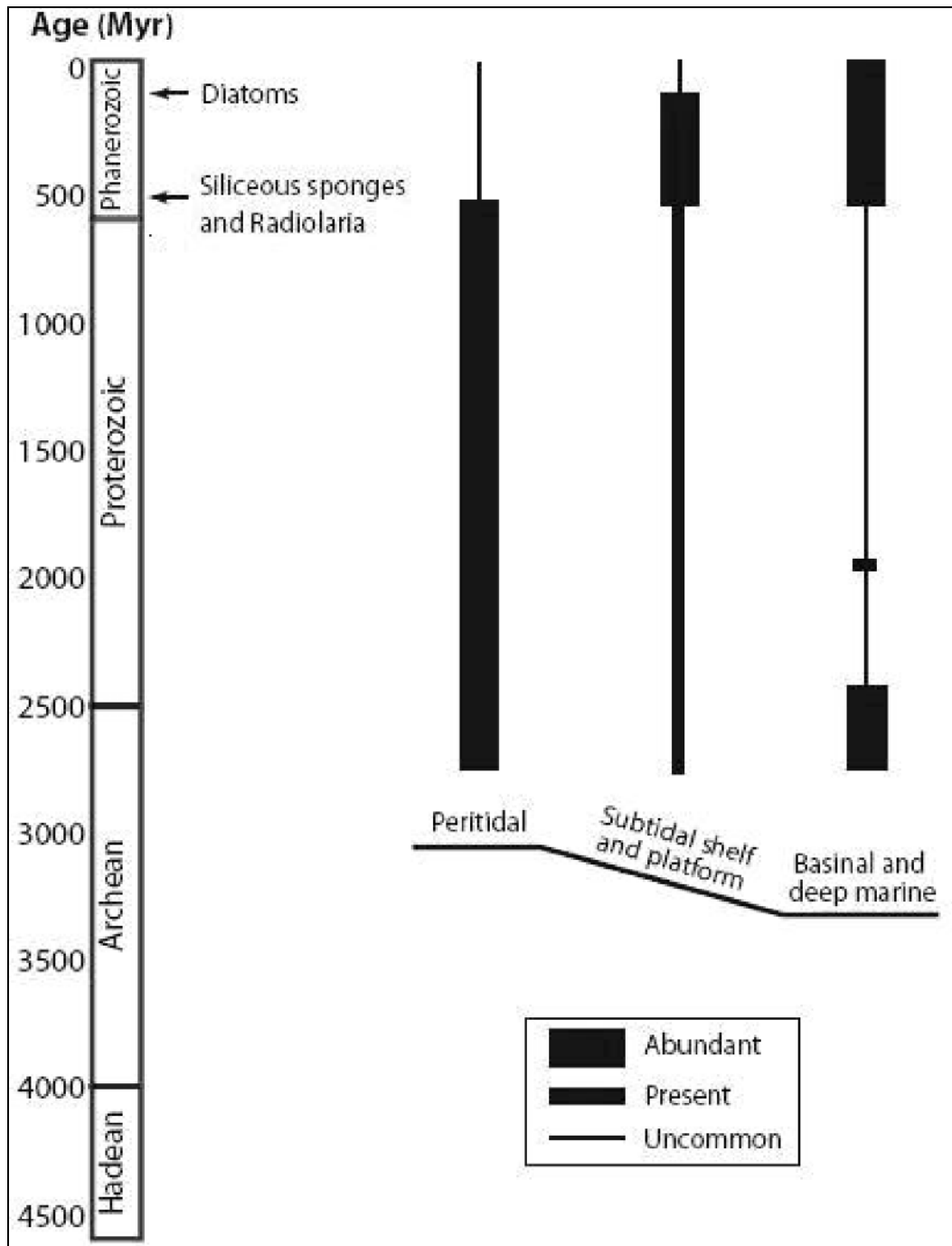


Figure 4.8 Early diagenetic chert distribution from late Archean to the present day. Peritidal chert accumulation is abundant in the Precambrian and in the Early Palaeozoic. Whereas, basinal cherts are only abundant until the end of Paleoproterozoic (approx. 1.8 Ga) and they disappear from the Mesoproterozoic to Cambro-Ordovician. End of BIF precipitation likely caused basinal chert disappearance from the Mesoproterozoic to Cambro-Ordovician. Evolution of the different silica-secreting organisms in the Phanerozoic shifted chert accumulation back to basinal and deep water settings. Therefore, during the Late Neoproterozoic to the Early Cambrian (Cambro-Ordovician), only peritidal chert accumulation is abundant and not basinal cherts. Modified after Maliva et al. (2005) and Fischer and Knoll (2009).

Chapter 5.

Lithofacies analysis and distribution

5.1 Introduction

This chapter outlines different lithofacies identified in this study. Individual samples are described in terms of their textural and compositional attributes, using data derived from visual core inspection, wireline logs, as well as petrographic description of the thin sections (both optical and SEM) and whole-rock geochemical XRD, XRF and TOC methods. The samples are grouped into lithofacies type and further grouped into four main lithofacies associations: (1) silica-rich facies that are present in the Athel Silicilyte; (2) Silt-rich facies, which are present in the U Shale; (3) evaporite-facies, which are present in the overlying evaporite unit of A5E; and (4) post-depositionally modified facies that are present in the Athel Silicilyte.

Each lithofacies description is followed by an interpretation. The silica-rich facies are interpreted together since they exhibit many of the same microtextural attributes, differing only slightly in their compositions. The evaporite-facies are also interpreted together. Lithofacies interpretations focus mainly on the controlling factors for their sedimentary textures and detrital content variation in order to interpret the depositional environment. A discussion of the various mechanisms that might have contributed to the origin of the silica is reviewed in Chapter 7. The temporal and spatial variability of all lithofacies is described and interpreted towards the end of this chapter. A summary of the main findings is also outlined at the end of this chapter.

5.2 Lithofacies

In total nine different lithofacies have been identified; a summary of lithofacies composition, distribution, and characteristics are given in Table 5.1. Silica-rich facies is first described, their numbering (LF1-LF3) is based on their dominate occurrence from the base to the top of the Athel Silicilyte, followed by silt-rich facies (LF4), evaporite facies (LF5-6) and then post-depositionally modified lithofacies.

The well locations in the South Oman Salt Basin are shown in Fig. 5.1. These wells are used to establish vertical and lateral variability in Fig. 5.2. A summary of the vertical stacking pattern in one well (ALNR-2) is shown in Fig. 5.3. The following subsections outline a detailed description of each lithofacies and then their interpretation. Core photographs from each sampled well accompanied by a comprehensive selection of thin sections are presented in Appendix II. The compositions of individual samples are given in Appendix III.

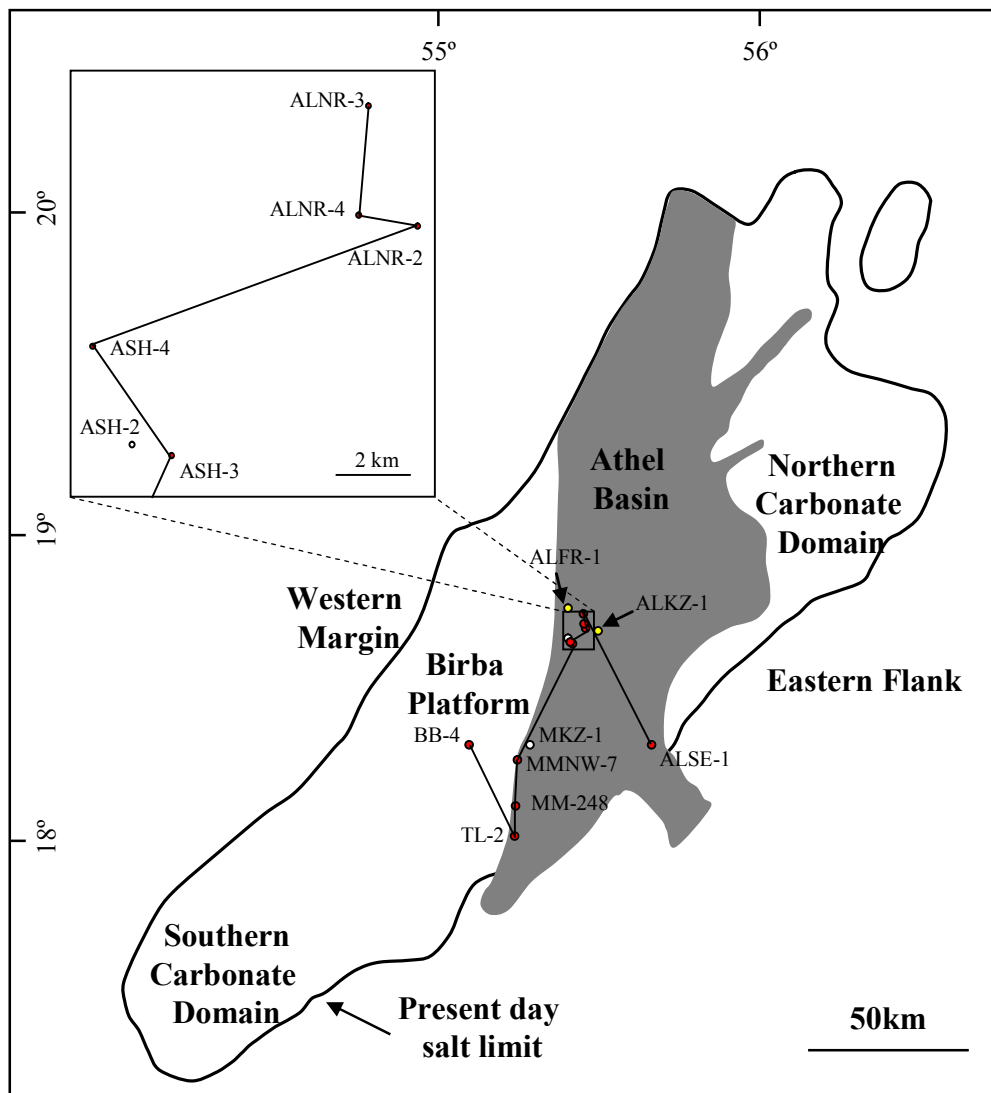


Figure 5.1. A map of the South Oman Salt Basin showing the Athel Basin (grey) and the carbonate platforms (white). The Athel Silicilyte and the bounding mudstones are only found in the Athel Basin, whilst the time-equivalent carbonate rocks are found on the platforms. It also shows wells location in Fig. 5.2 that are interpreted in this study. Upper left rectangular shows close-up map of wells location in Al Noor and Al Shomou fields. Red wells are included in wells correlation in Fig. 5.2 and white wells are interpreted but not used in the correlation (presented in Appendix I). The location of well ALKZ-1 and ALFR-1 are shown (yellow wells), which both did not encounter the Athel Silicilyte or the bounding mudstones (wireline data for these two wells are not available for this study). Modified after Amthor et al. (2005) and Schröder and Grotzinger (2007).

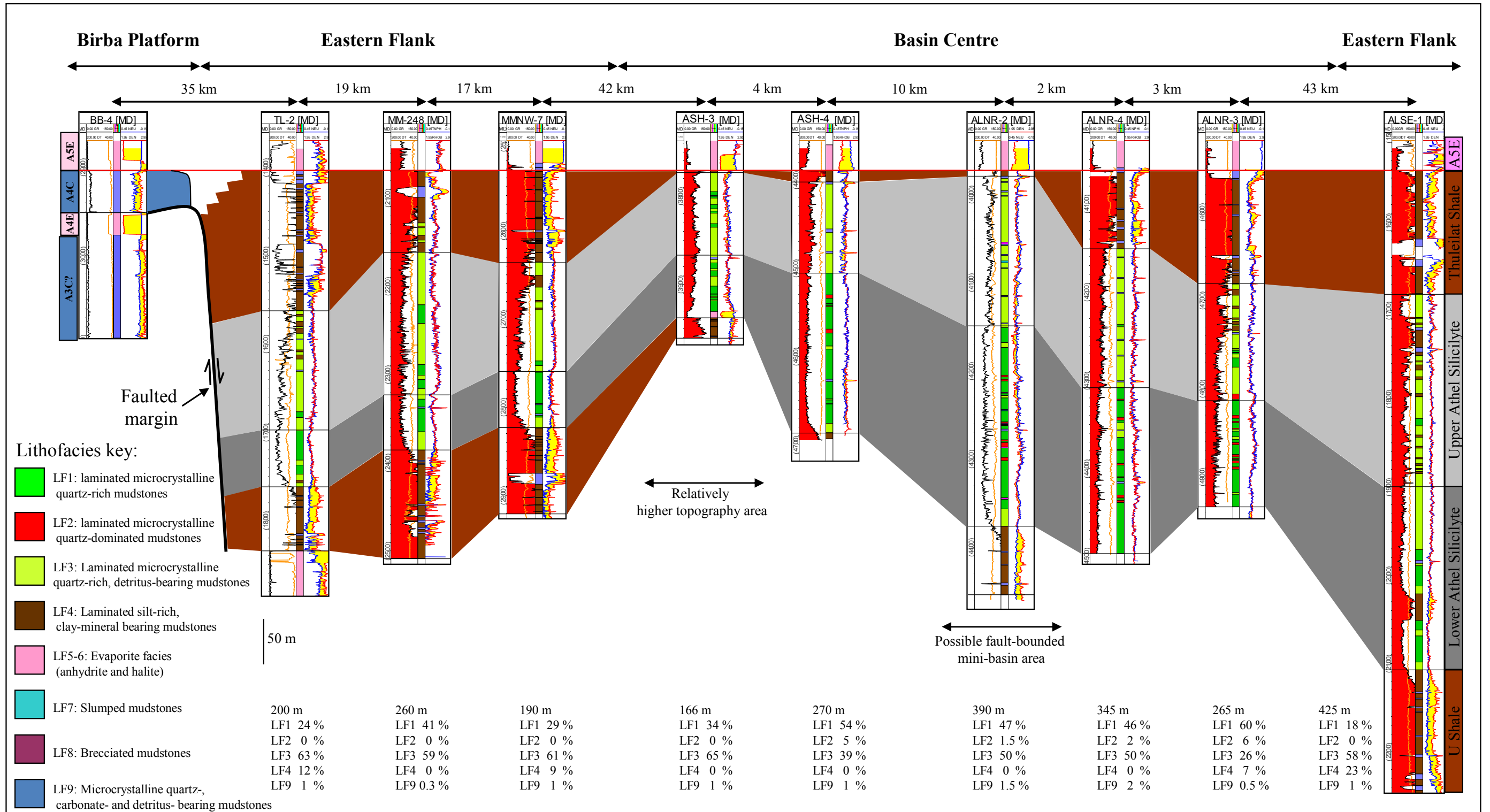
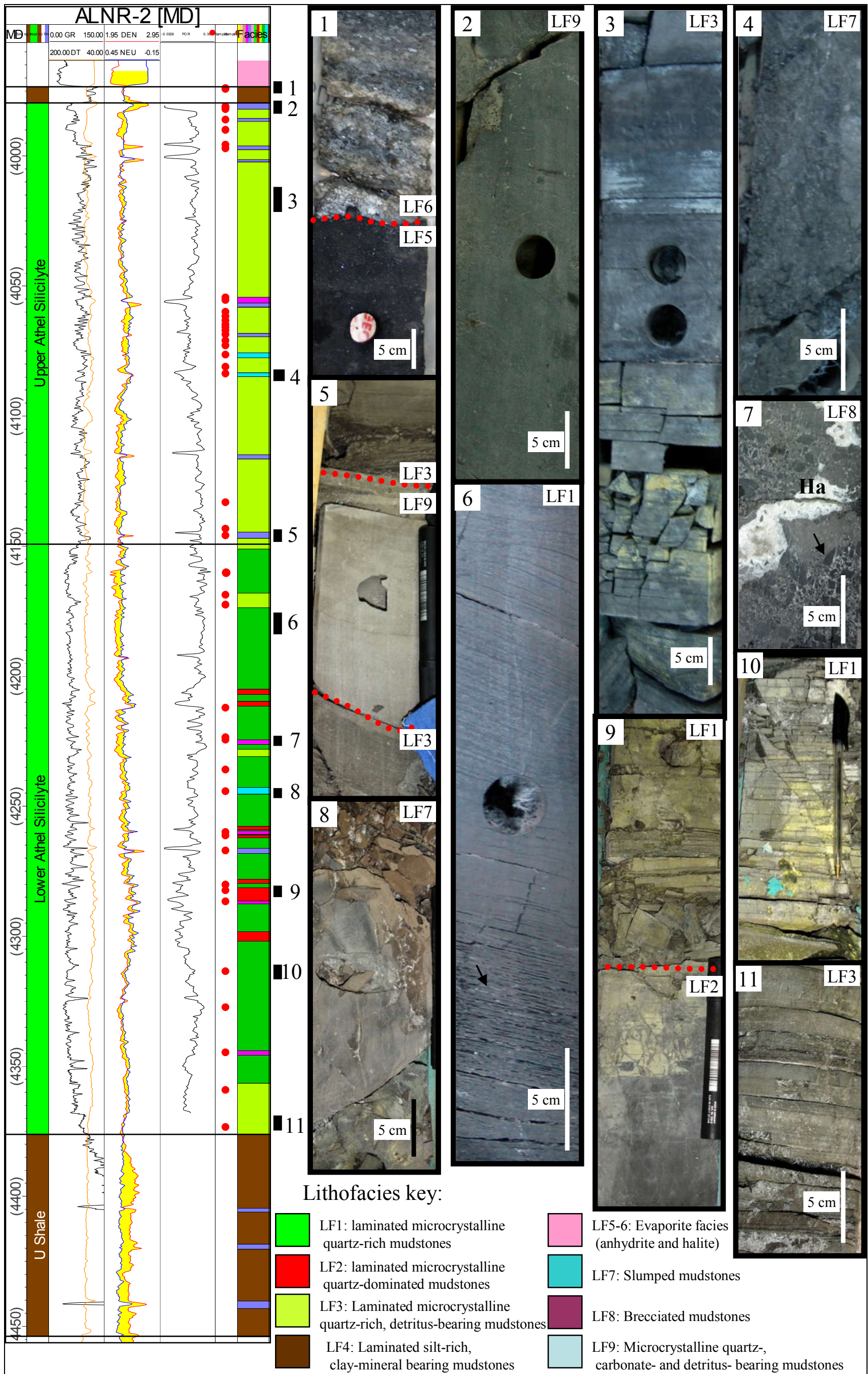


Figure 5.2. Well correlation from the Birba Platform through the Athel Basin margins and centre (indicated by the black line in Fig. 5.1). Each well shows measure depth (MD) in meters, GR values (0-150 API) filled in red colour and in the same panel sonic log (40-200 $\mu\text{m/s}$; reversed scale), interpreted lithofacies in the middle log, density log (1.95-2.95 g/cm^3) and in the same panel neutron log (-0.15-0.45 LPU; reversed scale). Also it shows the stratigraphic subdivision for the studied wells from the Birba Platform and the Athel Basin. On the platform only A4 carbonate (A4C) is present, whilst the U Shale, the Athel Silicilyte and the Thuleilat Shale are only present in the Athel Basin (Fig. 5.1). The Athel Silicilyte and time-equivalent platform carbonates are encased between two thick evaporite units of the A4 and A5 cycles. The Athel Silicilyte thickens towards the basin centre and the Thuleilat Shale thins. The tables below each well show the Athel Silicilyte thickness (m) and proportion (%) of each lithofacies (LF1-LF4 and LF9) in the Athel Silicilyte succession. LF1 and LF2 are volumetrically abundant in the Lower Athel Silicilyte, whilst LF3 is abundant in the Upper Athel Silicilyte. LF2 disappears towards the basin margins (e.g. TL-2, MM-246, MMNW-7 and ALSE-1). LF3 abundance increases towards the basin margins and LF1 abundance decreases, reflect a thinning of the Lower Athel Silicilyte (e.g. MM-248). In the basin centre both LF1 and LF2 abundance are approximately the same (e.g. ALNR-2). LF9 is relatively more common towards the Upper Athel Silicilyte and in the U Shale and the Thuleilat Shale. The upper part of the Upper Athel Silicilyte is interbedded with LF4 (silt-rich), especially in wells that encounter thick units of the Thuleilat Shale, located on the basin margins (e.g. ALSE-1, ALNR-3 and TL-2).



Caption next page

Figure 5.3. Wireline log data (GR, sonic, neutron, density and porosity) of well ALNR-2 and interpreted lithofacies, the samples taken from this well are shown in red circles. Lithofacies wireline signatures are derived by matching the studied cores/samples to the logs corresponding depth. The figure shows core photographs (1-11) and their depth is shown in black bars next to the wireline log data. Core photograph (1) represents LF5 and LF6 of the evaporite facies, LF5 is massive dark and mainly composed of anhydrite (optical and electron microscope images are shown in Fig. 5.15), LF6 is colourless and is mainly composed of halite. LF5 and LF6 are characterised by GR values ranging from 7-18 API, sonic from 43-55 $\mu\text{s/m}$, density from 2.8-3.0 g/cm^3 (LF5) and 2.0-2.2 g/cm^3 (LF6) and neutron are about zero limestone porosity units (LPUs). (2) Represents LF9, which is massive and shows no fissility, this lithofacies is mainly composed of dolomite/magnesite cement and microcrystalline quartz (microscopic images for this lithofacies are shown in Fig. 5.20). This lithofacies has GR values ranging from 35-75 API, sonic from 51-71 $\mu\text{s/m}$, density from 2.47-2.83 g/cm^3 , neutron from 0.11-0.24 LPUs and calculated porosity values is zero. (3) Represents LF3 and it is moderately fissile and laminated (microscopic images corresponding to this lithofacies are shown in Fig. 5.8). LF3 has GR values ranging from 68-93 API, sonic from 69-93 $\mu\text{s/m}$, density from 2.15-2.24 g/cm^3 , neutron from 0.23-0.33 LPUs and calculated porosity values is 16-25 %. (4) Represents LF7 (slumped) and it is massive (microscopic images are shown in Fig. 5.18). (5) Represents LF3 and in the middle LF9, LF9 is carbonate-bearing and its thickness normally 15 cm. (6) Represents LF1, it shows high fissility and very fine lamination, this lithofacies is mainly composed of microcrystalline quartz with a minor amount of detrital material (< 10 wt. %; microscopic images are shown in Fig. 5.4). LF1 has GR values ranging from 40-61 API, sonic from 70-95 $\mu\text{s/m}$, density from 2.09-2.28 g/cm^3 , neutron from 0.19-0.27 LPUs and calculated porosity values is 9-17 %. (7) Represents LF8 (brecciated), it shows angular clasts (arrowed) of the same composition as the surrounding fabric, original laminated fabric is destroyed, the white colour is halite (Ha) cementing fractures (microscopic images are shown in Fig. 5.19). (8) Represents LF7 and shows some foliation and soft-sediment deformation features (Fig. 5.18). (9) Represents LF2 (lower part of the picture), it is massive, dark and shows no fissility, LF2 is predominately composed of microcrystalline quartz, it is thickness normally varies from 20 to 40 cm (microscopic images are shown in Fig. 5.6), also it shows laminated LF1 (upper part of the picture). LF2 has GR values ranging from 40-60 API, sonic from 55-65 $\mu\text{s/m}$, density from 2.36-2.54 g/cm^3 , neutron from 0.06-0.13 LPUs and calculated porosity values is 3-12 %. (10) and (11) show highly fissile laminated LF1 and moderately fissile laminated LF3; respectively. This figure summarises the stratigraphic variability in one well.

Table 5.1. A summary of the lithofacies identified in this study.

Lithofacies	Occurrence & thickness	Textures	Average composition	Wireline signature, SiO ₂ /Al ₂ O ₃ ratio & porosity
<i>Silica-rich facies</i>				
LF1: Laminated microcrystalline quartz-rich mudstones (Fig. 5.4 & 5.5)	Vertically: Abundant in the Lower Athel Silicilyte Laterally: volumetrically thicker in the basin centre (47% of the Athel Silicilyte thickness, well ALNR-2) and thinner towards the basin margins (24 % of the Athel Silicilyte thickness, well TL-2)	In core: fissile and very finely laminated Microscopic analyses: wavy discontinuous lamination, each lamina extending for a few millimetres to up to 10 mm. Individual laminae comprise thin alternating strata of silica-rich layers and more organic/clay-rich layers; each layer is typically 20-30 µm thick.	Microcrystalline quartz (83 wt. %), clay minerals (6 wt. %), pyrite (3 wt. %), detrital quartz grains (1 wt. %), TOC (2.5 wt. %) and traces (< 5 wt. %) of evaporites (halite and anhydrite) found within fractures/stylolites	GR: 40-61 API Sonic: 70-95 µm/s Density: 2.09- 2.28 g/cm ³ Neutron: 0.19- 0.27 LPU Calculated log porosity: 9-17 % SiO ₂ /Al ₂ O ₃ ratio: 42 Core porosity: average 17.3 %
LF2: Laminated microcrystalline quartz-dominated mudstones (Fig. 5.6 & 5.7)	Vertically: present only in the Lower Athel Silicilyte as thin layers (20-50 cm) Laterally: only identified from wells in the basin centre and is not present in wells located in the basin margin. Represent 1.5-6 % of the Athel Silicilyte thickness	In core: dark-coloured, massive and shows no fissility Microscopic analyses: wavy discontinuous lamination, each lamina extending from few millimetres to up to 15 mm. Each laminae set comprises silica-rich and more organic-rich layers; each layer typically being-20 µm thick	Microcrystalline quartz (91 wt. %), and clay minerals (4 wt. %), pyrite (2 wt. %), organic carbon (TOC= 2 wt. %)	GR: 40-60 API Sonic: 55-65 µm/s Density: 2.36- 2.54 g/cm ³ Neutron: 0.06- 0.13 LPU Calculated log porosity: 3-12 % SiO ₂ /Al ₂ O ₃ ratio: 78 Core porosity: average 6.4
LF3: Laminated microcrystalline quartz-rich, detritus-bearing mudstones (Fig. 5.8 & 5.9)	Vertically: abundant in the Upper Athel Silicilyte Laterally: increases towards the basin margins (LF3= 63% of the Athel Silicilyte thickness, well TL-2). In the basin centre, its proportion roughly similar to LF1 (LF3= 50 % and LF1 =47 % of Athel Silicilyte thickness, well ALNR-2)	In Core: moderately fissile and laminated. Microscopic analyses: wavy discontinuous lamination similar to LF1& LF2. Individual laminae set comprises silica-rich and more organic/clay-rich layers. Each layer is slightly thicker than LF1, being 20-50 µm thick	Microcrystalline quartz (72 wt. %), clay minerals (12 wt. %), pyrite (4 wt. %), silt-sized detrital quartz grains (5 wt. %), organic carbon (TOC= 3 wt. %)	GR: 68-93 API Sonic: 69-93 µm/s Density: 2.15- 2.24 g/cm ³ Neutron: 0.23- 0.33 LPU Calculated log porosity: 16-25 % SiO ₂ /Al ₂ O ₃ ratio: 22 Core porosity: average 19.6 %

Lithofacies	Occurrence & thickness	Textures	Average composition	Wireline signature, SiO ₂ /Al ₂ O ₃ ratio & porosity
<i>Silt-rich facies</i>				
LF4: Laminated silt-rich, clay-mineral bearing mudstones (Fig. 5.12, 5.13 & 5.14)	Vertically: present above and below the Athel Silicilyte within the Thuleilat and U Shale, respectively. Laterally: The Thuleilat Shale thickness varies from 150 m to 5 and shows a decrease towards the basin centre. The U Shale has thickness varies from 75-150	In core: grey-dark grey, moderately laminated and fissile Microscopic analyses: parallel planner lamination, more continuous and straight compared with the laminae seen in LF1-LF3. Cross lamination is present too. Individual laminae comprise thin alternating detrital silt-sized grains of quartz, K-feldspar and mica-rich and more organic/clay-rich layers; each layer is typically 40-60 µm thick.	Detrital quartz (50 wt. %), feldspar (4 wt. %), mica (2 wt. %), clay minerals that include kaolonite, illite and smectite (27 wt. %), pyrite (8 wt. %), organic carbon (7 wt. %).	GR: 120-340 API Sonic: 80-95 µm/s Density: 2.38- 2.55 g/cm ³ Neutron: 0.18- 0.42 LPU Calculated porosity: na SiO ₂ /Al ₂ O ₃ ratio: 5.4 Core porosity: na
<i>Evaporite facies</i>				
LF5: Anhydrite- and detritus-bearing mudstones (Fig. 5.15 & 5.16)	Vertically: present on the top of Thuleilat Shale, which is the base of evaporite cycle (floor anhydrite) and it is overlain by LF6. Also it is present at top of each evaporite cycle (roof anhydrite) Laterally: in well ALNR-2 it has thickness of 0.8 m and it can reach to 20 m on the platforms.	In core: very dark and massive with some shiny crystals. Microscopic analyses: no lamination, euhedral anhydrite crystal is 20-200 µm across. The size of quartz grains is ranging from 20-500 µm	Euhedral anhydrite (42 wt. %), silt and sand-sized quartz grains (11 wt. %), microcrystalline-quartz (5 wt. %), euhedral magnesite (9 wt. %), clay minerals of predominately smectite/illite (17 wt. %), pyrite (6 wt. %), TOC (5 wt. %)	GR: 7-18 API Sonic: 43-55 µm/s Density: 2.80- 3.00 g/cm ³ Neutron: 0.00 LPU Calculated log porosity: na SiO ₂ /Al ₂ O ₃ ratio: na Core porosity: na
LF6: Halite-dominated mudstones (Fig. 5.17)	Vertically: above LF5, between floor and roof anhydrite Laterally: vary across the basin but can reach to up to 1,000 m. Evaporite lithofacies (LF5-6) are bracketing the Athel Silicilyte and bounding mudstones as well as age equivalent platform carbonates.	In core: colourless to white and alternate with relatively darker layers Microscopic analyses: na	Halite (94 wt. %) and minor anhydrite, pyrite and fluorite.	Similar to LF5. LF6 density is lower 2.0-2.2 g/cm ³

Lithofacies	Occurrence & thickness	Textures	Average composition	Wireline signature, SiO ₂ /Al ₂ O ₃ ratio & porosity
<i>Post-depositionally modified facies</i>				
LF7: Slumped mudstones (Fig. 5.18)	Vertically: equally present in the Upper and Lower Athel Silicilyte Laterally: only identified from core and lateral variation cannot be constrained using wireline data Typical thickness in core varies from 20 to 40 cm	In core: either massive or shows soft sediments deformation features Microscopic analyses: small scale folding and faulting, which caused disruption of original laminated fabric	Composition can vary between LF1 to LF3	Depend on composition
LF8: Brecciated mudstones (Fig. 5.19)	Same as LF7	In Core: broken angular clasts and original laminated fabric is destroyed. Microscopic analyses: each broken clast is up to 2 mm across and made of laminated microcrystalline quartz similar to the LF1-LF3. Small scale folding and faulting are present in some LF8 samples similar to LF7.	Same as LF7 Fractures and fault planes are normally cemented by magnesite, hydroxyfluorapatite, and/or evaporite minerals	Same as LF7
LF9: Microcrystalline quartz-, carbonate- and detritus-bearing mudstones (Fig. 5.20 & 5.21)	Vertically: present as thin layers, 15-50 cm, within the Athel Silicilyte and bounding mudstones. Rare in the Lower Athel Silicilyte and more abundant towards upper part of the Athel Silicilyte. More common within the bounding mudstones compared with the Athel Silicilyte Laterally: no variation observed	In core: light-coloured, massive and shows no fissility Microscopic analyses: either massive with cluster of dolomite grains within microcrystalline quartz framework, or exhibits wavy discontinuous lamination. Individual laminae comprise silica-rich and dolomite/magnesite-rich layers Laminae geometry and thickness are similar to LF1-LF3.	Microcrystalline quartz (31 wt. %), dolomite (36 wt. %), magnesite (5 wt. %), clay minerals (12 wt. %), pyrite (8 wt. %), detrital quartz grains (2 wt. %), TOC (2.5 wt. %) and traces (< 2 wt. %) of evaporites (halite and anhydrite)	GR: 35-71 API Sonic: 51-71 μm/s Density: 2.47- 2.83 g/cm ³ Neutron: 0.11- 0.24 LPU Calculated log porosity: 0-10 % SiO ₂ /Al ₂ O ₃ ratio: 10 Core porosity: average 4.9 %

5.2.1 Silica-rich facies

LF1: laminated microcrystalline quartz-rich mudstones

This lithofacies appears fissile and very finely laminated in core (Fig. 5.3.). Under optical and electronic microscope, it exhibits wavy discontinuous lamination; each lamina extends between 2 and 10 mm (Fig. 5.4). Individual laminae comprise thin alternating strata of silica-rich layers and more organic carbon/clay-rich layers; each layer is typically 20 to 30 μm thick. A combination of the petrographic, XRD (Fig. 5.5) and TOC results reveals that LF1 is mainly composed of microcrystalline quartz (average 83 wt. %), clay minerals (average 6 wt. %), pyrite framboids (average 3 wt. %), detrital quartz grains (average 1 wt. %), organic carbon (average TOC 2.5 wt. %) and traces (< 5 wt. %) of evaporite minerals (e.g. halite and anhydrite). The latter are particularly present within fractures and stylolites. The XRF results show that $\text{SiO}_2/\text{Al}_2\text{O}_3$ average ratio for LF1 is 42 (Appendix III).

Microcrystalline quartz crystals are typically 1-5 μm in diameter, and have euhedral-subhedral outlines. The individual crystals are mainly connected together with no visible grains (Fig. 5.4. F) forming networks of connected microcrystalline quartz. The microcrystalline quartz is non-luminescent under hot cathodoluminescence. Pyrite framboids have diameters ranging from 1.5 to 13.5 μm (pyrite size is discussed in section 5.3) and are evenly dispersed throughout the microcrystalline quartz framework in uncompacted pore spaces (Fig. 5.4 E). Pore spaces are also present between individual quartz grains and they are infilled with bitumen that contains a small amount of sulphur (Fig. 5.4 F). Core analysis shows that LF1 has an average helium porosity of 17.3 %.

In total 25 samples were analysed which represent this lithofacies (Appendix III) and they are principally present in the Lower Athel Silicilyte (Fig. 5.2 & 5.3). These samples in wireline logs are characterised by GR values that range from 40 to 61 API, sonic values from 70 to 95 $\mu\text{m/s}$, density values range from 2.09 to 2.28 g/cm^3 , neutron values range from 0.19 to 0.27 LPU (limestone porosity units) and calculated porosity values (from density log) range from 9 % to 17 % (Fig. 5.3).

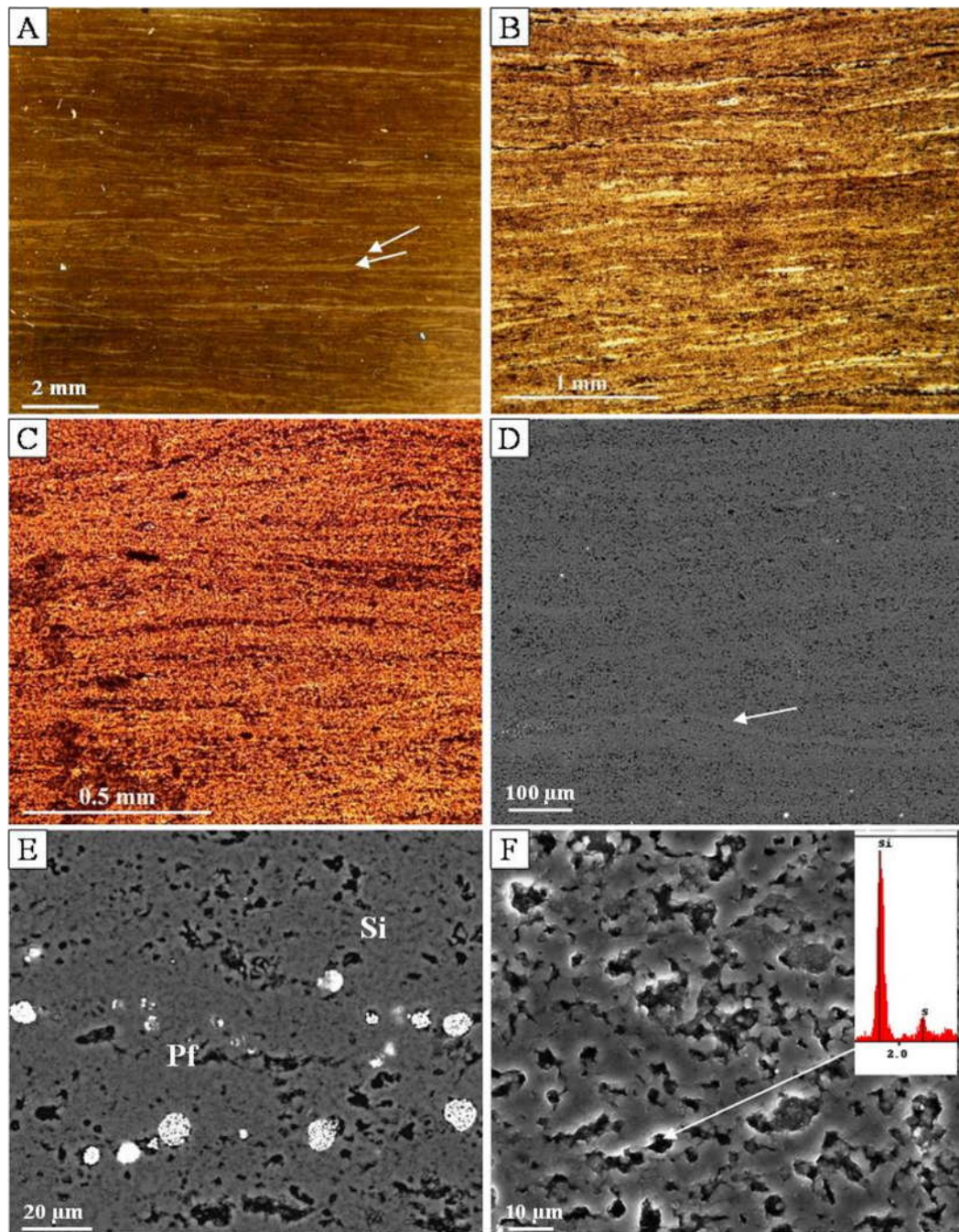


Figure 5.4. Photomicrographs of LF1. (A), (B) and (E) are from sample MKZ-1(4), (C) and (D) from sample ALNR-2(44) and (F) from sample ALNR-3(13). (A) A scanned-thin section that reveals lamination geometries. Here the laminae are wavy and discontinuous and each typically extends from a few millimetres to up to 10 mm. The pale laminae are silica-rich (arrowed) and the darker laminae are relatively more organic carbon- /clay-rich. (B) Plane-polarised (PPL) image of (A) that further illustrates lamination composition and geometry. Note each lamina is typically 20 to 30 μm thick. (C) PPL image also shows silica-rich (pale) and organic carbon-/clay-rich (dark) layers. (D) Back scattered electron image (BSEI) of (C), the similar Back Scattered Electron (BSE) coefficients (η) mean that silica framework, and silica-rich laminae (arrowed), are difficult to distinguish. However, organic carbon-/clay-rich laminae with lower η and very low η grains of organic carbon are present. Scattered pyrite framboids with high η are present. (E) BSEI showing close view of the silica framework and pyrite framboids (Pf), diameter of the pyrite framboids are typically 1 to 13 μm . (F) Secondary electron image (SEI) showing microcrystalline quartz crystals (typically individual crystal diameter varies from 1 to 5 μm) and they are connected and form a sheet of silica. Intercrystalline pore spaces are present (arrowed) and they are

normally infilled with hydrocarbon/bitumen. Energy-dispersive spectrometer indicates that the organic carbon contains some sulphur, small red peak marked by S, and the long peak represents silica (Si) from the background.

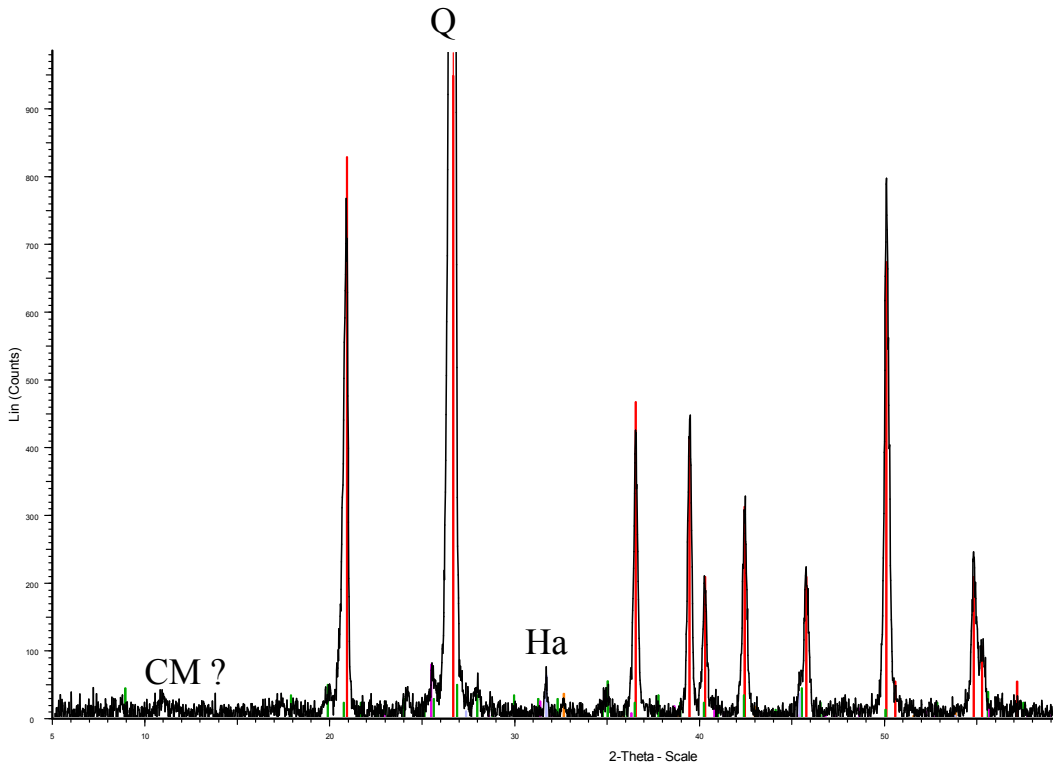


Figure 5.5. An XRD plot of LF1. The main minerals identified are quartz (Q; red peaks), clay minerals (CM [smectite/illite]; very small green peaks) and halite (Ha; pale blue). This plot was obtained from sample ALNR-2(44). Petrographical results of this sample are shown in Fig. 5.4.

LF2: laminated microcrystalline quartz-dominated mudstones

In core, LF2 is dark-coloured and homogeneous. Laminations are poorly developed and the core is not fissile (Fig. 5.3). Individual units of LF2 range in thickness from 0.2 to 0.50 m. Petrographical analyses reveal that LF2 comprises stacked wavy discontinuous lamination; each lamina extending from 2 to 15 mm (Fig. 5.6). Each laminae set comprises thin alternation of silica-rich layers and more organic carbon- and clay-rich layers; each layer typically being 20 μm thick. This lithofacies is predominately composed of microcrystalline quartz (average 91 wt. %), and clay minerals (average 4 wt. %), pyrite framboids (average 2 wt. %), organic carbon (average TOC= 2 wt. %) and traces (\approx 1 wt. %) of evaporite minerals cementing fractures (Fig. 5.7). The $\text{SiO}_2/\text{Al}_2\text{O}_3$ ratio of this lithofacies has an average of 78 (Appendix III).

The size, shape and other petrographic characteristics of each microcrystalline quartz crystal within this facies are similar to those in LF1; i.e. euhedral-subhedral and non-luminescent. The extremely high volume of quartz in this lithofacies results in a massive (sheet-like) connected network of microcrystalline quartz with low porosity, average helium core porosity is 6.4 %. (Fig. 5.4 F).

In total 8 samples were analysed which represent this lithofacies (Appendix III). These samples are present only in the Lower Athel Silicilyte as thin layers (20-50 cm thick; Fig. 5.2 & 5.3). This lithofacies is characterised by GR values ranging from 40 to 60 API, sonic values from 55 to 65 $\mu\text{m/s}$, density values from 2.36 to 2.54 g/cm^3 , neutron values from 0.06 to 0.13 LPU and porosity values from 3 % to 12 % (Fig. 5.3).

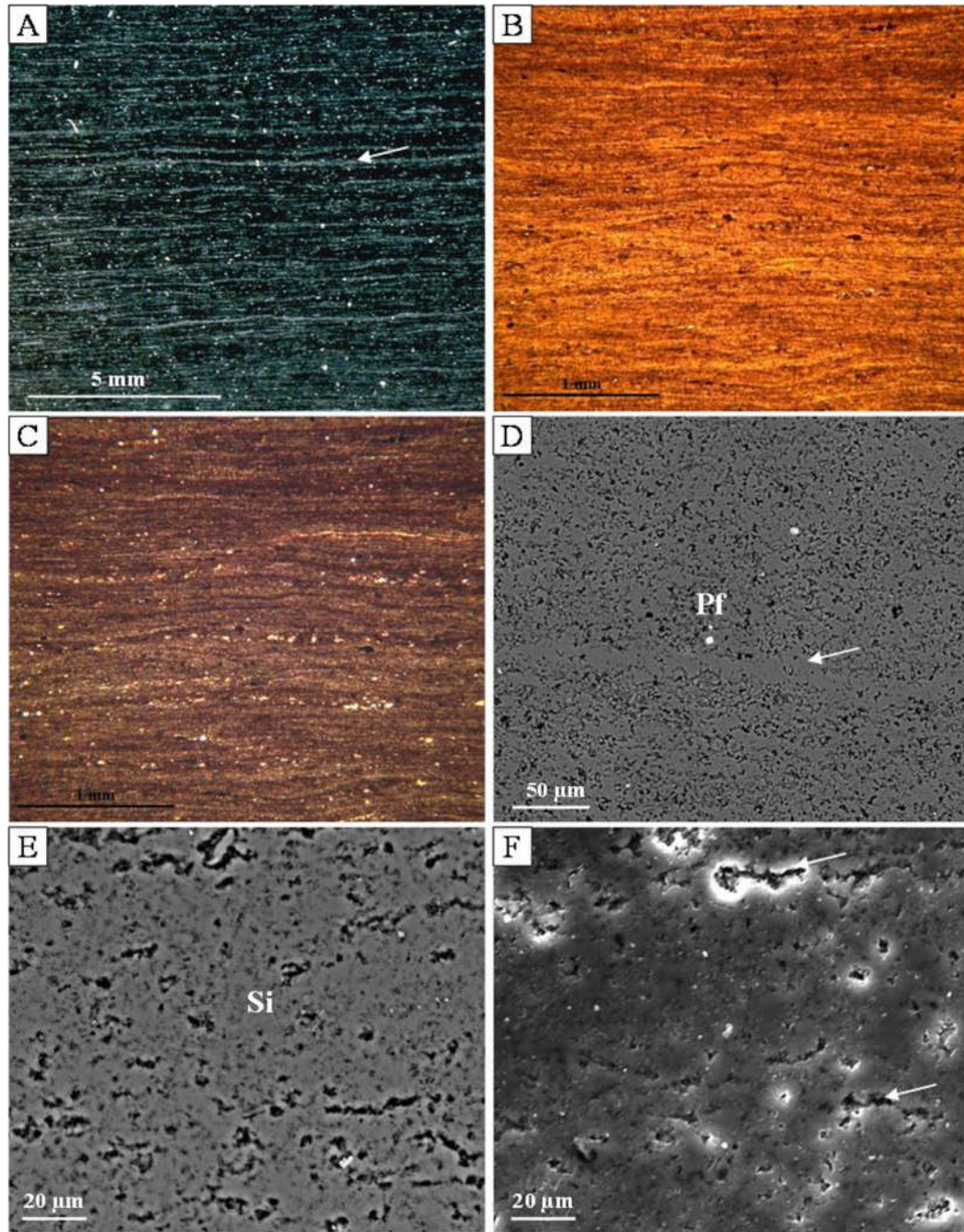


Figure 5.6. Photomicrographs of LF2. (A), (B), (C), (E) and (F) are from sample ALNR-2(33), (D) from sample ALNR-3(16). (A) A scanned-thin section shows wavy discontinuous lamination. Individual lamina typically extends from few millimetres to up to 15 mm across the field of view. The pale laminae are silica-rich (arrowed) and darker laminae are relatively more organic carbon- /clay-rich. (B) PPL and (C) cross-polarised (XPL) of (A) that also show silica-rich and relatively more organic carbon-rich layers. Here each layer is 10 to 20 μm thick. (D) BSEI showing silica-rich laminae (arrowed) whilst the organic carbon-/clay-rich laminae have lower η with some black dots. Pyrite framboids have high η . (E) BSEI showing close view of the silica framework of (A-C). (F) SEI showing microcrystalline quartz crystals and the individual quartz crystals are hard to distinguish as they are connected together to form a sheet of silica. Intercrystalline pore spaces are rare (arrowed).

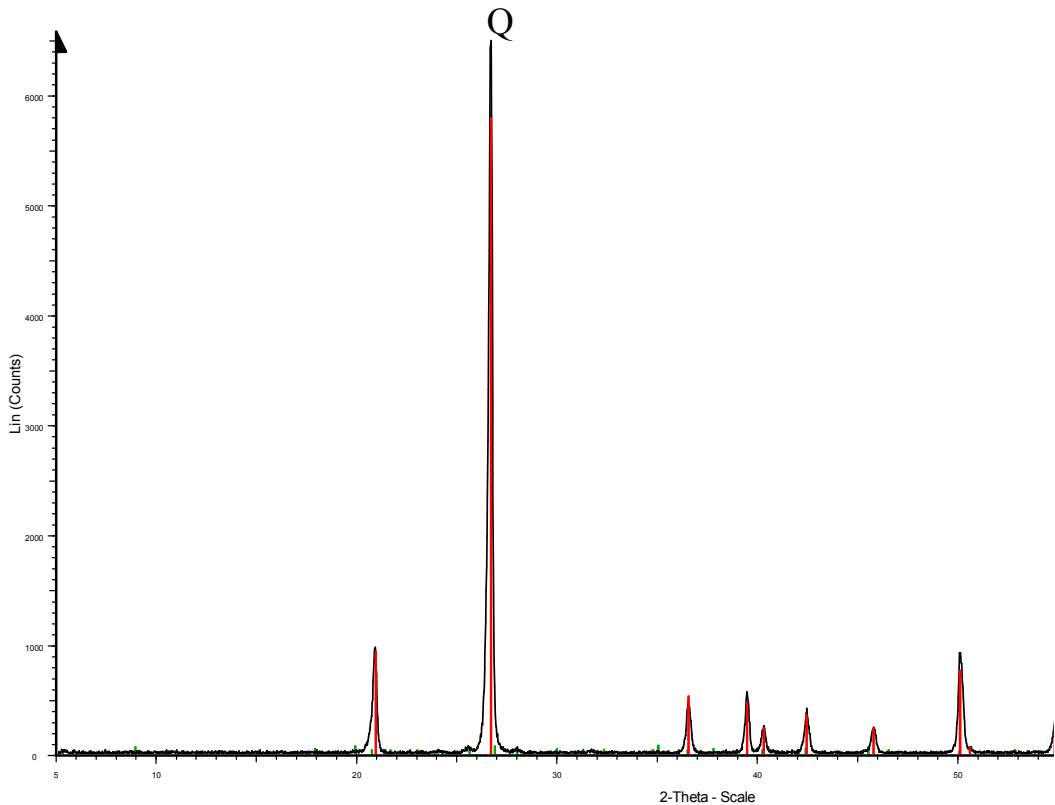


Figure 5.7. An XRD plot of LF2. The main minerals identified are quartz (Q; red peaks). Pyrite and clay minerals were not detected from XRD analysis as their concentrations are below detection limit; however, it was identified from the petrographical analyses. This plot was obtained from sample ALNR-2(33). Petrographical results of this lithofacies are shown in Fig. 5.4.

LF3: Laminated microcrystalline quartz-rich, detritus-bearing mudstones

LF3 appears in cores to be moderately fissile and laminated (Fig. 5.3). Under optical and electronic microscope, it reveals wavy discontinuous lamination similar to LF1 and LF2, (Fig. 5.8). Individual laminae comprise thin alternation of silica-rich layers and more organic carbon- and clay-rich layers. Each layer is slightly thicker than those in LF1 and LF2; being 20 to 50 μm thick. This lithofacies contains a much lower volume of microcrystalline quartz (average 72 wt. %) compared with LF1 and LF2. The other constituents include clay minerals (average 12 wt. %), pyrite (mainly framboidal; average 4 wt. %), silt-sized detrital quartz grains (average 5 wt. %), organic carbon (average TOC = 3 wt. %) and minor amounts (2-4 wt. %) of evaporite minerals and hydroxyfluorapatite cement (Fig. 5.9). The $\text{SiO}_2/\text{Al}_2\text{O}_3$ ratio of LF3 is lower than LF1 and LF2, with an average of 22 (Appendix III).

Microcrystalline quartz crystals have a similar size, shape and optical characteristics (1 to 5 μm , euhedral-subhedral and non-luminescent) to LF1 and LF2 (Fig. 5.6 F). Detrital quartz grains are loosely packed, not in contact with each other, and distributed randomly in the microcrystalline quartz framework (Fig. 5.8 B-D). Pyrite framboids dispersed throughout the microcrystalline quartz framework and seem to precipitate in uncompacted pore spaces (Fig. 5.8 F). In this lithofacies, the pore spaces are proportionally higher than LF1 and LF3 and are infilled with bitumen that shows a small amount of sulphur. This lithofacies has an average core porosity of 19.6 %.

In total 52 samples were analysed which represent this lithofacies (Appendix III) and they are mainly present in the Upper Athel Silicilyte, but also they are present at the base of the Lower Athel Silicilyte near the U Shale/Athel Silicilyte boundary (Fig. 5.2 & 5.3). These samples are characterised by GR values that range from 68 to 93 API, sonic values from 69 to 98 $\mu\text{m/s}$, density values from 2.15 to 2.24 g/cm^3 , neutron values from 0.23 to 0.33 LPU and calculated porosity values from 16 % to 25 % (Fig. 5.3). This lithofacies have higher GR values than LF1 and LF2. Spectral GR data of well ALNR-2 shows an increase in concentration of all GR components, i.e. potassium, thorium and uranium (Fig. 5.10).

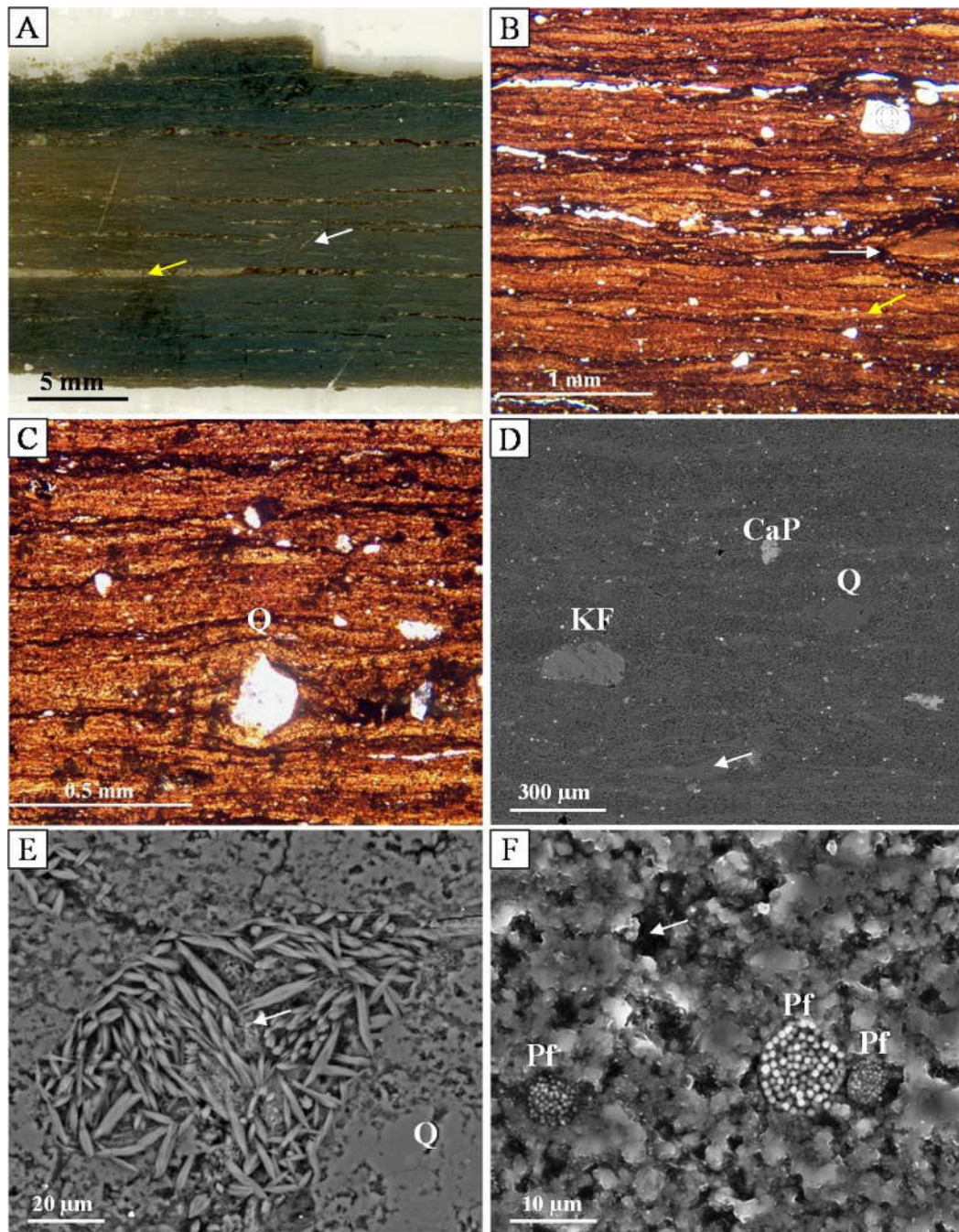


Figure 5.8. Photomicrographs of LF3. (A) to (D) are from sample ALNR-2(9), (E) from sample ALNR-2(15) and (F) from sample ALNR-2(22). (A) A scanned-thin section that reveals lamination geometries. It also shows fractures that were cemented by halite and anhydrite (yellow arrow) and a small-scale fault (white arrow). (B) PPL image of (A) shows silica-rich (pale: yellow arrow) and more organic carbon- and clay-rich layers (dark); each layer is 20 to 50 μm thick, and they exhibit wavy discontinuous laminae. Detrital silt-sized quartz grains (Q) are common and they are loosely packed within the microcrystalline quartz framework, black fracture (white arrow) is bitumen/clay minerals-rich. (C) PPL image shows detrital quartz (Q) and laminae above and below it are compacted. (D) BSEI showing silica-rich laminae (arrowed) whilst more organic carbon/clay-rich laminae have overall lower η and contain organic carbon (very low η). Also it shows quartz grains (Q), K-feldspar grain (KF) and hydroxyfluorapatite (CaP). Pyrite framboids have high η and are common compared with LF1 and LF2. (E) BSEI shows illite (nodular shape) and kaolinite (arrowed) clay minerals, as well as quartz grain (Q). Kaolinite and illite here appears to be replacing a detrital grain (possibly feldspar). (F) SEI shows microcrystalline quartz crystals (1-5 μm). Intercrystalline pore spaces (arrowed) are proportionally higher than LF1 and LF2.

LF2, which are infilled with bitumen. The pore spaces contain small amounts of sulphur (similar to LF1 in Fig. 5.4 F). Three very small pyrite framboids (Pf) are present (diameter ranging from to 3 to 7 μm), which are present within uncompacted pore spaces.

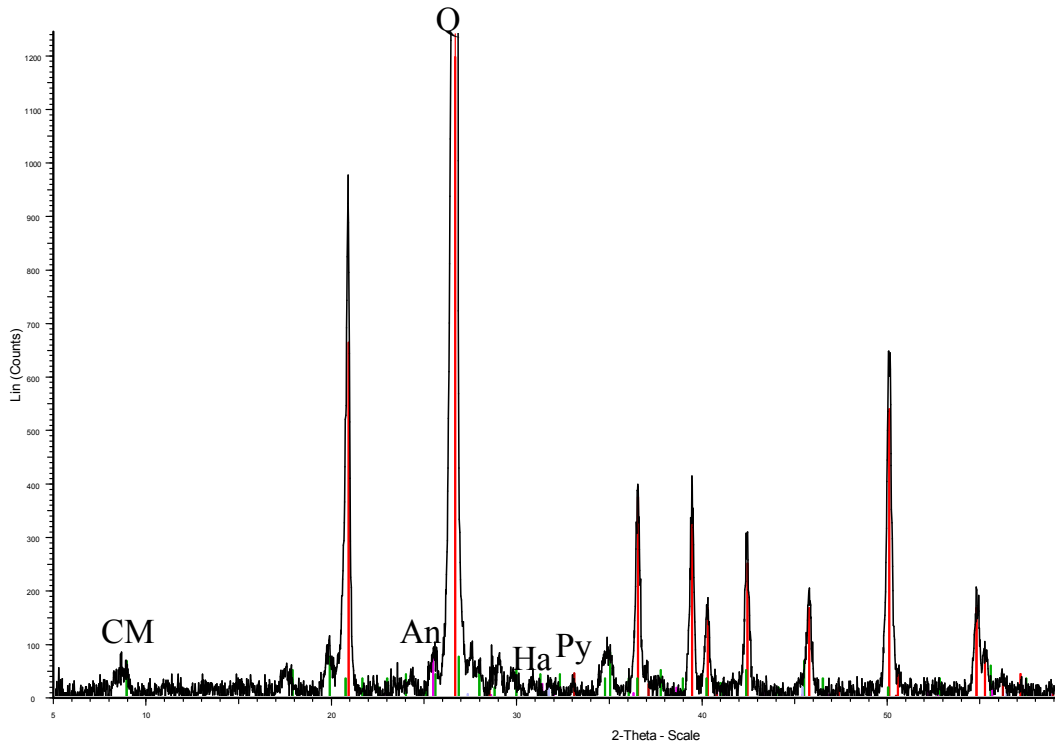
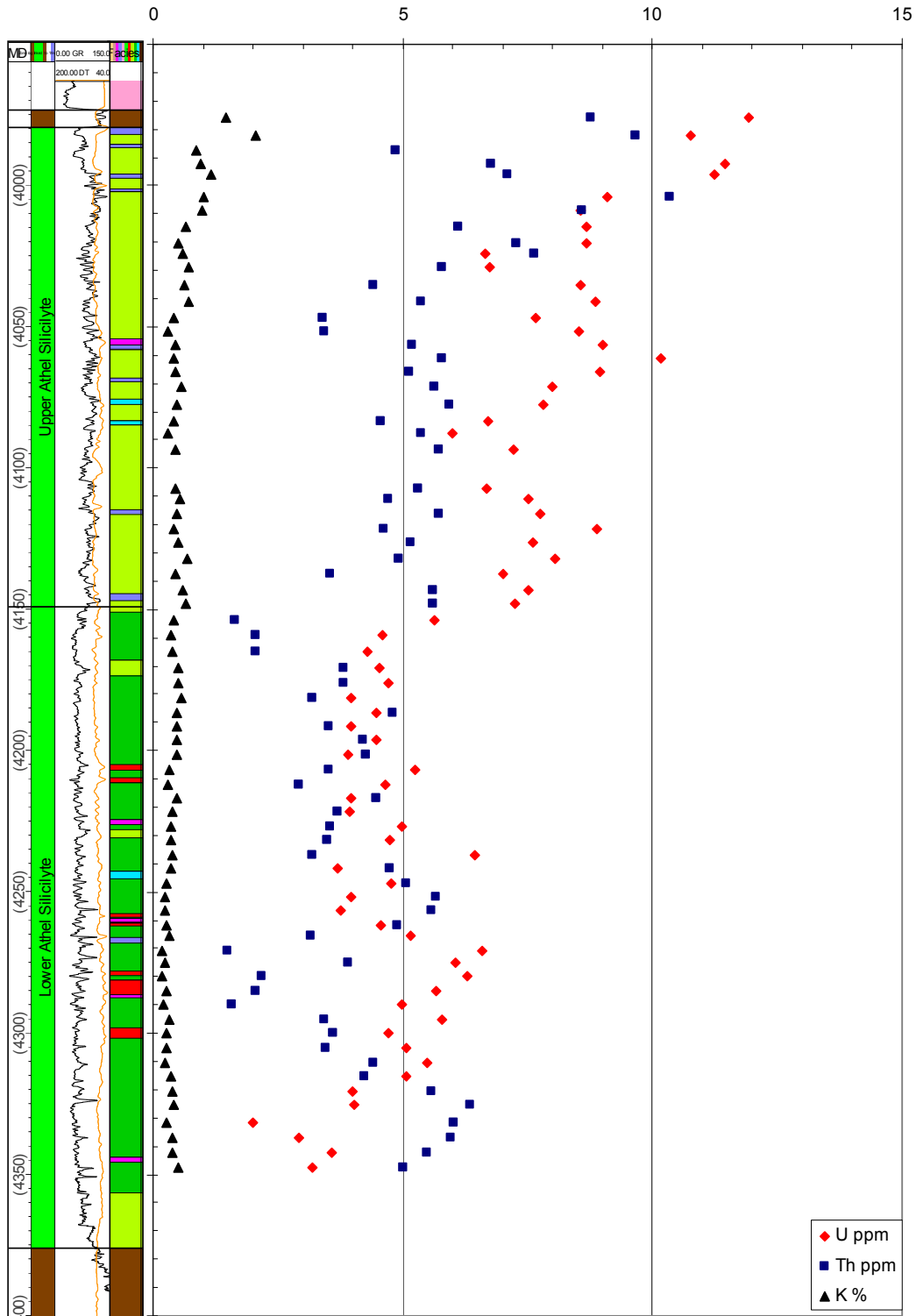


Figure 5.9. An XRD plot of LF3. The main minerals identified are quartz (Q; red peaks), clay minerals (CM [smectite/illite]; green peaks), anhydrite (An; purple peaks), pyrite (Py; dark red peaks) and halite (Ha; grey peaks). This plot was obtained from sample ALNR-2(9). The petrographical results of this lithofacies are shown in Fig. 5.8.



Lithofacies key:

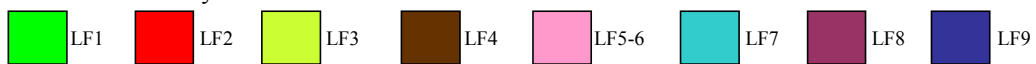


Figure 5.10. A plot showing spectral GR of well ALNR-2. Interpreted lithofacies and GR log are shown to the left of the graph (full lithofacies names are shown in Figs. 5.2 & 5.3). The increase in GR values towards the Upper Athel Silicilyte, mainly associated with LF3, results from the increase in all GR components; i.e. potassium, thorium and uranium. Spectral GR data were averaged every 5m and then they were plotted. Data from well ALNR-2 core analysis report (provided by PDO).

Interpretation of the silica-rich facies

The silica-rich facies (LF1-LF3) are in general characterised by wavy discontinuous laminations, high volumes of microcrystalline quartz (average LF1 = 83, LF2 = 91 and LF3 = 72 % wt.), relatively low contents of detrital material (average clay minerals and detrital quartz LF1 = 7, LF2 = 4 and LF3 = 16 % wt.), pyrite (average LF1 = 3, LF2 = 2 and LF3 = 4 % wt.) and organic carbon (average TOC of LF1 = 2.5 , LF2 = 2 and LF3 = 3 % wt.). The alternation between dark and light laminae and the shape of these laminae in addition to the absence of any inorganic physically induced laminations (e.g. parallel straight lamination produced by suspension sedimentations, graded lamination produced by low-density bottom currents and turbidity currents, or cross lamination/ripple marks structures produced by flowing bottom current), all suggest that lamination in the Athel Silicilyte is likely produced by accumulation of microbial layers in a deep low energy environment. These microbial layers could have been produced by: 1) microbial mat growth at the sediment-water interface, 2) microbial mat growth at the density contrast interface (seawater-brine interface) in the water column, or 3) derived from the water column by coagulation of single-celled plankton during sinking (i.e. marine snow/ sapropelic rain).

The Athel Silicilyte shows no crinkly lamination nor growth features, such as branching, shallow water domal structure or continuous laminae that normally characterise microbial mats growing on soft/hard substrata (Davies and Ludlam 1973; Schieber 1986; Noffke et al. 2002; Schieber et al. 2007a). In addition, a biomarker study on the Huqf Supergroup by Grosjean et al. (2009) shows that Athel Silicilyte biomarkers (from rock and oil samples) contain high amounts of a 2-methylhopanoids biomarker, which is a prominent lipid in the oxygenic photosynthesis of cyanobacteria (Summons et al. 1999), in similar quantities to the A4 and other Proterozoic stromatolitic carbonates. Furthermore, the Athel Silicilyte distinctively contains substantial amounts of 28,30-dinorhopane and 25,28,30-trinorhopane biomarkers, which suggest that the biomass was produced in an euxinic environment, possibly by sulphur oxidising bacteria (Williams 1984).

The absence of any features suggesting a microbial mat colonising soft/hard substrata and the unusual combination of photosynthetic and chemosynthetic biomarkers, together suggest that the microbial layers were not growing in the deep water at the sediment-water interface. These microbial layers were likely formed by coagulation of photosynthesising cyanobacteria during sinking. Once these microbial layers reached the bottom water (below the redox boundary; redox conditions are discussed in the following chapter), they were mineralised by sulphate reducing bacteria and the production of hydrogen sulphide stimulated sulphur oxidising bacteria biomass production. The biomass production by cyanobacteria and sulphur oxidising bacteria resulted in the unusual biomarker combination in the Athel Silicilyte. Alternatively, the microbial layers could also have been produced at the seawater-brine interface, where the density contrast facilitated growth of microbial mats. Growth of microbial mats at the seawater-brine interface is well documented from many modern environments (e.g. Red Sea and Mediterranean; Corselli and McCoy 1989; Erba 1991; Eder et al. 2001) where density contrast acts as trap for pelagic fall-out (inorganic and organic), which in turn stimulates microbial mat growth at the seawater-brine interface by chemosynthesis bacteria. The microbial layers would have been then delivered to the deep water as thin discontinuous layers due to the increased load of both organic and inorganic material (Erba 1991). Indeed, the alternation between silica-rich layers and clay-rich layers in the Athel Silicilyte (e.g. Fig. 5.8) could indicate that the microbial layers (formed by either of the mechanisms above) were likely delivered from shallow to deep water through the addition of small quantities of detrital material along with gravity settling.

The microbial laminae here are intensively silicified and they are composed of microcrystalline quartz (e.g. Fig. 5.4 D). The microcrystalline quartz characteristics (1 to 5 μm , euhedral-subhedral and non-luminescent) suggest that quartz precipitated *in situ* (authigenically). The homogeneity of the silicification style and the absence of any pre-existing pseudomorphs or textures indicating that the silica precipitated into pore spaces in all silica-rich facies across the basin, suggest that the silica in the Athel Silicilyte was a primary precipitate (syndepositional) in the microbial layers. This interpretation is also

reinforced by the following observations: 1) preservation of up to 390 m thick microbially laminated fabric; 2) loose packing of detrital grains (Fig. 5.8 B-D), suggesting that they accumulated during silica precipitation; and 3) association with pyrite framboids (either syngenetic or early diagenetic framboids; discussed further in Chapter 6; section 6.5), which are present within uncompacted pore spaces (Fig. 5.8 F). In addition, the thickness and the lateral extent of the Athel Silicilyte (Fig. 5.2) showing similar silicification style and composed of fairly homogeneous microcrystalline quartz make the Athel Silicilyte unlikely to be a secondary diagenetic product. If the Athel Silicilyte is a secondary diagenetic product, it would be expected to show some heterogeneity in the silicification style across the basin. The heterogeneity would be probably controlled by permeability and organic matter content. For example, documented diagenetic cherts are reported to have a few to 10s of centimetre thickness, which are normally cementing permeable/organic-rich facies and they normally found interbedded with other type of rocks (e.g. nodular chert in carbonates; section 4.3.2 & 4.3.3; Knauth 1979; Knoll 1985; Maliva et al. 2005).

The relative increase in the average concentration of detrital components, including both detrital quartz and clay minerals, between LF1 (7 wt. %), LF2 (4 wt. %) and LF3 (16 wt. %) is associated with a decrease in silica concentrations (LF1 = 83, LF2 = 91 and LF3 = 72 wt. %) and a decrease in $\text{SiO}_2/\text{Al}_2\text{O}_3$ ratios (LF1 = 42, LF 2 = 78 and LF3 = 22). This concomitant relation between the detrital component contents and the microcrystalline quartz contents might indicate that a higher detrital input to the Athel Basin resulted in a decrease in the silica precipitation rate in the microbial layers. This will be discussed in Chapter 7 (section 7.3.3), once the geochemical evaluations during precipitation have been established. The slight decrease in TOC contents between LF1 (2.5 wt. %), LF2 (2 wt. %) and LF3 (3 wt. %) can be interpreted by the decrease in the microcrystalline quartz contents in the same order. The extremely high volumes of precipitated silica likely diluted TOC contents (especially in LF2). Given that LF3 has higher content of clay minerals and slightly higher contents of organic carbon, they would explain the higher GR values in LF3 (68-93 API) relative to LF1 (40-61) API and LF2 (40-60 API). These higher values likely result from

the increase in concentrations of K, U and Th that contribute to the total GR value (Fig. 5.10).

The diminutive pyrite in the silica-rich facies are mostly framboidal and present within uncompact pore space (Fig. 5.8 F) suggesting that they precipitated during early diagenesis, either prior to significant burial or within the water column (Chapter 6; section 6.5), in a reducing environment. In these settings, sulphate reducing bacteria utilise organic carbon as a reductant and may ultimately cause pyrite to precipitate (Berner 1970; Wilkin and Barnes 1997; Taylor and Macquaker 2000). Here pyrite concentrations are broadly proportional to the clay mineral content (Fig. 5.11), consequently it is likely pyrite precipitation was limited by the availability of reactive iron, rather than by either the availability of sulphate or organic carbon. Crucially, the oil generated from the Athel is sulphur-rich (1.5 mol % H₂S; also see Fig. 5.4 F; Alixant et al. 1998; Amthor et al. 2005; Schröder and Grotzinger 2007). This suggests that the excess reduced sulphur produced by sulphate-reducing bacteria was incorporated into the organic matter during the formation of the Athel Silicilyte (Fig 5.4 E; Raiswell et al. 1993; Henneke et al. 1997; Passier et al. 1999).

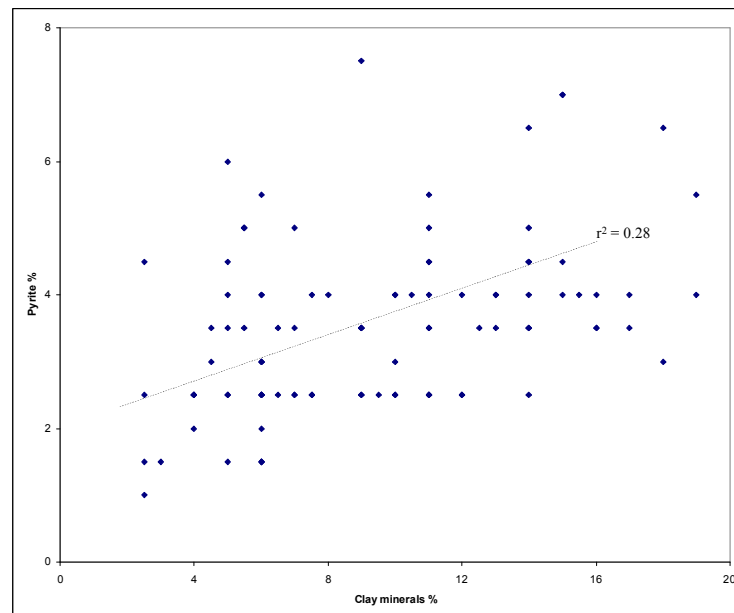


Figure 5.11. A graph showing the relation between clay minerals and pyrite contents in the silica-rich facies. As the contents of clay minerals increase, the pyrite (mostly framboidal) contents increase. Each component is estimated semiquantitatively from the petrographical results with aid from the XRD, XRF and TOC results. A very weak correlation ($r^2 = 0.28$) is probably resulted from the semi-quantitative estimation. Each sample mineralogical composition is shown in Appendix III.

5.2.2 *Silt-rich facies*

LF4: Laminated silt-rich, clay-mineral bearing mudstones

Laminated silt-rich, clay mineral bearing mudstones are identified from the U Shale and they are also abundant in the Thuleilat Shale, which is mineralogically and texturally similar to the U Shale (Amthor et al. 2005; Schröder and Grotzinger 2007). Ten samples were collected for petrographic and geochemical analysis from the U Shale (Appendix III). Microtexturally these mudstones exhibit parallel planar laminae (Fig. 5.12), which are more continuous and straight compared with the laminae described in the silica-rich facies. Ripple lamination is also present in one sample within the U Shale (Fig. 5.13). Individual laminae comprise thin alternating intercalations variously composed of detrital silt-sized grains of quartz, K-feldspar and mica- and finer grained more organic carbon- and clay-rich layers. Each lamina is typically 40 to 60 μm thick. A combination of the petrographic, XRD (Fig. 5.14) and TOC results reveals that this lithofacies is mainly composed of detrital quartz (average 50 wt. %), feldspar (average 4 wt. %), mica (average 2 wt. %), clay minerals including kaolinite, illite and smectite (average 27 wt. %), pyrite (mainly framboidal; average 8 wt. %), organic carbon (average TOC = 7 wt. %) and traces (< 2 %) of dolomite, barite and hydroxyfluorapatite. The XRF results show this lithofacies has an average $\text{SiO}_2/\text{Al}_2\text{O}_3$ ratio of 5.4 (Appendix III).

In this lithofacies the silt-sized detrital grains (ranging in diameter from 30 to 60 μm) are moderately-sorted and sub-angular to sub-rounded (Fig. 5.12 C-F). Dissolution of detrital grains (e.g. feldspar) and replacement by clay minerals (e.g. kaolinite) are common (Fig. 5.14 F). Pyrite framboids in this lithofacies are dispersed throughout the detrital quartz framework and have a diameter ranging from 1.5 to 10 μm (subsection 5.3 below) similar to the framboid diameter in the silica-rich facies (Fig. 5.12 E & F).

In wireline logs this lithofacies has high GR values ranging from 120 to 340 API, sonic values from 80 to 95 $\mu\text{m/s}$, density values from 2.38 to 2.55 g/cm^3 and neutron range from 0.18 to 0.42 LPU (Fig. 5.3).

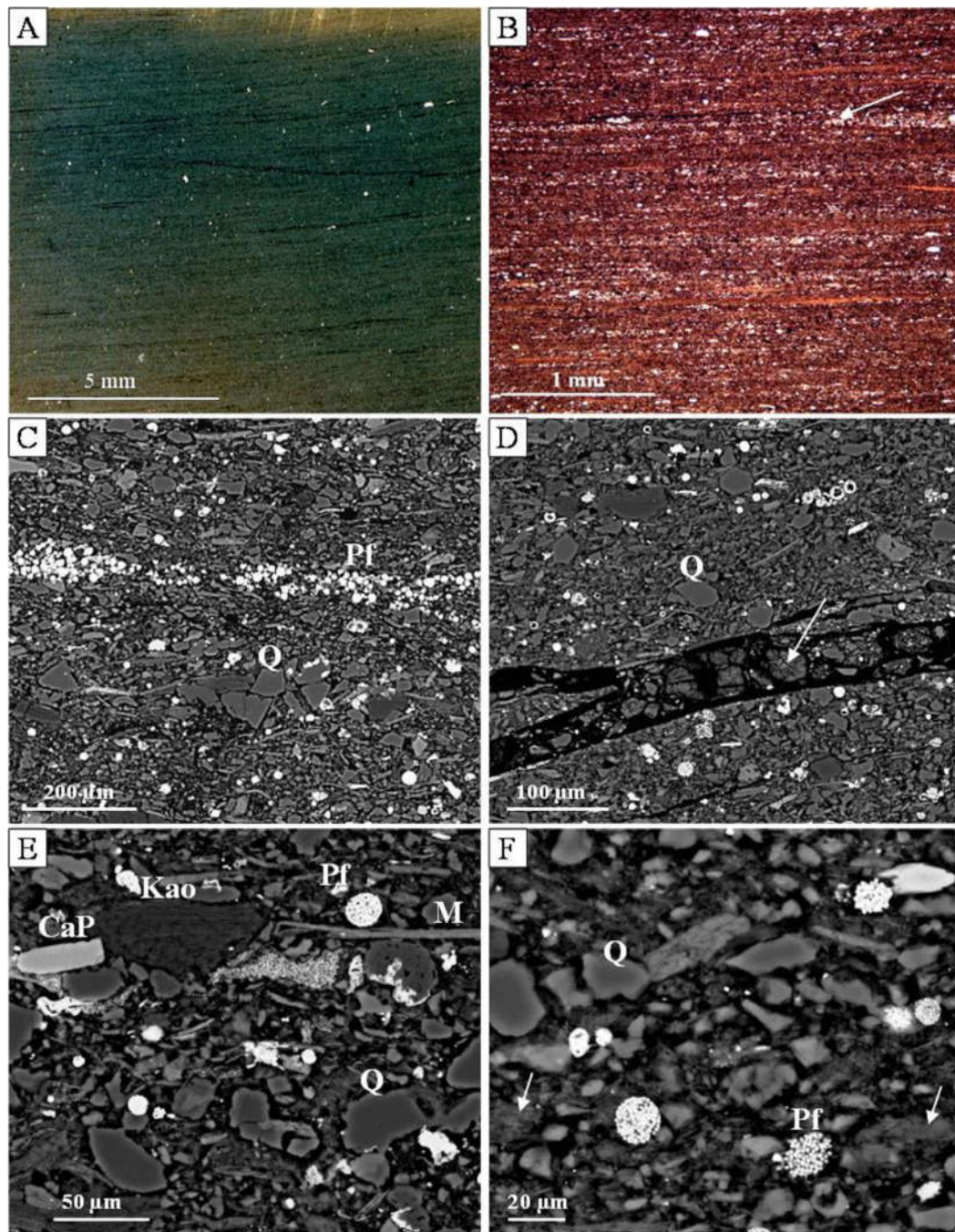


Figure 5.12. Photomicrographs illustrating the range of mineralogy and textures in LF4. (A), (B) and (F) are from sample AL-9(9), (C) and (E) from sample AL-9(4). (A) A scanned-thin section shows parallel continuous lamination, each laminae set consists of silt-rich layers and organic carbon- and clay-rich layers. (B) PPL image of (A) that further illustrates lamination composition and geometry, each lamina is typically 40 to 60 μm thick. (C) BSEI shows the intercalations of the silt-rich layers and organic carbon- and clay-rich layers. The framework is mainly composed of quartz grains (Q), pyrite framboids (Pf) and clay minerals. (D) BSEI shows a fracture within the sample that infilled with bitumen and sulphate minerals (anhydrite; arrowed). Also it shows quartz grains (Q). Pyrite framboids have high η . (E) BSEI shows a close view of LF4 framework, which is mainly consists of silt-sized quartz (Q), micas (M) and pyrite framboids (Pf). The diameters of the pyrite framboids vary from 1.5 to 10 μm . Clay minerals include kaolinite (Kao) and smectite/muscovite are common between the grains. It also shows hydroxyfluorapatite (CaP). (F) BSEI shows quartz grains (Q), grain dissolution (arrowed) and pyrite framboids (Pf), dark/black areas probably contain much organic carbon and clay minerals.

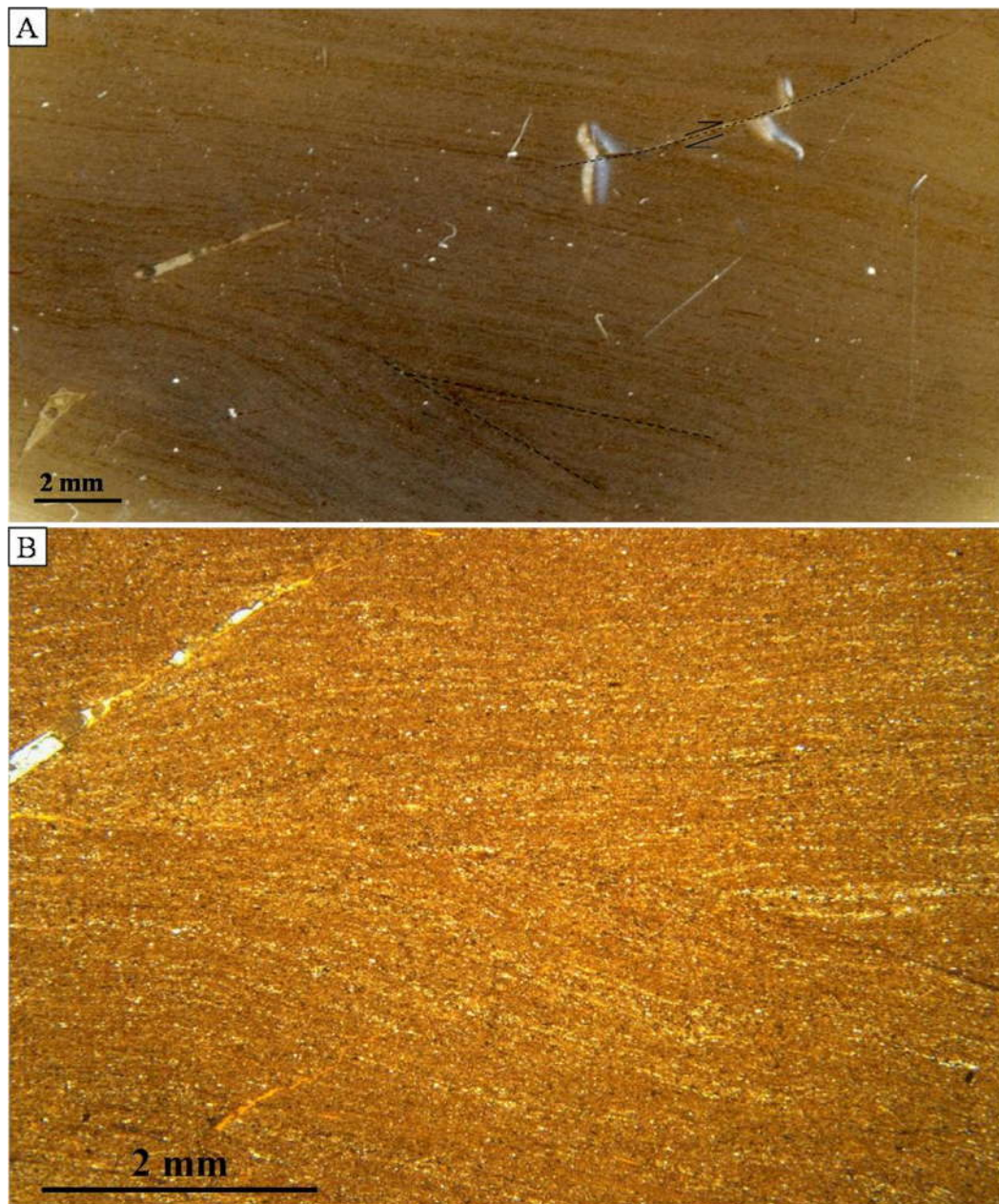


Figure 5.13. Photomicrographs illustrate ripple lamination in LF4. (A) A scanned-thin section shows the ripple lamination at the base (annotated with dotted lines). Here parallel strata on-lapping more tilted strata. A small fault at the top (annotated) with an offset of a few millimetres is also present. (B) PPL image that further illustrates the ripple lamination in (A). This sample consists of alternating silt-rich laminae and organic carbon- and clay-rich laminae. These photomicrographs are collected from sample AL-9(6).

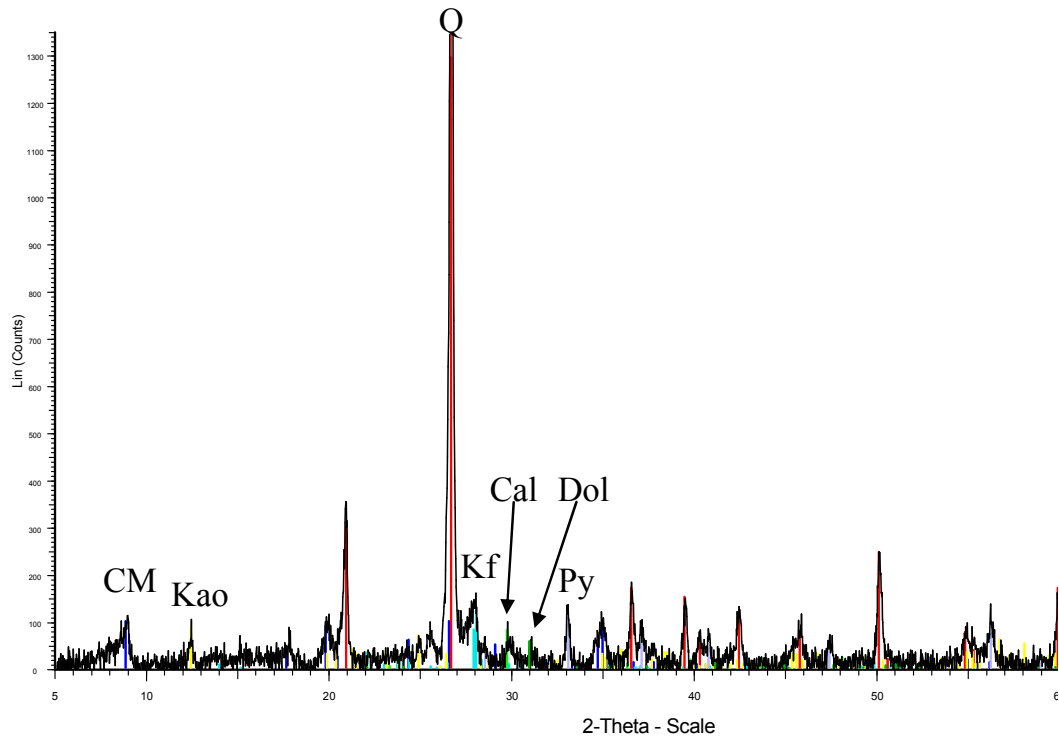


Figure 5.14. An XRD plot of LF4. The main minerals identified are quartz (Q; red peaks), feldspar (Kf), clay minerals (smectite/illite [CM] and kaolinite[Kao]), pyrite (Py), calcite (Cal) and dolomite(Dol). This plot is obtained from sample AL-2(9). Petrographical results of this lithofacies are shown in Fig. 5.12.

Interpretation of silt-rich facies

The presence of parallel laminations consisting of silt-sized grains layers and more organic carbon- and clay-rich layers plus the absence of wavy laminae that were described in the silica-rich facies, all suggest that the depositional environment during the silt-rich facies accumulation was dominated by suspension settling of detrital sediments in a low energy environment (e.g. O'Brien 1996; Noffke 1998; Schieber et al. 2007a). In addition, the presence of ripple laminae in one sample could record periodic higher energy conditions during accumulation of this unit, where advective sediment transport processes were operating (e.g. Macquaker and Bohacs 2007; Schieber et al. 2007b; Macquaker et al. 2010).

The high TOC values (up to 8 wt. %) in this lithofacies relative to the silica-rich facies could be interpreted as a result of higher primary productivity in surface waters, which was likely fuelled by higher nutrition supply (e.g. nitrogen and phosphorus) delivered along with the detrital material (e.g. Meyers 1993; Wignall 1994). Optimum sedimentation rate during deposition of the silt-rich

facies could also contribute to higher TOC values, as result of faster delivery to the seabed and faster burial, and as a consequence less organic matter was oxidised during delivery and burial. Anoxic conditions could also contribute to the high TOC values, as a result less organic matter would be oxidised. However, persistent bottom water anoxia during accumulation of this unit could not have occurred since the preserved ripples (Fig. 5.13) indicate that advective transport processes were operating at the sediment-water interface, at least periodically. The preservation of such high organic carbon therefore must have been due to a balance between high organic matter productivity, rapid delivery to the seabed and episodic burial (Macquaker et al. 1997; MacQuaker et al. 2007; Al Balushi et al. in press). Furthermore, the absence of microcrystalline quartz here means that organic matter was not diluted by silica precipitation.

The presence of pyrite framboids in this lithofacies suggests they were formed during early-diagenesis (at shallow burial depths or within the water column; discussed in section 6.5) in a reducing environment, as a result of bacterial sulphate reduction that oxidised organic carbon (e.g. Berner 1970; Taylor and Macquaker 2000). Higher proportions of pyrite (average 8 % wt.) relative to the silica-rich facies is consistent with higher clay mineral contents (average 27 % wt.) in the silt-rich facies, and hence more reactive iron was available to form pyrite.

5.2.3 *Evaporite lithofacies*

Six cycles of evaporite deposition have been recognised by previous workers in the Ara Group, which are found in both the carbonate platforms and the Athel Basin (Fig. 5.2; Mattes and Morris 1990; Grotzinger et al. 2002; Amthor et al. 2003; Schröder et al. 2003; Al-Siyabi 2005; Amthor et al. 2005). Each evaporite cycle in the Ara Group is normally found in the following order (from base to top): anhydrite- halite- potassium salt- halite- anhydrite (Mattes and Morris 1990; Schröder et al. 2003). This study only identified anhydrite (LF5) and halite (LF6) in ALNR-2 cores from the base of the overlying evaporite cycle (A5E).

LF5: Anhydrite- and detritus-bearing mudstones

In core this lithofacies is very dark and massive (Fig. 5.3). Only one sample from this lithofacies was described petrographically. The petrographical (Fig. 5.15), XRD (Fig. 5.16) and TOC results indicate that this lithofacies is composed of euhedral anhydrite (average 42 wt. %), silt and sand-sized quartz grains (average 11 wt. %), microcrystalline-quartz (average 5 wt. %), euhedral magnesite (average 9 wt. %), clay minerals that are predominately smectite/illite (average 17 wt. %), pyrite (average 6 wt. %), organic carbon (average TOC = 5 wt. %), and traces (< 5 wt. %) of barite and halite. The average $\text{SiO}_2/\text{Al}_2\text{O}_3$ ratio for this lithofacies is 3.5 (Appendix III). Individual euhedral anhydrite crystals have diameters of between 20 and 200 μm (Fig. 5.15D). The size of quartz grains ranges from 20 to 500 μm (Fig. 5.15). Quartz grains show intense dissolution features on both grain centre and edges (Fig. 5.15 F).

This lithofacies is present towards the transition from mudstones to the next evaporite cycle in well ALNR-2 core overlain by LF6 (halite; Fig. 5.3). Its total thickness in well ALNR-2 core is 0.8 m, however, on the platforms anhydrite units are reported to have a total thickness of up to 20 m (Schröder et al. 2003). LF5 is interpreted from wireline logs together with LF6 since they have a very similar log signature.

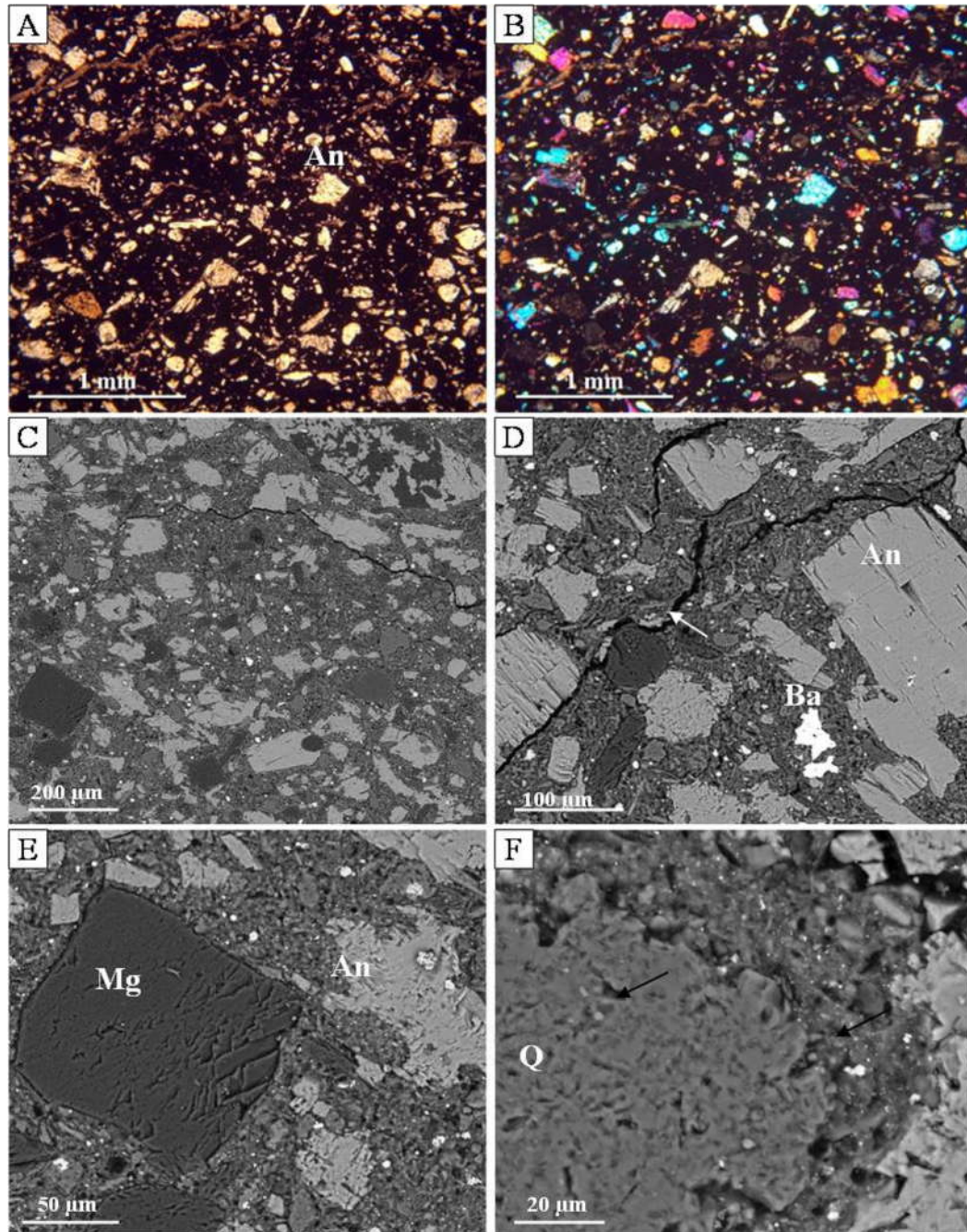


Figure 5.15. Photomicrographs of LF5 from sample ALNR-2(2). (A) PPL image and (B) XPL image show anhydrite crystals (An). Anhydrite shows moderate relief in PPL and bright second order interference colour in XPL. (C) BSEI shows anhydrite crystals and quartz grains (Q) in a matrix composed of clay minerals (illite/smectite) and microcrystalline quartz. Magnesite crystals (low η ; Mg) and barite (very high η ; Ba) are present too. (D) BSEI shows show euhedral anhydrite crystals (An; individual crystal size is ranging from 20-200 μm) and barites (Ba). Fractures (arrowed) are normally infilled with bitumen and/or halite. (E) BSEI shows a euhedral magnesite (Mg) surrounded by microcrystalline quartz and clay minerals. Anhydrites (An) of various sizes and pyrites (very high η) also present. (F) BSEI shows close view of a quartz grain (Q), note the dissolution affect on the quartz grains at the edge and the centre (arrowed).

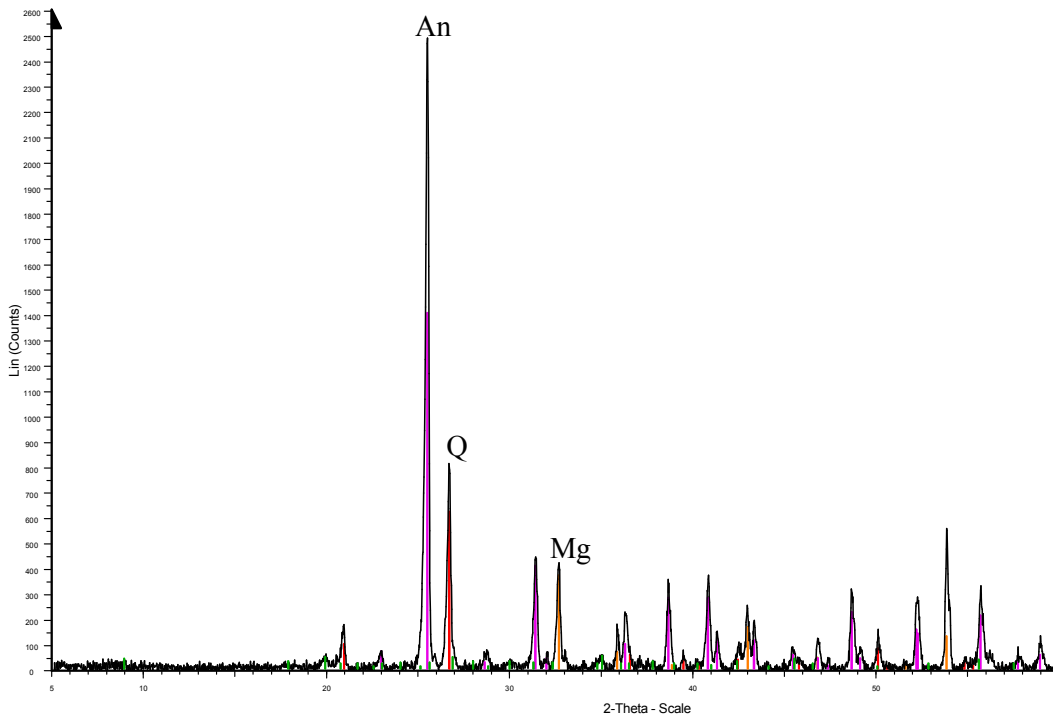


Figure 5.16. An XRD plot of LF5, the main minerals identified are Anhydrite (An; purple peaks), quartz (Q; red peaks) and magnesite (Mg; orange peaks). Pyrite and clay minerals were not detected from the XRD analysis as their concentrations are below detection limit, however, it was identified from the petrographical analyses. This plot is obtained from sample ALNR-2(2). The petrographical results of this sample are shown in Fig. 5.15.

LF6: Halite-dominated mudstones

Halite-dominated mudstones are colourless to white in core and alternate with relatively darker units, on a scale of 3-4 cm (Fig. 5.3). One sample was collected for geochemical analysis. Mineralogy of LF6 is described from the XRD analysis, which indicates that this lithofacies is predominately composed of halite (average 94 wt. %) and minor amounts (< 6 wt. %) of anhydrite, pyrite and fluorite (Fig. 5.17).

This lithofacies overlies LF5 in well ALNR-2 core. Its thickness is difficult to estimate since the core only recovered the first few centimetres of this unit (Fig. 5.2), but seismic and wireline logs suggest that it can reach to up to 1,000 m (Mattes and Morris 1990; Schröder et al. 2003). This lithofacies and LF5 are characterised by GR values ranging from 7 to 18 API, sonic values from 43 to 55 $\mu\text{s}/\text{m}$, density values from 2.8 to 3.0 g/cm^3 and 2 to 2.2 g/cm^3 for LF5 and LF6, respectively, and neutron values are about zero LPU (Fig. 5.1).

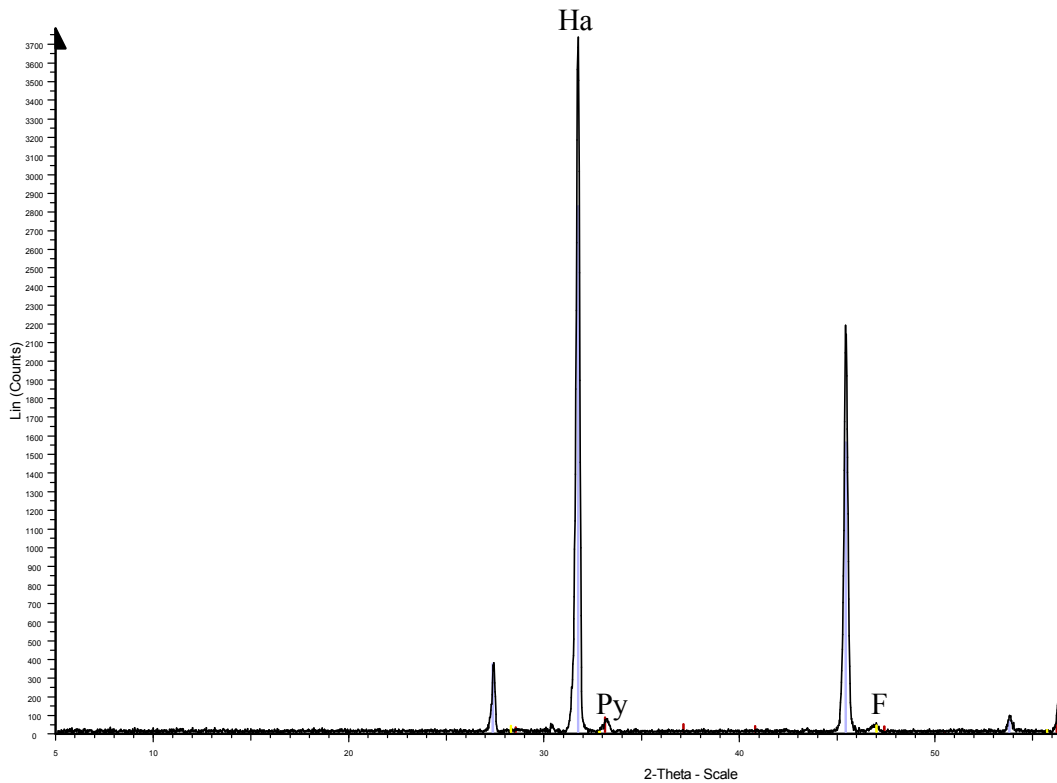


Figure 5.17. An XRD plot of LF6. The main minerals identified are halite (Ha; pale blue peaks), pyrite (Py; red peak), and fluorite (F; yellow peaks). This plot is obtained from sample ALNR-2(1).

Interpretation of the evaporite facies

The precipitation of LF5 (anhydrite) and LF6 (halite) marked a gradual increase in the basin water salinity, which is interpreted as a result of high evaporation and basin restriction (e.g. Kendall 1992; Schreiber and El Tabakh 2000). Anhydrites cementing the upper part of the Thuleilat Shale (LF4) mark the early stage of salinity rise. The euhedral textures of anhydrites are interpreted to be formed by replacement of gypsum precursors (e.g. Shearman 1985; Mattes and Morris 1990). The subsequent rise in salinity (> 35%; Mattes and Morris 1990) resulted in halite (LF6) precipitation on top of the anhydrite unit (e.g. Rosell et al. 1998). The dark and colourless units observed in core are probably composed of anhydrite-rich and halite-rich units, respectively. These alternations between the anhydrite- and the halite-rich units are interpreted to record salinity fluctuations, where the anhydrite units represent relatively lower salinity and the halite units represent a relatively higher salinity.

The dissolution of quartz grains in LF5 (Fig. 5.15 F) is interpreted to reflect high alkalinity, as a result of evaporation (e.g. Warren 2006). Such highly

alkaline environments will dissolve detrital quartz grains supplied to the basin and concentrate dissolved silica in the water body, e.g. Coorong Lagoon in Australia (Peterson and von der Borch 1965), Lake Magadi in Kenya (Eugster 1969; Warren 2006) and Albert Lake in the USA (Jones et al. 1967; Warren 2006).

5.2.4 *Post-depositionally modified lithofacies*

LF7: Slumped mudstones

In core, slumped mudstones show soft sediment deformation (Fig. 5.3). In total seven samples were collected from this facies. Higher resolution petrographical analyses reveal that small scale intraformational folding and fault are present, which disrupt the original laminated fabric (Fig. 5.18). The slumped mudstones have a similar composition to the silica-rich facies (LF1-LF3), and are mainly composed of microcrystalline quartz, clay minerals, detrital quartz grains and pyrite (Table 5.1). LF7 is identified only from the cores of well ALNR-2 and ALNR-3. It is present equally in the Upper and the Lower Athel Silicilyte (Fig. 5.2 and 5.3), with a thickness ranging from 20 to 40 cm. LF7 has similar wireline log characteristics to LF1 to LF3 and hence it could not be interpreted from the uncored intervals/wells. Core porosity values of this lithofacies are similar to silica-rich facies depending on microcrystalline quartz contents.

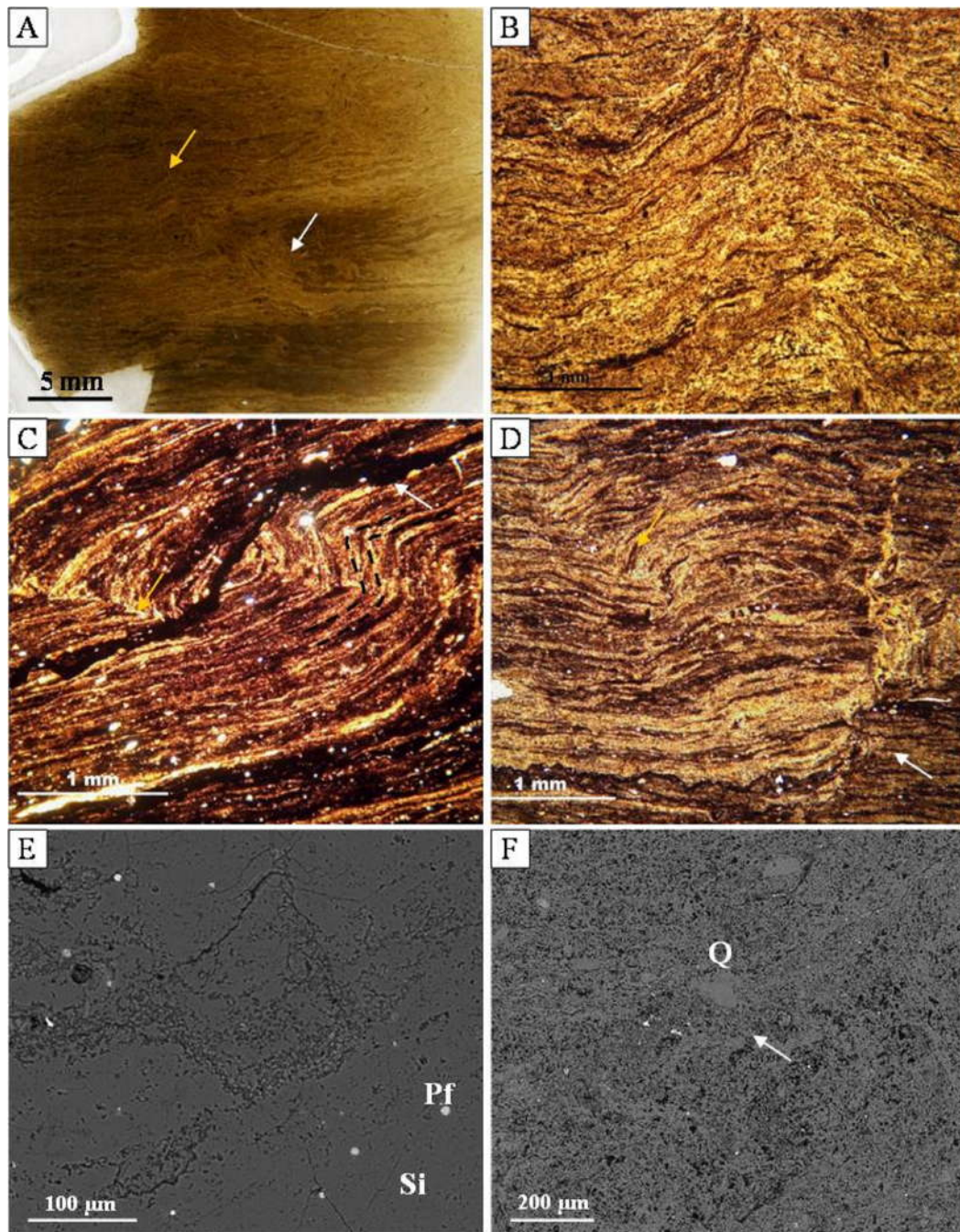


Figure 5.18. Photomicrographs illustrating the features of LF7. (A), (B) and (E) are from sample ALNR-2(35), (C) from sample ALNR-2(12) and (D) and (E) from sample ALNR-2(13). (A) A scanned-thin section shows primary laminae disrupted by soft sediment deformation (white arrow) underlying undeformed wavy laminae (bottom of the image). Here the pale laminae are silica-rich in contrast to the darker laminae that are relatively more organic carbon- and clay-rich. Yellow arrow shows concave structure. (B) PPL image of (A) that shows a close-up view of the convolute lamination; laminae are pushed upward. (C) PPL image shows small scale intraformational folding (annotated) and faulting (yellow arrow). Silt-sized grains with high relief are quartz. Fracture (white arrow) is rich with bitumen and clay minerals. (D) PPL image shows another slumped sample. White arrow indicates a fault plane, note that the laminae to the bottom right are undisrupted, and the yellow arrow show small scale folding. (E) BSEI of (A) and (B) show microcrystalline quartz (Si) and pyrite framboids (Pf). Lamination is not clear. (E) BSEI of (D) that show microcrystalline quartz, quartz grains (Q) and organic carbon (arrowed).

Interpretation of slumped lithofacies

The presence of small scale intraformational folds, soft-sediment deformation and the absence of brittle deformation, all suggest that deformation occurred shortly after initial lithification had been initiated, but prior to full lithification (e.g. Mills 1983). These features of soft-sediment deformation in LF7 were likely produced by downslope movement of the sediments under the influence of either gravity alone (e.g. Mills 1983; Fries and Parize 2003; Neuwerth et al. 2006) or by the combined effects of gravity and storms (e.g. Martel and Gibling 1993). While the latter is possible, the absence of rip up clasts, flat pebble conglomerates, or shallow water structures (ripple laminae or domal microbial structure) in the Athel Silicilyte makes it unlikely that there was a storm influence. The rarity of slumped facies in ALNR-2 core (< 0.5 % of the total Athel Silicilyte thickness) could suggest the slope angle was very gentle and did not produce a very thick slumped facies.

LF8: Brecciated mudstones

Brecciated mudstones in core comprise broken angular clasts of the laminated microcrystalline quartz lithofacies (LF1-LF3; Fig. 5.19). Four samples were collected from this lithofacies for higher resolution analyses. Petrographical analyses show that brecciation has disrupted much of the original bedding fabric (Fig. 5.3). Each broken clast is up to 2 mm across and has an angular shape (Fig. 5.19). Small scale folding and faulting are present in some samples of LF8 similar to LF7 (Fig. 5.19 C). The fault planes and fractures associated with LF8 are typically cemented by magnesite, hydroxyfluorapatite, and/or evaporite minerals (Fig. 5.19 E & F). This lithofacies is identified only from the cores of well ALNR-2 and it is present equally in the Lower and the Upper Athel Silicilyte. This lithofacies has thickness varies from 0.20 to 0.4 m and has core porosity values similar to silica-rich facies (LF1-LF3) depending on microcrystalline quartz contents.

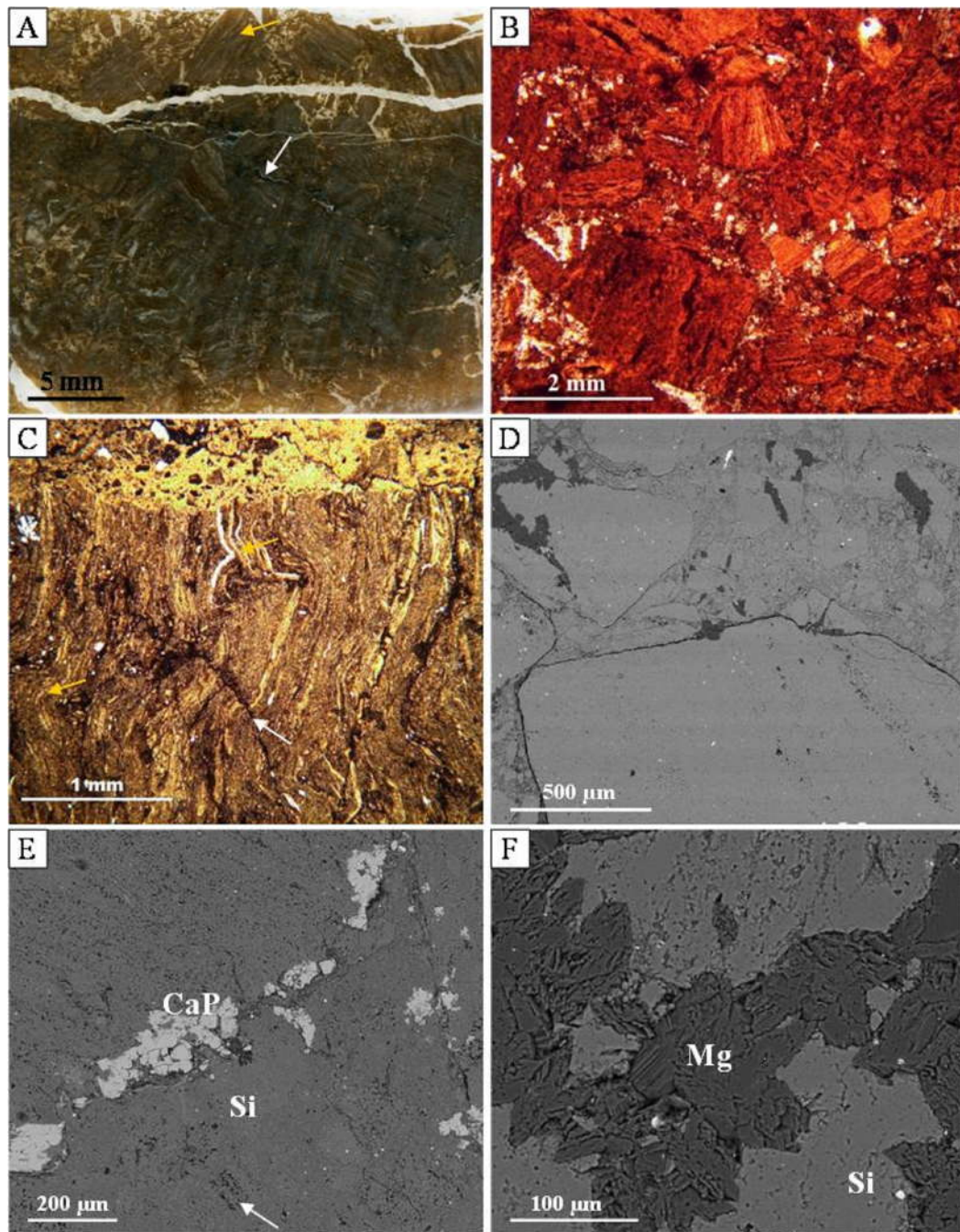


Figure 5.19. Photomicrographs illustrating features in LF8. (A), (B), (D) and (F) are from sample ALNR-2(37) and (C) and (E) from sample ALNR-2(26). (A) A scanned-thin section shows *in situ* breccia that consists of broken angular clasts (yellow arrow). The upper part of photograph shows fracture, which is post-dated brecciation and cemented by halite. It also shows stylolite (postdate brecciation) and cemented by magnesite (white arrow). (B) PPL image of (A) shows laminated angular clasts (up to 2 mm across) and they are made of microcrystalline quartz. Magnesite (high relief) presents between the broken clasts cementing fractures induced during brecciation. (C) PPL image of another sample showing breccia and very small scale faulting (white arrow) and foldings (yellow arrows). Each clast consists of laminated microcrystalline quartz. Small scale fold and faulting in this sample indicates brecciation predates full lithification. (D) BSEI of (A) and (B) show microcrystalline quartz within the broken clasts and magnesite cement (low η). Pyrites (very high η) are present, which are scattered within clasts and matrix. (E) BSEI of (C) shows microcrystalline quartz (Si), hydroxyfluorapatite (CaP) and small scale folding. Hydroxyfluorapatite in this sample is cementing the fracture between broken clasts and shows euhedral texture. (F) BSEI shows a close-up view of magnesite (Mg) and

microcrystalline quartz (Si) in (D). Magnesite shows euhedral texture and it is present within the fractures between laminated microcrystalline quartz clasts.

Interpretation brecciated lithofacies

The presence of angular broken clasts of the same composition as surrounding rocks (LF-LF3) suggests *in situ* brecciation of the lithified rocks. Small scale folding and faulting in some samples (Fig. 5.19 C) might suggest brecciation before full rock lithification (soft breccia). The brecciation of lithified rocks can be triggered by dissolution of intraformational evaporite (Matton et al. 2002), reworking by storms and waves (Bouchette et al. 2001), or by tectonism, e.g. earthquakes and instability of the basin floor (Rodriguez-Pascua et al. 2000). Given the absence of shallow water structures and primary interbedded evaporites and the abundance of faults (identified from core and seismic data; Amthor et al. 2005) in the Athel Silicilyte, brecciation is interpreted to be a direct *in situ* fault breccias that were tectonically triggered. Tectonism throughout the period of Ara Group sedimentation, related to the subduction of Proto-Tethyan oceanic crust along the formerly passive continental margin around the periphery of eastern Gondwana (section 3.3; Loosveld et al. 1996; Immerz et al. 2000; Allen 2007), would have led to localised faulting and fracturing. Fluid movement along fractures and fault planes probably led to cementation by magnesites, hydroxyfluorapatites and evaporites (Fig. 5.19 E & F).

LF9: Microcrystalline quartz-, carbonate- and detritus- bearing mudstones

This lithofacies in core is light grey and homogeneous. Laminations are poorly developed and it is not fissile (Fig. 5.3). In total, 11 samples (9 from the Athel Silicilyte and 2 from the U Shale) were collected for higher resolution analyses. This lithofacies under optical and electronic microscope is either largely homogeneous with clusters of dolomite crystals being present within a microcrystalline quartz framework or it exhibits wavy discontinuous lamination. Laminae geometry and thickness are similar to LF1-LF3 (wavy discontinuous laminations, 20 to 50 μm thick; Fig. 5.20). Individual laminae comprise thin alternating silica-rich and more magnesite/dolomite-rich layers and are crosscut

by stylolites (Fig. 5.20 B). A combination of the petrographic, XRD (Fig. 5.21) and TOC results reveal that LF9 is composed of microcrystalline quartz (average 31 wt. %), dolomite (average 36 wt. %), magnesite (average 5 wt. %), clay minerals (average 12 wt. %), pyrite (both framboidal and euhedral; average 8 wt. %), detrital quartz grains (average 2 wt. %), organic carbon (average TOC = 2.5 wt. %) and traces (< 2 wt. %) of evaporite minerals (halite and anhydrite) found within fractures/stylolites. The XRF results show that $\text{SiO}_2/\text{Al}_2\text{O}_3$ average ratio for LF1 is 10 (Appendix III).

The microcrystalline quartz crystals have a similar size and shape (1-5 μm , euhedral-subhedral) to those in LF1-LF3. In contrast, the dolomite and magnesite crystals are typically 10-50 μm in diameter and form euhedral-subhedral crystals (Fig. 5.20). These euhedral dolomite/magnesite crystals appear to be precipitated in the pore spaces and then continued growing on the original microcrystalline quartz fabric, post-dating microcrystalline quartz precipitation (Fig. 5.20 C-F). This lithofacies has a higher proportion of framboidal and euhedral pyrite compared with the silica-rich facies (Fig. 5.20 C & D). In addition, pyrites and dolomites concentrate locally within individual samples (Fig. 5.20 C & D). Dolomite crystals appear to be intergrown with pyrite framboids (Fig. 5.20E), whereas magnesite crystals were intergrown with framboidal and sometime with euhedral pyrites (Fig 5.20 D & F). This lithofacies has an average core porosity of 4.9 %, lower than the average of the silica-rich facies.

This lithofacies is present in the Athel Silicilyte and the U Shale as thin layers; typical thickness range from 0.15 to 0.50 m (Fig. 5.3). It is relatively more common in the upper part of Athel Silicilyte succession and in the bounding silt-rich units (Fig. 5.2 and 5.3). In wireline logs, LF9 is characterised by GR values ranging from 35 to 75 API, sonic values from 51 to 71 $\mu\text{m/s}$, density values from 2.47 to 2.83 g/cm^3 , neutron values from 0.11 to 0.24 LPUs and calculated porosity values are typically 0-10 % (Fig. 5.3).

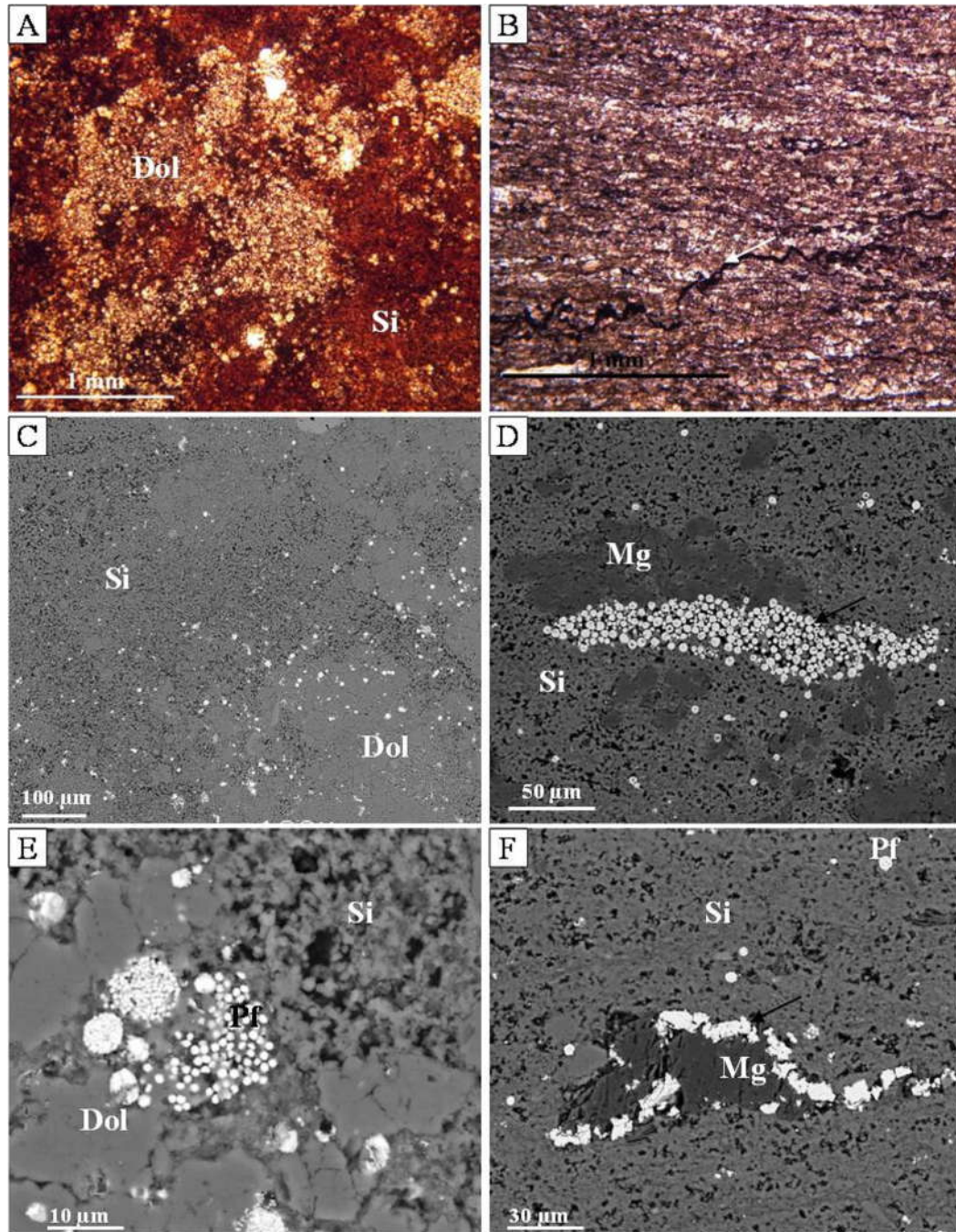


Figure 5.20. Photomicrographs of LF9. (A), (C), (E) are from sample ALNR-2 (10), (B) from sample ALNR-2(40), (D) from sample ALNR-2 (45) and (F) from sample ASH-4(1). (A) PPL image shows clustered dolomite grains (Dol) within microcrystalline quartz framework (Si). (B) PPL image shows laminated LF9, laminae comprise thin alternating strata of silica-rich layers and dolomite-rich layers. The dolomite-rich layers have a higher relief than the silica-rich layers. Stylolite (arrowed) crosscuts the dolomite-rich layers. (C) BSEI of (A) shows dolomite cements (Dol) and microcrystalline quartz framework (Si). Note framboidal pyrite (high η) is abundant where dolomite cement is present (lower part of the image), and it is rare in the microcrystalline quartz framework (upper part of the image). (D) BSEI shows magnesite (Mg) and microcrystalline quartz (Si). Note, magnesite is associated with pyrite framboids (arrowed) and it appears to precipitate over quartz framework. (E) A close up view of (C) shows pyrite framboids (Pf), and dolomite (Dol) is surrounding pyrite. Note, dolomite encloses microcrystalline quartz (Si). (F) BSEI shows magnesite grains (Mg) precipitated within microcrystalline quartz framework (Si) and euhedral pyrite (arrowed) is surrounding magnesite grain, whereas, pyrite framboids (Pf) is only present within microcrystalline quartz framework.

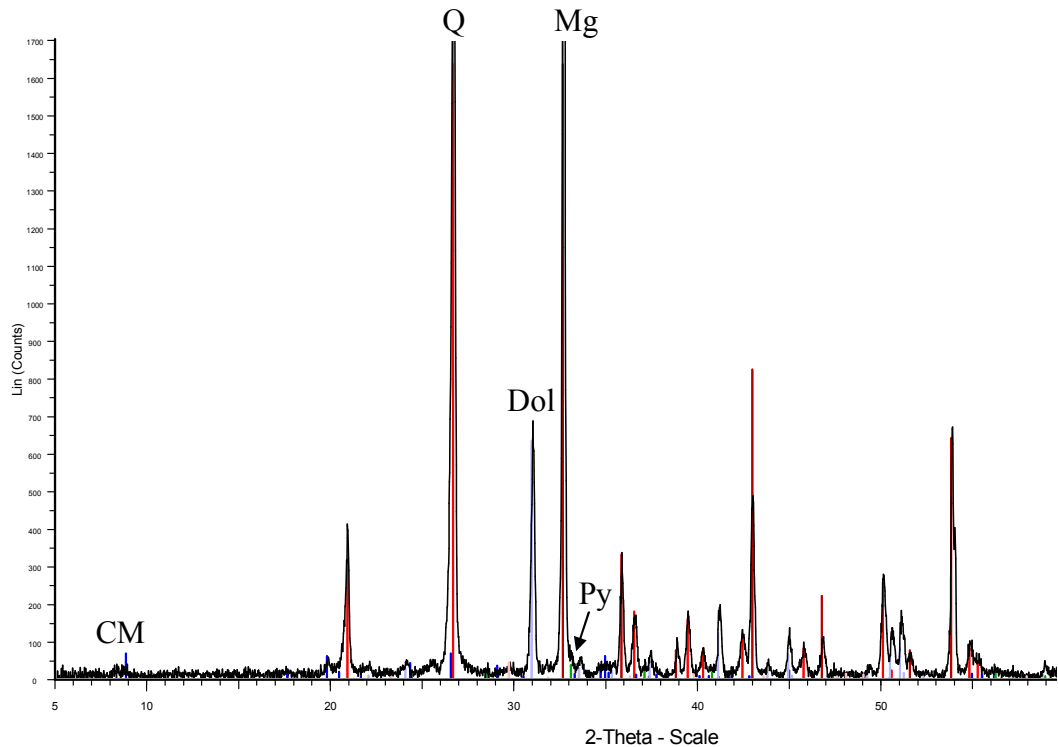


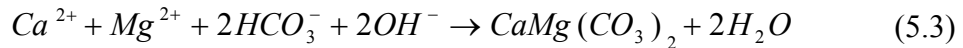
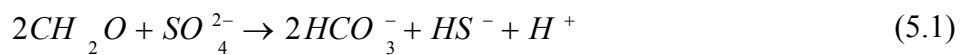
Figure 5.21. An XRD plot of LF9. The main minerals identified are quartz (Q; red peaks), dolomite (Dol; light blue peaks), magnesite (Mg; dark red peaks), clay minerals (smectite/illite [CM]; blue peaks) and pyrite (Py; green peaks). This plot was obtained from sample ALNR-2(21). Petrographical results of this lithofacies are shown in Fig. 5.20.

Interpretation of carbonate-cemented lithofacies

The presence of silt-sized euhedral-subhedral dolomite/magnesite crystals, that are crosscut by stylolites and were intergrown with early diagenetic framboidal pyrite, suggests that they precipitated during early-stage, shallow burial diagenesis before significant compaction. Magnesite associated with euhedral pyrite (which are formed during late stage diagenesis; e.g. Macquaker et al. 1997; Chapter 6), is interpreted to be formed during relatively late-diagenesis at deeper burial depth.

The higher proportion of pyrite in LF9, both euhedral and framboidal (average 8 % wt.), is interpreted to reflect organic matter diagenesis dominated by bacterial sulphate reduction (Berner 1970; Taylor and Macquaker 2000; Wilkin and Arthur 2001). The metabolic activities of sulphate reducing bacteria probably resulted in the removal of sulphate ions (SO_4^{2-} ; dolomite kinetic inhibitor, equation 5.1 below), and lead to an increase of the total alkalinity and pH of the porewaters (Baker and Kastner 1981; Compton 1988; Slaughter and Hill 1991; Wright 1999; Warthmann et al. 2000; Wright and Wacey 2005). Iron

reduction, associated with pyrite formation, will contribute to higher pH values since this reaction is a strong alkalinity pump (via OH⁻ production, equation 5.2 below; Lovley 1991; Macquaker et al. 1997). Dolomite and magnesite precipitation (equation 5.3 & 5.4, respectively) could have taken place deeper in the sulphate reduction zone where sulphate ion concentrations decrease and bicarbonate ion concentrations increase (Wright 1999; Wright and Wacey 2005). Of course, calcium and magnesium ions are available in seawater for dolomite and magnesite precipitation. This lithofacies is enriched with Mn (average 570 ppm) compared with the silica-rich facies (average 47.5 ppm, detailed results in Chapter 6; section 6.3.2), which is further support that carbonate precipitation took place in an oxygen-depleted environment (e.g. Hild and Brumsack 1998; Tribovillard et al. 2006).



The increase in the abundance of LF9 towards the upper Athel Silicilyte and in the bounding silt-rich units (Fig. 5.2) is interpreted as a result of higher detrital input, and hence availability of reducible iron. This also supports the role of iron in carbonate precipitation in the Athel Silicilyte.

5.3 Pyrite framboid size-distribution

Pyrite framboidal size-distributions could indicate redox conditions during sediment deposition, and therefore Athel Silicilyte pyrite size-distributions are described in order to investigate redox conditions during Athel Silicilyte precipitation. Pyrite morphology and size-distribution are outlined in this chapter, since this data collection is based on microscopic analysis. However, the significance of these data is discussed in Chapter 6 (section 6.5),

along with elemental concentrations. The results in this subsection are described based on lithofacies group, silica-rich facies (LF1-LF3) and silt-rich facies (LF4).

Three types of pyrite were identified during electronic petrographical analysis (BSEI) from the silica- and the silt-rich facies. The first type is the typical pyrite framboids (closely packed, spherical aggregates of uniform-sized microcrysts; Fig. 5.22 A & B). The second type of pyrite is similar to type one, but the microcrysts are scattered or less densely packed, which often show larger variability in diameter (Fig. 5.22 C). The third type is diagenetic pyrites, which occur as euhedral crystals and shows no microcrysts (Fig. 5.22 D). Among those types, type one is more abundant, whilst types two and three are less common, and the latter is mainly found in the silt-rich facies (LF4), as well as at the top and at the base of the Athel Silicilyte near the mudstone transition boundaries.

Petrographical results reveal that these framboids are present within uncompacted pore spaces of the silica-rich facies (Fig. 5.22). No secondary pyrite growth is seen in type one resulting in preservation of the primary textures of the framboids with no infilling or overgrowths of pyrite (Fig. 5.22). Pyrite contents, mostly framboidal, do not change significantly throughout the Athel Silicilyte (ranging from 2 to 8 wt. %; average 3 wt. %; Appendix III). In the silt-rich facies (LF4), pyrite contents can reach to up to 11 wt. %, with an average of 8 wt. % (Appendix III).

Statistics of pyrite framboid (type one) size distributions, i.e. number of framboids counted (n), average and maximum framboid diameter and standard deviation (SD), are shown stratigraphically in Fig. 5.23 with the GR log of well ALNR-2. These results were collected from the prepared thin sections using electronic microscopic techniques. Each sample was analysed over 5-10 closely spaced 15-25 mm vertical transects.

All samples, from the silica- and the silt-rich facies, have an average framboid diameter ranging from 3.4 to 4.0 μm . Maximum framboid diameter rarely exceeds 8.5 μm , only one sample (ALNR-2(44)) shows a diameter of 13.5 μm (Fig. 5.23). The average diameters of pyrite framboids do not significantly

vary between silica-rich facies (Fig. 5.23). These framboids are characterised by very narrow size distribution, SD ranges from 1.1 to 1.5 and less than 5 % of the measured framboids have diameter-size more than 7 μm .

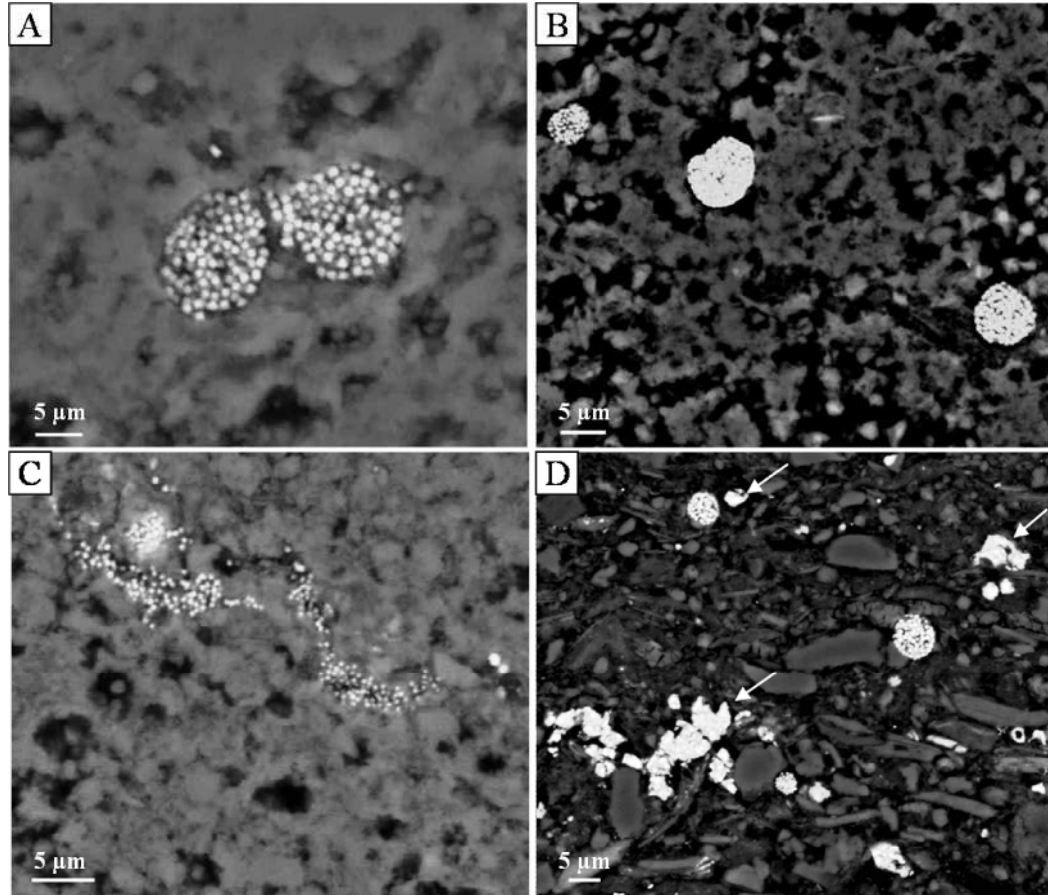
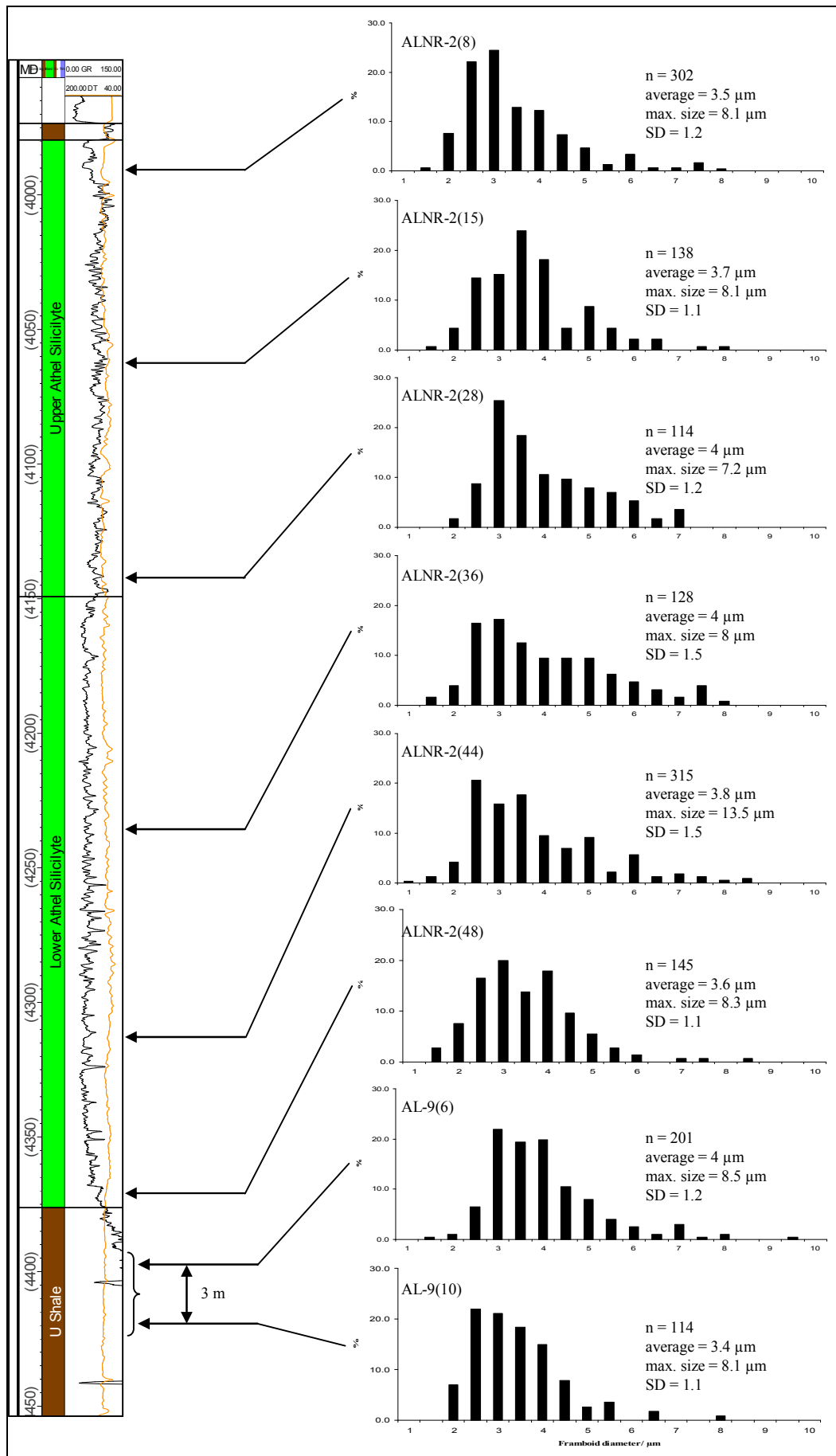


Figure 5.22. Back scattered electron images of identified pyrites from the silica-rich facies (A-C) and the silt-rich facies (D). (A) is from sample ALNR-2(12), (B) from sample ALNR-2(8), (C) is from sample ALNR-3 (6) and (D) from sample AL-9(6). (A) and (B) show pyrite framboids (type one), which are closely packed, spherical aggregates of uniform-sized microcrysts, that are present within uncompacted pore spaces. (C) Shows scattered pyrite microcrysts (type two) in the microcrystalline framework. (D) Shows pyrite framboids and euhedral pyrite (type three; arrowed) in the silt-rich facies.



Caption next page.

Figure 5.23. Shows pyrite framboid size distributions of the analysed samples from well ALNR-2. The silica-rich facies samples were selected from the Lower and Upper Athel Silicilyte from different depths in order to cover the full stratigraphic thickness. Two samples (three m apart) analysed from the silt-rich facies (the U Shale) from cores of well AL-9, but they are plotted in well ALNR-2 to compare pyrite framboid size distributions with the results from the Athel Silicilyte. Sample abbreviation, number of pyrite framboids (n), average diameter, framboid maximum size and standard deviation of each sample are shown on their size-distribution graph. All samples show more than 95 % of pyrite framboids are less than 7 μm with an average ranging from 3.4 to 4.0 μm .

5.4 Temporal and spatial variability of the Athel Silicilyte

The wireline log signatures of each lithofacies were previously described in section 5.2 and summarised in Table 5.1. The log signatures of each lithofacies can be differentiated, and hence the interpretation of uncored wells/intervals is facilitated. In total 12 wells were interpreted to establish the temporal and the spatial variability of the Athel Silicilyte from the Athel Basin (Fig. 5.1). These wells are distributed across the Athel Basin (Fig. 5.1); five wells from the basin margins (AMSE-1, MKZ-1, MMNW-7, MM-248 and TL-2), six wells from the basin centre (ALNR-2, ALNR-3, ALNR-4, ASH-2, ASH-3, and ASH-4) and one well from the Birba Platform (BB-4). The lithofacies variability in the basin centre and on the basin margin is summarised in Fig. 5.24, while each well variability, as well as Athel Silicilyte thickness and the proportions of each lithofacies in the Athel Silicilyte succession, are shown in Fig. 5.2.

The Athel Silicilyte is only present in the Athel Basin (Fig. 5.24) bounded below by the U Shale and above by the Thuleilat Shale, whereas time-equivalent carbonates are present on the platform. These units are all enclosed between two thick evaporite units (anhydrite [LF5] and halite [LF6] lithofacies) of the A4E and the A5E cycles (Fig. 5.24). The Athel Silicilyte is typically thicker in the basin centre than on the basin margins (e.g. 390 m thick in the basin centre [well ALNR-2] and 190 m thick on the basin margin [well MMNW-7]; Fig. 5.2). However, well ASH-3 in the basin centre encounters relatively thinner unit of the Athel Silicilyte (166 m thick; Fig. 5.2).

Expansion of the core interpretations to wireline log signatures supports the interpretation that laminated microcrystalline quartz-rich mudstones (LF1) are principally present in the Lower Athel Silicilyte (Fig. 5.2 & 5.24). They tend

to be volumetrically more significant in the basin centre than on the basin margins (e.g. their proportion is 47 % in the basin centre [well ALNR-2] and 18 % on the basin margin [well ALSE-1] of the total Athel Silicilyte thickness; Fig. 5.2). This is also reflected on the thinning of the Lower Athel Silicilyte towards the basin margins (Fig. 5.2). Laminated microcrystalline quartz-dominated mudstones (LF2) are also present in the Lower Athel Silicilyte only in the basin centre (their proportion ranges from 1.5 % to 6.0 % of the total Athel Silicilyte thickness; Fig. 5.2), and they are absent on the basin margins (Fig. 5.2 & 5.24). Laminated microcrystalline quartz-rich, detritus-bearing mudstones (LF3) are mainly present in the Upper Athel Silicilyte and at the base of the Lower Athel Silicilyte (just above the U Shale/Athel Silicilyte boundary; Fig. 5.24). LF3 passes vertically into laminated silt-rich, clay-mineral bearing mudstones (LF4) associated with a gradual increase in GR values (from around 85 to >150 API). However, LF3 is also interbedded with LF4 in a 1 to tens of metre scale in some wells, especially in wells located on the basin margins (e.g. ALSE-1, ALNR-3 and TL-2; Fig. 5.2 & 5.24). The proportion of LF3 in Athel Silicilyte succession increases towards the basin margin (e.g. 50 % in the basin centre [well ALNR-2] and 63 % on the basin margin [well TL-2] of the total Athel Silicilyte thickness; Fig. 5.2).

Across the entire Athel Basin area, the silica-rich facies (LF1-LF3) in the Athel Silicilyte are bounded between the silt-rich facies (LF4), which are present in the Thuleilat Shale and the U Shale. The Thuleilat Shale thickness across the basin varies from 175 m (e.g. well ALSE-1 on the basin margin; Fig. 5.2) to 3 m (e.g. well ANLR-2 and ASH-3 in the basin centre; Fig. 5.2) and it shows a decrease in thickness towards the basin centre. However, two wells (ALNR-4 and ALNR-3; Fig. 5.2) in the basin centre encountered a thick (85-175 m) unit of the Thuleilat Shale. The U Shale thickness variation across the basin is hard to constrain since wireline logs do not always cover the full stratigraphic thickness. Where there is a complete stratigraphic coverage, the U Shale has a thickness varying from 75-150m (e.g. TL-2 and ALSE-1; Fig. 5.2).

Slumped (LF7) and brecciated (LF8) mudstones are only identified from cores, both of which were sampled from the basin centre (well ALNR-2 and

ALNR-3). Their lateral variability could not be interpreted based on wireline logs, since their log signatures depend on their composition, which varies between LF1-LF3. Microcrystalline quartz-, carbonate- and detritus- bearing mudstones (LF9) become relatively more common towards the Upper Athel Silicilyte and within the enclosing silt-rich facies, whilst they show no lateral variability from the basin centre to the basin margins (0.5 % to 1.5 % of the total Athel Silicilyte thickness across the basin; Fig. 5.2).

Interpretation of Athel Silicilyte variability

Laminated microcrystalline quartz-rich mudstones (LF1) and laminated microcrystalline quartz-dominated mudstones (LF2) have high microcrystalline quartz contents (average LF1 = 83 and LF2 = 91 wt. %), lower detrital contents (LF1 = 7 and LF2 = 4 wt. %) and high $\text{SiO}_2/\text{Al}_2\text{O}_3$ ratios (LF1 = 42 and LF2 = 79), and they are concentrated in the Lower Athel Silicilyte (section 5.2.1). Whereas, laminated microcrystalline quartz-rich, detritus-bearing mudstones (LF3) have relatively lower microcrystalline quartz contents (72 wt. %), high detrital contents (17 wt. %) and low $\text{SiO}_2/\text{Al}_2\text{O}_3$ ratios (22), and they are concentrated in the Upper Athel Silicilyte. A similar trend showing a decrease in microcrystalline quartz content and an increase in detrital content is observed towards the basin margins. In addition, laminated silt-rich, clay-mineral bearing mudstones (LF4) are interbedded with LF3 towards the upper Athel Silicilyte on the basin margins. These observations show that there is an increase in detrital contents and a decrease in microcrystalline quartz contents towards the Upper Athel Silicilyte and towards the basin margins. This vertical and lateral variability of Athel Silicilyte lithofacies therefore suggests that silica precipitation dominated where there was less input of detrital material.

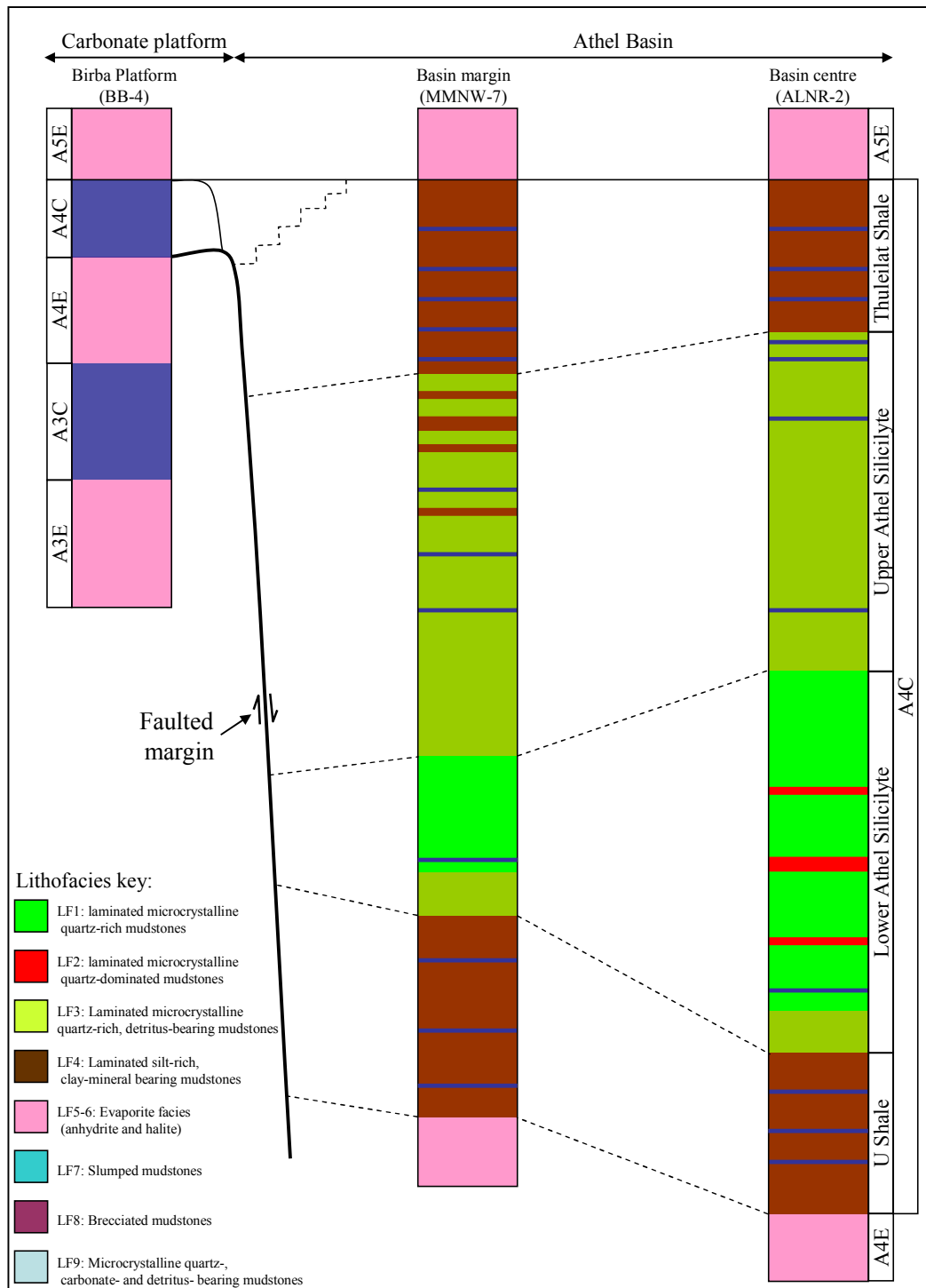


Figure 5.24. Summary logs, constructed from well-correlation in Fig. 5.2, showing lithofacies vertical and lateral variability in the Athel Basin (margin and centre). The Athel Silicilyte is only present in the Athel Basin enclosed by the U Shale and the Thuleilat Shale, whereas time-equivalent carbonates (A4C) are present in the platform (i.e. Birba Platform), which are all enclosed by two thick evaporite units of the A4 and the A5 cycle. Laminated microcrystalline quartz-rich mudstones (LF1) are mainly concentrated in the Lower Athel Silicilyte and they become volumetrically less significant on the basin margins. Laminated microcrystalline quartz-dominated mudstones (LF2) are present in the Lower Athel Silicilyte in the basin centre, while they are absent on the basin margins. Laminated microcrystalline quartz-rich, detritus-bearing mudstones (LF3) are mainly concentrated in the Upper Athel Silicilyte, as well as at the base of the Lower Athel Silicilyte, and they become volumetrically more significant towards the basin margins. At the basin margins, the upper most of the Athel Silicilyte is interbedded with the silt-rich facies (LF4).

In addition, well correlation (Fig. 5.24) shows that the Athel Silicilyte is generally thickening towards the basin centre, whilst the Thuleilat Shale is thinning in the same direction. However, within the basin centre they also show a quite significant variability. For example, well ASH-3 (Fig. 5.2) encounters relatively thinner units of the Athel Silicilyte (166 m thick) and the Thuleilat Shale (3 m thick) relative to the other wells in the basin centre (Fig. 5.2). Their thickness variation in the basin centre is quite ambiguous and likely related to the basin topography during deposition. The Athel Basin is thought to contain palaeogeographic lows and highs, which were developed due to strong differential fault-related subsidence during Ara tectonism, resulting in a series of fault-bounded mini-basins and non-depositional high areas (Fig. 5.25; see also Fig. 3.5 and subsection 3.5.2; Mattes and Morris 1990; Loosveld et al. 1996; Amthor et al. 2005). Certainly, well ALKZ-1 and ALFR-1 were drilled within the Athel Basin centre (Fig. 5.25), which both neither encounter the Athel Silicilyte nor the bounding mudstones. This is interpreted to reflect a presence of topographic highs that represent areas of non-deposition during the A4C cycle (Mattes and Morris 1990; Lake and Richard 1998; Amthor et al. 2005). The significant variation in the basin floor topography therefore might explain the variation in thicknesses of the Athel Silicilyte and the Thuleilat Shale in well ASH-3. This well could have been drilled in a topographically higher area where relatively less accommodation was available during deposition. The significant relief on the basin floor is also evident by the presence of soft-sediment deformation features in slumped lithofacies (LF7; Fig. 5.18) that was possibly produced by sediment downslope movements.

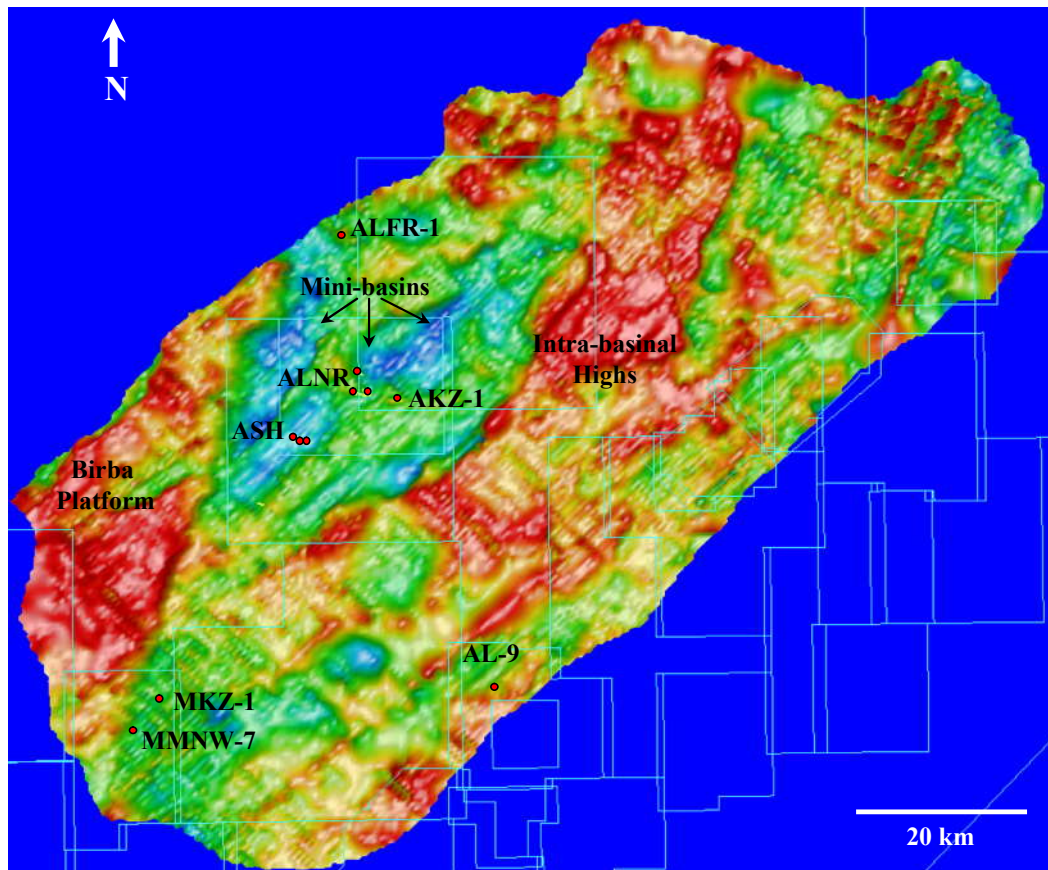


Figure 5.25. Paleotopographical map of the Athel Basin based on regional 3D-seismic data. This map shows paleotopographical high areas in red (Birba Platform and intra-basinal high). The deep basin (mini-basins) is in blue and dark green. The Athel Silicilyte precipitated only in the deepest parts of the basin. AKZ-1 and ALFR-1 encounter no Athel Silicilyte or U/Thuleilat Shale due to the presence of topographical high areas (yellow colour) within the Athel Basin (Fig. 5.1). Modified after Amthor et al. (2005).

Notwithstanding the thickness variability of the Athel Silicilyte and the Thuleilat Shale, the microcrystalline quartz content overall decreases towards the Upper Athel Silicilyte (ranging from 3 to 30 wt. %; Appendix III) and towards the basin margins, whilst detrital contents increase. This relation could suggest that higher detrital input reduced the silica precipitation rate in the microbial layers. Based on this, the source and the controls on distribution of detrital material in the Athel Basin must be considered. This is discussed in the following paragraph, whilst the role of detrital input on reducing silica precipitation will be considered in Chapter 7 (section 7.3.3).

The source of the detrital material could be fluvial or windblown. However, the climate aridity during Ara sedimentation (Mattes and Morris 1990; Schröder et al. 2003) and the absence of any evidence for fluvial channels on adjacent rocks (Nicholas 2006; Gold 2010), together suggest that fluvial detrital

input is unlikely. Based on the fine-silt sized detrital grains (section 5.2.2) and the climate aridity, the detrital material was most likely windblown. The spatial distribution of detrital accumulation was likely controlled by relative sea-level. A4 represents a transgressive-regressive cycle (section 3.5). The evaporite unit (A4E) accumulated during periods of relative sea-level low and basin restriction on top of the carbonate platforms and in the Athel Basin (Fig. 5.24; Mattes and Morris 1990; Schröder et al. 2003). Whereas, the Athel Silicilyte precipitated only in deep waters (mini-basins; Fig. 5.25) within the Athel Basin during relative sea-level rise (section 3.5; Amthor et al. 2005; Schröder et al. 2005). Therefore, detrital input in the mini-basins was likely restricted during maximum relative sea-level rise as palaeo-shoreline step onshore. This is consistent with the increase in detrital contents towards the basin margins, i.e. more proximal waters. The increase in detrital contents towards the upper Athel Silicilyte could suggest shallowing upward, consistent with the accumulation of silt-rich unit of the Thuleilat Shale and low-stand evaporites on top of the Athel Silicilyte. The Upper/Lower Athel Silicilyte boundary, marking the relative increase in detrital contents, therefore probably indicates the maximum water depth during Athel Silicilyte precipitation.

5.5 Summary

The summary of this chapter is:

- The Athel Silicilyte and bounding mudstones (U and Thuleilat Shale) are only present in the deep Athel Basin, whereas time-equivalent carbonates are present in the proximal setting (the Birba Platform).
- Six lithofacies were identified in the Athel Silicilyte that reflect variability in detrital material contents (silica-rich facies), sediment remobilisation (slumped and brecciated lithofacies) and diagenetic modification (carbonate-bearing lithofacies). The silica-rich facies being the most abundant (representing more than 97 % of the total Athel Silicilyte thickness).
- The silica-rich facies are predominately composed of microcrystalline quartz, and show wavy discontinuous lamination of microbial origin, suggesting that silica precipitation took place in microbial layers. These microbial layers were likely produced by coagulation of photosynthesising

single-celled plankton during sinking or formed by microbial mat bloom at the seawater-brine interface.

- The homogeneity of silica-rich facies (apart from variation in detrital contents), the loose packing of detrital grains and the preservation of thick laminated fabric (166-390 m thick) suggest that the Athel Silicilyte precipitated syndepositionally in microbial layers during low detrital input.
- The increase in detrital contents towards the upper Athel Silicilyte and towards the basin margins (from 3 to up to 30 wt. %; Appendix III) suggest relatively higher detrital input in the Upper Athel Silicilyte and on the basin margins. Detrital input was likely controlled by the relative sea-level, an increase in detrital contents suggests a drop in relative sea-level or that precipitation took place in more proximal settings.
- The bounding mudstones were deposited during an increase in detrital input to the Athel Basin, which probably inhibited silica precipitation in the microbial layers.
- Significant thickness variations of the Athel Silicilyte and bounding mudstones in the Athel Basin centre are probably due to the presence of intrabasinal high and low areas that controlled accommodation availability during deposition.
- Brecciation and soft sediment deformation most likely indicate that the basin was tectonically active resulting in significant relief within the basin floor.
- Carbonates cementing the Athel Silicilyte and the bounding mudstones are interpreted as early diagenetic products, precipitated deep in the sulphate reduction zone due to the availability of reducible iron.

Chapter 6.

Inorganic geochemistry

6.1 Introduction

This chapter investigates: 1) where the sediment that forms the Athel Silicilyte (silica-rich facies; LF1-LF3) and the U Shale (silt-rich facies; LF4) were derived, and 2) the redox conditions that were likely to have existed during the deposition of these units. The materials that formed these sediments may have been derived from the following sources: 1) detrital input to the basin, 2) primary production within the basin (organic carbon), and 3) as chemical precipitates in response to either hydrothermal activity in the basin or diagenesis occurring in the water column or in the porewaters. The principle problem addressed here is the source of the silica present in the Athel Silicilyte. The sediments forming the U Shale are most likely to consist of terrigenous (detrital) material.

Here, major, trace and Rare Earth Element (REE) concentrations are used to investigate the geochemical signatures of hydrothermal and seawater precipitates. In addition, they are used to assess redox conditions during Athel Silicilyte and U Shale accumulation. These elemental concentrations are also reviewed in the context of the mineralogical variability described previously in Chapter 5. To achieve the above aims, a background is first outlined describing how elemental concentrations can inform this discussion and secondly the data from the Athel Silicilyte and the U Shale are presented. Finally, the implications of these data for the origin of these sediments are discussed.

6.2 Background

6.2.1 Detrital monitor

Elements, such as aluminium (Al), titanium (Ti), potassium (K) and zirconium (Zr), are normally concentrated in detrital aluminosilicate phases (e.g. Taylor and McLennan 1985; Condie and Wronkiewicz 1990; Murray 1994). These elements are usually immobile during diagenesis and therefore their concentrations should reflect the intensity of the detrital input (Taylor and McLennan 1985; Hild and Brumsack 1998; Tribovillard et al. 2006).

6.2.2 *Hydrothermal signature*

Sediments that accumulate in hydrothermal environments are commonly enriched in elements such as Fe and Mn (e.g. Bonatti 1983; Adachi et al. 1986; Murray 1994; Sugitani et al. 2002). These element enrichments or depletions are monitored relative to another detrital concentration proxy such as $\text{Al}_2\text{O}_3/(\text{Al}_2\text{O}_3 + \text{Fe}_2\text{O}_3 + \text{MnO})$ or $\text{Fe}_2\text{O}_3/\text{TiO}_2$. Typically sediments that are deposited in hydrothermal environments are characterised by $\text{Al}_2\text{O}_3/(\text{Al}_2\text{O}_3 + \text{Fe}_2\text{O}_3 + \text{MnO})$ ratios less than 0.35 and $\text{Fe}_2\text{O}_3/\text{TiO}_2$ ratios higher than 20 (Bonatti 1983; Adachi et al. 1986; Chavagnac et al. 2005).

In addition, hydrothermal sediments typically have distinctive REE signatures in shale-normalised patterns (here discussed relative to Post-Archean Australian Shale [PAAS]; Taylor and McLennan 1985), including light REE (LREE; La to Sm) enrichments and pronounced positive Eu anomalies (McLennan 1989; German et al. 1990; Klinkhammer et al. 1994; Bau and Dulski 1999). LREE enrichments are interpreted as the entry of REE into hydrothermal fluids during plagioclase leaching, which strongly fractionates the heavy REE (HREE; Gd to Lu) relative to the rest of REE (Klinkhammer et al. 1994). The positive Eu anomalies imply contributions of the reduced Eu^{2+} that is enriched in plagioclase (e.g. German et al. 1990; German et al. 1991a; Chavagnac et al. 2005; Slack et al. 2007). Eu is only reduced (Eu^{3+} to Eu^{2+}) under strongly reducing conditions, such as those found in the mantle or lower crust, which will result in an increase in the ionic radius (German et al. 1991a; Klinkhammer et al. 1994). Reduced Eu has a higher mobility and substitutes for elements with a similar ionic radius (e.g. Sr) in plagioclase. Consequently, dissolution of plagioclase will result in fluids characterised by pronounced positive Eu anomalies.

6.2.3 *Seawater signature*

Seawater precipitates show REE characteristics (in PAAS-normalised patterns) similar to modern seawater, including: 1) depleted LREE relative to HREE; 2) weak-moderate positive La and Eu anomalies; 3) strong negative Ce

anomalies; and 4) positive Y anomalies (e.g. German et al. 1995; Bolhar et al. 2004; Friend et al. 2008). The LREE-depletion in seawater precipitates is believed to be due to the progressive enrichment from LREE to HREE as a result of increasing affinity for solution complexation and decreasing affinity for surface complexation with the increase in atomic mass (e.g. Lee and Byrne 1992; Sholkovitz et al. 1994). The LREE are therefore scavenged preferentially by Fe- and Mn-oxyhydroxide particles from the water column relative to the HREE, leaving seawater depleted in LREE (German and Elderfield 1989; Sholkovitz et al. 1994). Positive La and Eu anomalies are also attributed to the higher affinity to solution complexation of these elements relative to their neighbouring elements, which in turn might be due to the configuration of inner 4f electrons (De Baar et al. 1991; Sholkovitz et al. 1994; Bau et al. 1995; Alibo and Nozaki 1999). The negative Ce anomalies result from oxidation of Ce^{3+} to the stable form of Ce^{4+} , which is removed by adsorption onto Fe- and Mn- oxy-hydroxides (German and Elderfield 1989; Sholkovitz et al. 1992; German et al. 1995). Whereas, Ce in anoxic conditions is characterised by weak negative to positive anomalies (e.g. German and Elderfield 1990). Positive Y anomalies in seawater are attributed to the fractionation during weathering of the continental material and/or due to the inefficient removal of Y from seawater relative to its neighbour (Ho) due to their different stabilities (Bau et al. 1995).

6.2.4 *Redox monitor*

Elements, such as U, V, Mo and Mn, have a transfer rate from seawater to sediments that is controlled by redox state during deposition (e.g. Morford and Emerson 1999; Algeo 2004). They are therefore commonly used to assess redox conditions during sedimentary rock accumulation (e.g. Klinkhammer and Palmer 1991; Jones and Manning 1994; Crusius et al. 1996; Rimmer 2004; Tribovillard et al. 2006). Assessing redox conditions typically means determining whether the conditions were either oxidising (oxic) or reducing (anoxic). Reducing conditions can be non-sulphidic or sulphidic (free H_2S within the water column); in the latter case, they are also called euxinic.

Uranium is present as dissolved uranyl ions (U^{6+}) in oxic seawater, which bind to carbonate ions forming $UO_2(CO_3)_3^{4-}$ (Langmuir 1978; Morford and Emerson 1999; Tribovillard et al. 2006). Dissolved U is neither reduced to the stable U^{4+} nor is it scavenged by particulates in oxic settings (Anderson et al. 1989; Algeo 2004). Whereas, under highly reducing conditions in presence of hydrogen sulphide, U^{6+} is reduced to the thermodynamically favoured U^{4+} leading to U enrichment in the sediments by adsorption onto organic carbon (Klinkhammer and Palmer 1991; Morford et al. 2001).

Vanadium is present as V^{5+} in the form of vanadate $H_2VO_4^-$ in oxic waters, which is adsorbed to both manganese and iron oxyhydroxides (Wehrli and Stumm 1989; Tribovillard et al. 2006) and possibly kaolinite (Breit and Wanty 1991). In anoxic waters, vanadate however is reduced to vanadyl (VO^{2+}) ions, which might then be removed from the water column to the sediments by surface adsorption processes or by the formation of organometallic ligands (Emerson and Huested 1991; Morford and Emerson 1999). In euxinic basins, free H_2S can cause V to be further reduced to V^{3+} and then precipitate as a solid oxide (V_2O_3) or a hydroxide $V(OH)_3$ resulting in further V enrichment (Breit and Wanty 1991; Wanty and Goldhaber 1992).

Molybdenum is present as Mo^{6+} in oxic water in the form of molybdate (MoO_4^{2-}), which is easily captured by Mn-oxides/hydroxides ($MnO_2/MnOOH$; Crusius et al. 1996; Morford and Emerson 1999). Subsequent reduction of Mn-oxides/hydroxides at the redox boundaries release adsorbed Mo to porewaters or water column (depending on redox boundary position; Crusius et al. 1996). Mo scavenging from waters to the sediment occurs in the presence of HS^- where sulphur replaces oxygen on molybdate (MoO_xS_{4-x} , $X=0-3$), resulting in a complex that makes the Mo compound more likely to adsorb onto organic matter and authigenic Fe-sulphides (e.g. pyrite; Helz et al. 1996; Erickson and Helz 2000; Zheng et al. 2000; Algeo and Lyons 2006).

Manganese is delivered to seawater as oxide coatings on the detrital phases and by hydrothermal fluxes (Calvert and Pedersen 1993; Russell and Morford 2001; Tribovillard et al. 2006). Reduction of the Mn-oxyhydroxides in

reducing conditions liberates soluble Mn^{2+} into waters, which diffuses away from anoxic waters leading to Mn-depletion in the sediments, if not trapped by carbonate minerals (Jenkyns et al. 1991; Calvert and Pedersen 1996; Hild and Brumsack 1998; Morford et al. 2001). Dissolved Mn^{2+} in oxygenated waters is oxidised to insoluble Mn^{3+} and Mn^{4+} (e.g. Calvert and Pedersen 1996; Morford and Emerson 1999; Tribovillard et al. 2006).

These elements are reduced according to their redox potential value, which quantifies the affinity of an element to acquire an electron and thus to be reduced. Elements with higher redox potential are reduced first compared with elements that have lower redox potential value. For example, Fe^{3+} reduction to Fe^{2+} has a redox potential value of + 0.77 volts and reduction of Mn^{4+} to Mn^{2+} has a redox potential value of +1.23 volts (Krauskopf 1982). Therefore, Mn^{4+} is reduced before Fe^{3+} , and vice versa for oxidation.

Mobility of the redox-sensitive elements varies for each element during reoxygenation events. For example, U can be lost from sediments if oxygen penetrates to a depth where authigenic U has accumulated, which can erase the primary U signal by migration of U from sediments to the overlying water column (Anderson et al. 1989; Morford et al. 2001; McManus et al. 2005). Oxygen penetrating sediments has a lesser effect on the other redox-elements (e.g. V and Mo) and if they are remobilised, they would be transported only for a short distance (< 5 cm; Thomson et al. 1998; Morford et al. 2001; Tribovillard et al. 2006). For precise redox-condition construction, therefore, multi-element distribution (U, V, Mo and Mn) should be used.

6.3 Results

6.3.1 Data presentation and normalisation

All samples were analysed for major and trace element concentrations (117 samples) and only selected samples (21 samples) were analysed for REE concentrations. Major and trace element concentrations were measured using XRF analysis. From each sample 12 g of powder was obtained and mixed with

3g wax. The mixture was pressed under high pressure in a pellet, which was analysed in an Axios Sequential XRF Spectrometer operating under various voltages and currents depending on elements to be identified. The average error of this technique is 1.8 % for major oxides and 4.5 % for trace elements (section 2.4.2; Tables 2.2 & 2.3). The REE concentrations were measured using LA-ICP-MS. The samples were prepared by obtaining a small piece (20 by 15 mm) from each hand specimen. Each piece was fitted in a rounded disk made of resin and the samples upper surface was exposed. The upper surface was ablated along a defined line of only silica-rich laminae, for 17 seconds at a speed of 10 $\mu\text{m/s}$, on a New Wave Research-Merchantek Product Up 213 laser ablation connected to a Agilent 7500 Series ICP-MS. The REE results were corrected using the XRF results by comparing mutual analysed elements from both techniques (section 2.4.3).

Concentrations for the major elements are reported in wt. %, trace element and REE are reported in ppm. Standard deviation (\pm) is always reported next to the average. The major and the trace element average concentrations are reported and plotted per lithofacies, per facies group (i.e. silica- and silt-rich facies), and per well in order to investigate the variability between lithofacies, as well as the vertical and the lateral variability. The average REE concentrations are only reported per lithofacies and facies group (most of analysed samples are from well ALNR-2). A summary of the major and trace element concentrations is given in Table 6.1 and REE summary is given in Table 6.2. Concentrations of the individual samples are given in Appendix III.

Elemental concentrations are compared with PAAS average compositions in order to constrain either their enrichment or depletion relative to this standard. PAAS is considered to represent the average crustal composition and is used as a baseline for rocks deposited under oxic conditions (Taylor and McLennan 1985). Redox-sensitive element results were normalised to Al contents to highlight fluxes of these elements relative to a detrital fraction and to eliminate the effect of dilution by authigenic components. They were then compared to PAAS values by calculating the enrichment factor (EF); EF of element X = $(X/Al)_{\text{sample}} / (X/Al)_{\text{PAAS}}$. If EF_X is greater than 1, then element X is described as enriched relative to

PAAS and as depleted if the EF_x is less than 1 (Tribovillard et al. 2006). The REE results are also normalised to their concentrations in PAAS to investigate REE characteristics, i.e. LREE depletion relative to heavy HREE and La, Ce, Eu and Y anomalies. Such characteristics are used to interpret sediment source and redox conditions during precipitation. These were calculated according to methods by Bau and Dulski (1996) and Bolhar et al. (2004) as follows:

$$Eu_{anom.} = [Eu/(2/3Sm + 1/3Tb)]_{PAAS-Normalised}$$

$$Ce_{anom.} = [Ce/(2Pr - Nd)]_{PAAS-Normalised}$$

$$La_{anom.} = [La/(3Pr - 2Nd)]_{PAAS-Normalised}$$

$$Y_{anom.} = Y/Ho$$

$$LREE\text{-depletion/enrichment} = (Pr/Yb)_{PAAS-Normalised}$$

Anomalies are described as positive if their value is more than 1, and negative if it is less than 1, apart from Y anomalies, which are described as positive if Y/Ho ratio is more than 27 (PAAS ratio) and negative if it is less than 27. LREE is described as enriched if $(Pr/Yb)_{PAAS-Normalised}$ is more than 1 and depleted if it is less than 1.

Table 6.1. The average concentrations of the major and selected trace elements summarised per lithofacies, lithofacies group and per well. Standard deviation values are shown in parentheses. n stand for number of samples, na for not available and dash (-) not applicable.

	LF1 ¹ n = 25	LF2 ¹ n = 8	LF3 ¹ n = 52	LF4 ¹ n = 7	LF9 ¹ n = 9	LF-LF3 (silica-rich ; all wells) n = 85	Well ALNR-2 (LF1-LF3) n = 28	Well ALNR-3 (LF1-LF3) n = 14	Well ALNR-4 (LF1-LF3) n = 8	Well ASH-2 (LF1-LF3) n = 8	Well ASH-4 (LF1-LF3) n = 20	Well MKZ-1 (LF1-LF3) n = 7	PAAS ² n = 1
LOI (wt. %)	5.67 (1.67)	4.17 (1.90)	8.37 (2.81)	18.3 (1.50)	26.4 (6.45)	7.25 (2.94)	8.90 (3.71)	7.04 (2.16)	6.61 (2.22)	7.70 (2.04)	5.61 (1.48)	5.85 (1.05)	na
Na₂O	0.39 (0.18)	0.35 (0.20)	0.50 (0.33)	0.48 (0.02)	1.42 (2.89)	0.46 (0.29)	0.57 (0.44)	0.43 (0.18)	0.37 (0.14)	0.34 (0.04)	0.47 (0.20)	0.28 (0.09)	1.19
MgO	0.49 (0.44)	0.31 (0.29)	0.64 (0.40)	1.26 (0.25)	6.66 (3.78)	0.57 (0.41)	0.38 (0.19)	0.51 (0.33)	0.58 (0.38)	1.12 (0.66)	0.68 (0.45)	0.48 (0.19)	2.19
Al₂O₃	2.25 (0.65)	1.26 (0.51)	3.88 (1.20)	10.6 (0.87)	4.20 (1.67)	3.21 (1.62)	3.02 (1.20)	2.85 (1.22)	2.80 (0.90)	4.35 (1.30)	3.71 (1.53)	1.61 (0.54)	18.8
SiO₂	86.3 (2.80)	90.6 (3.20)	78.6 (4.70)	54.7 (1.39)	42.2 (12.8)	81.7 (6.40)	79.3 (6.53)	83.1 (5.26)	83.2 (4.65)	78.8 (5.35)	83.2 (5.11)	87.9 (2.40)	62.4
P₂O₅	0.05 (0.05)	0.04 (0.03)	0.13 (0.11)	0.21 (0.15)	0.74 (0.31)	0.10 (0.10)	0.16 (0.11)	0.05 (0.04)	0.13 (0.08)	0.11 (0.06)	0.08 (0.12)	0.04 (0.04)	0.16
SO₃	2.18 (0.71)	1.33 (0.50)	3.72 (1.23)	5.16 (0.73)	2.09 (0.69)	3.06 (1.38)	3.53 (1.47)	2.97 (1.39)	2.95 (0.85)	3.59 (1.21)	2.85 (1.20)	1.43 (0.32)	na
Cl	0.78 (0.40)	0.73 (0.32)	0.82 (0.49)	0.03 (0)	0.55 (0.33)	0.81 (0.45)	0.85 (0.59)	0.68 (0.37)	0.72 (0.35)	0.64 (0.21)	0.80 (0.35)	1.18 (0.36)	na
K₂O	0.51 (0.17)	0.30 (0.11)	0.96 (0.29)	2.61 (0.30)	1.06 (0.50)	0.78 (0.40)	0.83 (0.35)	0.71 (0.32)	0.64 (0.22)	1.10 (0.34)	0.77 (0.34)	0.37 (0.09)	3.68
CaO	0.16 (0.09)	0.09 (0.06)	0.35 (0.28)	1.08 (0.69)	12.4 (6.91)	0.27 (0.25)	0.21 (0.14)	0.38 (0.43)	0.52 (0.24)	0.18 (0.09)	0.25 (0.19)	0.14 (0.04)	1.29
Fe₂O₃	0.96 (0.35)	0.53 (0.18)	1.66 (0.59)	4.93 (0.58)	1.69 (0.65)	1.38 (0.70)	1.44 (0.68)	1.40 (0.72)	1.18 (0.32)	1.76 (0.53)	1.37 (0.59)	0.60 (0.19)	7.18
TiO₂	0.14 (0.05)	0.07 (0.02)	0.32 (0.12)	0.92 (0.07)	0.32 (0.17)	0.25 (0.15)	0.25 (0.11)	0.25 (0.16)	0.28 (0.09)	0.38 (0.19)	0.23 (0.12)	0.09 (0.03)	0.99
Total	99.9 (0.08)	99.8 (0.13)	99.7 (1.51)	99.9 (0.45)	99.7 (0.27)	99.8 (1.16)	99.4 (2.06)	99.9 (0.13)	100 (0.04)	100 (0.13)	99.9 (0.09)	99.9 (0.03)	na
V (ppm)	139 (50.8)	74.9 (41.3)	274 (102)	1056 (245)	391 (229)	220 (129)	236 (115)	218 (125)	202 (104)	285 (94.4)	198 (112)	119 (52.6)	150
Mn	32.6 (13.2)	23.0 (15.3)	56.8 (19.4)	175 (47.9)	570 (177)	47.4 (22.8)	47.7 (20.7)	51.9 (24.3)	50.2 (20.2)	62.3 (20.4)	42.0 (19.1)	23.3 (8.38)	1400
Zr	21.9 (6.21)	24.0 (13.4)	44.9 (13.6)	115 (13.0)	99.7 (45.6)	37.3 (19.1)	38.3 (12.6)	36.8 (19.9)	36.5 (10.7)	50.1 (20.2)	33.4 (15.8)	17.8 (4.03)	210
Mo	25.2 (10.6)	19.2 (6.14)	31.2 (14.6)	122 (14.6)	12.1 (8.85)	30.2 (24.2)	26.7 (10.3)	35.0 (15.3)	19.6 (6.32)	25.7 (6.34)	33.8 (17.2)	17.5 (4.73)	1.50
U	5.16 (1.85)	3.07 (1.06)	10.7 (4.74)	22.9 (6.80)	8.31 (3.45)	8.52 (5.19)	9.57 (6.12)	7.37 (4.64)	10.2 (2.17)	11.2 (4.15)	7.30 (3.60)	3.81 (1.18)	3.10
Fe₂O₃/TiO₂	7.25 (2.15)	7.23 (1.42)	5.74 (2.87)	5.40 (0.90)	5.92 (2.17)	6.38 (2.67)	6.48 (3.17)	7.09 (3.05)	4.36 (0.79)	5.51 (2.73)	6.72 (2.17)	6.68 (1.41)	na
Fe₂O₃/(Fe₂O₃ + Al₂O₃ + Mn)	0.70 (0.05)	0.70 (0.05)	0.70 (0.06)	0.67 (0.03)	0.70 (0.04)	0.70 (0.06)	0.68 (0.06)	0.69 (0.08)	0.70 (0.02)	0.71 (0.07)	0.69 (0.17)	0.73 (0.04)	-
U (EF)	14.6 (5.11)	16.5 (8.64)	17.8 (9.59)	13.6 (4.49)	14.0 (7.44)	16.5 (8.27)	20.6 (11.4)	12.7 (2.23)	23.2 (4.82)	15.4 (3.35)	11.9 (4.45)	15.0 (5.67)	-
V (EF)	7.98 (2.60)	7.37 (2.38)	8.87 (2.75)	12.9 (2.90)	14.8 (12.8)	8.36 (2.72)	9.82 (3.14)	8.08 (1.49)	8.69 (1.83)	8.15 (1.68)	6.30 (2.20)	9.20 (2.57)	-
Mo (EF)	145 (54.8)	210 (72.9)	102 (40.9)	151 (26.5)	48.9 (48.6)	125 (56.0)	123 (51.5)	179 (79.0)	89.8 (21.7)	78.3 (23.8)	115 (33.0)	140 (29.4)	-
Mn (EF)	0.20 (0.07)	0.20 (0.07)	0.20 (0.06)	0.23 (0.08)	2.23 (1.29)	0.21 (0.12)	0.21 (0.06)	0.20 (0.06)	0.24 (0.07)	0.19 (0.04)	0.16 (0.08)	0.20 (0.03)	-

¹ LF1: microcrystalline quartz-rich lithofacies, LF2: microcrystalline quartz-dominated lithofacies, LF3: microcrystalline quartz-rich and detritus-bearing lithofacies; LF4: silt-rich, clay-mineral bearing mudstones and LF9: microcrystalline-, carbonate- and detritus-bearing lithofacies.

² PAAS data from Taylor and McLennan (1985).

Table 6.2. A summary of the average REE composition and anomalies per lithofacies. PAAS, modern oxic/anoxic and hydrothermal fluids compositions are included for comparison. Standard deviation values are shown in parentheses.

	LF1	LF2	LF3	LF4 (silt-rich)	LF9	Silica-rich (LF-LF3)	PAAS ¹	South Pacific (2500 m) ¹	North Pacific (2500 m) ¹	Black Sea (180 m) ¹	Saanich Inlet (165m) ¹	Hydrothermal (H.Temp.) ¹	Hydrothermal (L.Temp.) ¹
	ppm n = 3	ppm n = 1	ppm n = 9	ppm n = 5	ppm n = 3	ppm n = 13	ppm n = 1	pmol/kg n = 1	pmol/kg n = 1	pmol/kg n = 1	pmol/kg n = 1	pmol/kg n = 1	pmol/kg n = 1
La	8.73 (6.90)	8.60	18.3 (13.1)	36.9 (8.94)	14.0 (7.98)	15.4 (12.0)	38.2	29.0	38.7	76	58.2	1301	545
Ce	14.1 (11.8)	14.84	32.3 (21.5)	65.7 (15.4)	27.5 (16.3)	26.8 (20.2)	79.6	4.50	4.32	145	38.4	2670	1258
Pr	1.55 (1.37)	1.52	3.49 (2.31)	7.77 (1.56)	3.20 (2.09)	2.89 (2.18)	8.83	3.90	5.10	na	na	311	130
Nd	6.55 (5.15)	7.79	14.2 (9.56)	30.9 (6.36)	14.3 (8.04)	11.9 (8.82)	33.9	18.0	23.7	59.3	23.3	1219	490
Sm	1.30 (1.08)	1.17	2.63 (1.79)	6.59 (1.44)	4.00 (2.01)	2.22 (1.66)	5.55	3.20	4.42	11.9	4.29	282	102
Eu	0.26 (0.21)	0.24	0.61 (0.47)	1.39 (0.36)	1.04 (0.51)	0.50 (0.43)	1.08	0.86	1.22	3.32	1.18	1419	156
Gd	0.87 (0.72)	0.82	1.73 (1.29)	4.86 (1.24)	3.11 (0.91)	1.46 (1.17)	4.66	4.80	6.76	16.1	6.08	290	87.7
Tb	0.13 (0.07)	0.14	0.28 (0.20)	0.83 (0.23)	0.61 (0.12)	0.23 (0.18)	0.77	0.87	1.14	na	na	38.8	10.1
Dy	0.85 (0.43)	1.07	1.87 (1.69)	4.76 (1.38)	4.51 (1.43)	1.57 (1.47)	4.68	6.60	8.43	19.3	5.24	214	55.4
Y	6.08 (2.63)	7.85	13.7 (8.39)	31.6 (7.31)	37.4 (13.6)	11.5 (7.76)	27	229	238	na	na	1880	628
Ho	0.19 (0.08)	0.22	0.40 (0.26)	1.28 (0.38)	1.23 (0.39)	0.33 (0.24)	0.99	1.90	2.33	na	na	34.2	9.72
Er	0.52 (0.22)	0.72	1.26 (0.78)	3.14 (0.91)	3.36 (1.22)	1.05 (0.73)	2.85	6.60	7.95	14.8	3.98	75.7	25.3
Tm	0.08 (0.02)	0.10	0.18 (0.12)	0.56 (0.15)	0.51 (0.22)	0.15 (0.11)	0.41	1.00	1.22	na	na	8.71	3.10
Yb	0.59 (0.24)	0.70	1.35 (0.92)	3.21 (0.79)	3.78 (1.81)	1.13 (0.84)	2.82	6.90	8.40	13.9	4.71	44.3	17.6
Lu	0.08 (0.02)	0.10	0.20 (0.13)	0.44 (0.10)	0.56 (0.28)	0.16 (0.12)	0.43	1.20	1.46	2.26	0.65	5.03	2.53
ΣREE	41.9 (30.9)	45.9	92.6 (61.0)	200.0 (43.5)	119.1 (29.5)	77.3 (56.7)	212	-	-	-	-	-	-
Pr/Yb	0.76	0.69	0.84	0.79	0.35	0.81	-	0.18	0.19	0.36	0.41	2.24	2.36
La_{anom.}	1.21	4.03	1.40	1.24	1.27	1.56	-	2.89	3.01	2.09	2.95	1.01	0.94
Ce_{anom.}	1.47	1.64	1.11	0.99	1.33	1.23	-	0.16	0.12	1.35	0.80	0.97	1.05
Eu_{anom.}	1.11	1.08	1.30	1.12	1.26	1.24	-	1.10	1.11	1.19	1.15	25.9	8.68
Y/Ho	32.51	35.61	35.24	25.41	30.98	34.64	27.3	121	102	na	na	55.0	64.6

¹Data source: PAAS from Taylor and McLennan (1985)., South Pacific from Zhang and Nozaki (1996) at the location (27°15.37S, 175°25.04E), North Pacific from Alibo and Nozaki (1999) at the location of (34°419N, 139°549E), the Black Sea from German et al. (1991b) at the station BS3-6, Saanich Inlet from German and Elderfield (1989) and high and low temperature hydrothermal fluids from Bau and Dulski (1999)

6.3.2 Major and trace elements

All silica-rich facies (LF1-LF3) contain high SiO_2 concentrations (81.7 ± 6.4) and minor concentrations of detrital components ($\text{Al}_2\text{O}_3 = 3.21 \pm 1.62$, $\text{K}_2\text{O} = 0.78 \pm 0.4$, $\text{TiO}_2 = 0.25 \pm 0.15$ and $\text{Zr} = 37.3 \pm 19.1$; Table 6.1). Detrital parameters show a good positive cross-correlation ($r^2 = 0.83 - 0.95$ for Al_2O_3 vs. K_2O , TiO_2 , and Zr ; Fig. 6.1), as well as with Fe_2O_3 concentrations ($r^2 = 0.83$ for Al_2O_3 vs. Fe_2O_3 ; Fig. 6.1 B). However, they show a negative correlation with SiO_2 ($r^2 = 0.80$ for Al_2O_3 vs. SiO_2 ; Fig. 6.2 A). There are systematic decreases in SiO_2 concentrations from microcrystalline quartz-dominated lithofacies to (LF2) microcrystalline quartz-rich lithofacies (LF1) to microcrystalline quartz-rich and detritus-bearing lithofacies (LF3), whilst concentrations of detrital parameters increase in the same order (Fig. 6.2 A). Stratigraphically, silica-rich facies from well ALNR-2 show a decrease in SiO_2 concentrations towards the Upper Athel Silicilyte, as well as at the base of Athel succession near the U Shale and Athel Silicilyte boundary, associated with an increase in detrital parameter concentrations (Fig. 6.3). There is no systematic relation between SiO_2 and detrital parameter (e.g. Al_2O_3) between different wells (Fig. 6.2 B).

The silt-rich facies (LF4) is characterised by relatively lower SiO_2 concentrations (54.7 ± 1.39) and much higher detrital parameters concentrations ($\text{Al}_2\text{O}_3 = 10.6 \pm 0.87$, $\text{K}_2\text{O} = 2.61 \pm 0.3$, $\text{TiO}_2 = 0.92 \pm 0.05$ and $\text{Zr} = 115 \pm 13.0$). In microcrystalline-, carbonate- and detritus-bearing lithofacies (LF9), the concentrations of SiO_2 are much lower (42.2 ± 12.8), whilst the concentrations of MgO (6.66 ± 3.78) and CaO (12.4 ± 6.91), are higher relative to the silica-rich facies. In comparison to PAAS, the silica-rich facies are significantly enriched in SiO_2 and strongly depleted in detrital parameters, whilst the silt-rich facies have similar concentrations to PAAS (Fig. 6.1).

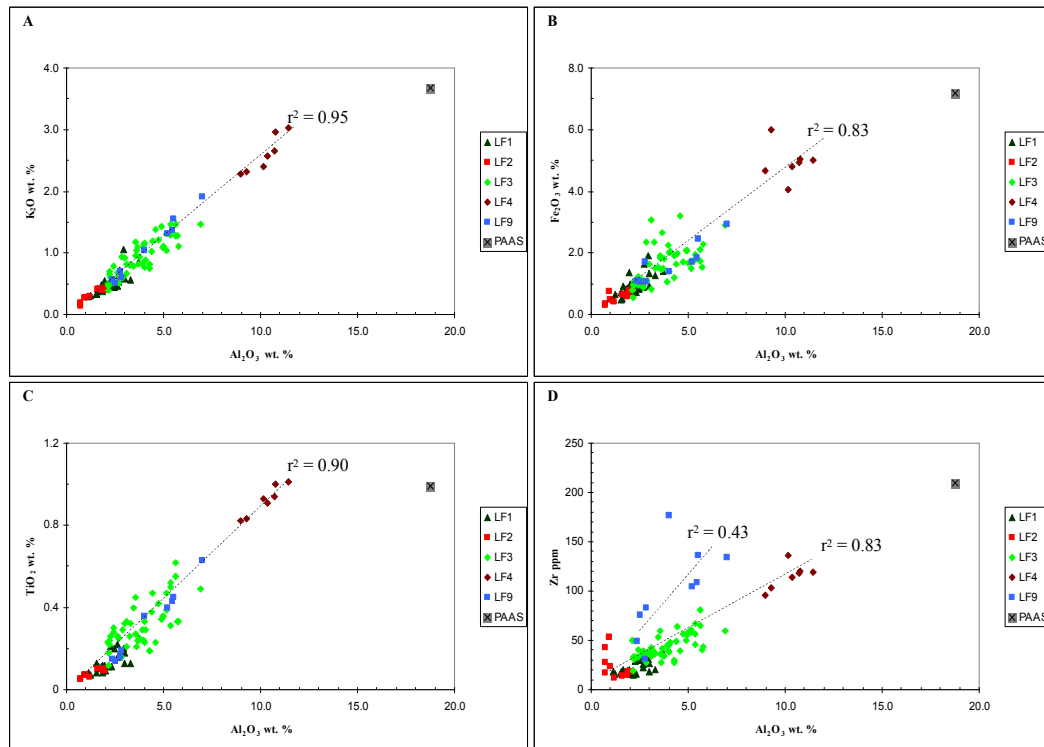


Figure 6.1. (A-D) plots of Al_2O_3 vs. K_2O , Fe_2O_3 , TiO_2 and Zr , respectively. All elements show positive correlation (r^2 ranges from 0.43 to 0.95). These element concentrations show an increase from microcrystalline quartz-dominated lithofacies (LF2) to microcrystalline quartz-rich lithofacies (LF1) to microcrystalline quartz-rich and detritus-bearing lithofacies (LF3) and highest in silt-rich, clay-mineral bearing mudstones LF4, whilst microcrystalline-, carbonate- and detritus-bearing lithofacies (LF9) show concentrations similar to LF1-LF3. The concentrations in the silica-rich facies (LF1-LF3) are strongly depleted relative to PAAS, but they are relatively closer in the silt-rich facies (LF4). Average PAAS composition is obtained from Taylor and McLennan (1985).

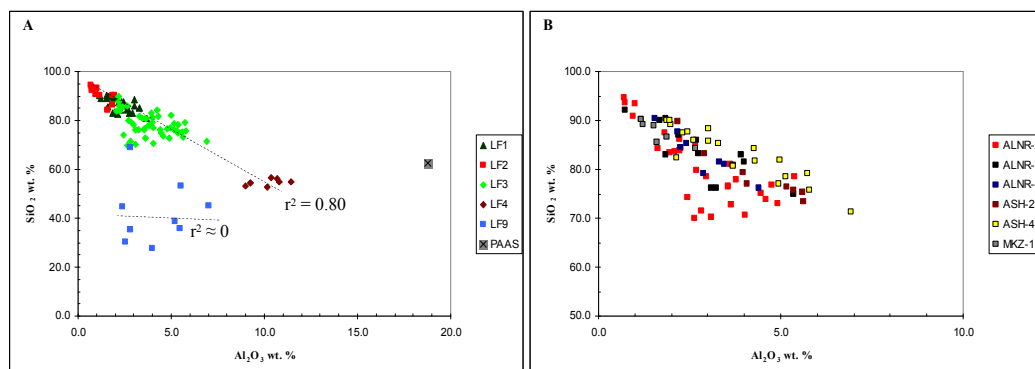


Figure 6.2. (A) Plot showing SiO_2 vs. Al_2O_3 concentration. An increase in SiO_2 concentrations is associated with a decrease in Al_2O_3 concentrations. The silica-rich facies are characterise by high SiO_2 (up to 95 %) concentrations (LF2 being the highest and LF3 being the lowest) relative to the silt-rich facie and PAAS. The silt-rich facies are characterised by relatively lower SiO_2 concentrations and higher Al_2O_3 concentrations similar to PAAS. SiO_2 and Al_2O_3 show negative correlation ($r^2 = 0.80$). LF4 shows the lowest concentrations of SiO_2 that show no correlation with Al_2O_3 contents ($r^2 \approx 0$). (B) shows the same plot as (A), but only for the silica-rich facies (LF1-LF3) plotted per well. No significant variation in concentrations is observed between different wells. Note; LF4 and LF9 are not included in (B) as they identified only from a single well (LF4 from well AL-9 and LF9 from well ALNR-2).

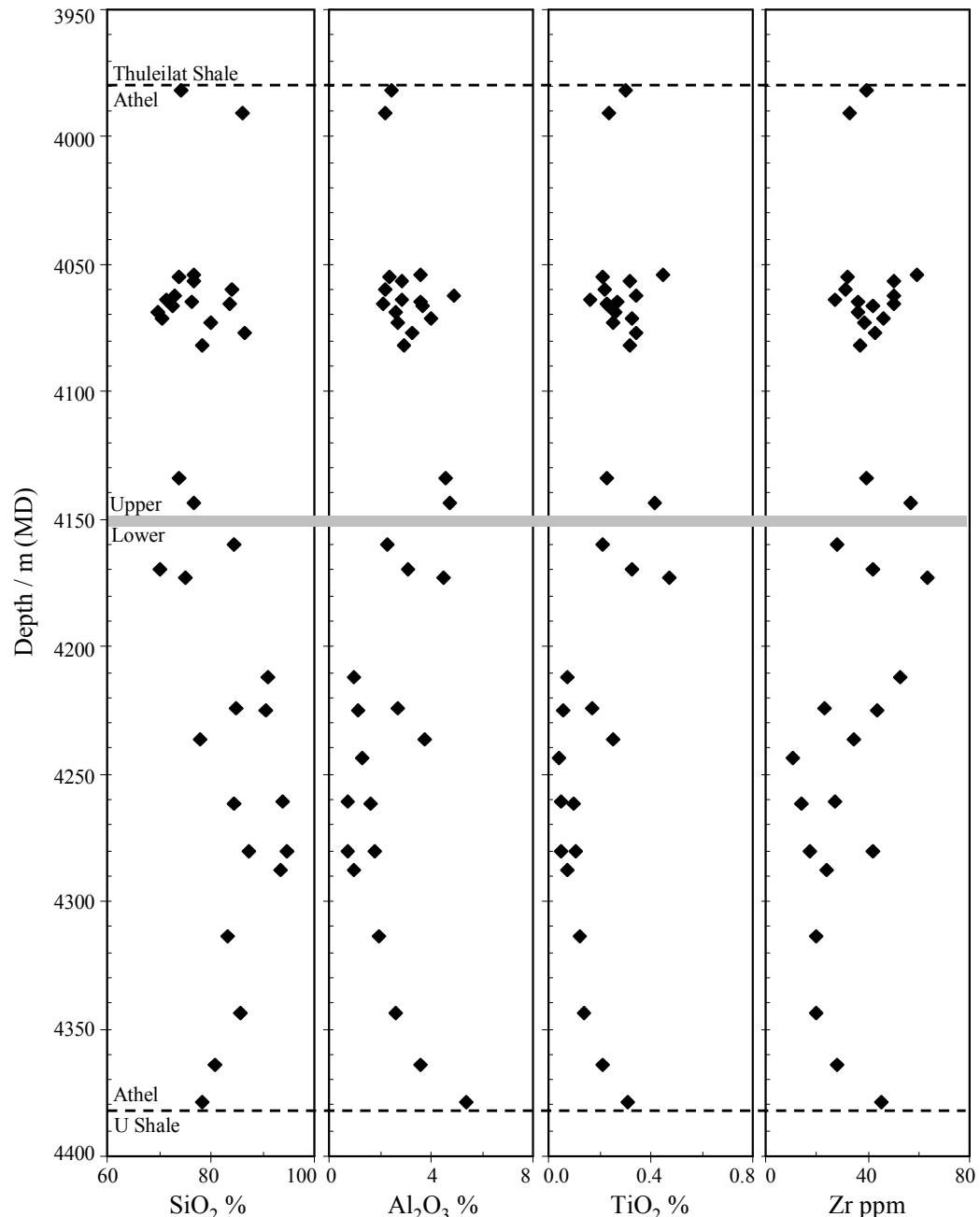


Figure 6.3. A stratigraphic plot of SiO_2 and selected detrital element (Al_2O_3 , TiO_2 and Zr) concentrations of the silica-rich facies in well ALNR-2 throughout the Athel Silicilyte succession to investigate vertical variability. Grey horizontal bar is the boundary between the Upper and Lower Athel Silicilyte (identified by increase in GR response; see Fig. 5.3). A decrease in SiO_2 concentrations is associated with a concomitant increase in detrital parameter concentrations. The concentrations of detrital parameters are relatively higher in the Upper Athel Silicilyte and at the base of the Lower Athel Silicilyte near the boundary between the Athel Silicilyte and the U Shale. Data gap in the Upper Athel Silicilyte make this relation less clear, however, the average concentrations of samples from the Upper Athel Silicilyte show an overall lower SiO_2 concentrations and higher detrital element concentrations (Appendix III).

In order to assess whether hydrothermal signature present or not, the average ratio of $\text{Al}_2\text{O}_3/(\text{Al}_2\text{O}_3 + \text{Fe}_2\text{O}_3 + \text{MnO})$ and $\text{Fe}_2\text{O}_3/\text{TiO}_2$ were calculated for all lithofacies (LF1-LF4 and LF9). The silica-rich facies (LF1-LF3) have an

average ratio of $\text{Al}_2\text{O}_3/(\text{Al}_2\text{O}_3 + \text{Fe}_2\text{O}_3 + \text{MnO})$ equal to 0.70 ± 0.06 and $\text{Fe}_2\text{O}_3/\text{TiO}_2$ equal to 6.38 ± 2.67 . These ratios neither change significantly per lithofacies, nor between wells (Fig. 6.4 and Table 6.1).

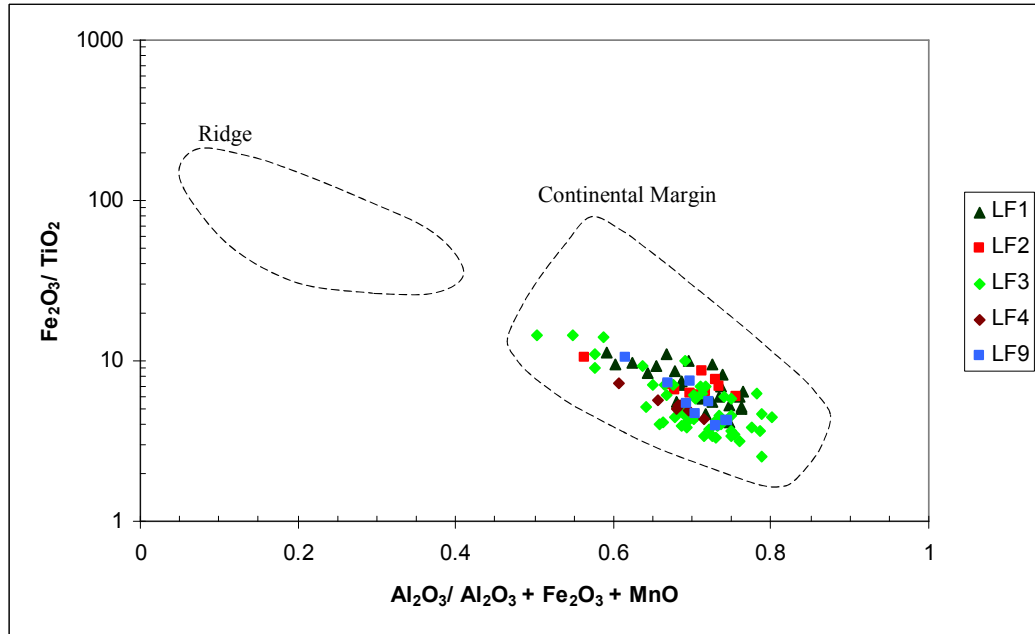


Figure 6.4. A plot shows $\text{Al}_2\text{O}_3/(\text{Al}_2\text{O}_3+\text{Fe}_2\text{O}_3 + \text{MnO})$ vs. $\text{Fe}_2\text{O}_3/\text{TiO}_2$ ratios of the silica-rich facies (LF1-LF3), the silt-rich facies (LF4) and microcrystalline-, carbonate- and detritus-bearing lithofacies (LF9). The average ratio of $\text{Al}_2\text{O}_3/(\text{Al}_2\text{O}_3+\text{Fe}_2\text{O}_3+\text{MnO})$ and $\text{Fe}_2\text{O}_3/\text{TiO}_2$ is 0.70 (0.06) and 6.38 (2.67), respectively, for the silica-rich facies (for the average per sub-lithofacies see table 6.1). All lithofacies ratios fall within the continental margin field identified by Murray (1994).

The average concentrations of redox-sensitive elements are enriched in the silica-rich facies ($U = 8.52 \pm 5.19$, $V = 220 \pm 129$, $\text{Mo} = 220 \pm 129$ and $\text{Mn} = 47.4 \pm 22.8$) silt-rich facies ($U = 22.9 \pm 6.80$, $V = 1056 \pm 245$, $\text{Mo} = 122 \pm 14.6$ and $\text{Mn} = 175 \pm 47.9$), and LF9 ($U = 8.31 \pm 3.45$, $V = 391 \pm 229$, $\text{Mo} = 12.1 \pm 8.85$ and $\text{Mn} = 570 \pm 177$) relative to PAAS ($U = 3.10$, $V = 150$, $\text{Mo} = 1.5$ and $\text{Mn} = 1400$; Fig. 6.5; Table 6.1). The silica-rich sub-lithofacies (LF1-LF3) are also on average enriched relative to PAAS, apart from 4 samples that are U-depleted and 22 samples that are V-depleted (all being LF1-LF2; Fig. 6.5; Appendix III). To ensure that there is no misinterpretation of the redox-sensitive element results, they must be normalised to Al contents and then compared to PAAS. This was achieved by calculating the enrichment factor (EF; section 6.3.1 above) to eliminate the fractions of redox-sensitive elements that are bound in

detrital material and to remove a dilution effect caused by any authigenic components.

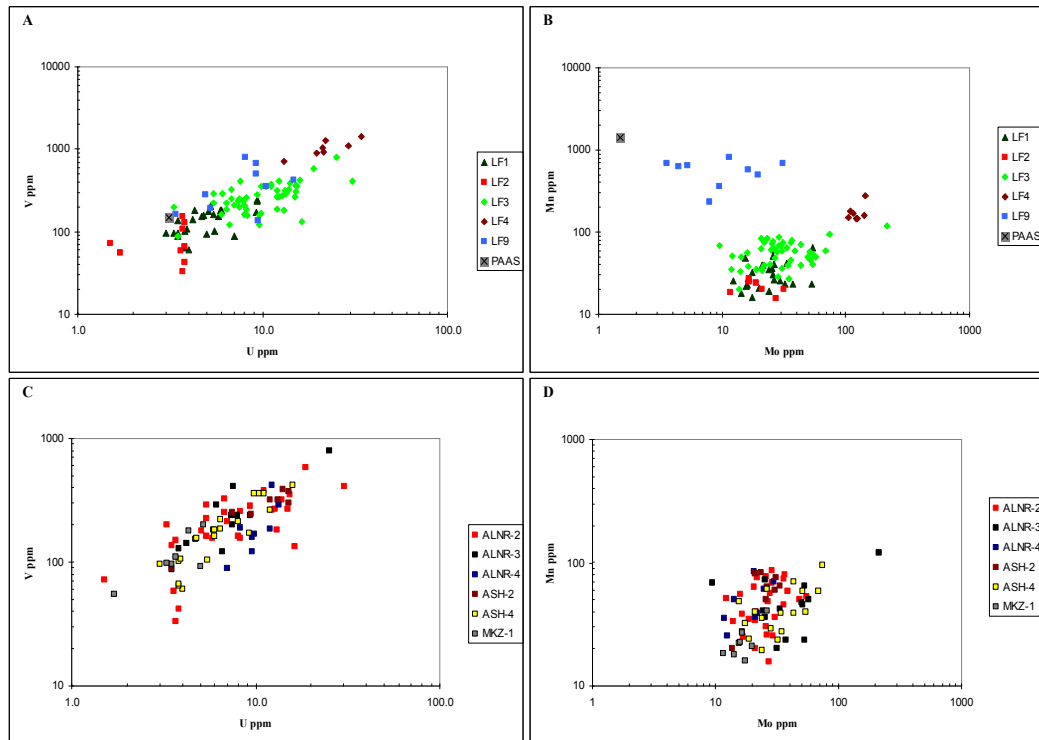


Figure 6.5. Cross plots of redox-sensitive element concentrations. (A) a plot shows U vs. V and (B) a plot shows Mo vs. Mn for the silica-rich facies (LF1-LF3), silt-rich facies (LF4) and microcrystalline-, carbonate- and detritus-bearing lithofacies (LF9), as well as for PAAS for comparison purpose. U, V and Mo are enriched in most lithofacies compared to PAAS (apart from some samples that belong to LF1 and LF2), whilst Mn is strongly depleted. (C) and (D) show the same plots as (A) and (B) for the silica-rich facies only plotted per well. No relation in elemental concentrations is observed between different wells. PAAS values are obtained from Taylor and McLennan (1985).

Results from EF calculations show that redox-sensitive elements (U, V and Mo) are enriched relative to PAAS in the silica-rich facies ($U = 16.5 \pm 8.27$, $V = 8.37 \pm 2.72$ and $Mo = 125 \pm 56.0$), the silt-rich facies ($U = 13.6 \pm 4.49$, $V = 12.9 \pm 2.9$ and $Mo = 151 \pm 26.5$), and LF9 ($U = 14.0 \pm 7.44$, $V = 14.8 \pm 12.8$ and $Mo = 48.9 \pm 48.6$; Fig. 6.6 A & B). Mn is the only depleted redox-sensitive element in the silica-rich facies ($EF = 0.21 \pm 0.12$) and the silt-rich facies ($EF = 0.23 \pm 0.08$), but it is enriched in LF9 ($EF = 2.23 \pm 1.29$; Fig. 6.6 B). The EF values neither show systematic increase/decreases per lithofacies nor between wells (Fig. 6.6). Stratigraphically, silica-rich facies from well ALNR-2 are enriched with U, V and Mo and Mn-depleted. The EF values of each element do not vary significantly throughout the Athel Silicilyte succession (Fig. 6.7).

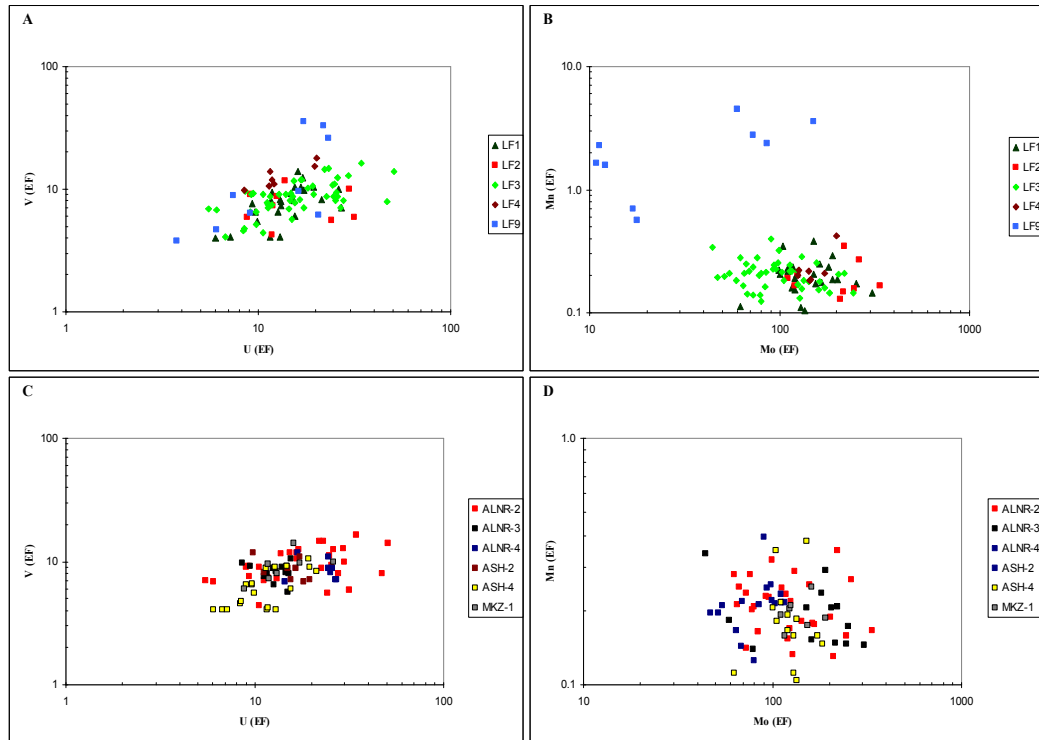


Figure 6.6. Cross plots of redox-sensitive element enrichment factor (EF) values. (A) Plot shows EF values for U vs. V and (B) Mo vs. Mn for the silica-rich facies (LF1-LF3), silt-rich facies (LF4) and microcrystalline-, carbonate- and detritus-bearing lithofacies (LF9). All lithofacies are enriched with the respect to U, V and Mo and Mn-depleted relative to PAAS. LF9 is only Mn-enriched, apart from two samples. The EF values show no relation per lithofacies. (C) and (D) show the same plots as (A) and (B) for the silica-rich facies only plotted per well. Also, no relation in the EF values is observed between different wells.

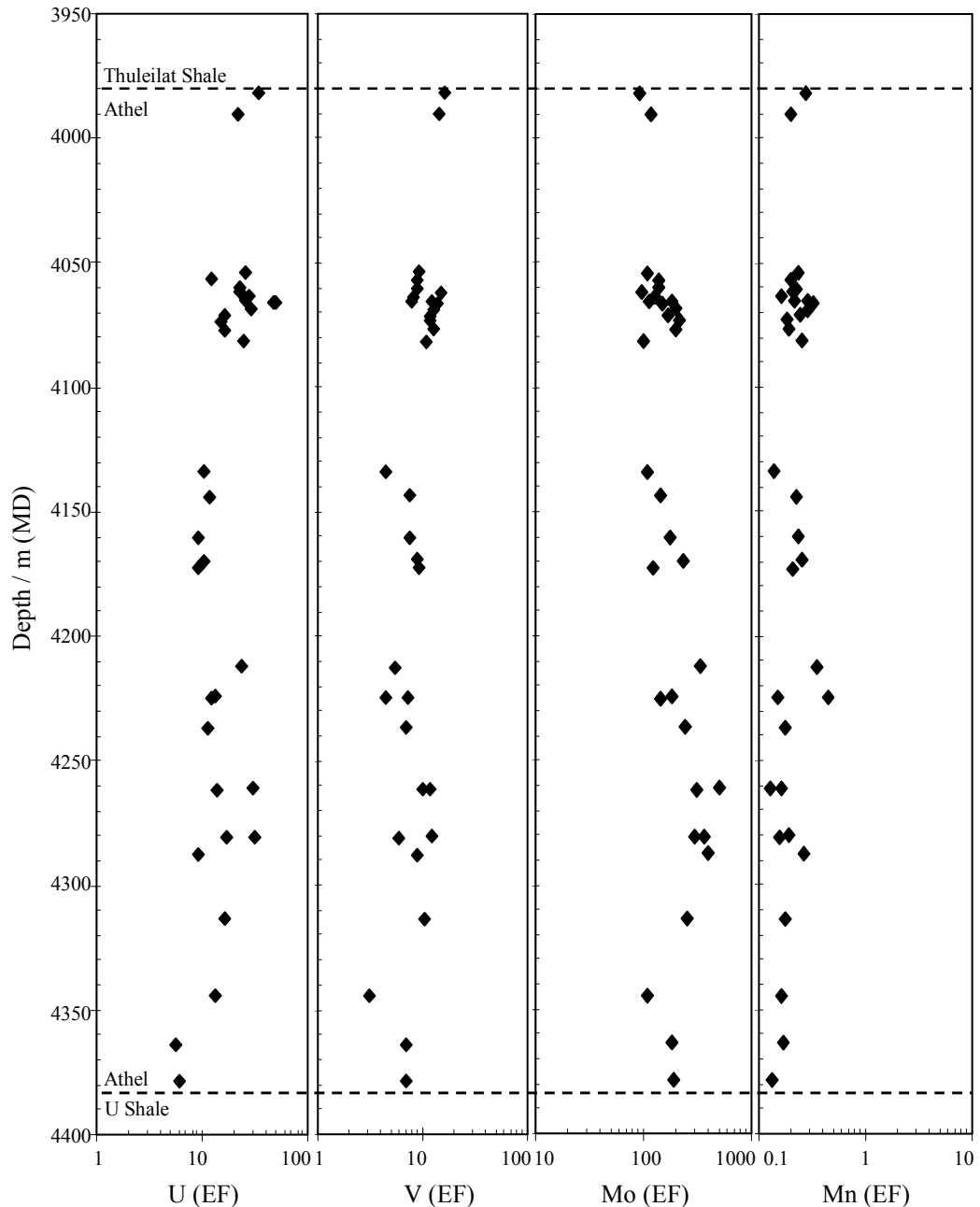


Figure 6.7. A stratigraphic plot of redox-sensitive element EF values for the silica-rich facies from well ALNR-2 throughout the Athel Silicilyte succession. U, V and Mo are all enriched and Mn is depleted relative to PAAS. The EF values for each element show no significant variation throughout stratigraphic section of the Athel Silicilyte from well ALNR-2.

6.3.3 Rare Earth Elements

The total REE (Σ REE) concentrations in the silica-rich facies (77.3 ± 56.7) are lower than in the silt-rich facies (200 ± 43.5), whilst microcrystalline-, carbonate- and detritus-bearing lithofacies (LF9) show similar values (119 ± 29.5) to the silica-rich facies (Fig. 6.8 A). Only the silt-rich facies samples show

Σ REE close to PAAS (212), whereas the silica-rich facies and LF9 are relatively depleted (Fig. 6.8; Table 6.2). The Σ REE concentrations show a good positive correlation with TiO_2 concentrations ($r^2 = 0.68$; Fig. 6.8 A).

Anomalies of Y in the silica-rich facies (34.6 ± 5.01) are higher than the PAAS ratio (27), as well as in LF9 (31.0 ± 7.73 ; apart from one sample having a value of 22.1). There is no significant variation in Y anomalies between silica-rich sub-lithofacies (Fig. 6.8 B; Table 6.2). In the silt-rich facies, Y anomalies (25.4 ± 4.50) are close to the PAAS value. There is no correlation between Y anomalies and TiO_2 concentrations ($r^2 \approx 0$; Fig. 6.8 B).

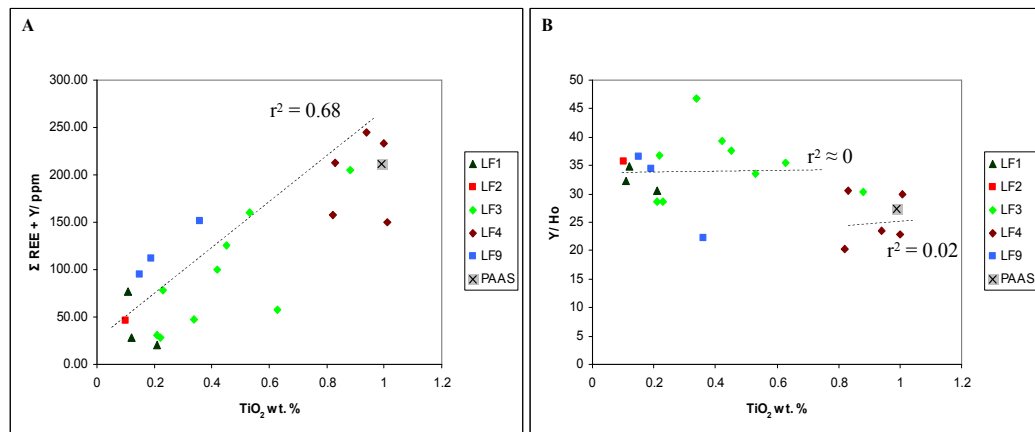


Figure 6.8. (A) and (B) plots show TiO_2 concentrations vs. Σ REE concentrations and Y/Ho ratios; respectively. The Σ REE concentrations in the silica-rich facies (LF1-LF3) and microcrystalline-, carbonate- and detritus-bearing lithofacies (LF9) are lower than PAAS, whereas Σ REE in the silt-rich facies (LF4) reach PAAS concentration. The Σ REE show a good positive correlation with TiO_2 ($r^2 = 0.68$). The silica-rich facies and LF9 have Y/Ho ratios higher than PAAS (apart from one LF9 sample), whereas the silt-rich facies have similar values to the PAAS. There is no correlation between Y/Ho and TiO_2 . The PAAS data are from Taylor and McLennan (1985).

Patterns of the PAAS-normalised REE in the silica-rich facies and LF9 show an overall shift in the ratios (from 0.1 to 1) towards the Upper Athel Silicilyte (Fig. 6.9 A). This also represents an increase in the Σ REE concentration, whereas the ratios in the silt-rich facies patterns are clustered around 1 (Fig. 6.9 B). LREE are depleted (monitored by $\text{Pr}/\text{Yb}_{\text{PAAS-normalised}}$) in the silica-rich facies (0.81 ± 0.26 ; except in four samples), in the silt-rich facies (0.79 ± 0.11) and in LF9 (0.35 ± 0.33 ; Fig. 6.10 A & 6.11 A). Positive La anomalies are developed in the silica-rich facies (1.56 ± 0.78 ; except in two samples), in the silt-rich facies (1.24 ± 0.29) and in LF9 (1.27 ± 0.21 ; Fig. 6.10 A

& 6.11 A). Ce anomalies are also on average positive in the silica-rich facies (1.23 ± 0.36 ; except three samples that showing negative or no anomalies, 0.98-0.99), in the silt-rich facies (1.33 ± 0.50 ; except in one sample) and in LF9 (1.33 ± 0.50 ; Fig. 6.10 B & 6.11 B). Positive Eu anomalies are also developed in the silica-rich facies (1.24 ± 0.36 ; except in two samples), in the silt-rich facies (1.12 ± 0.10) and in LF9 (1.26 ± 0.39 ; except in one sample; Fig. 6.10 B & 6.11 B) There are no significant variations in these anomalies within the silica-rich sub-lithofacies (Fig. 6.10; Table 6.2).

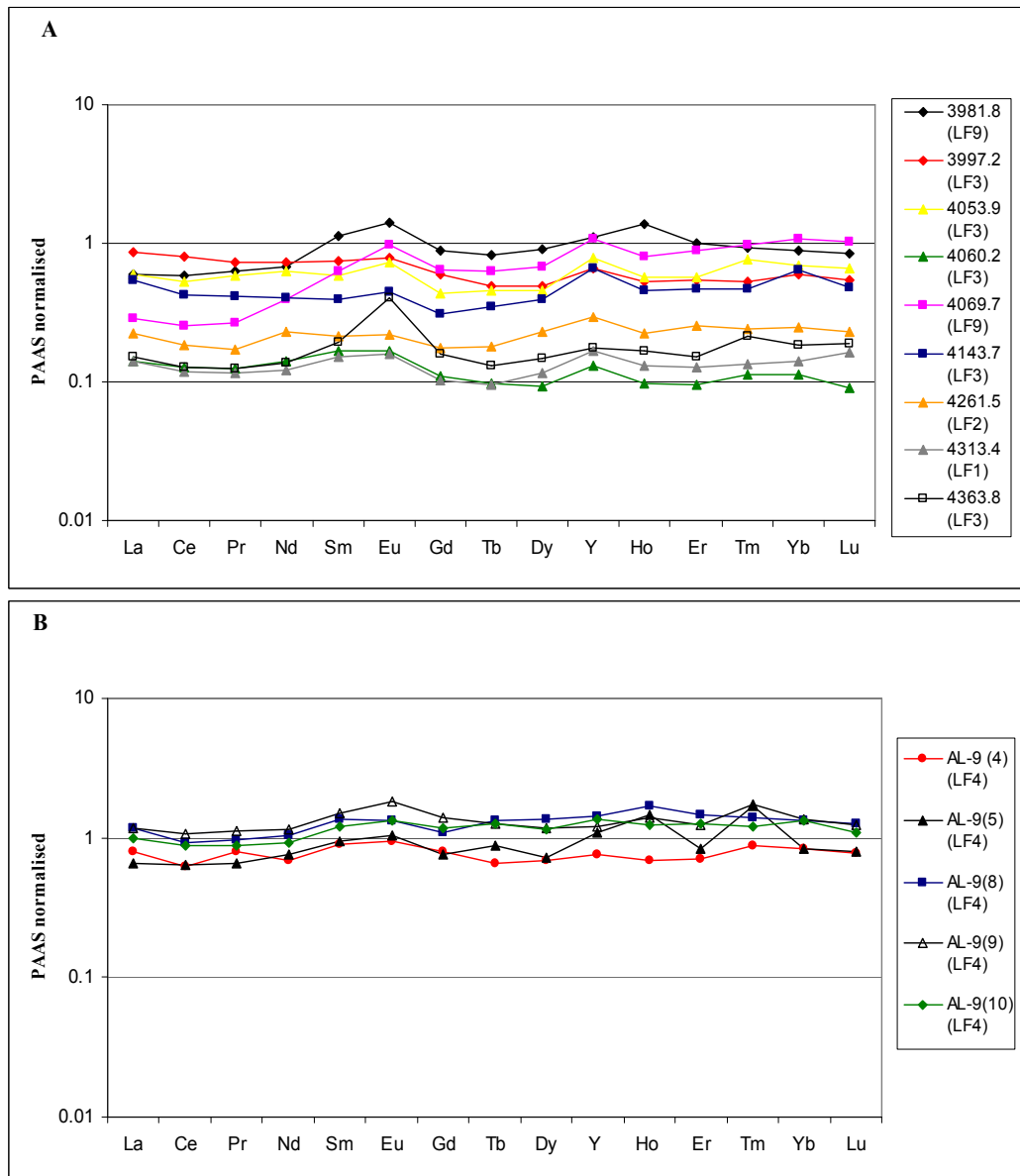


Figure 6.9. Patterns of the PAAS-normalised ratios for the REE in (A) the silica-rich facies (LF1-LF3) and microcrystalline-, carbonate- and detritus-bearing lithofacies (LF9) from well ALNR-2 and (B) the silt-rich facies. The silica-rich facies show an overall increase in PAAS-normalised ratios from 0.1 to 1 towards the Upper Athel Siliclyte and the patterns are generally characterised by LREE-depletion, positive La, Ce, Eu and Y anomalies (see also Fig. 6.8 and 6.9 for anomalies value). The depths (log depth) are in metre. The silt-rich facies show PAAS-normalised ratios around 1 and the patterns show similar REE characteristics (LREE-depletion, positive La, Ce and Eu anomalies but negative Y anomalies) to the silica-rich facies.

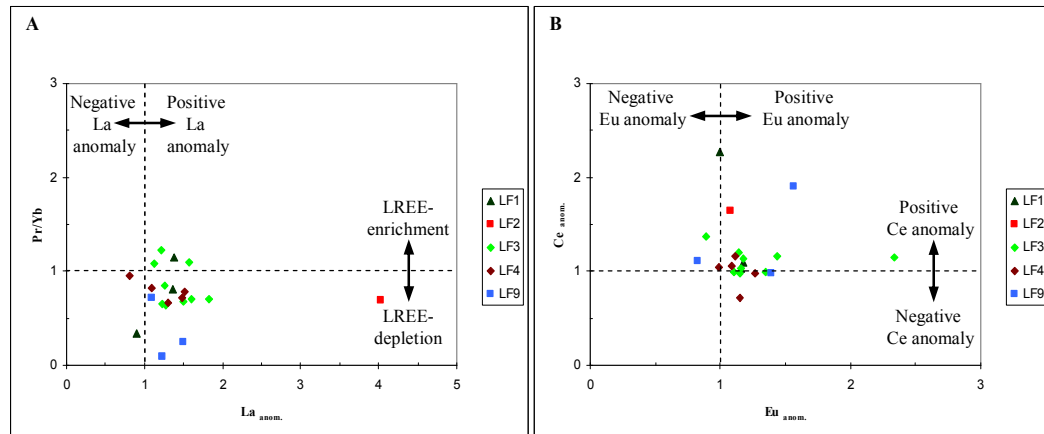


Figure 6.10. (A) and (B) plots shows Pr/Yb ratios vs. La anomalies and Ce anomalies vs. Eu anomalies, respectively, for the silica-rich facies (LF1-LF3), silt-rich facies and microcrystalline-, carbonate- and detritus-bearing lithofacies(LF9). All lithofacies are on average characterised by LREE-depletion ($\text{Pr/Yb}_{\text{PAAS-normalised}}$ ratios < 1 ; apart from four samples from LF2 and LF3). La anomalies are positive in all lithofacies (apart from two samples from LF2 and LF4). Ce anomalies are positive (or very weak negative) in all lithofacies. Positive Eu anomalies are also developed in most samples (apart from three samples from the silica-rich facies and LF9 that show very weak negative anomalies). Average values per lithofacies are shown in Table 6.2 and plotted in Fig. 6.11.

6.4 Origin of rock components

6.4.1 Detrital inputs

Previous observations from the core and the petrographical data revealed that the silica-rich facies (LF1-LF3) exhibit wavy discontinuous lamination, suggesting that this facies likely precipitated during accumulation of microbial layers, which were derived from the water column. The silica-rich facies, up to 390 m thick, are composed of syndepositionally (primary) microcrystalline quartz (average = 80 wt. %) with minor contents of detrital material (quartz grains and clay minerals; average = 13 wt. %), pyrite (4 wt. %) and organic carbon (average TOC = 3 wt. %). The microcrystalline quartz contents decrease from microcrystalline quartz-dominated lithofacies (LF2) to microcrystalline quartz-rich lithofacies (LF1) and are lowest in quartz-rich and detritus-bearing lithofacies (LF3) (91, 83 and 72 wt. %, respectively), whilst the detrital contents increase in the same order (4, 7 and 17 wt. %, respectively). The silt-rich facies (LF4), present in the bounding mudstones (U and Thuleilat Shale), exhibit straight parallel laminations. The silt-rich facies are mainly composed of detrital material (> 83 wt. %), including silt-sized quartz, feldspar and clay minerals with minor contents of pyrite (8 wt. %) and organic carbon (TOC = 7 wt. %). Their

deposition likely took place during intense detrital input to the Athel Basin (section 5.2.2). Microcrystalline-, carbonate- and detritus-bearing lithofacies (LF9) contains significant amounts of precompaction carbonate cement (average = 41 wt. %), microcrystalline quartz (31 wt. %), detrital material (14 wt. %), with minor contents of pyrite (8 wt. %) and organic carbon (TOC = 3 wt. %). LF9 is mainly found as thin layers (0.15-0.5 thick m) within the Athel Silicilyte and the bounding mudstones. Carbonate cement is interpreted to be precipitated during early-stage, shallow burial diagenesis (section 5.2.4).

The strong enrichments of SiO_2 (81.7 ± 6.4) and the strong depletions of detrital parameters ($\text{Al}_2\text{O}_3 = 3.21 \pm 1.62$, $\text{K}_2\text{O} = 0.78 \pm 0.4$, $\text{TiO}_2 = 0.25 \pm 0.15$ and $\text{Zr} = 37.3 \pm 19.1$; Table 6.1) in the silica-rich facies relative to PAAS (Fig. 6.1; Table 6.1) are consistent with the core/petrographical observations that they are mainly composed of microcrystalline quartz with small amounts of detrital material. The high concentrations of detrital parameters (close to PAAS values) in the silt-rich facies ($\text{Al}_2\text{O}_3 = 10.6 \pm 0.87$, $\text{K}_2\text{O} = 2.61 \pm 0.3$, $\text{TiO}_2 = 0.92 \pm 0.05$ and $\text{Zr} = 115 \pm 13.0$), are also consistent with high detrital contents in this facies. Detrital parameters show very strong cross-correlation ($r^2 = 0.83 - 0.95$ for Al_2O_3 vs. K_2O , TiO_2 , and Zr ; Fig. 6.1 A-C), suggesting that the detrital material are derived from the same source, weathering products from the surrounding hinterland. In addition, the total Fe_2O_3 concentrations (Fe^{2+} and Fe^{3+}) show a strong correlation with the Al_2O_3 ($r^2 = 0.83$, Fig. 6.1 D). Such a relationship is consistent with the previous conclusion from the petrographical observations that iron was delivered to the Athel Basin with aluminium-rich minerals and that pyrite formation was limited by iron availability (section 5.2.1; Fig. 5.11).

Although the silica-rich facies are strongly depleted in all the detrital parameters, there is a gradual increase in detrital parameter concentrations from LF2 to LF1 and highest in LF3 (e.g. Al_2O_3 concentrations = 1.26 ± 0.51 , 2.25 ± 0.65 and 3.88 ± 1.2 , respectively; Fig. 6.2 A), as well as an increase toward the Upper Athel Silicilyte and near the bounding mudstones boundaries (Fig. 6.3), suggesting an increase in background detrital input. The increase in the detrital parameter concentrations is associated with a decrease in SiO_2 concentrations from LF2 to LF1 and lowest in LF3 (90.6 ± 3.2 , 86.3 ± 2.80 and 78.6 ± 4.70 ,

respectively), which is supported by strong negative correlation between Al_2O_3 and SiO_2 ($r^2 = 0.80$; Fig. 6.2 A). This relation confirms the previous conclusion from petrographical observations that the higher detrital input towards the Upper Athel Silicilyte reduced the amount of precipitated silica in the microbial layers (section 5.4). However, the elemental concentrations cannot provide supporting evidence for the lateral variation, since samples only cover small intervals of the Athel succession towards the basin margin (see Chapter 2; Fig. 2.2). These intervals can be dominated by one lithofacies type and do not represent the average composition of the Athel Silicilyte succession in that well.

The high enrichment of SiO_2 in the silica-rich facies relative to PAAS (Fig. 6.2), therefore suggests the presence of another source responsible for their enrichment. Since silica-rich deposits can be found in hydrothermal settings, where hydrothermal fluids supply dissolved silica, and in marine settings, it is crucial to investigate if the silica in the Athel Silicilyte was sourced by hydrothermal fluids or from seawater. Therefore, the signatures of hydrothermal and seawater sources were investigated using major element and REE results. However, the presence of detrital material in marine or hydrothermal precipitates can contaminate original REE signatures (Webb and Kamber 2000; Bolhar et al. 2004). Hence, before interpreting REE data from this study, detrital contamination to the REE system must be investigated. Detrital contamination therefore is considered first and then hydrothermal and seawater signatures are discussed.

6.4.2 *Detrital contamination to REE*

In detrital-free precipitates (such as BIFs, cherts and stromatolitic carbonates), REE are almost transferred quantitatively (i.e. unchanged) from seawater to sediments (e.g. McLennan 1989; Bolhar et al. 2004). REE have low mobility during diagenesis (Parekh et al. 1977; McLennan 1989; Alt and Teagle 2003). Certainly, quantitative modelling suggests that extremely high water/rock ratios (> 1000) are required to alter REE signatures during diagenesis (Banner et al. 1988). Hence, detrital-free precipitates are likely to preserve the signature of original fluids that they precipitated from (e.g. McLennan 1989; German et al.

1990; Webb and Kamber 2000). In contrast, REE compositions in deposits with significant detrital contents should reflect the REE composition of PAAS (Taylor and McLennan 1985; McLennan 1989). In addition, detrital material should depress Y/Ho ratios to the PAAS ratio of around 27, due to the preferential Y complexation to particulate matter relative to Ho (e.g. Zhang et al. 1994; Nozaki et al. 1997).

The silica-rich facies and LF9 samples have up to 10 times lower $\Sigma\text{REE} + \text{Y}$ concentrations (77.3 ± 51.9 and 119 ± 29.5 , respectively) than PAAS (212). They are also characterized by Y/Ho ratios (34.6 ± 5.01 and 31.0 ± 7.73 , respectively) higher than the average PAAS value (27), apart from one LF9 sample that was obtained from just beneath the silt-rich Thuleilat Shale, which contains more than 15 wt. % detrital material. Most importantly, the Y/Ho ratios show no correlation with the TiO_2 (detrital parameter) concentrations ($r^2 \approx 0$; Fig. 6.8 A). These observations suggest that detrital contamination is negligible in the silica-rich facies and LF9. Furthermore, REE were deliberately measured only from the silica-rich laminae, which contain no detrital material (Chapter 2; section 2.4.3), to eliminate the effect of detrital contamination. Consequently, the REE signature of silica-rich facies and LF9 should reflect the signature of fluids that they precipitated from. The increase in the ΣREE concentrations towards the Upper Athel Silicilyte and the good correlation with the TiO_2 could be attributed to a decrease in the silica dilution effect. The increase in the detrital content is associated with a decrease in the microcrystalline content as previously established.

The silt-rich facies, however, have ΣREE (200 ± 43.5) and Y/Ho ratio (25.4 ± 4.50) similar to PAAS (Fig. 6.8 A & 6.9 B). Therefore, the REE composition in this facies is dominated by detrital input, which is consistent with the previous petrographical results. Hence, the REE results from silt-rich facies cannot be used to interpret the water chemistry during deposition.

6.4.3 Hydrothermal source

The average ratio of $\text{Al}_2\text{O}_3/(\text{Al}_2\text{O}_3 + \text{Fe}_2\text{O}_3 + \text{MnO})$ and $\text{Fe}_2\text{O}_3/\text{TiO}_2$ in silica-rich facies is 0.70 ± 0.06 and 6.38 ± 2.67 ; respectively (Table 6.1). These average values are not consistent with cherts that precipitated in hydrothermal settings (e.g. spreading ridges), but resemble the cherts accumulated in continental margins (Fig. 6.4; section 6.2.2). Cherts found close to the East Pacific Rise, for example, have $\text{Al}_2\text{O}_3/(\text{Al}_2\text{O}_3 + \text{Fe}_2\text{O}_3 + \text{MnO})$ ratio as low as 0.01, as a result of high Fe and Mn content in the hydrothermal fluids; whereas cherts precipitated at continental margins have an average ratio of 0.7 (Bonatti 1983; Adachi et al. 1986; Murray 1994).

In addition, the silica-rich facies (LF1-LF3) and microcrystalline-, carbonate- and detritus-bearing lithofacies (LF9) are characterised on average by LREE-depletion ($\text{Pr}/\text{Yb}_{\text{PAAS-normalised}}$ ratios = 0.81 ± 0.26 and 0.35 ± 0.33 ; respectively) and weak positive Eu anomalies (1.24 ± 0.36 and 1.30 ± 0.42 ; respectively; Fig. 6.11 & 6.12; Table 6.2). These characteristics are inconsistent with hydrothermal precipitates, which are typically characterised by LREE-enrichment and pronounced positive Eu anomalies (e.g. McLennan 1989; German et al. 1990; Klinkhammer et al. 1994; Bau and Dulski 1999). For example, low (42°C) and high (360°C) temperature hydrothermal fluids show LREE-enrichments ($\text{Pr}/\text{Yb}_{\text{PAAS-normalised}}$ ratios = 2.36 and 2.24; respectively) and pronounced positive Eu anomalies (8.68 and 25.9; respectively; Fig. 6.11 & 6.12; Table 6.2). These distinctive REE signatures characterising hydrothermal fluids are attributed to the strong fractionation of HREE relative to the rest of REE and supply of reduced Eu (section 6.2.2; e.g. German et al. 1990; Klinkhammer et al. 1994). Therefore, in the absence of any hydrothermal signature from major element and REE results, silica was unlikely to have been sourced from hydrothermal fluids during Athel Silicilyte precipitation.

6.4.4 Seawater source

The silica-rich facies (LF1-LF-3) and microcrystalline-, carbonate- and detritus-bearing lithofacies (LF9) are characterised on average by LREE-

depletion (0.81 ± 0.26 and 0.35 ± 0.33 ; respectively), positive La anomalies (1.56 ± 0.78 and 1.27 ± 0.21 ; respectively), weak positive Eu anomalies (1.24 ± 0.36 and 1.30 ± 0.42 ; respectively) and positive Y anomalies (34.6 ± 5.01 and 31.0 ± 7.73 ; respectively; Fig. 6.11 & 6.12; Table 6.2). These characteristics are consistent with the modern seawater REE signature (section 6.2.3; e.g. German et al. 1995; Bolhar et al. 2004; Friend et al. 2008). For example, water samples from the South and the North Pacific oceans (at a depth of 2500 m) show LREE-depletion (0.18 and 0.19; respectively), positive La anomalies (2.89 and 3.01; respectively), weak positive Eu anomalies (1.10 and 1.11; respectively) and positive Y anomalies (121 and 102; respectively; Fig. 6.11 & 6.12; Table 6.2). Such characteristics are related to the different affinity of each element in the REE group relative to its neighbour to solution/particle complexation, resulting in preferential scavenging by particles (section 6.2.3; e.g. German and Elderfield 1989; De Baar et al. 1991; Sholkovitz et al. 1994). In addition, marine precipitates (microbialites) in ancient (Archean) and modern (Holocene) environments show similar REE characteristics to modern seawater (Kamber and Webb 2001; Shields and Webb 2004). The similarity in REE characteristics between ancient precipitates and modern seawater (and precipitates) led to the suggestion that the seawater REE composition has hardly changed throughout the Archean to the present day (Webb and Kamber 2000; Shields and Webb 2004; cf. Picard et al. 2002).

Based on: 1) silica-rich facies (and LF9) show REE concentrations characteristic of modern seawater, 2) REE composition of Precambrian seawater was similar to modern seawater and 3) the silica-rich facies are not enriched with detrital material or hydrothermal products, the Athel Silicilyte is interpreted to reflect a seawater precipitate. Consequently, silica present in the Athel Silicilyte was most likely to be derived from seawater. The silica source is discussed in more depth in Chapter 7 (section 7.2) by integrating all evidence from this chapter and Chapter 5, and by performing mass-balance calculations.

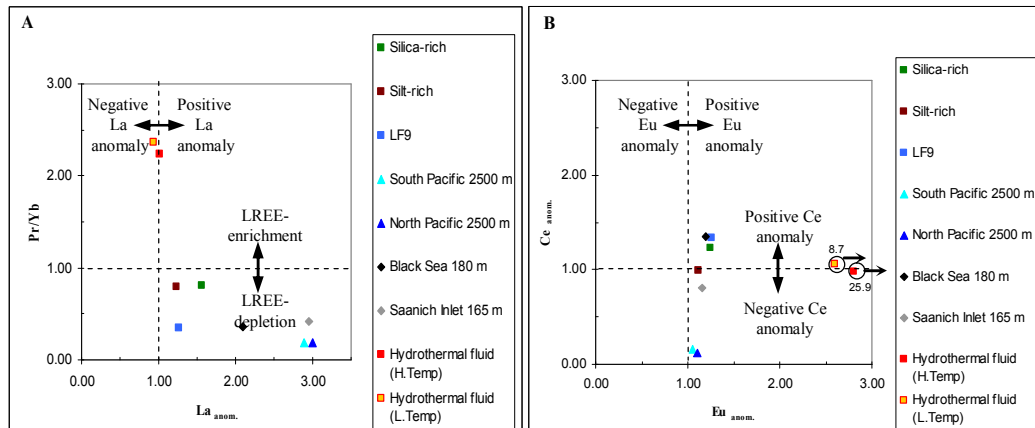


Figure 6.11. (A) and (B) plots showing Pr/Yb ratios vs. La anomalies and Ce anomalies vs. Eu anomalies, respectively of the average silica-rich facies, silt-rich facies, LF9, South Pacific (depth 2500 m), North Pacific (depth 2500 m), Black Sea (depth 180 m), Saanich Inlet (depth 165 m), high temperature hydrothermal fluid (360 °C) and low temperature hydrothermal fluid (42 °C). Note, some REEs (Pr, Tb, Y, Ho, and Tm) are not reported in the Black Sea and Saanich Inlet, consequently the next neighbouring element to the missing element was used to calculate the different anomalies. These data are presented in Table 6.2.

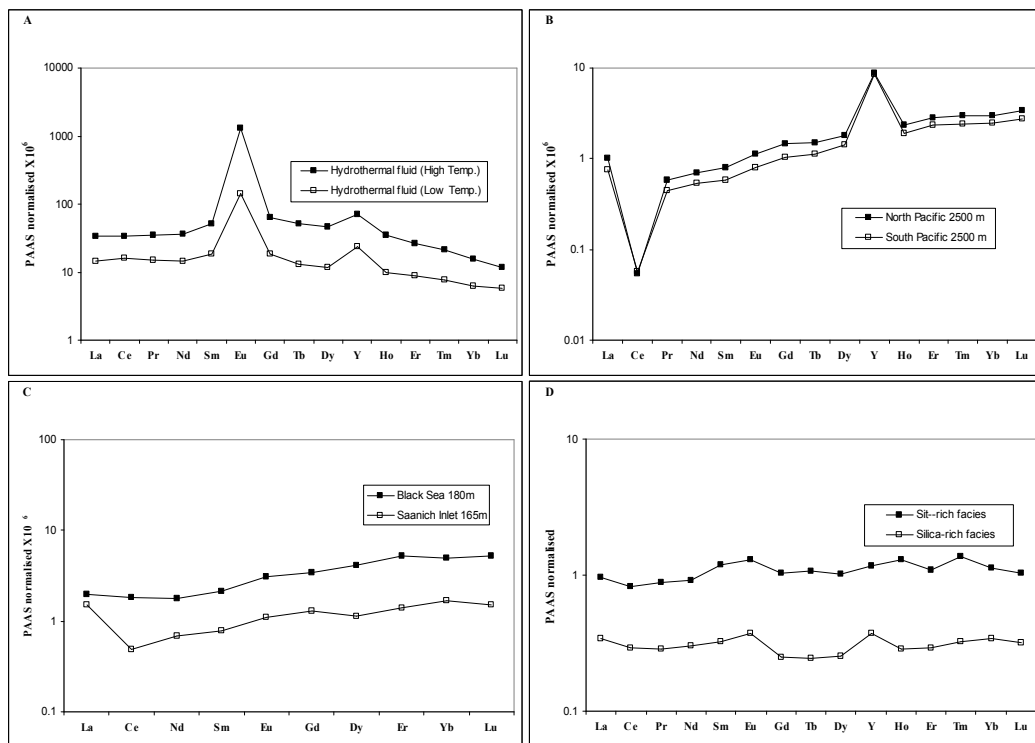


Figure 6.12. PAAS-normalised patterns of the REEs of (A) high (360 °C) and low (42 °C) temperature hydrothermal fluids, (B) oxic seawater at a depth of 2500 m from the South and North Pacific, (C) anoxic basins (the Black Sea and Saanich Inlet) and (D) the average silica- and the silt-rich facies. Data source are shown in Table 6.2 caption.

6.5 Redox conditions

In this section, redox conditions during Athel Silicilyte and U Shale deposition are discussed using REE and redox-sensitive element concentrations,

as well as pyrite framboid size-distribution results that were outlined in Chapter 5 (section 5.3).

REE characteristics of the Athel Silicilyte and modern seawater were discussed in section 6.4.4 to establish the silica source. Both the Athel Silicilyte and modern seawater show similar REE characteristics, including LREE-depletion, positive La, Eu and Y anomalies (Fig. 6.11 & 6.12). However, the silica-rich facies and microcrystalline-, carbonate- and detritus-bearing lithofacies (LF9) show positive/weak negative Ce anomalies (1.23 ± 0.36 and 1.33 ± 0.50 ; respectively) and weaker LREE-depletion relative to modern seawater, which is characterised by strong negative Ce anomalies (South Pacific = 0.16 and North Pacific = 0.12) and strong LREE-depletion (Fig. 6.11 & 6.12; Table 6.2). The Ce anomaly values of the silica-rich facies and LF9 are comparable to the values from modern anoxic basins, the Black Sea (1.35) and Saanich Inlet (0.8; Fig. 6.11 B & 6.12 C; Table 6.2).

The positive/weak negative Ce anomalies in the silica-rich facies and LF9 throughout the Athel Silicilyte succession (Fig. 6.10; Appendix III), suggest that the redox conditions were anoxic during precipitation of these lithofacies. In anoxic conditions, Ce is not oxidised and remains stable (as Ce^{3+}), resulting in weak negative (and sometime positive) Ce anomalies in anoxic environments. Whereas, in oxic environments, Ce is oxidised to the stable form of Ce^{4+} and removed from waters by adsorption onto Fe- and Mn-oxyhydroxides, resulting in negative Ce anomalies in the water column/porewaters (e.g. Elderfield 1988; German and Elderfield 1989; McLennan 1989; Sholkovitz et al. 1992). The weak LREE-depletion in the silica-rich facies and LF9 relative to modern seawater is also attributed to anoxic conditions. Below the redox boundary, dissolution of settling Fe- and Mn-oxyhydroxide particles, which are enriched with LREE relative to HREE (due to the fact that LREE has a higher affinity to particle complexation) releases LREE back to the water column, resulting in weak LREE-depletion in anoxic environments relative to oxic environments (German and Elderfield 1989; Sholkovitz et al. 1992; Bolhar et al. 2004). The Black Sea, for example, shows strong negative Ce anomalies and strong LREE-depletion in the oxic water column, but below the redox boundary it shows positive Ce

anomalies and weak LREE-depletion, accompanied by a sharp increase in the dissolved Mn and Fe concentrations (German et al. 1991b).

The positive/weak negative Ce anomalies and the weak LREE-depletion in the Athel Silicilyte lithofacies (LF1-LF3 and LF9) and the U Shale (silt-rich facies; LF4), therefore suggest that they precipitated in an anoxic environment. Nevertheless, positive/weak negative Ce anomalies (and LREE-depletion) can be produced in an anoxic water column and in anoxic porewaters that are overlain by an oxic/dysoxic water column (German and Elderfield 1990). Therefore, anoxic conditions probably existed at least below the sediment-water interface. However, because of this latter possibility, it is not possible to infer water column anoxia based solely on the REE results (e.g. German and Elderfield 1990; Sholkovitz and Schneider 1991; Sholkovitz et al. 1992). More robust evidence for whether anoxia was in the water column or only in the porewaters is provided from redox-sensitive elements and pyrite framboidal size-distributions, which is discussed in the following paragraphs.

Redox-sensitive elements (U, V and Mo) are enriched relative to PAAS in the silica-rich facies (LF1-LF3; average EF for U = 16.5 ± 8.27 , V = 8.37 ± 2.72 and Mo = 125 ± 56.0), in the silt-rich facies (LF4; average EF for U = 13.6 ± 4.49 , V = 12.9 ± 2.9 and Mo = 151 ± 26.5), and in microcrystalline-, carbonate- and detritus-bearing lithofacies (LF9; average EF for U = 14.0 ± 7.44 , V = 14.8 ± 12.8 and Mo = 48.9 ± 48.6 ; Fig. 6.6 A & B; Table 6.1). Mn is the only depleted redox-sensitive element (average EF in the silica-rich facies = 0.21 ± 0.12 , the silt-rich facies = 0.23 ± 0.08), but it is enriched in LF9 (average EF = 2.23 ± 1.29 ; Fig. 6.6 B; Table 6.1).

The strong enrichment of U, V and Mo and depletion of Mn relative to PAAS suggests their enrichments took place in euxinic environments. In oxic environments, U, V and Mo exist in soluble forms as U^{6+} , V^{5+} and Mo^{6+} , and hence they diffuse away from precipitation sites, resulting in their depletion (e.g. Jones and Manning 1994; Morford et al. 2005). Whereas, in an anoxic environment with the presence of dissolved sulphide (euxinic), they are reduced to the stable forms of U^{4+} , $V^{4+/3+}$ and Mo^{4+} leading to their enrichment in

sediments by adsorption onto organic matter and iron sulphide (section 6.2.4; e.g. Morford et al. 2001; Algeo 2004). Mn in anoxic conditions is reduced to soluble Mn^{2+} , which diffuses away from the reduction sites to oxic water where it is oxidised to the insoluble Mn^{+3} and Mn^{+4} (e.g. Morford et al. 2001; Tribovillard et al. 2006). However, dissolved Mn in anoxic waters could be bound to carbonate minerals and result in Mn-enrichment (section 6.2.4; e.g. Jenkyns et al. 1991; Hild and Brumsack 1998). This would explain the relative enrichment of Mn in microcrystalline-, carbonate- and detritus-bearing lithofacies (LF9).

Enrichment of the redox sensitive elements could occur in euxinic sediments under dysoxic or oxic water column. However, their very strong enrichment (particularly Mo; enriched on average by 125 fold above oxic PAAS) throughout the Athel succession (Fig. 6.7) suggests that the water column was euxinic. The redox element concentrations in this study are also comparable to other modern sediment concentrations where the water column is euxinic (e.g. the Black Sea and Cariaco Basin in Venezuela; Lyons et al. 2003; Algeo and Lyons 2006). The consistent enrichments of U, V, Mo and Mn- depletion in all silica-rich sub-lithofacies (LF1-LF3) as well as the fact that each element enrichment does not change significantly (per lithofacies, well or stratigraphically; Fig. 6.6 & 6.7; Table 6.1) suggest that the euxinic conditions were dominant throughout the Athel Silicilyte precipitation in the water column of the mini-basins (Fig. 3.6 & 5.25).

Additional evidence for euxinia in the water column comes from framboidal pyrites. In particular, their size-distributions could help to interpret whether redox conditions existed in porewaters or in the water column (e.g. Wilkin et al. 1996; Wilkin and Barnes 1997; Wignall and Newton 1998; Zhou and Jiang 2009; Bond and Wignall 2010; Wignall et al. 2010). To understand how this technique might be used to construct redox conditions, it is necessary to review pyrite formation processes and their locus beforehand.

The formation of pyrite framboids requires reduced iron and sulphide, which in turn depends on the availability of terrigenous iron, dissolved sulphate and organic carbon quantity/quality for the metabolic activities of sulphate and

iron reducing bacteria (e.g. Westrich and Berner 1984; Canfield et al. 1992; Taylor and Macquaker 2000). Pyrite formation is believed to occur during the replacement of progressively more sulphur-rich phases, Fe-monosulphide → greigite → pyrite (e.g. Berner 1970; Rickard and Luther 1997). The formation of Fe-monosulphide and pyrite require reducing conditions, whereas greigite formation requires weakly oxidising conditions in order to supply sulphur intermediates, like elemental sulphur and polysulphides (Raiswell 1982; Canfield and Thamdrup 1994; Wilkin and Barnes 1996; cf. Millero 1991; Rickard and Luther 1997).

The sites of maximum simultaneous production rates of these reactants are at the redox boundary, which separates oxygen-bearing and hydrogen sulphide-bearing waters (e.g. Jorgensen et al. 1991; Wilkin et al. 1996; Wilkin and Barnes 1997). These redox boundaries are normally located within a few centimetres beneath the sediment/water interface. However, in restricted (silled) basins and where mixing of water masses is limited, the oxygen renewal rate to bottom waters can be less than the rate of organic matter oxidation. Consequently the redox boundaries can move upward above the bottom sediments into the water column and therefore the locus of pyrite formation (e.g. Wilkin et al. 1996). At these settings, pyrite framboids are unable to reach appreciable sizes before they sink to the sea bed as a result of pyrite hydrodynamic instability in the water column (Wilkin et al. 1996). Additional confirmation that pyrite framboids are not formed in the sediment overlain by euxinic water column comes from sulphur isotopes. The sulphur isotopic composition of pyrite framboids found suspended and in laminated sediments (top 30 cm) in the Black Sea, are characterised by sulphur isotopic compositions that resemble dissolved sulphide just below the chemocline, heavier by 4-7 ‰ relative to deep-water dissolved sulphide (Muramoto et al. 1991; Lyons and Berner 1992; Calvert et al. 1996).

A detailed study of pyrite framboid sizes was conducted by Wilkin et al. (1996) from recently deposited sediments in euxinic (e.g. the Black Sea and Framvaren Fjord, Norway), dysoxic (Peru Margin) and oxic (e.g. Wallops Island, Virginia, USA) environments. The average framboid diameter in euxinic

sediments is 5.0 μm , whilst in dysoxic and oxic sediments is 7.7 μm . Framboid size in euxinic sediments is also characterised by a narrow size distribution (fewer than 4% of framboids are $>10 \mu\text{m}$) and consequently have a smaller standard deviation ($\pm 1.7 \mu\text{m}$), whereas framboid diameter in dysoxic and oxic sediments have a broader size distribution (10-50% of framboids are $> 10 \mu\text{m}$) and consequently have a larger standard deviation ($\pm 4.1 \mu\text{m}$). Pyrite framboid size-distributions therefore can help to reconstruct redox conditions for ancient sedimentary rocks.

In order to investigate redox-conditions in this study using this technique, eight samples (6 from the Athel Silicilyte [silica-rich facies] and two from the U Shale [silt-rich facies]) were selected for detailed framboidal pyrite size-distributions. Pyrite size was measured from the prepared thin sections using electronic microscopic analysis (each sample was analysed over 5-10 closely spaced 15-25 mm vertical transects; section 2.3.4). At least 100 pyrite framboids were measured from each sample to ensure a maximum accuracy of pyrite framboids size-distributions (Fig. 5.23).

Detailed SEM analysis reveals that there is no secondary pyrite growth in the framboids, resulting in the preservation of the primary textures (Fig. 5.22). All analysed samples from the silica- and the silt-rich facies are characterised by very small average framboid diameters, range from 3.4 to 4.0 μm (Fig. 5.23). Less than 5 % of the measured framboids have diameter-size more than 7 μm and therefore they are characterised by very narrow size distribution, standard deviations range from 1.1 to 1.5 (Fig. 5.23).

The absence of secondary pyrite growth and the preservation of original framboid textures in the silica- and in the silt-rich facies suggest that framboids did not continue to grow at deeper burial depths during mid-late diagenesis. Consequently their size distributions can be used to interpret the redox conditions during deposition. The small size and narrow distribution of pyrite framboid from the silica- and the silt-rich facies are interpreted to be a result of: 1) short growth times of pyrite framboids in the water column as a result of their hydrodynamic instability, or 2) lack of reduced sulphur and/or iron. Lack of

reduced sulphur is unlikely since the oil produced from the Athel is S-rich (1.5 mol % H₂S; Alixant et al. 1998), suggesting that reduced sulphur was available, in order to incorporate into organic carbon. The contents of pyrite in the silt-rich facies (average = 8 wt. %) is higher than in the silica-rich facies (average of LF1-LF3 = 4 wt. %), and consequently reducible iron availability was likely to be higher during silt-rich facies deposition. However, the average pyrite framboid size does not vary significantly between the silica- and the silt-rich facies (Fig. 5.23), and therefore the availability of reduced iron was unlikely controlled pyrite size, but likely to have controlled pyrite proportions. The small size framboidal pyrite in the silica- and in the silt-rich facies therefore probably resulted from short growth times at the redox-boundary that was likely to have been located in the water column. Consequently, pyrite framboid hydrodynamic instability in the water column led to short growth times, before they sank and ceased to grow. Small sizes of pyrite framboids throughout the Athel Silicilyte stratigraphic section in well ALNR-2 (Fig. 5.23) could indicate that the redox boundary was located in the water column throughout Athel Silicilyte precipitation.

The results from REE, redox-sensitive elements and pyrite framboid size distributions all point to euxinic conditions during Athel Silicilyte precipitation. These euxinic conditions were likely extended to the water column in the mini-basins within the Athel Basin (Fig. 3.6 & 5.25). Such conditions most likely resulted from the dominant role of sulphate reducing bacteria that were mineralising the organic matter during Athel Silicilyte precipitation. Further support for this conclusion comes from the strong segregation in $\delta^{34}\text{S}$ between sulphate [37.7 ‰ CDT] and sulphide [0.81 ‰ CDT]) and the increase in $\delta^{98/95}\text{Mo}$ from 0.79 to 1.30 [J&M Mo standard] at the base of the U Shale and throughout the Athel Silicilyte (reviewed in section 3.7; Schröder et al. 2004; Wille et al. 2008;). The dominate process of sulphate reduction bacteria may have led to the strong segregation in sulphur isotopes (light sulphur isotopes in hydrogen sulphide incorporated into pyrites and heavy sulphur isotopes incorporated into sulphate minerals), and may also have resulted in the enrichment of bottom waters with dissolved hydrogen sulphide that caused the removal of Mo isotopes without fractionation from the water column (Arnold et

al. 2004), and hence the spike in $\delta^{98/95}\text{Mo}$. In addition, the time-equivalent shallow water carbonates (A4C) record negative $\delta^{13}\text{C}_{\text{carb}}$ values (from +2 ‰ to -6 ‰ [PDB]) that lasted for around one million years, as well as record the disappearance of marine fossils (*Cloudina* and *Namacalathus*) at this time (section 3.7 & 3.8; Amthor et al. 2003). This negative carbon isotope excursion has been interpreted as being due to the overturn or expansion of the euxinic bottom waters enriched with light carbon (^{12}C), thus affecting the A4C isotopic record. The disappearance of sessile shallow marine organisms could therefore have been caused by the expansion of toxic hydrogen sulphide-rich bottom waters (Wille et al. 2008). The record of anoxia in the shallow water carbonates could suggest that the euxinic conditions in the mini-basins were very extreme during Athel Silicilyte precipitation. In addition, these biogeochemical observations (S, C and Mo isotopes) and marine fossil extinction in the South Oman Salt Basin have been recorded globally in Precambrian-Cambrian strata, which has led previous workers to suggest a global anoxia at this time (Brasier 1989; Kimura et al. 1997; Knoll and Carroll 1999; Kimura and Watanabe 2001; Amthor et al. 2003; Schröder and Grotzinger 2007; Wille et al. 2008; Halverson et al. 2009).

6.6 Summary

The main findings of this chapter are:

- Elemental concentrations show a very good agreement with the mineralogical compositions identified in Chapter 5. The silica-rich facies are characterised by high SiO_2 concentrations and low concentrations of detrital parameters, whereas silt-rich facies show higher concentrations of detrital parameters.
- The variations of elemental concentrations stratigraphically in well ALNR-2 are also consistent with the lithofacies vertical variability. Since only short intervals were sampled from the other wells, lateral variability cannot be confirmed using elemental concentrations.
- Major element and REE results do not suggest a hydrothermal source for the silica in the Athel Silicilyte. The REE results in the Athel Silicilyte show characteristics similar to modern seawater, and therefore the Athel Silicilyte

could reflect a seawater precipitate. Hence, silica present in the Athel Silicilyte was likely to have been derived from seawater.

- The strong enrichments of the redox-sensitive elements, Ce anomalies, weak LREE-depletion and the pyrite framboid size-distribution throughout Athel Silicilyte succession, suggest that the water column was euxinic. In addition, these observations also recorded in the studied interval (≈ 10 m thick) of the U Shale, suggest euxinic conditions also existed during its interval of deposition.

Chapter 7.

Origin of the Athel Silicilyte

7.1 Introduction

Detailed petrographical analysis, wireline log interpretation and trace element analysis outlined in Chapters 5 and 6 were used to sedimentologically and geochemically characterise the Athel Silicilyte and its spatial distribution in the Athel Basin. The results from these analyses reveal that the Athel Silicilyte comprises of up to 390 m of microbially laminated microcrystalline quartz, with minor amounts of detrital quartz that are loosely packed, clay minerals, pyrite and organic carbon (section 5.2.1; Table 5.1). In addition, the Athel Silicilyte shows strong enrichments of redox-sensitive elements, positive Ce anomalies and narrow size distributions of framboidal pyrites (section 5.3 and 6.3.2). These results together have been used to argue that the Athel Silicilyte precipitated syndepositionally during very low detrital input euxinic conditions (section 5.2.1 and 6.5).

This chapter builds on this interpretation to determine the possible sources of silica in the Athel Silicilyte and silica precipitation mechanism. This discussion is further constrained by performing mass-balance calculations to estimate the mass of silica required to form the Athel Silicilyte, and the likely mass of silica that would have been released from the silicate mineral transformation reactions in this setting during burial. Reaction path modelling results (using Geochemist's Workbench software; section 2.6) are also included in this chapter, in order to test how sulphate reduction might constrain the pH of the bottom seawater column, and how microbial respiration might influence silica precipitation reactions in this context.

7.2 Silica source

The possible sources of silica present in cherts found in sedimentary strata of Proterozoic and Phanerozoic ages were reviewed in section 4.3, and are: 1) dissolution of siliceous organism tests (e.g. radiolaria, diatoms and sponges), 2) direct precipitation from silica-rich hydrothermal fluids, 3) silica release during burial from either silicate mineral dissolution (e.g. feldspar /muscovite dissolution) or another silicate mineral transformation (e.g. smectite

transformation to illite and/or illite transformation to muscovite), and 4) direct precipitation at low temperatures from a dissolved silica-rich water column (e.g. from either marine or lacustrine waters). These possible sources are discussed in terms of their suitability for the precipitation of the Athel Silicilyte below.

In the absence of mineralised skeletal remains within any sample of the Athel Silicilyte, a biogenic source for the silica seems unlikely. The Athel Silicilyte has been dated at the Precambrian-Cambrian boundary (Amthor et al. 2003; Bowring et al. 2007), prior to the major evolution of silica-secreting organisms (Siever 1992; Maliva et al. 2005). Therefore, the silica present in the Athel Silicilyte does not favour the dissolution of biogenic precursor. Although siliceous sponge spicules have been found in some Ediacaran-aged sediments (Gehling and Rigby 1996; Brasier et al. 1997), they are volumetrically insignificant and therefore unlikely to have played a major role in silica precipitation until at least the Late Ordovician (discussed previously in Chapter 4, section 4.4 ; Maliva et al. 1989; Kidder and Erwin 2001).

Evidence for a hydrothermal source was considered in Chapter 6 (section 6.4.3) using the geochemical data (major elements and REEs) collected in this study. These data are inconsistent with a hydrothermal source. In particular: 1) major element ratios ($\text{Al}_2\text{O}_3/[\text{Al}_2\text{O}_3 + \text{Fe}_2\text{O}_3 + \text{MnO}]$ and $\text{Fe}_2\text{O}_3/\text{TiO}_2$) are inconsistent with those found in cherts that precipitated from hydrothermal fluids at the spreading-ridges (Fig. 6.4; Bonatti 1983; Adachi et al. 1986); and 2) the absence of hydrothermal REE characteristics (Eu anomalies and LREE-enrichments; Fig. 6.10 & 6.11; e.g. German et al. 1990), and therefore a hydrothermal origin for the Athel Silicilyte is ruled out.

Silica sourced from silicate mineral dissolution/transformation is likely to be significant in silicate mineral-rich successions beneath at least 1 km burial depth (e.g. Murray et al. 1992; Maliva 2001; de Kamp 2008). Cherts formed in this way are normally found replacing pre-existing minerals or occurring as a diagenetic cement (e.g. chert-shale couplet; Murray et al. 1992). The absence of any pre-existing pseudomorphs or textures within the Athel Silicilyte suggest that the silica is neither replacive nor has precipitated as a cement in the pore spaces

during early-late diagenesis. The Athel Silicilyte therefore was unlikely sourced from silica released during silicate minerals dissolution and diagenesis. This interpretation is further supported by mass-balance calculations in section 7.2.1 below.

Given that the Athel Silicilyte is a syndepositional precipitate (based on the preservation of homogeneous laminated fabric, loose packing of detrital grains and association with syngentic pyrite; section 5.2.1), the possibility that the Athel Silicilyte precipitated directly from the water column can be explored. Such an interpretation is consistent with the previous REE observations discussed in Chapter 6 (section 6.4.3). The REE characteristics of the Athel Silicilyte mimic seawater precipitates, including LREE-depletion and positive La, Eu, Y anomalies (Fig. 6.11; section 6.4.3; e.g. Elderfield 1988; McLennan 1989; Webb and Kamber 2000; Bolhar et al. 2004; Friend et al. 2008). There is therefore good support for the notion that silica in the Athel Silicilyte was derived directly from Precambrian seawater. It has long been recognised that Precambrian seawater must have been rich in dissolved silica compared to modern seawater as a result of the absence of any effective biogenic mechanism for silica removal (Siever 1991; Siever 1992; Saylor et al. 1998; Maliva et al. 2005; Perry and Leticariu 2007). Values of 60-140 ppm of dissolved silica have been proposed for Precambrian seawater (Siever 1992; Morris 1993). These figures are estimated based on experimental determinations of solubility and silica sorption on clay minerals and zeolites, which were likely to have been a major sink for dissolved silica in the Precambrian oceans (Siever 1992).

The next question is whether the available dissolved silica-rich seawater mass in the Athel Basin was sufficient to supply the silica mass in the Athel Silicilyte. In order to answer this question, it is vital to broadly estimate the silica mass present in the Athel Silicilyte and then the corresponding required seawater mass can be determined at various silica concentrations (at 60, 100 and 140 ppm) that could possibly exist in the Athel Basin. After estimating the required seawater mass, the available seawater mass in the Athel Basin can be estimated in order to investigate if it was enough to precipitate the silica present in the

Athel Silicilyte. The necessary mass-balance calculations required to answer the above questions are discussed in the following section.

7.2.1 Mass-balance calculations

Silica mass in the Athel Silicilyte

In order to broadly estimate the mass of silica in the Athel Silicilyte, various parameters are constrained. These parameters are summarised in Table 7.1 and reviewed in the following paragraphs.

1) *Areal distribution of the Athel Silicilyte*: in order to estimate the area where the Athel Silicilyte is present, a palaeogeographical map of the Athel Basin was used (Fig. 7.1; Amthor et al. 2005). Within the Athel Basin, the Athel Silicilyte is only present in the deepest parts of the basin in the fault-bounded mini-basins (section 5.4; Fig. 3.5 & 7.1). Whereas, on the intrabasinal highs, the Athel Silicilyte is not encountered and is assumed not to accumulate (Fig. 7.1). This interpretation is suggested by the drilled wells in the mini-basins (Fig. 5.2) that encountered the Athel Silicilyte, whereas wells that were drilled in the intrabasinal high areas encountered no Athel Silicilyte (e.g. well ALKZ-1 and ALFR-1; section 5.4). Therefore, the deep areas in the palaeogeographical map, where the Athel Silicilyte is likely present aided by the locations of drilled wells, are considered in this calculation (Fig. 7.1). The deepest areas are shown in blue and dark green colour in Fig. 7.1 within the dashed line. The estimation of the area where the Athel Silicilyte might be present (blue and dark green areas) can be quite erroneous given the limited number of drilled wells. To account for this uncertainty, a low, medium and high case are estimated, where the low case only considers blue areas ($\approx 20\%$ of the total area), the high case considers blue and dark green areas ($\approx 40\%$ of the total area) and the medium case is the average of the low and the high case. The total estimated area for the low case is $0.86 \times 10^9 \text{ m}^2$, the medium case is $1.29 \times 10^9 \text{ m}^2$ and the high case is $1.72 \times 10^9 \text{ m}^2$.

2) *The average thickness of the Athel Silicilyte*: based on the interpreted wells from the Athel Basin shown in Fig. 5.2, the Athel Silicilyte has a thickness

range from 166 to 390 m from nine wells (TL-2, MM-248, MMNW-7, ASH-3, ASH-4, ALNR-2, ALNR-3, ALNR-4 and ALSE-1). These wells are included in the well-correlation (Fig. 5.2) and likely define the thickness of the Athel Silicilyte on the basin margins and in the basin centre. The average calculated thickness from these nine wells is 279 ± 91 m. A low and high case are calculated by subtracting and adding standard deviation value, respectively, and the medium case is the average thickness (low = 188, medium = 279 and high = 370 m).

- 3) *The volume of microcrystalline quartz in each lithofacies:* petrographical techniques indicate that microcrystalline quartz is only present in microcrystalline quartz-rich lithofacies (LF1), microcrystalline quartz-dominated lithofacies (LF2), microcrystalline quartz-rich and detritus-bearing lithofacies (LF3) and in microcrystalline-, carbonate- and detritus-bearing lithofacies (LF9; section 5.2; Table 5.1). The average proportions in each lithofacies were semiquantitatively estimated using XRD and point count data (Table 5.1; section 5.2). The average microcrystalline quartz content in LF1 is 83 ± 2.7 wt. % (ranging from 79 to 88 wt. %), LF2 is 91 ± 1.6 wt. % (ranging from 90 to 94 wt. %), LF3 is 72 ± 5.8 wt. % (ranging from 52 to 87 wt. %) and in LF9 is 31 ± 12.6 wt. % (ranging from 16 to 66 wt. %; Table 7.1).
- 4) *Proportions of lithofacies containing microcrystalline quartz in the Athel succession:* since the microcrystalline quartz content in each lithofacies varies significantly, it is important to estimate the proportion of each lithofacies in the Athel Silicilyte succession. The average proportion of microcrystalline quartz in microcrystalline quartz-rich lithofacies is 39.2 ± 14.0 % (ranging from 18 to 60 %), microcrystalline quartz-dominated lithofacies is 1.61 ± 2.3 % (ranging from 0 to 6 %), microcrystalline quartz-rich and detritus-bearing lithofacies is 52.3 ± 12.7 % (ranging from 26 to 65 %) and in microcrystalline-, carbonate- and detritus-bearing lithofacies is 1.14 ± 0.6 % (ranging from 0.3 to 2 %; Table 7.1). The proportions of each lithofacies in each well are shown in Fig. 5.2.

5) *Average porosity of each lithofacies*: the porosity present in each lithofacies represents unfilled volume and therefore its presence may significantly affect the total volume of the rock. In order to account for this potential source of error, the average helium core plug porosity for each lithofacies was used (Table 7.1). The average helium porosity in microcrystalline quartz-rich lithofacies is 17.3 ± 7.0 % (ranging from 7.1 to 26.9 %), microcrystalline quartz-dominated lithofacies is 6.4 ± 6.2 % (ranging from 0.3 to 9.4 %), microcrystalline quartz-rich and detritus-bearing lithofacies is 19.6 ± 4.5 % (ranging from 8.0 to 34.0 %) and microcrystalline-, carbonate- and detritus-bearing lithofacies is 4.9 ± 2.9 % (ranging from 0.9 to 10.8 %; Table 7.1). The only porosity present here is intercrystalline porosity and no secondary porosity is observed from the petrographical analysis.

Using the above parameters, the volume of the silica present in the Athel Silicilyte can be estimated using the equation below:

$$\text{volume (m}^3\text{)} = \text{area (m}^2\text{)} \times \text{average thickness (m)} \times \text{proportion of each lithofacies (\%)} \times \text{quartz contents (\%)} \times (1 - \text{porosity})$$

After that, the mass of silica can be calculated using the equation below:

$$\text{mass (kg)} = \text{volume (m}^3\text{)} \times \text{density (kg/m}^3\text{)}, \text{ where quartz density} = 2650 \text{ kg/m}^3$$

The total silica mass present in the Athel Silicilyte is calculated using low, medium and high case values of the total area and thickness. Since the other parameters are proportional, they can add up to more or less than 100 % if their maximum/minimum values are used. Thus, their average values are used for the three cases. These calculations show that the total mass of silica in the Athel Silicilyte is 25.2×10^{13} kg for the low case, 56.2×10^{13} kg for the medium case and 99.2×10^{13} kg for the high case (Table 7.1).

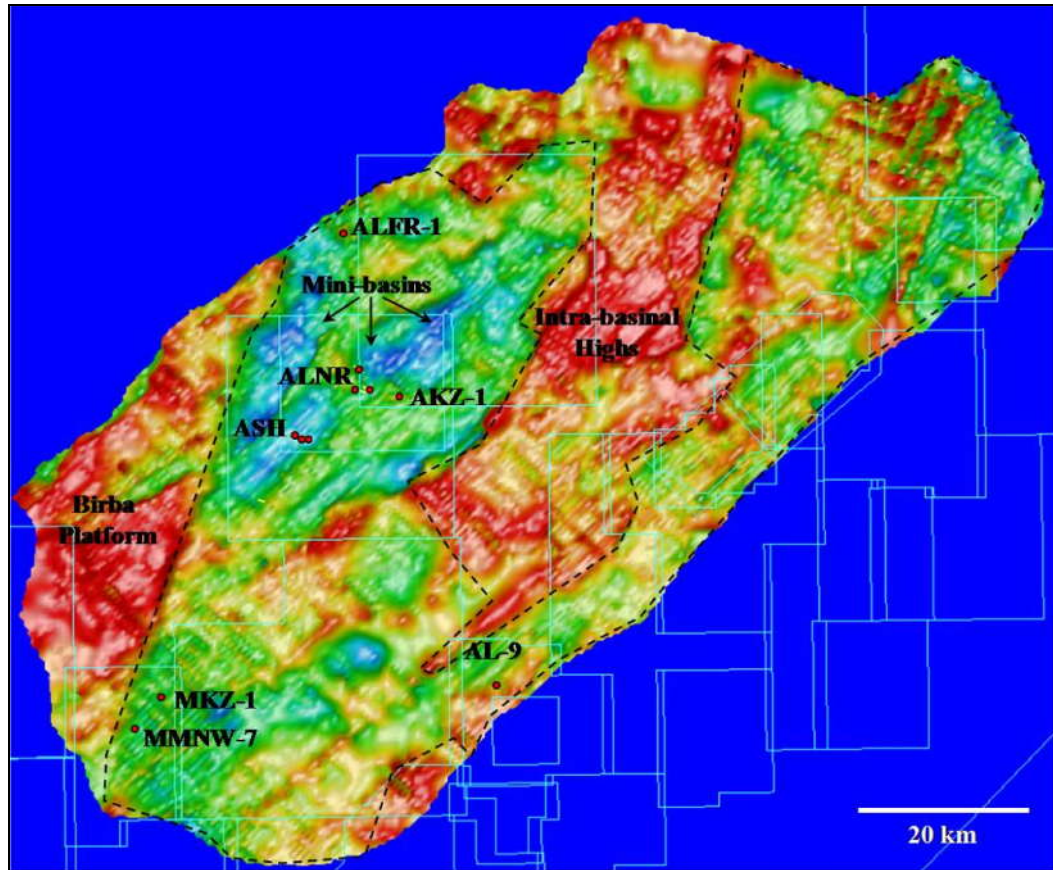


Figure 7.1. Paleotopographical map of the Athel Basin based on regional 3D-seismic data. This map shows Birba Platform and intra-basinal high in red. The deep basin is in blue and dark green. The Athel Silicilyte is only present in the deepest parts of the basin (in the mini-basins). Note AKZ-1 and ALFR-1 encounter no Athel Silicilyte due to the presence of topographical high areas (yellow colour) within the Athel Basin (Fig. 5.1). The estimated area within the dashed line where the Athel might be present is roughly 20 % for the low case (only blue areas are considered) and 40 % for the high case (blue and dark green areas are considered), the medium case is the average of the low and the high case. The total area estimated is $0.86 \times 10^9 \text{ m}^2$ for the low case, $1.29 \times 10^9 \text{ m}^2$ for the medium case and $1.72 \times 10^9 \text{ m}^2$ for the high case. Modified after Amthor et al. (2005).

Silica mass released from silicate minerals

In order to test the hypothesis that silicate mineral dissolution/diagenesis were not a major source for the silica in the Athel Silicilyte, the mass of silica released from silicate minerals was estimated and compared to the silica mass in the Athel Silicilyte.

Silica can be released during the transformation of smectite to illite and illite to muscovite as well as the transformation of feldspar to kaolinite (e.g. Lynch et al. 1997; Wilkinson et al. 2001; de Kamp 2008). The released silica can be precipitated as cement or as chert-rich layers during diagenesis. The low volumes of feldspar and kaolinite minerals in the Athel Silicilyte suggest that

feldspar diagenetic reactions were not a significant silica source, and consequently it is not considered further. Since the petrographical and XRD results indicate that the predominate clay mineral present in the Athel Silicilyte is illite, only the smectite to illite diagenetic reaction is considered as a possible source of silica. Further transformation of illite to muscovite is not discussed since muscovite was not identified within this study. The transformation of illite to muscovite takes place in temperatures ranging from 190 to 500 °C (e.g. de Kamp 2008), whereas the maximum temperature during Athel Silicilyte burial did not exceed 120 °C (Amthor et al. 2005). This low temperature most likely caused by the salt that enclosed the Athel Silicilyte (Fig. 1.2). Salt has a high thermal conductivity (e.g. Mello et al. 1995; Warren 2006) and consequently the Athel Silicilyte is kept relatively cool compared to other non-intra salt rocks that are buried at similar depths.

The total mass of illite in each lithofacies was calculated following the same steps as for calculation of the silica mass, with substitution of the average illite content and illite density (2770 kg/ m³). The average illite content in microcrystalline quartz-rich lithofacies is 6 ± 0.9 wt. % (ranging from 4 to 8 wt. %), microcrystalline quartz-dominated lithofacies is 4 ± 1.16 wt. % (ranging from 2 to 6 wt. %), microcrystalline quartz-rich and detritus-bearing lithofacies is 12 ± 4.2 wt. % (ranging from 6.0 to 29.0 wt. %) and microcrystalline-, carbonate- and detritus-bearing lithofacies is 12 ± 4.9 wt. % (ranging from 6 to 19.0 wt. %; Table 7.1). These average values yielded a total mass of illite in the Athel Silicilyte of 3.22 × 10¹³ kg for the low case, 7.21 × 10¹³ kg for the medium case and 12.7 × 10¹³ kg for the high case. Quantitative analysis of smectite to illite transformation indicates that each 100 g of smectite releases 71.5 g illite and 18 g silica (de Kamp 2008). Based on this quantitative analysis and the estimated illite mass in the Athel Silicilyte, the mass of smectite and consequently the mass of silica released can be estimated. Calculations show that the total mass of silica released from the smectite to illite transformation is 0.81 × 10¹³ kg for the low case, 1.8 × 10¹³ kg for the medium case and 3.2 × 10¹³ kg for the high case (Table 7.1). The released silica mass would therefore accounts for only 3.21 % (average silica mass released/ average silica mass required) of the silica mass in the Athel Silicilyte. Therefore, clay mineral diagenetic reactions are unlikely to be a major

source for the silica in the Athel Silicilyte, consistent with petrographical observations that suggest the Athel Silicilyte precipitated syndepositionally before major burial diagenesis reactions took place (section 5.2.1).

Table 7.1. Shows the different parameters used in the mass-balance calculations.

		LF1 ¹	LF2 ¹	LF3 ¹	LF9 ¹	Total
Microcrystalline quartz contents (wt. %)		83	91	72	31	
Illite (wt. %)		6	4	12	12	
Proportion in the Athel succession (%)		39	2	52	1	
Porosity (%)		17	6	20	5	
Thickness (m)	L ²	74	3	98	2	
	M ²	109	4	146	3	
	H ²	145	6	194	4	
Volume ($\times 10^{11}/\text{m}^3$)	L	0.63	0.03	0.85	0.02	
	M	1.40	0.06	1.90	0.04	
	H	2.50	0.10	3.30	0.07	
Silica mass in the Athel Silicilyte ($\times 10^{13}/\text{kg}$)	L	11.5	0.60	13.0	0.14	25.2
	M	25.7	1.31	28.9	0.32	56.2
	H	45.4	2.31	51.1	0.57	99.3
Illite mass ($\times 10^{13}/\text{kg}$)	L	0.87	0.03	2.26	0.06	3.22
	M	1.94	0.06	5.03	0.13	7.16
	H	3.43	0.11	8.90	0.23	12.7
Smectite mass ($\times 10^{13}/\text{kg}$)	L	1.22	0.04	3.16	0.81	4.50
	M	2.71	0.08	7.04	1.80	10.0
	H	4.80	0.15	12.4	3.20	17.7
Silica released from smectite to illite transformation ($\times 10^{13}/\text{kg}$)	L	0.22	0.01	0.57	0.02	0.81
	M	0.49	0.02	1.27	0.03	1.80
	H	0.86	0.27	2.24	0.06	3.19

¹ LF1: microcrystalline quartz-rich lithofacies, LF2: microcrystalline quartz-dominated lithofacies, LF3: microcrystalline quartz-rich and detritus-bearing lithofacies and LF9: microcrystalline-, carbonate- and detritus-bearing lithofacies.

² L: Low case, which is calculated based on area of $0.86 \times 109 \text{ m}^2$ and total Athel Silicilyte thickness of 188 m. M: Medium case, which is calculated based on area of $1.29 \times 109 \text{ m}^2$ and total Athel Silicilyte thickness of 279 m. H: High case, which is calculated based on area of $1.72 \times 109 \text{ m}^2$ and total Athel Silicilyte thickness of 370 m. The average values are used for the other parameters in estimating silica mass in the Athel Silicilyte and the silica mass released from the smectite to illite transformation.

7.2.2 Required vs. available seawater mass

The required volumes of seawater needed to precipitate the silica mass present in the Athel Silicilyte can be estimated at various concentrations of silica in seawater using the following equation: water mass required (kg) = mass of silica in the Athel Silicilyte (kg)/ silica concentrations (kg/ litre), where 1 litre of

seawater = 1 kg and 1 ppm = 1×10^{-6} kg/ litre. It is not unreasonable to assume that silica concentrations in ambient seawater during precipitation of the Athel Silicilyte were in the range of silica concentrations proposed for Precambrian seawater (60-140 ppm; Siever 1992; Morris 1993). Therefore, concentrations of 60, 100 and 140 ppm are used to estimate the water mass required to precipitate the low, the medium and the high case silica mass in the Athel Silicilyte. Calculations show that the water mass required ranges from 1.8×10^{18} kg (low case silica mass at highest silica concentration of 140 ppm) to 16.6×10^{18} kg (high case silica mass at lowest silica concentration of 60 ppm) with an average of 5.62×10^{18} kg (medium case silica mass at medium silica concentration of 100 ppm). These results are summarised in Table 7.2.

The water mass in the Athel Basin must be estimated in order to test if the required water masses were available during Athel Silicilyte precipitation. The available water mass in the Athel Basin depends on its area and the water depth during the Athel Silicilyte precipitation. The basin area considered in this calculation is the entire Athel Basin (Fig. 5.1). Although the Athel Silicilyte is only present in the deepest parts of the Athel Basin, this estimation is realistic for the water mass since dissolved silica diffuses to depths of lower concentrations (i.e. depths where silica was precipitating). The dimensions of the Athel Basin are roughly 6.0×10^4 by 20.0×10^4 m (Fig. 5.1). The water depth, however, is hard to constrain given the presence of deep mini-basins and intra-basinal highs within the Athel Basin (Fig. 7.1). Reconstruction of the Athel Basin indicates that the water depths exceeded 100-200 m in most of the Athel Basin and may have exceeded 300-400 m in the mini-basins (Fig. 3.5; Section 3.5; Amthor et al. 2005).

Given these uncertainties for the water depth, the water mass is estimated at various depths (100 m, 200 m and 300 m) and the water mass available at these depths are 1.2×10^{15} kg, 2.4×10^{15} kg and 3.6×10^{15} kg, respectively, 1 m³ of seawater = 1000 kg (Table 7.2). Based on the calculation above of the seawater mass required and the seawater mass available, the silica mass present in the Athel Silicilyte is higher than the dissolved silica mass in the water column by at least 501 times (for the low case silica mass, 300 m water depth and 140

ppm silica concentration), and up to 13794 times (for the high case silica mass, 100 m water depth and 60 ppm silica concentration) with an average of 2340 times (for the medium case silica mass, 200 m water depth and 100 ppm silica concentration; Table 7.2).

Table 7.2. Shows required water masses, available water masses and their ratios at various concentrations (60 ppm, 100 ppm and 140 ppm) and depths (100 m, 200 m and 300 m) for the low case (L), the medium case (M) and the high case (H) silica mass.

		60 ppm	100 ppm	140 ppm
Required water mass at various concentrations (kg)	L	4.21×10^{18}	2.52×10^{18}	1.80×10^{18}
	M	9.36×10^{18}	5.62×10^{18}	4.01×10^{18}
	H	16.6×10^{18}	9.93×10^{18}	7.09×10^{18}
		100 m	200 m	300 m
Available water mass at various depths (Kg)		1.20×10^{15}	2.40×10^{15}	3.60×10^{15}
Water mass required/ water mass available ratios (at various concentrations and depths)¹				
		60 ppm	100 ppm	140 ppm
100 m	L	3504	2103	1502
	M	7801	4681	3343
	H	13794²	8276	5912
200 m	L	2103	1051	751
	M	4681	2340³	1672
	H	8276	4138	2956
300 m	L	1168	701	501⁴
	M	2600	1560	1114
	H	4598	2759	1971

¹ This is also the silica mass in the Athel Silicilyte /dissolved silica mass in the water column. These ratios indicate how many extra water masses are required to precipitate the silica present in the Athel Silicilyte.

² The maximum extra water mass required for the high case silica mass at lowest silica concentration (60 ppm) and minimum water depth (100 m).

³ The average extra water mass required for the medium case silica mass at average silica concentration (100 ppm) and average water depth (200 m).

⁴ The minimum water mass required for the low case silica mass at highest silica concentration (140 ppm) and maximum water depth (300 m).

Clearly the estimated available masses of dissolved silica in the water column at one time were much less than the silica mass in the Athel Silicilyte. Nevertheless, the Athel Basin was connected to the open ocean during the Athel Silicilyte precipitation (section 3.5; Mattes and Morris 1990; Amthor et al. 2005; Schröder et al. 2005; Schröder and Grotzinger 2007) and therefore the dissolved silica could have been continuously supplied from the open ocean. The marine connection likely restored ambient seawater composition in the Athel Basin. It is therefore necessary to determine whether ambient seawater composition in the Athel Basin was renewed sufficiently frequently to supply the necessary silica

mass for Athel Silicilyte precipitation. The renewal rate of the seawater composition depends on the renewal time (seawater age). By identifying ambient seawater renewal time and the duration of the Athel Silicilyte precipitation (i.e. duration of half A4 cycle), the number of times that the composition had been renewed can be estimated. This is discussed in the following section.

7.2.3 Seawater renewal time

The renewal time of seawater in restricted or semi-restricted basins can be defined as the time required to restore the ambient seawater composition (e.g. Algeo and Lyons 2006). The renewal time depends largely on the basin hydrography, which in turn depends on the degree of the basin restriction from the open oceans (Stigebrandt and Molvaer 1988; Holmen and Rooth 1990; Millero 1996). Highly restricted basins such as the Black Sea have long renewal times (> 500 years), whilst weakly restricted basins such as Saanich Inlet have short renewal times (< 2 years; Algeo and Lyons 2006). These modern restricted basins show that the amount of Mo taken up by the sediment per unit of organic carbon (Mo/TOC) positively correlates with the dissolved Mo in the water column (Algeo and Lyons 2006, p.15). For example, moving from the Black Sea to Saanich Inlet, dissolved Mo rises from < 5 % to 100 % of open ocean value ($105 \pm 5 \text{ nmol kg}^{-1}$) and (Mo/TOC)_s ratios of sediments rise from $4.5 \pm 1 \times 10^{-4}$ to $45 \pm 5 \times 10^{-4}$ (Algeo and Lyons 2006). This suggests that the removal rate of Mo from the water column is not only controlled by the redox conditions and the availability of organic matter (host phase) as discussed in Chapter 6 (section 6.2.4), but also by the supply rate of dissolved Mo from open oceans to restricted basins, which in turn depends on ambient seawater renewal times of restricted basins.

Several types of age tracers (e.g. ^{14}C and tritium) and model ages (^{226}Ra , trace elements and Si) show an inverse relationship between the (Mo/TOC)_s in the sediment and average ambient seawater renewal times (Fig. 7.2; Algeo and Lyons 2006 and references therein). This relationship is consistent with Mo uptake being controlled by the availability of dissolved Mo in the water column.

Therefore, (Mo/TOC) ratios of the Athel Silicilyte can be used to estimate the degree of restriction and average ambient seawater renewal time (Fig. 7.2).

The (Mo/TOC)_s ratio of the Athel Silicilyte is $10.9 \pm 4.86 \times 10^{-4}$ (Appendix III). Projecting this ratio in the graph of (Mo/TOC)_s against average renewal times of modern restricted basins (Fig. 7.2) can give an estimation of the average renewal time of the ambient seawater in the Athel Basin. The (Mo/TOC)_s ratio of the Athel Silicilyte yielded an average renewal time of 65 years (rangings from 25 to 300 years; Fig. 7.2) during Athel Silicilyte precipitation. The average renewal time suggests that the Athel Basin was less restricted than the Black Sea, which is reasonable since the present day Black Sea is completely restricted, whilst the Athel Basin during Athel Silicilyte precipitation was connected to the open ocean, during relative sea-level rise (section 3.5 & 5.4; Mattes and Morris 1990; Amthor et al. 2005; Schröder et al. 2005).

To estimate how many times the water mass in the Athel Basin was renewed based on the average renewal time, the duration of Athel Silicilyte precipitation must be estimated. The duration of the half A4 cycle was estimated by U/Pb age from two ash beds found at the top of A3C cycle and at the base of A4C cycle (Fig. 3.2; section 3.6), suggesting a duration of half A4 cycle ranges from 1.1 to 1.6 Myr (Bowring et al. 2007). The Athel Silicilyte precipitated during the A4C cycle (half cycle) and therefore Athel Silicilyte precipitation could have lasted from 1.1 to 1.6 Myr. Based on the 65 years average renewal time and the duration of the half A4 cycle, the ambient seawater during Athel Silicilyte precipitation was renewed at least 16,923 times (1.1 Myr duration) to a maximum of 24,615 times (1.6 Myr duration), with an average of 20,770 times (1.35 Myr duration). The minimum number of ambient seawater renewal events (16,923) is more than the maximum number of extra water masses (13,795) required to precipitate the high case silica mass (9.93×10^{14} kg) at lowest silica concentration (60 ppm) and minimum water depth (100 m; Table 7.2.). This suggests that the minimum number of renewal events that restored ambient seawater composition was enough to precipitate silica mass in the Athel Silicilyte.

The effectiveness of silica removal from the ambient seawater can be estimated by dividing the average extra seawater masses required (2,340; Table 7.2) over the average number of renewal events (20,770). The estimated effectiveness of silica removal from the water column is around 11 % of the total available dissolved silica. The removal of 11 % of the dissolved silica from the ambient seawater seems a very reasonable amount given that experimental works utilising microbial mats that removed similar amounts (15-25 %) of dissolved silica within 30 hours from solutions contain 150-400 ppm dissolved silica (Birnbaum and Wireman 1985; Birnbaum et al. 1989; Amores and Warren 2007).

The events that restored ambient seawater compositions in the Athel Basin could also have supplied dissolved oxygen to the deep water. However, redox-sensitive elements, Ce anomalies and small-narrow size distributions of pyrite framboids suggest that the water column was euxinic throughout the Athel succession (Chapter 6; section 6.5). These renewal events could have been only at the shallower water column (e.g. shallow storm mixing) and did not introduce dissolved oxygen to the depth where the Athel Silicilyte was precipitating. Nevertheless, dissolved silica was still supplied to precipitation depths via chemical diffusion as a result of different silica concentrations at shallow and deeper waters, where silica was removed from the water column. Alternatively, the rate of oxygen consumed by organic matter diagenesis in deep waters was likely higher than the rate of oxygen supplied, resulting in no oxygenation events recorded in the Athel Silicilyte.

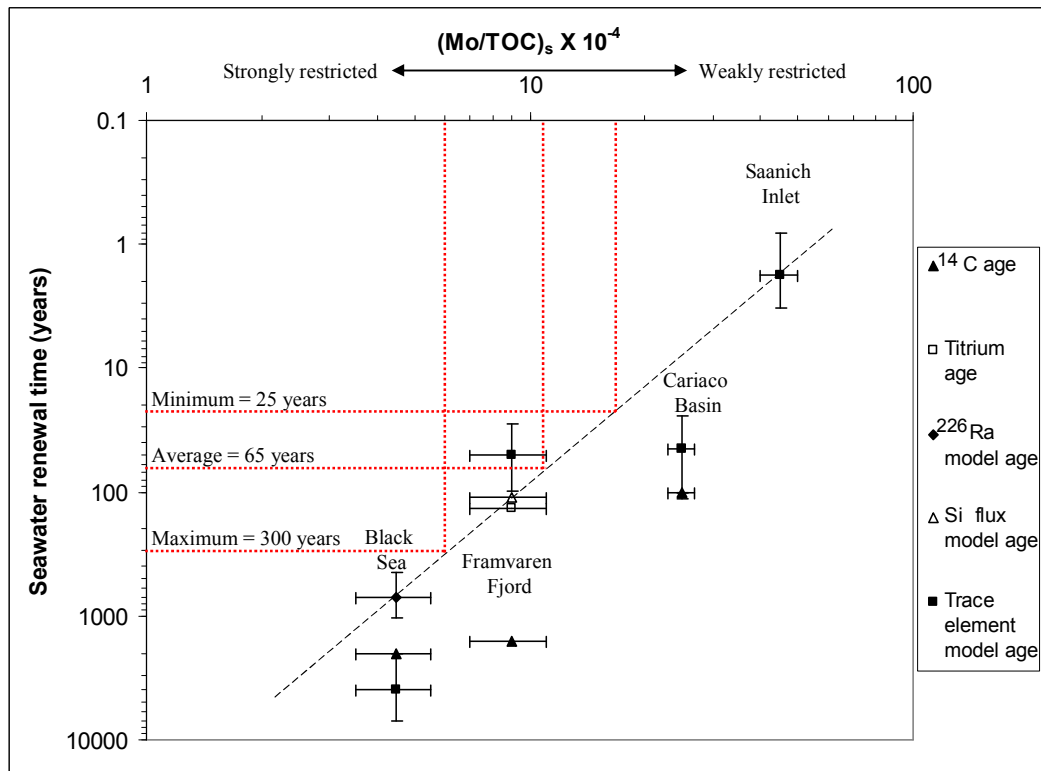


Figure 7.2. Sediment Mo/TOC ratios vs. average renewal times of modern restricted basins (Saanich Inlet, Cariaco Basin, Framvaren Fjord and Black Sea). The average renewal times were estimated using ^{14}C age tracer, tritium age trace, and model ages of ^{226}Ra , Si flux and trace elements. Red dashed lines show the Athel Silicilyte Mo/TOC ratios ($10.9 \pm 4.86 \times 10^{-4}$) and estimated renewal times (25-300 years; average ≈ 65 years), minimum and maximum renewal time was estimated by subtracting and adding standard deviation from Mo/TOC average ratio. Note the best fit line was drawn taken into account two criteria: 1) cross maximum number of points and 2) cross maximum different types of age tracers/models. Modified after Algeo and Lyons (2006).

In summary, the petrographical observations and the geochemical data suggest that the silica mass in the Athel Silicilyte was sourced from the ambient seawater. The mass-balance calculations helped to estimate the silica mass present in the Athel Silicilyte and helped to test the feasibility of the ambient seawater in the Athel Basin to source the required silica mass. These calculations are performed based on the data available for this study, which have a range of uncertainties that likely affect the final silica mass required and the water mass available. However, the mass-balance calculation results indicate that silica-rich Precambrian seawater was the most feasible source for the three cases (low, medium and high) silica mass in the Athel Silicilyte. These calculations therefore provide a confirmation to the conclusion drawn from the petrographical observations and the geochemical data that the silica mass in the Athel Silicilyte was sourced from the ambient seawater.

7.3 Precipitation mechanism

Petrographic analyses demonstrate that the Athel Silicilyte consists predominately of microcrystalline quartz, with a crystallite size ranging from 1 to 5 μm (section 5.21). The crystals are connected to one another in the form of sheets or networks of silica aggregates (Fig. 7.3 A & B), which are the dominant habit of the silica present. This habit of microcrystalline quartz suggests that silica precipitation was initiated in many places at the same time rather than being concentrated onto the surfaces of pre-existing minerals. Such a habit suggests that the ambient seawater at precipitation sites was supersaturated with respect to amorphous silica. Furthermore, this silica habit might indicate that silica precipitation was initiated by the formation of silica gel, linked nano- to micro-sized ultimately spherical particles of amorphous silica, in which there were large numbers of nucleation sites (Fig. 7.3 C & D; e.g. Iller 1979). The initial step in precipitating silica from a liquid medium to form a silica aggregate is to concentrate dissolved silica above amorphous silica solubility (120-140 ppm at 25 °C; Iller 1979). Such high silica concentrations might have not been reached or sustained during Athel Silicilyte precipitation in the ambient seawater of South Oman Salt Basin. If the silica concentrations in the ambient seawater were above amorphous silica solubility, then the Athel Silicilyte would be expected to precipitate everywhere in the South Oman Salt Basin, as well as in all previous cycles. Nevertheless, Athel Silicilyte precipitation only took place during the A4C cycle in the mini-basins (section 3.5 & 5.4; Fig. 7.1).

Therefore, there should be a mechanism responsible for concentrating dissolved silica above amorphous silica solubility in the mini-basins during Athel Silicilyte precipitation. The possible mechanisms that might have operated are high evaporation, hypersaline waters mixing with fresh water, sorption on iron oxide surfaces and/or silica precipitation related to organic matter availability and diagenesis. These mechanisms are discussed in terms of their suitability to precipitate the Athel Silicilyte in the following paragraphs.

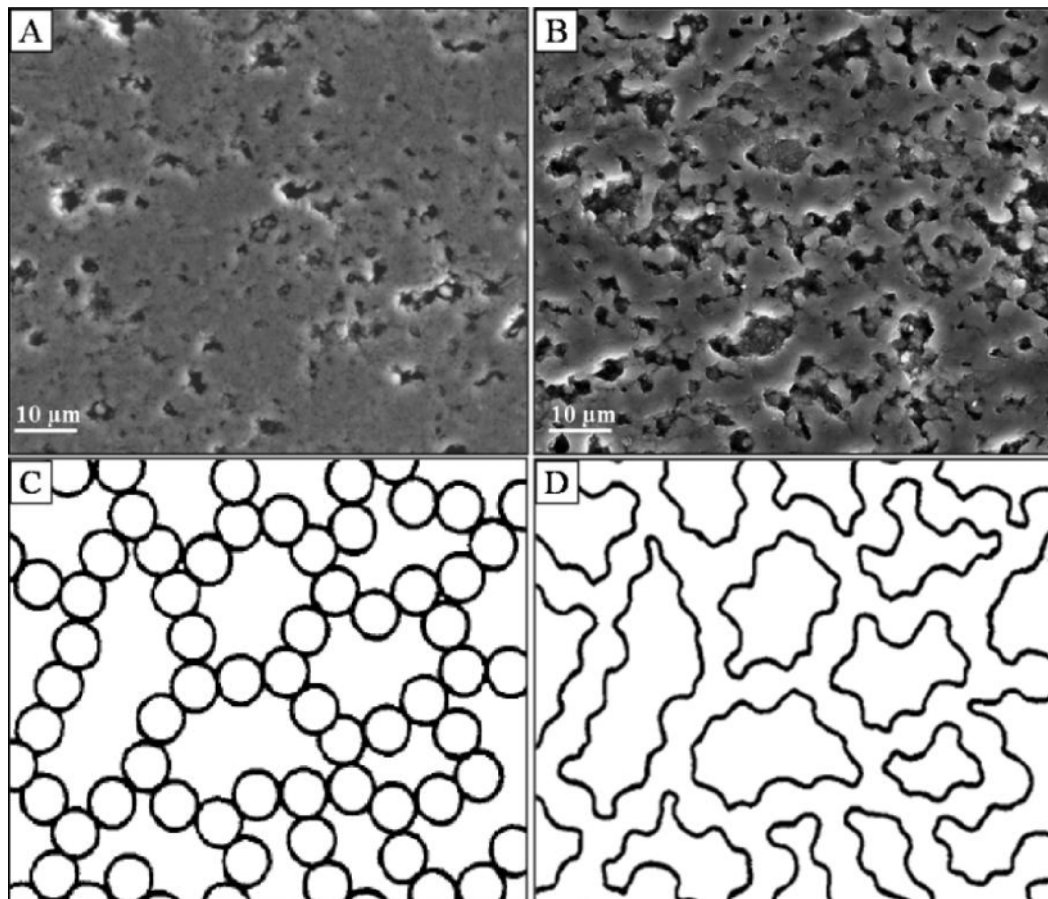


Figure 7.3. (A) and (B) secondary electron images showing microcrystalline quartz textures in forms of (A) a sheet-like and (B) linked-networks of microcrystalline quartz. Here, the individual quartz grains are hard to distinguish, but typically each crystal has a diameter ranges from 1-5 μm . (A) is from sample MK-1(4) and (B) from sample ALNR-3(13). (C) a representation showing development of spherical silica polymers with low molecular weight and (D) showing silica aggregate (gel) texture after silica polymers aggregate into three dimensional linked-network. C and D from Iller (1979).

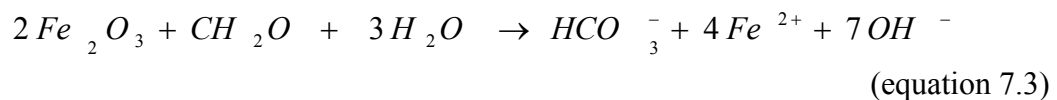
Evaporation of water bodies will result in volume reduction and dissolved silica may pass a threshold and become supersaturated. Under these supersaturated conditions, silica will precipitate in porewaters by gradually replacing evaporite minerals, possibly triggered by mixing with less saline water (e.g. meteorite waters in the mixing zone) that dissolved evaporite minerals and replaced them with silica (Eugster 1969; Milliken 1979). Less saline waters are characterised by lower pH values and upon mixing with hypersaline porewaters, silica solubility will be reduced. The variation in pH in a narrow range between 11 and 9 can significantly affect silica solubility, however the solubility of amorphous silica hardly changes below pH 9 (Fig. 4.2; section 4.2.2; Krauskopf 1967; Iller 1979). Similarly, influx of fresh waters into silica-rich hypersaline waters can drop the pH and cause supersaturation with respect to amorphous

silica and consequently silica precipitates (e.g. magadiite in Lake Magadi; section 4.3.1; Eugster 1969; Schubel and Simonson 1990). Nevertheless, the absence of silicified evaporite minerals or any primary interbedded evaporite beds in the Athel Silicilyte rule out evaporation and fresh water input as a possible mechanism of silica precipitation. If significant volumes of fresh water were supplied to the Athel Basin, it would have had a significant effect on pH in the mixing zone (at the basin margin) and consequently the Athel Silicilyte would be restricted to the basin margins. Moreover, the absence of any fluvial input records (Gold 2010) and the climate aridity during Ara times (e.g. Schröder et al. 2003) do not favour this hypothesis.

Many experiments have shown that dissolved silica has a strong affinity to ferric iron hydroxide surfaces (e.g. Davis et al. 2001; Davis et al. 2002; Yee et al. 2004). Such a mechanism has been invoked to concentrate and transport dissolved silica to basinal waters during deposition of Banded Iron Formations (e.g. Melnik 1982; Ewers 1983; Fischer and Knoll 2009). This mechanism would require high concentrations of dissolved iron hydroxides in the ambient seawater during precipitation. However, the Athel Silicilyte is characterised by low iron concentration (total iron = 1.67 ± 0.70 wt. %; Table 6.1) and so this mechanism is unlikely to be responsible for Athel Silicilyte precipitation.

Correlation of early diagenetic chert replacements with organic matter-rich facies and their absence in organic-matter poor facies in many Proterozoic and Phanerozoic carbonates suggests that organic matter can play a role in silica precipitation during early diagenesis (e.g. Knoll 1985; Siever 1992, cf. Knauth 1979). Silica precipitation is interpreted to occur during early diagenesis before significant compaction (1-10 m burial depth; Knauth 1994), when dissolved silica is available, from either silica-rich Precambrian seawater or from dissolution of siliceous organisms. Organic matter seems to mediate silica precipitation principally by dropping the silica solubility within the porewaters and/or by concentrating dissolved silica within organic tissues by hydrogen bonding with dissolved silica. The silica solubility, as mentioned above, hardly changes below pH 9. The organic matter can therefore mediate silica precipitation if the original porewater pH is above 9 by decreasing the local pH

below 9, and hence decreasing silica solubility. Decreasing the local pH is attributed to production of CO_2 , H^+ , HS^- and oxidation of HS^- at the redox boundary during organic matter diagenesis (equations 7.1-7.3). In the absence of reducible iron or after all reducible iron is exhausted, the acidity builds up, leading to carbonate dissolution and silica precipitation (e.g. flint formation in Cretaceous chalk; Clayton 1986). The Athel Silicilyte, however, shows no carbonate inclusions and was precipitated syndepositionally under euxinic conditions, suggesting that the pH of ambient seawater was unlikely to have been more than 9 during precipitation. In addition, the Precambrian seawater had pH values similar to modern seawater [8.1] and hardly dropped below 7.5 or exceeded 9 (Grotzinger and Kasting 1993). Therefore, the change in the silica solubility by decreasing pH below 9 is ruled out as a precipitation mechanism for the Athel Silicilyte.



Organic matter can also mediate silica precipitation by forming hydrogen bonds with dissolved silica. In order to understand this mechanism, it is important to discuss first the silica polymerisation process and then the formation of hydrogen bonds. After that, the viability of this mechanism for Athel Silicilyte precipitation can be explored. These are discussed in the following sections.

7.3.1 Silica polymerisation

The dominant species of dissolved silica below pH 9 is the neutral monosilicic acid $\text{Si}(\text{OH})_4$, which is ionised to H_3SiO_4^- and $\text{H}_2\text{SiO}_4^{2-}$ above pH 9. In supersaturated solution with respect to amorphous silica and below pH 9, monosilicic acid species are likely to polymerise and nucleate into nano-size spherical particles of low molecular weight (e.g. Iller 1979; Westall et al. 1995;

Orange et al. 2009). The polymerisation process occurs by condensing silanol groups (SiOH), forming siloxane bonds (Si-O-Si) and partial dehydration (Fig. 7.4). This process is catalysed by OH⁻ and by H⁺ above and below pH 2 ± 0.5; respectively. Therefore silica polymerisation is at a minimum around pH 2 ± 0.5 and it increases as pH increases; e.g. it is faster by two folds at pH 6 than at pH 4 (Iller 1979). These form nano-sized silica polymers as nuclei, which develop into larger particles at the expense of dissolved silica, or upon dissolution of smaller particles (since they have a higher solubility) to precipitate on the larger ones by Ostwald ripening (Iller 1979; Williams and Crerar 1985; Gorbach et al. 2006). As the smaller spherical silica polymers grow in size, they develop a negative charge on their surfaces due to the external silanol groups exhibiting a residual negative surface charge (e.g. Gorbach et al. 2006). This negative charge is more pronounced above pH 7. As a result, these small spherical particles repel each other and prevent silica polymer aggregation, so particle growth continues without aggregation by forming siloxane bonds with neutral Si(OH)₄ (opal-A precipitation; e.g. Williams and Crerar 1985). Since the negative ionic charge on silica polymers drops with the pH (reaching zero at pH 2 ± 0.5), silica polymers can aggregate below pH 7 into single layers of siloxane chains (opal-CT precipitation; e.g. Williams and Crerar 1985). Once these single layers of siloxane chains are formed, they become reactive sites for further silica precipitation, which then branch and cross-link to form a three-dimensional molecular network of silica aggregates leading to an increase in the total molecular weight of silica (Fig. 7.4; Iller 1979).

7.3.2 *Hydrogen bonding*

Dissolved silica can nucleate on or in the organic matter of the microbial layers (or mats) due to the availability of reactive functional groups, such as carboxyl and hydroxyl groups that are associated with proteins, lipids and cellulose (e.g. Phoenix et al. 2002; Konhauser et al. 2004; Konhauser et al. 2008). The OH⁻ groups in the functional groups and monosilicic acid are capable of forming hydrogen bonds (Fig. 7.4; e.g. Leo and Barghoorn 1976; Knoll 1985; Ferris et al. 1988; Renaut et al. 1998; Konhauser and Urrutia 1999; Konhauser et al. 2001; Konhauser et al. 2004; Konhauser et al. 2008). The functional group

availability tends to increase as the microbial layers degrade resulting in the formation of more hydrogen bonds between dissolved silica and the microbial layers (Knoll 1985; Ferris et al. 1988). Nevertheless, these functional groups are less reactive to dissolved silica above pH 7 because they are deprotonated and exhibit negative charges that repel negatively charged silica polymers (discussed above; e.g. Iller 1979; Konhauser et al. 2004). Indeed, no interaction was recorded between organic molecules and silica polymers from silica-supersaturated hydrothermal solution in sinters at a pH around 8 (e.g. Konhauser et al. 2008). In contrast, between pH 5-7, the different functional groups in the microbial layers exhibit low positive and low negative ionic charges that give the microbial layers overall a neutral net charge (Phoenix et al. 2002; Konhauser et al. 2004; Yee et al. 2004). Therefore, below pH 7, microbial layers are neutral and silica polymers have less pronounced negative charges (discussed above in section 7.3.1). Consequently, they are less repulsive to each other and hence, the formation of hydrogen bonds between them is likely (e.g. Coradin and Livage 2001). Although the dissolved silica might have a neutral charge, if they polymerise above pH 7, the combined negative charge on silica polymers and the functional groups will likely break the formed hydrogen bonds. Consequently, silica precipitation is inhibited or becomes insignificant in microbial layers. Whereas, if the pH is less than 5, the functional groups are fully protonated and exhibit overall positive ionic charges (van der Wal et al. 1997; Yee et al. 2004), and therefore the polymerised silica can be further attached to microbial layers by electrostatic attraction (e.g. Amores and Warren 2007).

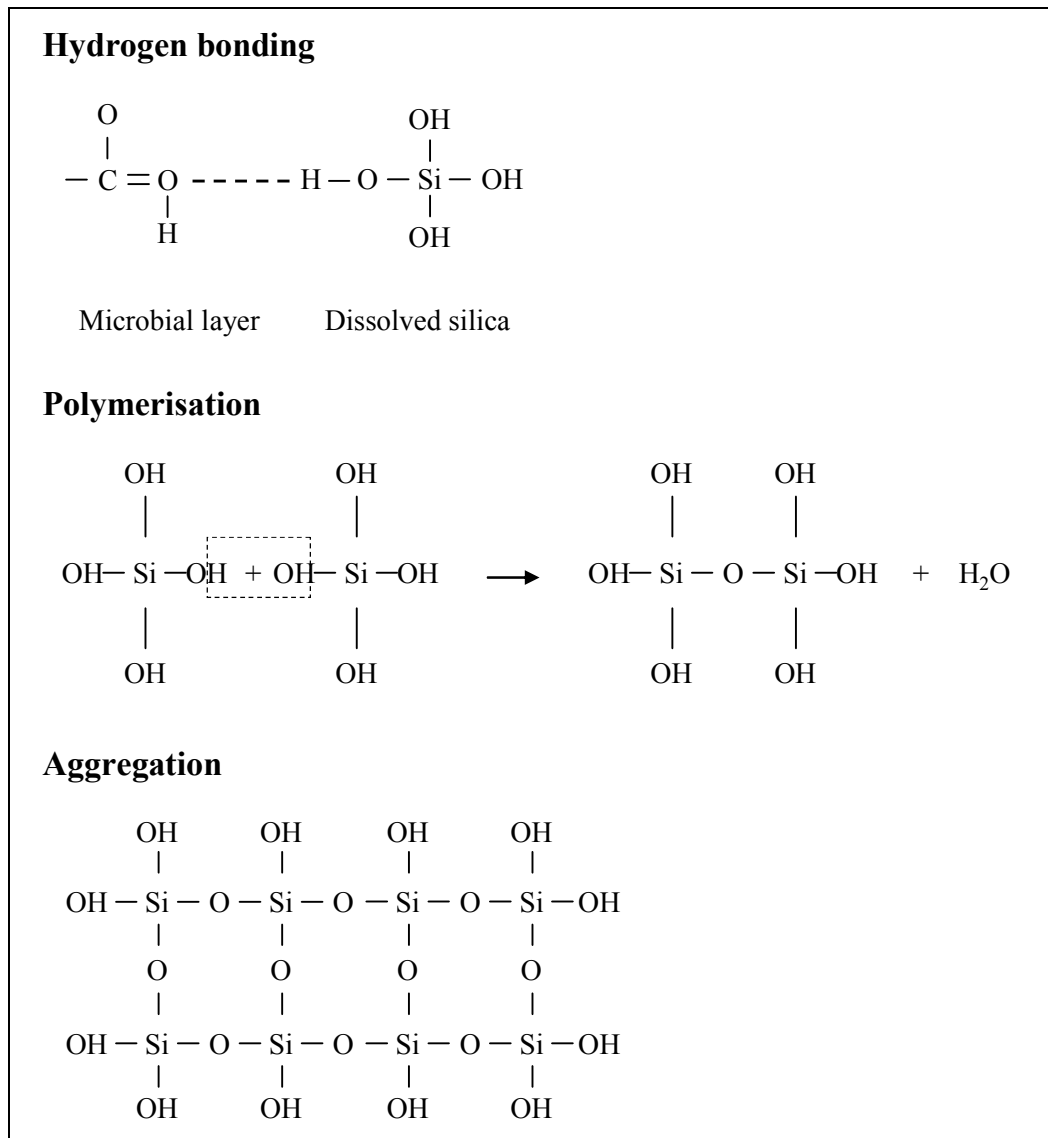


Figure 7.4. Shows hydrogen bonding, polymerisation and aggregation process. A hydrogen bond (dashed line) formed between dissolved silica (monosilicic acid) and carboxyl group found in microbial layers. Hydrogen bonds can be formed between a hydrogen atom attached to an oxygen atom in one molecule and an oxygen atom in another molecule (intermolecular bond). Also, this figure shows polymerisation reaction between two monosilicic acids by condensing silanol groups, form siloxane bond (Si-O-Si) and partial dehydration. Silica aggregate (gel) is formed by cross-link silica polymers to form three dimensional networks of silica polymers bonded by siloxane bonds; uncondensed silanol groups decrease.

Therefore, silica-microbial interactions by the formation of hydrogen bonds require a pH value of less than 7 to concentrate dissolved silica within microbial layer microenvironments. Once the dissolved silica reaches levels above amorphous silica solubility, dissolved silica will polymerise and aggregate according to the process described in silica polymerisation section above (7.3.1). However, as the pH drops, the polymerisation process can be much slower since

it is catalysed by OH^- (section 7.3.1). The optimum pH values for the formation of hydrogen bonds and silica polymerisation seem to be in range of 5-7.

7.3.3 *Athel Silicilyte precipitation and distribution*

Based on the interpretation that wavy laminations in Athel Silicilyte have a microbial origin and precipitation took place under euxinic conditions (section 5.2.1 and 6.5), the pH values below the redox boundary could have been optimal for the formation of hydrogen bonds between dissolved silica and microbial layers. Lower pH values than for the normal seawater below the redox boundary were likely caused by sulphate reduction, which was the dominant process in the mini-basins; as suggested by 1) the strong enrichment of redox-sensitive elements, 2) positive Ce anomalies and 3) small framboidal size (section 6.5), as well as sulphur-rich oil produced from the Athel Silicilyte (Alixant et al. 1998; Amthor et al. 2005). Sulphate reducing bacteria utilise dissolved sulphate to support their metabolic activities and they lower pH by producing H^+ and HS^- (equation 7.1). The produced HS^- was likely diffused across the redox boundary to the overlying oxic waters where it was oxidised by sulphur oxidising bacteria leading to a further drop in the pH (equation 7.2). Together these reactions would have increased bottom water acidity during Athel Silicilyte precipitation. The limited availability of iron in the Athel Silicilyte (section 5.2.1 and 6.4.1) suggests that iron reduction was not acting as an effective alkalinity buffer (equation 7.3). Therefore, during Athel Silicilyte precipitation, pH values below the redox boundary could have dropped below neutrality. The reaction-path modelling results also show that sulphate reduction can drop pH from the normal seawater value of 8.1 to less than 7 below the redox boundary (Fig. 7.5). This model was set up assuming that acetate (the reductant) reacted with the solutes present in 1 kg of seawater (in which the sulphate was the main oxidant). The concentrations of oxygen and Fe(III) were kept close to zero in order to model only the sulphate reduction reaction. As the reaction proceeded, the pH of the medium dropped as HS^- concentrations increased (Fig.7.5; for detailed methodology see section 2.6 and for full composition of the medium see Appendix IV).

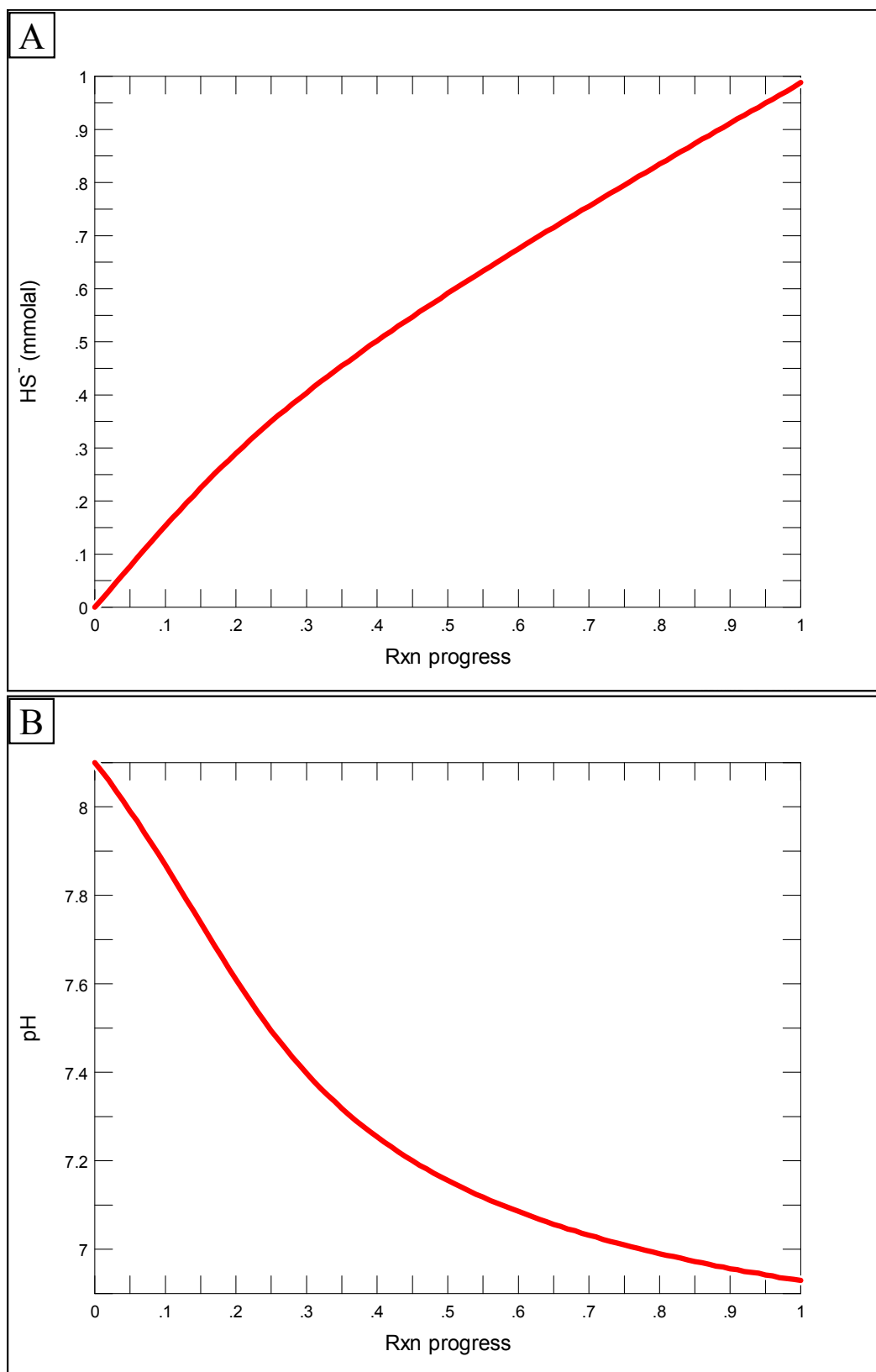


Figure 7.5. Reaction path modelling results using React tool in Geochemist's Workbench by theoretically creating 1 kg of seawater composition and adding 1 mg of acetate (as reductant). Oxygen and iron (FeIII) concentrations in this model are nearly zero in order to only run the sulphate reduction reaction (see Appendix IV for full composition of the medium). As sulphate reduction proceeded from zero to one scale (represent start and end of the reaction), (A) HS^- concentrations increased and (B) pH dropped from 8.1 to 6.9.

Based on the above, dissolved silica from the ambient seawater during precipitation of the Athel Silicilyte could have been bound to the microbial layers by the formation of hydrogen bonds. Dissolved silica binding could have taken place at or below the redox boundary in the water column once the microbial layers, which are derived from shallow water or formed at the seawater-brine interface (subsection 5.2.1), reached the redox boundary. Consequently, microbial layer microenvironments became supersaturated with respect to amorphous silica. Ultimately, concentrated dissolved silica polymerised (section 7.3.1) within the microbial layers. Once these networks of silica polymers were formed in the microbial layers, they continued to grow, filling unoccupied pore spaces between siloxane chains for as long as dissolved silica was available (section 7.3.1). This continuous growth likely led to the formation of connected microcrystalline quartz networks or sheet-like structures that are seen in all Athel Silicilyte samples (Fig. 7.3; also section 5.2.1). In this context, the variations in the microcrystalline quartz content in the Athel Silicilyte lithofacies could be interpreted as controlled by the availability of dissolved silica. Dissolved silica availability should not have varied significantly in the water column or at the sediment-water interface since dissolved silica could have freely diffused through the water column. However, below the sediment-water interface, silica diffusion from the ambient seawater was likely very limited given the locked structures of silica aggregates (Fig. 7.4). Consequently further silica precipitation probably ceased once the microbial layers were buried below the sediment-water interface. This would explain the decrease in the microcrystalline quartz contents as the detrital contents increase in the Athel Silicilyte (Table 5.1 and Fig. 6.3). The relatively high detrital input towards the Upper Athel Silicilyte (in detritus-bearing, microcrystalline quartz-rich lithofacies) probably led to a relatively faster burial of the microbial layers (section 5.4 and 6.4.1). Reducing further silica precipitation means more pore spaces were left unoccupied in the silica polymer networks and therefore higher porosity values in microcrystalline quartz-rich, detritus-bearing lithofacies (average porosity = 19.6 %), compared to microcrystalline quartz-dominated lithofacies (average porosity = 6.4 %). The intense input of detrital material during deposition of the Thuleilat Shale and U Shale resulted in rapid rates of sedimentation and did not allow enough time for silica to precipitate in the microbial layers at and above the sediment-water

interface before burial, and hence Athel Silicilyte precipitation was terminated during intense detrital input.

In summary, the availability of microbial layers during Athel Silicilyte precipitation played a role in silica precipitation by providing the functional groups that bound with dissolved silica by hydrogen bonds. Sulphate reducing bacteria were critical to precipitation by lowering the pH to the optimal values for the formation of hydrogen bonds, as well as for silica polymerisation and aggregation (pH = 5-7; section 7.3.2). Therefore, organic matter in the microbial layers and sulphate reducing bacteria in combination created a unique environment for silica precipitation (probably as opal-CT) from the ambient seawater at or below the redox boundary, resulting in deposition of the microbially laminated silica-rich Athel Silicilyte.

Euxinic conditions required to precipitate silica were probably met only during the A4C cycle in the deep waters within the mini-basins. Based on $\delta^{13}\text{C}$, $\delta^{34}\text{S}$ and redox-sensitive element data of the Ara Group (Amthor et al. 2003; Fike et al. 2006; Fike 2007; Fike and Grotzinger 2008), there is no firm evidence that euxinic conditions were developed in the South Oman Salt Basin during previous Ara cycles. Therefore, the localised precipitation of the Athel Silicilyte in the mini-basins during the A4C cycle was likely controlled by development of euxinic conditions in the deep water (200-400 m; Fig.7.6; section 3.5.2).

The time-equivalent carbonate succession (A4C) from the Birba Platform thins out towards the west and shows relatively thicker outer ramp facies in the same direction, based on seismic reflection and wireline logs of the A4 carbonates (Schröder et al. 2005), suggesting that the carbonate platform dipped to the west (Fig. 7.6). If this was the case, then equivalent facies to the Athel Silicilyte could have precipitated below the carbonate compensation depth (i.e. below the redox boundary) and therefore the area to the west of Birba Platform should be considered in future exploration strategies.

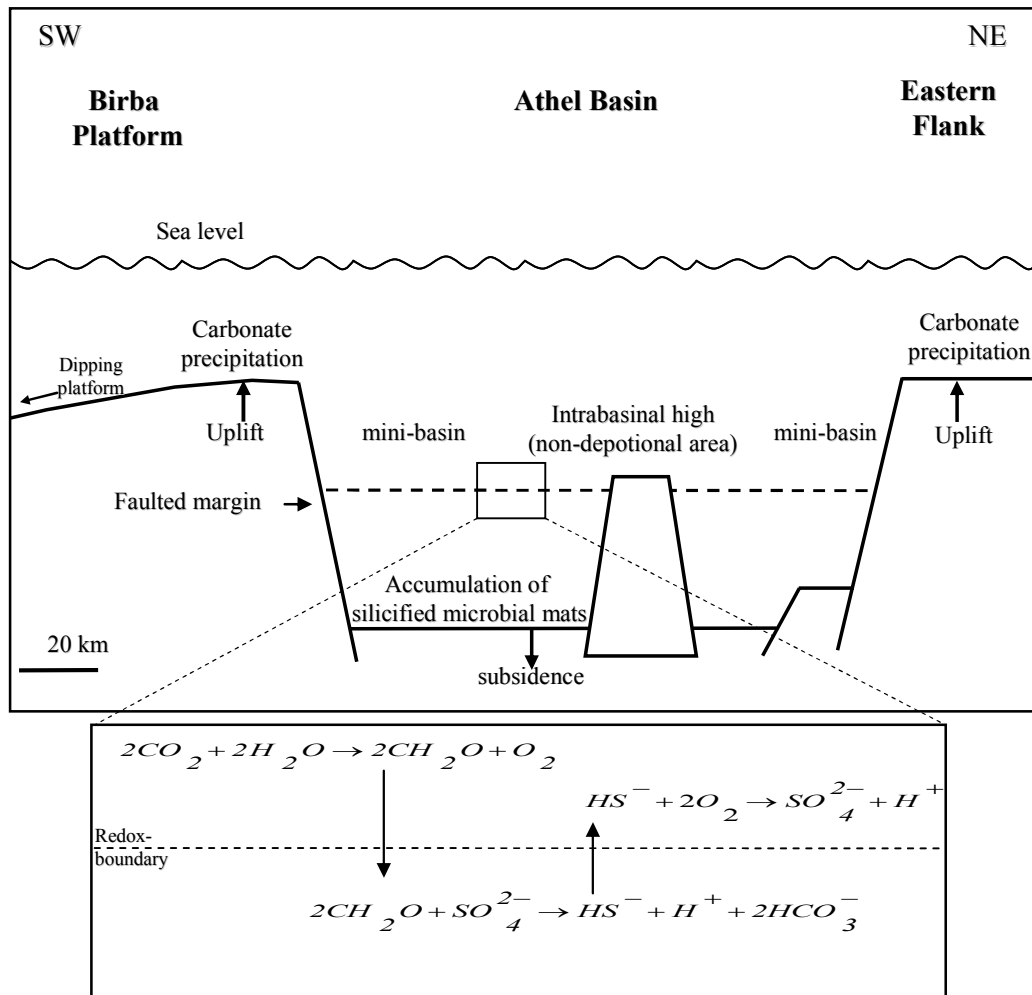


Figure 7.6. Showing the depositional model for the Athel Silicilyte. Silica precipitation in the microbial layers took place at or below the redox boundary in the fault-bounded mini-basin within the Athel Basin. The microbial layers were likely produced in the photic zone or at the seawater-brine interface and then delivered to the mini-basins, where they were mineralised by sulphate reducing bacteria. Produced sulphide by sulphate reducing bacteria was likely oxidised at the redox-boundary by sulphur oxidising bacteria. The platforms were the sites for carbonate precipitation. Note, the Birba Platform is dipping towards the west. Consequently deep waters were likely present further to the west where the Athel Silicilyte might have accumulated below the redox-boundary. Basin geometry in this model was constructed based on Ara Group basin reconstruction from Fig. 3.5 and it is approximately representing across section running from the NE to the SW in Fig. 7.1. Modified after Amthor et al. (2005).

7.4 Locus of primary chert precipitation during the Precambrian

Siever (1992) and Maliva et al. (2005) have demonstrated that cherts in upper Precambrian (Mesoproterozoic and Neoproterozoic) mainly precipitated during early diagenesis below the sediment-water interface and their main locus was shallow peritidal environments (section 4.4; Fig. 4.8). The cherts that they described were principally nodular formed by replacements of peritidal carbonate

rocks and/or by filling pore spaces and cavities (section 4.3.3; e.g. Knoll 1985; Maliva et al. 1989; Siever 1992; Maliva et al. 2005). The Athel Silicilyte, on the other hand, is different as: 1) it does not replace any pre-existing minerals, but represents primary silica precipitation from seawater in microbial layers; 2) it is a thick homogeneous unit of predominately microcrystalline quartz; up to 390 m thick and each slab approximately cover an area of 2 by 6 km; and 3) precipitation took place in basinal deep marine waters. These observations suggest that the Athel Silicilyte is a unique example of Precambrian cherts. This study therefore suggests that cherts during the Precambrian could precipitate directly from seawater above or at the sediment-water interface, rather than being restricted to shallow waters during early diagenesis.

The likely prerequisites for primary chert precipitation from silica-rich Precambrian seawater identified from this study are: 1) availability of organic matter; 2) development of euxinic conditions in the water column; and 3) siliciclastic sediment starvation. Few similar depositional conditions to the Athel Silicilyte have been defined in the literature, but one such potential analogue is the Liuchapo Formation in south China. The Liuchapo Formation is a 90 m thick unit of fairly homogeneous chert bounded between two siliciclastic mudstone-rich units and it has been interpreted to have precipitated in deep basinal waters at the Precambrian-Cambrian boundary (Chang et al. 2009). The Liuchapo Formation is characterized by very low detrital content (but increasing upwards in the stratigraphic), and shows high enrichment of redox-sensitive elements and positive Ce anomalies, suggesting the deep waters were euxinic and siliciclastic material-starved. No microscopic photographs have been published from this formation, but outcrop photographs show fine laminations that are very similar to the Athel Silicilyte. The precipitation of the Athel Silicilyte and the Liuchapo Formation at the Precambrian-Cambrian boundary could suggest that they represent a global deep water facies related to euxinic conditions at this boundary. The Liuchapo Formation therefore can be a potential analogue for the subsurface Athel Silicilyte.

7.5 Summary

The main findings of this chapter are:

- The silica mass present in the Athel Silicilyte was likely sourced from seawater. This interpretation is based on the Athel Silicilyte is a syndepositional precipitate and that it shows REE characteristics similar to modern seawater characteristics (LREE-depletion and positive La, Eu and Y anomalies). Mass balance calculations also support a seawater source and demonstrate that silica-rich Precambrian seawater could have sourced the large mass of silica necessary to precipitate the Athel Silicilyte.
- Athel Silicilyte precipitation in the microbial layers was likely a result of hydrogen bonding between dissolved silica and the functional groups (carboxyl and hydroxyl) in the microbial layers. The formation of hydrogen bonds concentrated dissolved silica in the microbial layers above amorphous silica solubility. Ultimately, dissolved silica nucleated and polymerised within these microbial layers.
- Formation of hydrogen bonds between dissolved silica and organic matter requires pH of less than 7; lower than normal seawater pH of 8.1. Lower pH values reduced repulsion forces between dissolved silica and the functional groups by reducing their negative charge. Subsequently, dissolved silica was able to bind within the microbial layers.
- Low pH conditions probably occurred at or below the redox-boundary as a result of H^+ and HS^- production by sulphate reducing bacteria and HS^- oxidation by sulphur oxidising bacteria. Therefore, Athel Silicilyte precipitation was restricted to the deep euxinic mini-basins within the Athel Basin.
- Higher detrital input towards the Upper Athel Silicilyte resulted in relatively faster burial of the microbial layers, and hence silica precipitation ceased due to the lack of dissolved silica below the sediment-water interface.
- The observations from the Athel Silicilyte suggest that the locus for primary chert precipitation during the Precambrian was microbially-rich, sediment-starved euxinic basins.

Chapter 8.

Conclusions

Various techniques were employed in this study to investigate the variability and to interpret the origin (silica source and precipitation mechanism) of the Athel Silicilyte. These techniques included core description, petrographical techniques (optical and SEM), wireline log interpretation, whole-rock geochemistry (XRF, XRD, LA-ICP-MS and TOC), mass-balance calculations and reaction-path modelling. The main outcomes of this study are:

- The Athel Silicilyte is present in the deepest parts (in the mini-basins) with the fault-bounded Athel Basin bounded by two silt-rich mudstones (below by the U Shale and above by the Thuleilat Shale). Its thickness varies across the basin from 166 to 390 m. The thickness variations are related to the topographic variations in the Athel Basin, which in turn controlled accommodation availability during Athel Silicilyte precipitation.
- Six lithofacies were recognised in the Athel Silicilyte that reflect variability in detrital material contents (silica-rich facies), sediment remobilisation (slumped and brecciated lithofacies) and diagenetic modification (carbonate-bearing lithofacies). Silica-rich facies represent more than 97 % of the total Athel Silicilyte thickness and they contain three sub-lithofacies; laminated microcrystalline quartz-rich mudstones, laminated microcrystalline quartz-dominated mudstones and laminated microcrystalline quartz-rich, detritus-bearing mudstones.
- Another three lithofacies were recognised: one from the bounding silt-rich mudstones (U Shale; laminated silt-rich, clay-mineral bearing mudstones) and two from the overlying evaporite unit (A5E); anhydrite- and detritus-bearing mudstones and halite-dominated mudstones.
- Texturally, the Athel Silicilyte exhibits discontinuous wavy lamination, with each lamina set alternating between silica-rich layers and more clay mineral-/organic matter-rich layers. These lamina geometries are interpreted to have a microbial origin. These microbial layers could have been formed by

coagulation of photosynthesising single-celled plankton or by microbial mat growth at the seawater-brine interface.

- Compositionally, the Athel Silicilyte is fairly homogeneous and it is predominately composed of connected networks or sheet-like forms of euhedral-subhedral microcrystalline quartz; average microcrystalline quartz content in the silica-rich facies is 80 wt. % and each crystal is typically 1-5 μm . The microcrystalline quartz crystallography suggests that that quartz precipitated *in situ*. The Athel Silicilyte also contains minor amounts of detrital quartz grains (3 wt. %), illite (10 wt. %), pyrite (4 wt. %) and organic carbon (TOC = 3 wt. %).
- The main heterogeneity in the Athel Silicilyte is the relative increase in detrital contents towards the Upper Athel Silicilyte and basin margins (ranging from 3 to 30 wt. %); an increase in detrital contents is associated with a decrease in microcrystalline quartz contents. The minor contents of detrital material suggest that Athel Silicilyte precipitation took place during very low detrital input (detrital-starvation). The increase in detrital input towards the Upper Athel Silicilyte marks gradual shift from silica precipitation to detrital material sedimentation during bounding mudstone deposition. Influx of detrital sediment to the Athel Basin was likely controlled by the change in the relative sea-level.
- Homogeneity of the Athel Silicilyte across the Athel Basin, absence of any pseudomorphs, preservation of 390 m thick laminated fabric, loose packing of detrital grains and association with syngentic framboidal pyrites suggest that the Athel Silicilyte precipitated syndepositionally in microbial layers.
- Strong enrichment of redox-sensitive elements (U, V and Mo), Mn-depletion, positive Ce anomalies and framboidal pyrite size-distributions (3.6-4 μm ; formed in the water column) suggest that the water column in the mini-basins was euxinic throughout Athel Silicilyte precipitation. The record of anoxia (negative $\delta^{13}\text{C}$ excursion and the extension of marine fossils) in the shallow

water carbonates could suggest that the euxinic conditions in these mini-basins were very extreme.

- In the absence of any mineralised skeleton remains within any sample of the Athel Silicilyte alongside the age of the Athel Silicilyte; Infra-Cambrian prior to the major evolution of silica-secreting organisms, the Athel Silicilyte is unlikely to have a biogenic origin. A hydrothermal origin is strongly ruled out by geochemical data. In particular, ratios of $\text{Al}_2\text{O}_3/(\text{Al}_2\text{O}_3 + \text{Fe}_2\text{O}_3 + \text{MnO})$ and $\text{Fe}_2\text{O}_3/\text{TiO}_2$, weak positive Eu anomalies and light REE-depletion are inconsistent with a hydrothermal source.
- A syndepositional origin for the Athel Silicilyte alongside REE characteristics of modern seawater (positive La, Eu and Y anomalies) strongly suggests that the silica present in the Athel Silicilyte was sourced from the ambient seawater. Mass balance calculations support this assertion and demonstrate that silica-rich Precambrian seawater could have provided the significant mass of silica necessary to precipitate the Athel Silicilyte.
- Silica precipitation within the microbial layers was likely driven by the ability of dissolved silica to form hydrogen bonds with the functional groups (carboxyl and hydroxyl) in the organic layers. Consequently, dissolved silica became supersaturated with respect to amorphous silica within the microbial layer microenvironment, resulting in silica nucleation and polymerisation in the microbial layers.
- Silica precipitation initiated at or below the redox-boundary in the water column at low pH values (< 7). Lower pH value than for the normal seawater were related to the production of acidic H^+ and HS^- by sulphate reducing bacteria and HS^- oxidation by sulphur oxidising bacteria. The main effect of the lowered pH conditions was to reduce negative charges on dissolved silica and functional groups, and hence reducing repulsion forces between them.

The absence of repulsion forces allowed dissolved silica to bind with the microbial layers by forming hydrogen bonds.

- Silica nucleation and polymerisation likely ceased after microbial layers burial as a result of the lack of dissolved silica below the sediment-water interface. During periods of higher detrital influx, relatively faster microbial burial occurred, inhibiting silica precipitation by reducing microbial layers residence times within the water column and at the sediment-water interface. Therefore, the microcrystalline quartz contents in the Athel Silicilyte decrease as detrital contents increase.
- This study shows that primary cherts could be precipitated directly from seawater during the Precambrian, instead of being restricted to early-late diagenesis below the sediment-water interface to form nodules or thin beds. The likely environments for this to happen were microbially-rich detrital-starved euxinic basins. Therefore, the Athel Silicilyte could represent euxinic basinal facies related to the development of anoxia conditions at the Precambrian-Cambrian boundary.

References

- ADACHI, M., YAMAMOTO, K., and SUGISAKI, R., 1986, Hydrothermal Chert and Associated Siliceous Rocks from the Northern Pacific - Their Geological Significance as Indication of Ocean Ridge Activity: *Sedimentary Geology*, v. 47, p. 125-148.
- ADAMS, L.K., MACQUAKER, J.H.S., and MARSHALL, J.D., 2006, Iron(III)-reduction in a low-organic-carbon brackish-marine system: *Journal of Sedimentary Research*, v. 76, p. 919-925.
- AGILENT, 2005, ICP-MS: Inductively Coupled Plasma Mass Spectrometry: A Primer, v. Publication No. 5989-3526EN: USA Agilent Technologies Inc, 84 p.
- AL-SIYABI, H.A., 2005, Exploration history of the Ara intrasalt carbonate stringers in the South Oman Salt Basin: *Georabia*, v. 10, p. 39-72.
- AL BALUSHI, S.A.K., MACQUAKER, J.H.S., and HOLLIS, C., in press, High-resolution lithofacies analyses of predominantly fine-grained carbonates in and around an intrashelf basin: An example from the Upper Cretaceous Natih-B Member source rock, North Oman: *Sedimentary Geology*.
- AL BALUSHI, S.K., and MACQUAKER, J.H.S., in press, Sedimentological evidence for bottom-water oxygenation during deposition of the Natih-B intrashelf basin sediments: Upper Cretaceous carbonate source rock, Natih Formation, North Oman: *GeoArabia*.
- ALGEO, T.J., 2004, Can marine anoxic events draw down the trace element inventory of seawater?: *Geology*, v. 32, p. 1057-1060.
- ALGEO, T.J., and LYONS, T.W., 2006, Mo-total organic carbon covariation in modern anoxic marine environments: Implications for analysis of paleoredox and paleohydrographic conditions: *Paleoceanography*, v. 21, p. PA 1016.
- ALIBO, D.S., and NOZAKI, Y., 1999, Rare earth elements in seawater: Particle association, shale-normalization, and Ce oxidation: *Geochimica Et Cosmochimica Acta*, v. 63, p. 363-372.
- ALIXANT, J.L., FREWIN, N., NEDERLOF, P., and AL RUWEHY, N., 1998, Characterisation of the Athel Silicilyte source rock/reservoir: Petrophysics meets geochemistry: SPWLA 39th Annual Logging Symposium p. 1-14.
- ALLEN, P.A., 2007, The huqf supergroup of Oman: Basin development and context for neoproterozoic glaciation: *Earth-Science Reviews*, v. 84, p. 139-185.

- ALLEN, P.A., and LEATHER, J., 2006, Post-Marinoan marine siliciclastic sedimentation: The Masirah Bay Formation, Neoproterozoic Huqf Supergroup of Oman: *Precambrian Research*, v. 144, p. 167-198.
- ALT, J.C., and TEAGLE, D.A.H., 2003, Hydrothermal alteration of upper oceanic crust formed at a fast-spreading ridge: mineral, chemical, and isotopic evidence from ODP Site 801: *Chemical Geology*, v. 201, p. 191-211.
- AMORES, D.R., and WARREN, L.A., 2007, Identifying when microbes biosilicify: The interconnected requirements of acidic pH, colloidal SiO₂ and exposed microbial surface: *Chemical Geology*, v. 240, p. 298-312.
- AMTHOR, J.E., GROTZINGER, J.P., SCHRÖDER, S., BOWRING, S.A., RAMEZANI, J., MARTIN, M.W., and MATTER, A., 2003, Extinction of *Cloudina* and *Namacalathus* at the Precambrian-Cambrian boundary in Oman: *Geology*, v. 31, p. 431-434.
- AMTHOR, J.E., RAMSEYER, K., FAULKNER, T., and LUCAS, P., 2005, Stratigraphy and sedimentology of a chert reservoir at the Precambrian-Cambrian boundary: the Al Shomou Silicilyte, South Oman Salt Basin: *Georabia*, v. 10, p. 89-122.
- AMTHOR, J.E., SMITS, W., NEDERLOF, P., FREWIN, N.L., and LAKE, S., 1998, Prolific oil production from a source rock-the Athel silicilyte source-rock play in south Oman: *American Association of Petroleum Geologists Annual Convention*, p. A22.
- ANDERSON, R.F., FLEISHER, M.Q., and LEHURAY, A.P., 1989, Concentration, Oxidation-State, and Particulate Flux of Uranium in the Black-Sea: *Geochimica Et Cosmochimica Acta*, v. 53, p. 2215-2224.
- ARNOLD, G.L., ANBAR, A.D., BARLING, J., and LYONS, T.W., 2004, Molybdenum isotope evidence for widespread anoxia in mid-proterozoic oceans: *Science*, v. 304, p. 87-90.
- ASTOR, S.R., 1983, Natural water and atmospheric chemistry of silicon. , *in* Astor, S.R., ed., *Silicon Geochemistry and Biogeochemistry*: London, Academic Press, p. 77-100.
- BAKER, P.A., and KASTNER, M., 1981, Constraints on the Formation of Sedimentary Dolomite: *Science*, v. 213, p. 214-216.
- BANERJEE, D.M., SCHIDLowski, M., SIEBERT, F., and BRASIER, M.D., 1997, Geochemical changes across the Proterozoic-Cambrian transition in the Durmala phosphorite mine section, Mussoorie hills, Garhwal Himalaya, India: *Palaeogeography Palaeoclimatology Palaeoecology*, v. 132, p. 183-194.
- BANNER, J.L., HANSON, G.N., and MEYERS, W.J., 1988, Rare-Earth Element and Nd Isotopic Variations in Regionally Extensive Dolomites from the Burlington-Keokuk Formation (Mississippian) - Implications for Ree

- Mobility during Carbonate Diagenesis: *Journal of Sedimentary Petrology*, v. 58, p. 415-432.
- BARLING, J., ARNOLD, G.L., and ANBAR, A.D., 2001, Natural mass-dependent variations in the isotopic composition of molybdenum: *Earth and Planetary Science Letters*, v. 193, p. 447-457.
- BARTLEY, J.K., POPE, M., KNOLL, A.H., SEMIKHATOV, M.A., and PETROV, P.Y.U., 1998, A Vendian-Cambrian boundary succession from the northwestern margin of the Siberian Platform: stratigraphy, palaeontology, chemostratigraphy and correlation: *Geological Magazine*, v. 135, p. 473-494.
- BAU, M., and DULSKI, P., 1996, Distribution of yttrium and rare-earth elements in the Penge and Kuruman iron-formations, Transvaal Supergroup, South Africa: *Precambrian Research*, v. 79, p. 37-55.
- BAU, M., and DULSKI, P., 1999, Comparing yttrium and rare earths in hydrothermal fluids from the Mid-Atlantic Ridge: implications for Y and REE behaviour during near-vent mixing and for the Y/Ho ratio of Proterozoic seawater: *Chemical Geology*, v. 155, p. 77-90.
- BAU, M., DULSKI, P., and MOLLER, P., 1995, Yttrium and Holmium in South-Pacific Seawater - Vertical-Distribution and Possible Fractionation Mechanisms: *Chemie Der Erde-Geochemistry*, v. 55, p. 1-16.
- BERNER, R.A., 1970, Sedimentary Pyrite Formation: *American Journal of Science*, v. 268, p. 1-23.
- BEUKES, N.J., and KLEIN, C., 1990, Geochemistry and Sedimentology of a Facies Transition - from Microbanded to Granular Iron-Formation - in the Early Proterozoic Transvaal Supergroup, South-Africa: *Precambrian Research*, v. 47, p. 99-139.
- BEUKES, N.J., and KLEIN, C., 1992, Models for iron-formation deposition, *in* Schopf, J.W., and Klein, C., eds., *The Proterozoic biosphere*: New York, Cambridge University Press, p. 147-151.
- BIRNBAUM, S.J., and WIREMAN, J.W., 1984, Bacterial sulfate reduction and pH: implications for early diagenesis: *Chemical Geology*, v. 43, p. 143-149.
- BIRNBAUM, S.J., and WIREMAN, J.W., 1985, Sulfate-Reducing Bacteria and Silica Solubility - a Possible Mechanism for Evaporite Diagenesis and Silica Precipitation in Banded Iron Formations: *Canadian Journal of Earth Sciences*, v. 22, p. 1904-1909.
- BIRNBAUM, S.J., WIREMAN, J.W., and BOROWSKI, R., 1989, Silica precipitation induced by the anaerobic sulfate reducing bacterium *Desulfovibrio desulfuricans*: effects upon the cell morphology and implications for preservation, *in* Crick, R.E., ed., *Origin, Evolution, and Modern Aspects of Biomineralization in Plants and Animals*: New York, Plenum Press, p. 289-298.

- BOLHAR, R., KAMBER, B.S., MOORBATH, S., FEDO, C.M., and WHITEHOUSE, M.J., 2004, Characterisation of early Archaean chemical sediments by trace element signatures: *Earth and Planetary Science Letters*, v. 222, p. 43-60.
- BONATTI, E., 1983, Hydrothermal metal deposits from the oceanic rifts: A classification, *in* Rona, P.A., Boström, K., Laubier, L., and Smith, K.L., eds., *Hydrothermal Processes at Seafloor Spreading Centers*: New York, Plenum Press, p. 491-502.
- BOND, D.P.G., and WIGNALL, P.B., 2010, Pyrite framboid study of marine Permian-Triassic boundary sections: A complex anoxic event and its relationship to contemporaneous mass extinction: *Geological Society of America Bulletin*, v. 122, p. 1265-1279.
- BOUCHETTE, F., SEGURET, M., and MOUSSINE-POUCHKINE, A., 2001, Coarse carbonate breccias as a result of water-wave cyclic loading (uppermost Jurassic-South-East Basin, France): *Sedimentology*, v. 48, p. 767-789.
- BOWRING, S.A., GROTZINGER, J.P., CONDON, D.J., RAMEZANI, J., NEWALL, M.J., and ALLEN, P.A., 2007, Geochronologic constraints on the chronostratigraphic framework of the neoproterozoic Huqf Supergroup, Sultanate of Oman: *American Journal of Science*, v. 307, p. 1097-1145.
- BOWRING, S.A., GROTZINGER, J.P., ISACHSEN, C.E., KNOLL, A.H., PELECHATY, S.M., and KOLOSOV, P., 1993, Calibrating Rates of Early Cambrian Evolution: *Science*, v. 261, p. 1293-1298.
- BRASIER, M., GREEN, O., and SHIELDS, G., 1997, Ediacarian sponge spicule clusters from southwestern Mongolia and the origins of the Cambrian fauna: *Geology*, v. 25, p. 303-306.
- BRASIER, M., MCCARRON, G., TUCKER, R., LEATHER, J., ALLEN, P., and SHIELDS, G., 2000, New U-Pb zircon dates for the Neoproterozoic Ghubrah glaciation and for the top of the Huqf Supergroup, Oman: *Geology*, v. 28, p. 175-178.
- BRASIER, M.D., 1989, On mass extinctions and faunal turnover near the end of the Precambrian, *in* Donovan, and S.K., eds., *Mass extinctions, processes, and evidence*: New York, Columbia University Press, p. 73-88.
- BRASIER, M.D., 1992, Background to the Cambrian Explosion: *Journal of the Geological Society*, v. 149, p. 585-587.
- BRASIER, M.D., MAGARITZ, M., CORFIELD, R., LUO, H.L., WU, X.C., LIN, O.Y., JIANG, Z.W., HAMDI, B., HE, T.G., and FRASER, A.G., 1990, The Carbon-Isotope and Oxygen-Isotope Record of the Precambrian Cambrian Boundary Interval in China and Iran and Their Correlation: *Geological Magazine*, v. 127, p. 319-332.

- BREIT, G.N., and WANTY, R.B., 1991, Vanadium Accumulation in Carbonaceous Rocks - a Review of Geochemical Controls during Deposition and Diagenesis: *Chemical Geology*, v. 91, p. 83-97.
- BROUWER, P., 2003, Theory of XRF: getting acquainted with the principles: Almelo, PANalytical B.V., 71 p.
- BROWN, T.L., LEMAY, J., H. E., and BURSTEN, B.E., 2000, Chemistry: the central science: Upper Saddle River: New Jersey, Prentice-Hall, 328 p.
- CADY, L., and FARMER, J.D., 1996 Fossilization processes in siliceous thermal springs: trends in preservation along thermal gradients. , *in* Block, G.R., and Goode, J.A., eds., *In Evolution of Hydrothermal Ecosystems on Earth (and Mars?)* West Sussex, Wiley, p. 150-173.
- CALVERT, S.E., and PEDERSEN, T.F., 1993, Geochemistry of Recent Oxidic and Anoxic Marine-Sediments - Implications for the Geological Record: *Marine Geology*, v. 113, p. 67-88.
- CALVERT, S.E., and PEDERSEN, T.F., 1996, Sedimentary geochemistry of manganese: Implications for the environment of formation of manganese black shales: *Economic Geology*, v. 91, p. 36-47.
- CALVERT, S.E., THODE, H.G., YEUNG, D., and KARLIN, R.E., 1996, A stable isotope study of pyrite formation in the Late Pleistocene and Holocene sediments of the Black Sea: *Geochimica Et Cosmochimica Acta*, v. 60, p. 1261-1270.
- CANFIELD, D.E., 1998, A new model for Proterozoic ocean chemistry: *Nature*, v. 396, p. 450-453.
- CANFIELD, D.E., RAISWELL, R., and BOTTRELL, S., 1992, The Reactivity of Sedimentary Iron Minerals toward Sulfide: *American Journal of Science*, v. 292, p. 659-683.
- CANFIELD, D.E., and THAMDRUP, B., 1994, The Production of S-34-Depleted Sulfide during Bacterial Disproportionation of Elemental Sulfur: *Science*, v. 266, p. 1973-1975.
- CHANG, H.J., CHU, X.L., and FENG, L.J., 2009, Terminal Ediacaran anoxia in deep-ocean: Trace element evidence from cherts of the Liuchapo Formation, South China: *Science in China Series D: Earth Sciences*, v. 52.
- CHAVAGNAC, V., GERMAN, C.R., MILTON, J.A., and PALMER, M.R., 2005, Sources of REE in sediment cores from the Rainbow vent site (36 degrees 14 ' N, MAR): *Chemical Geology*, v. 216, p. 329-352.
- CLAYPOOL, G.E., HOLSER, W.T., KAPLAN, I.R., SAKAI, H., and ZAK, I., 1980, The Age Curves of Sulfur and Oxygen Isotopes in Marine Sulfate and Their Mutual Interpretation: *Chemical Geology*, v. 28, p. 199-260.

- CLAYTON, C.J., 1986, The chemical environment of flint formation in Upper Cretaceous chalks, *in* Sieveking, G.d.G., and Hart, M.B., eds., *The Scientific Study of Flint and Chert*: Cambridge, Cambridge University Press, p. 43-54.
- COMPTON, J.S., 1988, Degree of Supersaturation and Precipitation of Organogenic Dolomite: *Geology*, v. 16, p. 318-321.
- CONDIE, K.C., and WRONKIEWICZ, D.J., 1990, The Cr/Th Ratio in Precambrian Pelites from the Kaapvaal Craton as an Index of Craton Evolution: *Earth and Planetary Science Letters*, v. 97, p. 256-267.
- CORADIN, T., and LIVAGE, J., 2001, Effect of some amino acids and peptides on silicic acid polymerization: *Colloids and Surfaces B-Biointerfaces*, v. 21, p. 329-336.
- CORSELLI, C., and MCCOY, F.W., 1989, Sedimentation of organic matter, Bacino Bannock, *in* Cita, M.B., Camerlenghi, A., and Corselli, C., eds., *Anoxic Basins of the Eastern Mediterranean*, *Ric. Sci. Suppl.*, p. 50-53.
- COZZI, A., ALLEN, P.A., and GROTZINGER, J.P., 2004a, Understanding carbonate ramp dynamics using delta $\delta^{13}\text{C}$ profiles: examples from the Neoproterozoic Buah Formation of Oman: *Terra Nova*, v. 16, p. 62-67.
- COZZI, A., GROTZINGER, J.P., and ALLEN, P.A., 2004b, Evolution of a terminal Neoproterozoic carbonate ramp system (Buah Formation, Sultanate of Oman): Effects of basement paleotopography: *Geological Society of America Bulletin*, v. 116, p. 1367-1384.
- CRUSIUS, J., CALVERT, S., PEDERSEN, T., and SAGE, D., 1996, Rhenium and molybdenum enrichments in sediments as indicators of oxic, suboxic and sulfidic conditions of deposition: *Earth and Planetary Science Letters*, v. 145, p. 65-78.
- DAVIES, G.R., and LUDLAM, S.D., 1973, Origin of Laminated and Graded Sediments, Middle-Devonian of Western Canada: *Geological Society of America Bulletin*, v. 84, p. 3527-3545.
- DAVIS, C.C., CHEN, H.W., and EDWARDS, M., 2002, Modeling silica sorption to iron hydroxide: *Environmental Science & Technology*, v. 36, p. 582-587.
- DAVIS, C.C., KNOCKE, W.R., and EDWARDS, M., 2001, Implications of aqueous silica sorption to iron hydroxide: Mobilization of iron colloids and interference with sorption of arsenate and humic substances: *Environmental Science & Technology*, v. 35, p. 3158-3162.
- DE BAAR, H.J.W., SCHIJF, J., and BYRNE, R.H., 1991, Solution Chemistry of the Rare-Earth Elements in Seawater: *European Journal of Solid State and Inorganic Chemistry*, v. 28, p. 357-373.

- DE KAMP, P.C.V., 2008, Smectite-illite-muscovite transformations, quartz dissolution, and silica release in shales: *Clays and Clay Minerals*, v. 56, p. 66-81.
- DERRY, L.A., and JACOBSEN, S.B., 1990, The Chemical Evolution of Precambrian Seawater - Evidence from Rees in Banded Iron Formations: *Geochimica Et Cosmochimica Acta*, v. 54, p. 2965-2977.
- DOVE, P.M., 1994, The Dissolution Kinetics of Quartz in Sodium-Chloride Solutions at 25 °C to 300 °C: *American Journal of Science*, v. 294, p. 665-712.
- DREVER, J.I., 1974, Geochemical Model for Origin of Precambrian Banded Iron Formations: *Geological Society of America Bulletin*, v. 85, p. 1099-1106.
- EDER, W., JAHNKE, L.L., SCHMIDT, M., and HUBER, R., 2001, Microbial diversity of the brine-seawater interface of the Kebrit Deep, Red Sea, studied via 16S rRNA gene sequences and cultivation methods: *Applied and Environmental Microbiology*, v. 67, p. 3077-3085.
- ELDERFIELD, H., 1988, The Oceanic Chemistry of the Rare-Earth Elements: *Philosophical Transactions of the Royal Society of London Series a-Mathematical Physical and Engineering Sciences*, v. 325, p. 105-126.
- ELZEA, J.M., and RICE, S.B., 1996, TEM and X-ray diffraction evidence for cristobalite and tridymite stacking sequences in opal: *Clays and Clay Minerals*, v. 44, p. 492-500.
- EMERSON, S.R., and HUESTED, S.S., 1991, Ocean Anoxia and the Concentrations of Molybdenum and Vanadium in Seawater: *Marine Chemistry*, v. 34, p. 177-196.
- ERBA, E., 1991, Deep Mid-Water Bacterial Mats from Anoxic Basins of the Eastern Mediterranean: *Marine Geology*, v. 100, p. 83-101.
- ERICKSON, B.E., and HELZ, G.R., 2000, Molybdenum(VI) speciation in sulfidic waters: Stability and lability of thiomolybdates: *Geochimica Et Cosmochimica Acta*, v. 64, p. 1149-1158.
- EUGSTER, H.P., 1969, Inorganic Bedded Cherts from Magadi Area Kenya: *Contributions to Mineralogy and Petrology*, v. 22, p. 1-31.
- EVERSULL, L.G., and FERRELL, R.E., 2008, Disordered silica with tridymite-like structure in the Twiggs clay: *American Mineralogist*, v. 93, p. 565-572.
- EWERS, W.E., 1983, Chemical factors in the deposition and diagenesis of banded iron-formation, *in* Trendall, A.F., and Morris, R.C., eds., *Iron Formation Facts and Problems*: Amsterdam, Elsevier, p. 491-512.
- FAIRCHILD, I.J., KNOLL, A.H., and SWETT, K., 1991, Coastal Lithofacies and Biofacies Associated with Syndepositional Dolomitization and

- Silicification (Draken Formation, Upper Riphean, Svalbard): *Precambrian Research*, v. 53, p. 165-197.
- FERRIS, F.G., BEVERIDGE, T.J., and FYFE, W.S., 1986, Iron-silica crystallite nucleation by bacteria in a geothermal sediment: *Nature*, v. 320, p. 609-611.
- FERRIS, F.G., FYFE, W.S., and BEVERIDGE, T.J., 1988, Metallic ion binding by *Bacillus subtilis*: Implications for the fossilization of microorganisms: *Geology* v. 16, p. 149-152.
- FIKE, D.A., 2007, Carbon and sulfur isotopic constraints on Ediacaran biogeochemical processes, Huqf Supergroup, Sultanate of Oman [unpublished Ph.D. thesis]: Massachusetts Institute of Technology, Massachusetts, USA.
- FIKE, D.A., and GROTZINGER, J.P., 2008, A paired sulfate-pyrite $\delta^{34}\text{S}$ approach to understanding the evolution of the Ediacaran-Cambrian sulfur cycle: *Geochimica et Cosmochimica Acta*, v. 72, p. 2636-2648.
- FIKE, D.A., GROTZINGER, J.P., PRATT, L.M., and SUMMONS, R.E., 2006, Oxidation of the Ediacaran Ocean: *Nature*, v. 444, p. 744-747.
- FISCHER, W.W., and KNOLL, A.H., 2009, An iron shuttle for deepwater silica in Late Archean and early Paleoproterozoic iron formation: *Geological Society of America Bulletin*, v. 121, p. 222-235.
- FRIEND, C.R.L., NUTMAN, A.P., BENNETT, V.C., and NORMAN, M.D., 2008, Seawater-like trace element signatures (REE+Y) of Eoarchean chemical sedimentary rocks from southern West Greenland, and their corruption during high-grade metamorphism: *Contributions to Mineralogy and Petrology*, v. 155, p. 229-246.
- FRIES, G., and PARIZE, O., 2003, Anatomy of ancient passive margin slope systems: Aptian gravity-driven deposition on the Vocontian palaeomargin, western Alps, south-east France: *Sedimentology*, v. 50, p. 1231-1270.
- GAO, G.Q., and LAND, L.S., 1991, Nodular Chert from the Arbuckle Group, Slick Hills, Sw Oklahoma - a Combined Field, Petrographic and Isotopic Study: *Sedimentology*, v. 38, p. 857-870.
- GEHLING, J.G., and RIGBY, J.K., 1996, Long expected sponges from the Neoproterozoic Ediacara fauna of South Australia: *Journal of Paleontology*, v. 70, p. 185-195.
- GERMAN, C.R., and ELDERFIELD, H., 1989, Rare-Earth Elements in Saanich Inlet, British-Columbia, a Seasonally Anoxic Basin: *Geochimica Et Cosmochimica Acta*, v. 53, p. 2561-2571.

- GERMAN, C.R., and ELDERFIELD, H., 1990, Application of the Ce anomaly as a paleoredox indicator: The ground rules: *Paleoceanography*, v. 5, p. 823-833.
- GERMAN, C.R., FLEER, A.P., BACON, M.P., and EDMOND, J.M., 1991a, Hydrothermal Scavenging at the Mid-Atlantic Ridge - Radionuclide Distributions: *Earth and Planetary Science Letters*, v. 105, p. 170-181.
- GERMAN, C.R., HOLLIDAY, B.P., and ELDERFIELD, H., 1991b, Redox Cycling of Rare-Earth Elements in the Suboxic Zone of the Black-Sea: *Geochimica Et Cosmochimica Acta*, v. 55, p. 3553-3558.
- GERMAN, C.R., KLINKHAMMER, G.P., EDMOND, J.M., MITRA, A., and ELDERFIELD, H., 1990, Hydrothermal Scavenging of Rare-Earth Elements in the Ocean: *Nature*, v. 345, p. 516-518.
- GERMAN, C.R., MASUZAWA, T., GREAVES, M.J., ELDERFIELD, H., and EDMOND, J.M., 1995, Dissolved Rare-Earth Elements in the Southern-Ocean - Cerium Oxidation and the Influence of Hydrography: *Geochimica Et Cosmochimica Acta*, v. 59, p. 1551-1558.
- GERMS, G.J.B., 1972, New Shelly Fossils from Nama Group, South West-Africa: *American Journal of Science*, v. 272, p. 752-761.
- GOLD, S.E.P., 2010, Stratigraphy and correlation of the Sarab Formation, Al huqf area, with the subsurface Ara Group play systems of Oman [unpublished PhD thesis]: University of Dublin, Trinity College, Dublin, Ireland, 394 p.
- GORBACH, V.A., POTAPOV, V.V., KASHPURA, V.N., TYURINA, N.A., and ZUBAHA, S.V., 2006, Silicic acid polymerization in hydrothermal solution, 31st Workshop on Geothermal Reservoir Engineering, Stanford University.
- GORIN, G.E., RACZ, L.G., and WALTER, M.R., 1982, Late Precambrian-Cambrian Sediments of Huqf Group, Sultanate of Oman: *Aapg Bulletin-American Association of Petroleum Geologists*, v. 66, p. 2609-2627.
- GREENSMITH, J.T., 1988, *Petrology of the Sedimentary Rocks*: London, UNWIN HYMAN, 262 p.
- GROSJEAN, E., LOVE, G.D., STALVIES, C., FIKE, D.A., and SUMMONS, R.E., 2009, Origin of petroleum in the Neoproterozoic-Cambrian South Oman Salt Basin: *Organic Geochemistry*, v. 40, p. 87-110.
- GROTZINGER, J.P., AL-SIYABI, H.A., AL-HASHIMI, R.A., and COZZI, A., 2002, New model for tectonic evolution of Neoproterozoic-Cambrian Huqf Supergroup basins Oman: *GeoArabia*, v. 7, p. 241.
- GROTZINGER, J.P., BOWRING, S.A., SAYLOR, B.Z., and KAUFMAN, A.J., 1995, Biostratigraphic and Geochronological Constraints on Early Animal Evolution: *Science*, v. 270, p. 598-604.

- GROTZINGER, J.P., and KASTING, J.F., 1993, New Constraints on Precambrian Ocean Composition: *Journal of Geology*, v. 101, p. 235-243.
- GROTZINGER, J.P., WATTERS, W.A., and KNOLL, A.H., 2000, Calcified metazoans in thrombolite-stromatolite reefs of the terminal Proterozoic Nama Group, Namibia: *Paleobiology*, v. 26, p. 334-359.
- GUNNARSSON, I., and ARNÓRSSON, S., 2000, Amorphous silica solubility and the thermodynamic properties of H_4SiO_4 in the range of 0° to 350°C at P_{sat} : *Geochimica et Cosmochimica Acta*, v. 64, p. 2295-2307.
- HALVERSON, G.P., HURTGEN, M.T., PORTER, S.M., COLLINS, A.S., and CLAUDIO GAUCHER, A.N.S.H.E.F.A.G.P.H., 2009, Chapter 10 Neoproterozoic-Cambrian Biogeochemical Evolution, *Developments in Precambrian Geology*, Elsevier, p. 351-365.
- HAMADE, T., KONHAUSER, K.O., RAISWELL, R., GOLDSMITH, S., and MORRIS, R.C., 2003, Using Ge/Si ratios to decouple iron and silica fluxes in Precambrian banded iron formations: *Geology*, v. 31, p. 35-38.
- HEIN, J.R., SCHOLL, D.W., BARRON, J.A., JONES, M.G., and MILLER, J., 1978, Diagenesis of late Cenozoic diatomaceous deposits and formation of the bottom-simulating reflector in the southern Bering Sea: *Sedimentology*, v. 25, p. 144-181.
- HELZ, G.R., MILLER, C.V., CHARNOCK, J.M., MOSSELMANS, J.F.W., PATRICK, R.A.D., GARNER, C.D., and VAUGHAN, D.J., 1996, Mechanism of molybdenum removal from the sea and its concentration in black shales: EXAFS evidence: *Geochimica et Cosmochimica Acta*, v. 60, p. 3631-3642.
- HENCHIRI, M., and SLIM-S'HIMI, N., 2006, Silicification of sulphate evaporites and their carbonate replacements in Eocene marine sediments, Tunisia: two diagenetic trends: *Sedimentology*, v. 53, p. 1135-1159.
- HENNEKE, E., LUTHER, G.W., DELANGE, G.J., and HOEFS, J., 1997, Sulphur speciation in anoxic hypersaline sediments from the eastern Mediterranean Sea: *Geochimica Et Cosmochimica Acta*, v. 61, p. 307-321.
- HESSE, R., 1989, Silica Diagenesis - Origin of Inorganic and Replacement Cherts: *Earth-Science Reviews*, v. 26, p. 253-284.
- HEWARD, A.P., 1990, Salt Removal and Sedimentation in Southern Oman: *Geology and Tectonics of the Oman Region*, v. 49, p. 637-652.
- HILD, E., and BRUMSACK, H.J., 1998, Major and minor element geochemistry of Lower Aptian sediments from the NW German Basin (core Hoheneggelsen KB 40): *Cretaceous Research*, v. 19, p. 615-633.
- HINMAN, N.W., 1998, Sequences of silica phase transitions: effects of Na, Mg, K, Al, and Fe ions: *Marine Geology*, v. 147, p. 13-24.

- HINMAN, N.W., and LINDSTROM, R.F., 1996, Seasonal changes in silica deposition in hot spring systems: *Chemical Geology*, v. 132, p. 237-246.
- HOFMANN, A., and HARRIS, C., 2008, Silica alteration zones in the Barberton greenstone belt: A window into subseafloor processes 3.5-3.3 Ga ago: *Chemical Geology*, v. 257, p. 224-242.
- HOFMANN, H.J., and MOINTJOY, E.W., 2001, Namacalathus-Cloudina assemblage in Neoproterozoic Miette Group (Byng Formation), British Columbia: Canada's oldest shelly fossils: *Geology*, v. 29, p. 1091-1094.
- HOLLAND, H.D., 1984, *The chemical evolution of the atmosphere and oceans*: Princeton: New Jersey, Princeton University Press, 582 p.
- HOLMEN, K.J., and ROTH, C.G.H., 1990, Ventilation of the Cariaco Trench, a Case of Multiple Source Competition: *Deep-Sea Research Part a-Oceanographic Research Papers*, v. 37, p. 203-225.
- HSÜ, K.J., and MCKENZIE, J.A., 1985, A "strangelove" ocean in earliest Tertiary, *in* Sundquist, E.T., and Broecker, W., eds., *The Carbon Cycle and Atmospheric CO₂: Natural Variations Archean to Present*: Washington, D.C., Geophysical Monograph Series, p. 487-492.
- HUSSEINI, M.I., and HUSSEINI, S.I., 1990, Origin of the Infracambrian Salt Basins of the Middle-East: *Classic Petroleum Provinces*, v. 50, p. 279-292.
- IJIMA, A., HEING, J.R., and SIEVER, R., 1983, *Siliceous deposits in the Pacific region*: New York, Elsevier, 472 p.
- ILLER, R.K., 1979, *The chemistry of silica: Solubility, Polymerization, Colloid and Surface Properties, and Biochemistry*: New York, NY, John Wiley & Sons, 866 p.
- IMMERZ, P., OTERDOOM, W.H., and EL TONBARY, M., 2000, The Huqf/Haima hydrocarbon system of Oman and the terminal phase of the Pan-African Orogeny: evaporite deposition in a compressive setting: *GeoArabia*, v. 5, p. 113-114.
- JAMES, H.L., 1954, Sedimentary facies of iron formations: *Economic Geology and the Bulletin of the Society of Economic Geologists*, v. 49, p. 235-293.
- JAMES, H.L., and TRENDALL, A.F., 1982, Banded iron formation: Distribution in time and paleoenvironmental significance *in* Holland H.D., a.S., M, ed., *Mineral deposits and the evolution of the biosphere*: New York Springer-Verlag, p. 199-218.
- JENKYN, H.C., GECZY, B., and MARSHALL, J.D., 1991, Jurassic Manganese Carbonates of Central-Europe and the Early Toarcian Anoxic Event: *Journal of Geology*, v. 99, p. 137-149.

- JONES, B., and MANNING, D.A.C., 1994, Comparison of geochemical indices used for the interpretation of palaeoredox conditions in ancient mudstones: *Chemical Geology*, v. 111, p. 111-129.
- JONES, B.F., RETTIG, S.L., and EUGSTER, H.P., 1967, Silica in Alkaline Brines: *Science*, v. 158, p. 1310-1314.
- JORGENSEN, B.B., FOSSING, H., WIRSEN, C.O., and JANNASCH, H.W., 1991, Sulfide Oxidation in the Anoxic Black-Sea Chemocline: *Deep-Sea Research Part a-Oceanographic Research Papers*, v. 38, p. S1083-S1103.
- KAMBER, B.S., and WEBB, G.E., 2001, The geochemistry of late Archaean microbial carbonate: Implications for ocean chemistry and continental erosion history: *Geochimica Et Cosmochimica Acta*, v. 65, p. 2509-2525.
- KASTNER, M., and SIEVER, R., 1983, Siliceous Sediments of the Guaymas Basin - the Effect of High Thermal-Gradients on Diagenesis: *Journal of Geology*, v. 91, p. 629-641.
- KAUFMAN, A.J., CORSETTI, F.A., and VARNI, M.A., 2007, The effect of rising atmospheric oxygen on carbon and sulfur isotope anomalies in the Neoproterozoic Johnnie Formation, Death Valley, USA: *Chemical Geology*, v. 237, p. 47-63.
- KELLER, M.A., and ISAACS, C.M., 1985, An Evaluation of Temperature Scales for Silica Diagenesis in Diatomaceous Sequences Including a New Approach Based on the Miocene Monterey Formation, California: *Geo-Marine Letters*, v. 5, p. 31-35.
- KENDALL, A.C., 1992, Evaporites, in Walker, R.G., and James, N.P., eds., *Facies Models -Response to Sea Level Change* St John's, Geological Association of Canada, p. 375-409.
- KIDDER, D.L., and ERWIN, D.H., 2001, Secular distribution of biogenic silica through the phanerozoic: Comparison of silica-replaced fossils and bedded cherts at the series level: *Journal of Geology*, v. 109, p. 509-522.
- KIDDER, D.L., and MUMMA, S.A., 2003, Silica-replaced oolites, bedded shelf cherts and Paleozoic changes in the silica cycle: *Sedimentary Geology*, v. 162, p. 159-166.
- KIMURA, H., MATSUMOTO, R., KAKUWA, Y., HAMDI, B., and ZIBASERESHT, H., 1997, The Vendian-Cambrian $\delta^{13}\text{C}$ record, North Iran: Evidence for overturning of the ocean before the Cambrian Explosion: *Earth and Planetary Science Letters*, v. 147, p. E1-E7.
- KIMURA, H., and WATANABE, Y., 2001, Oceanic anoxia at the Precambrian-Cambrian boundary: *Geology*, v. 29, p. 995-998.
- KLEIN, C., 2005, Some Precambrian banded iron-formations (BIFs) from around the world: Their age, geologic setting, mineralogy, metamorphism, geochemistry, and origin: *American Mineralogist*, v. 90, p. 1473-1499.

- KLEIN, C., and BEUKES, N.J., 1992, Time distribution, stratigraphy, and sedimentologic setting, and geochemistry of Precambrian iron-formations, , *in* Schopf, J.W., and Klein, C., eds., *The Proterozoic Biosphere: A Multidisciplinary Study*: Cambridge, UK, Cambridge University Press, p. 139-147.
- KLEIN, C.J., HURLBUT, C.S., and DANA, J.D., 1993, *Manual of Mineralogy: After James D. Dana*: New York, John Wiley & Sons, 681 p.
- KLINKHAMMER, G.P., ELDERFIELD, H., EDMOND, J.M., and MITRA, A., 1994, Geochemical Implications of Rare-Earth Element Patterns in Hydrothermal Fluids from Mid-ocean Ridges: *Geochimica Et Cosmochimica Acta*, v. 58, p. 5105-5113.
- KLINKHAMMER, G.P., and PALMER, M.R., 1991, Uranium in the oceans: Where it goes and why: *Geochimica et Cosmochimica Acta*, v. 55, p. 1799-1806.
- KNAUTH, L.P., 1979, A model for the origin of chert in limestone: *Geology*, v. 7, p. 274-277.
- KNAUTH, L.P., 1994, Petrogenesis of Chert, Silica: Physical Behavior, Geochemistry and Materials Applications: *Reviews in Mineralogy*: Washington, Mineralogical Soc America, p. 233-258.
- KNOLL, A.H., 1982, Micro-Fossils from the Late Precambrian Draken Conglomerate, New-York Friesland, Svalbard: *Journal of Paleontology*, v. 56, p. 755-790.
- KNOLL, A.H., 1985, Exceptional preservation of photosynthetic organisms in silicified carbonates and silicified peats.: Extraordinary fossil biotas: their ecological and evolutionary significance, p. 111-122.
- KNOLL, A.H., BAMBACH, R.K., CANFIELD, D.E., and GROTZINGER, J.P., 1996, Comparative earth history and Late Permian mass extinction: *Science*, v. 273, p. 452-457.
- KNOLL, A.H., and CARROLL, S.B., 1999, Early animal evolution: Emerging views from comparative biology and geology: *Science*, v. 284, p. 2129-2137.
- KNOLL, A.H., GROTZINGER, J.P., KAUFMAN, A.J., and KOLOSOV, P., 1995, Integrated Approaches to Terminal Proterozoic Stratigraphy - an Example from the Olenek Uplift, Northeastern Siberia: *Precambrian Research*, v. 73, p. 251-270.
- KNOLL, A.H., HAYES, J.M., KAUFMAN, A.J., SWETT, K., and LAMBERT, I.B., 1986, Secular Variation in Carbon Isotope Ratios from Upper Proterozoic Successions of Svalbard and East Greenland: *Nature*, v. 321, p. 832-838.
- KNOLL, A.H., SWETT, K., and MARK, J., 1991, Paleobiology of a Neoproterozoic Tidal Flat Lagoonal Complex - the Draken Conglomerate Formation, Spitsbergen: *Journal of Paleontology*, v. 65, p. 531-570.

- KNOLL, A.H., and WALTER, M.R., 1992, Latest Proterozoic Stratigraphy and Earth History: *Nature*, v. 356, p. 673-678.
- KONHAUSER, K.O., and FERRIS, F.G., 1996, Diversity of iron and silica precipitation by microbial mats hydrothermal waters, Iceland: Implications for Precambrian iron formations: *Geology*, v. 24, p. 323-326.
- KONHAUSER, K.O., HAMADE, T., RAISWELL, R., MORRIS, R.C., FERRIS, F.G., SOUTHAM, G., and CANFIELD, D.E., 2002, Could bacteria have formed the Precambrian banded iron formations?: *Geology*, v. 30, p. 1079-1082.
- KONHAUSER, K.O., JONES, B., PHOENIX, V., FERRIS, G., and RENAUT, R., 2004, The microbial role in hot spring silicification: *Ambio*, v. 33, p. 552-558.
- KONHAUSER, K.O., LALONDE, S.V., and PHOENIX, V.R., 2008, Bacterial biomineralization: Where to from here?: *Geobiology*, v. 6, p. 298-302.
- KONHAUSER, K.O., PHOENIX, V.R., BOTTRELL, S.H., ADAMS, D.G., and HEAD, I.M., 2001, Microbial-silica interactions in Icelandic hot spring sinter: possible analogues for some Precambrian siliceous stromatolites: *Sedimentology*, v. 48, p. 415-433.
- KONHAUSER, K.O., and URRUTIA, M.M., 1999, Bacterial clay authigenesis: a common biogeochemical process: *Chemical Geology*, v. 161, p. 399-413.
- KRAUSKOPF, K.B., 1967, *Introduction to Geochemistry*: New York, McGraw-Hill, 721 p.
- KRAUSKOPF, K.B., 1982, *Introduction to geochemistry*: Singapore, McGraw Hill Book Company, 617 p.
- LAKE, S.D., and RICHARD, P.D., 1998, The Athel Silicilyte Play in South Oman: an history of transtension and transpression, *Explortion Note No. 213*: Muscat, Petroleum Development of Oman, p. 38.
- LANGMUIR, D., 1978, Uranium Solution-Mineral Equilibria at Low-Temperatures with Applications to Sedimentary Ore-Deposits: *Geochimica Et Cosmochimica Acta*, v. 42, p. 547-569.
- LE GUERROUE, E., ALLEN, P., and COZZI, A., 2005, Two distinct glacial successions in the Neoproterozoic of Oman: *Georabia*, v. 10, p. 17-34.
- LE GUERROUE, E., ALLEN, P.A., and COZZI, A., 2006a, Chemostratigraphic and sedimentological framework of the largest negative carbon isotopic excursion in earth history: The neoproterozoic Shuram formation (Nafun Group, Oman): *Precambrian Research*, v. 146, p. 68-92.
- LE GUERROUE, E., ALLEN, P.A., and COZZI, A., 2006b, Parasequence development in the Ediacaran Shuram Formation (Nafun Group, Oman): High-resolution stratigraphic test for primary origin of negative carbon isotopic ratios: *Basin Research*, v. 18, p. 205-219.

- LEATHER, J., ALLEN, P.A., BRASIER, M.D., and COZZI, A., 2002, Neoproterozoic snowball earth under scrutiny: Evidence from the Fiq glaciation of Oman: *Geology*, v. 30, p. 891-894.
- LEE, J.H., and BYRNE, R.H., 1992, Examination of Comparative Rare-Earth Element Complexation Behavior Using Linear Free-Energy Relationships: *Geochimica Et Cosmochimica Acta*, v. 56, p. 1127-1137.
- LEO, R.F., and BARGHOORN, E.S., 1976, Silicification of wood, Botanical Museum Leaflets, Harvard University, p. 1-47.
- LEWIS, D.W., and MCCONCHIE, D.M., 1994, *Analytical sedimentology*, Chapman & Hall, 197 p.
- LOOSVELD, R.J.H., BELL, A., and TERKEN, J.J.M., 1996, The tectonic evolution of interior Oman: *GeoArabia* v. 1, p. 28-51.
- LOVLEY, D.R., 1991, Dissimilatory Fe(III) and Mn(IV) Reduction: *Microbiological Reviews*, v. 55, p. 259-287.
- LYNCH, F.L., MACK, L.E., and LAND, L.S., 1997, Burial diagenesis of illite/smectite in shales and the origins of authigenic quartz and secondary porosity in sandstones: *Geochimica Et Cosmochimica Acta*, v. 61, p. 1995-2006.
- LYONS, T.W., and BERNER, R.A., 1992, Carbon Sulfur Iron Systematics of the Uppermost Deep-Water Sediments of the Black-Sea: *Chemical Geology*, v. 99, p. 1-27.
- LYONS, T.W., WERNE, J.P., HOLLANDER, D.J., and MURRAY, R.W., 2003, Contrasting sulfur geochemistry and Fe/Al and Mo/Al ratios across the last oxic-to-anoxic transition in the Cariaco Basin, Venezuela: *Chemical Geology*, v. 195, p. 131-157.
- MACQUAKER, J.H.S., and ADAMS, A.E., 2003, Maximizing information from fine-grained sedimentary rocks: An inclusive nomenclature for mudstones: *Journal of Sedimentary Research*, v. 73, p. 735-744.
- MACQUAKER, J.H.S., BENTLEY, S.J., and BOHACS, K.M., 2010, Wave-enhanced sediment-gravity flows and mud dispersal across continental shelves: Reappraising sediment transport processes operating in ancient mudstone successions: *Geology*, v. 38, p. 947-950.
- MACQUAKER, J.H.S., and BOHACS, K.M., 2007, *Geology* - On the accumulation of mud: *Science*, v. 318, p. 1734-1735.
- MACQUAKER, J.H.S., CURTIS, C.D., and COLEMAN, M.L., 1997, The role of iron in mudstone diagenesis: Comparison of Kimmeridge clay formation mudstones from onshore and offshore (UKCS) localities: *Journal of Sedimentary Research*, v. 67, p. 871-878.

- MACQUAKER, J.H.S., and KELLER, M.A., 2005, Mudstone sedimentation at high latitudes: Ice as a transport medium for mud and supplier of nutrients: *Journal of Sedimentary Research*, v. 75, p. 696-709.
- MACQUAKER, J.H.S., TAYLOR, K.G., and GAWTHORPE, R.L., 2007, High-resolution facies analyses of mudstones: Implications for paleoenvironmental and sequence stratigraphic interpretations of offshore ancient mud-dominated successions: *Journal of Sedimentary Research*, v. 77, p. 324-339.
- MALIVA, R.G., 1987, Quartz Geodes - Early Diagenetic Silicified Anhydrite Nodules Related to Dolomitization: *Journal of Sedimentary Petrology*, v. 57, p. 1054-1059.
- MALIVA, R.G., 2001, Silicification in the Belt Supergroup (Mesoproterozoic), Glacier National Park, Montana, USA: *Sedimentology*, v. 48, p. 887-896.
- MALIVA, R.G., KNOLL, A.H., and SIEVER, R., 1989, Secular Change in Chert Distribution a Reflection of Evolving Biological Participation in the Silica Cycle: *Palaios*, v. 4, p. 519-532.
- MALIVA, R.G., KNOLL, A.H., and SIMONSON, B.M., 2005, Secular change in the Precambrian silica cycle: Insights from chert petrology: *Geological Society of America Bulletin*, v. 117, p. 835-845.
- MALIVA, R.G., and SIEVER, R., 1988a, Mechanism and Controls of Silicification of Fossils in Limestones: *Journal of Geology*, v. 96, p. 387-398.
- MALIVA, R.G., and SIEVER, R., 1988b, Pre-Cenozoic Nodular Cherts - Evidence for Opal-Ct Precursors and Direct Quartz Replacement: *American Journal of Science*, v. 288, p. 798-809.
- MALIVA, R.G., and SIEVER, R., 1989a, Chertification Histories of Some Late Mesozoic and Middle Paleozoic Platform Carbonates: *Sedimentology*, v. 36, p. 907-926.
- MALIVA, R.G., and SIEVER, R., 1989b, Nodular Chert Formation in Carbonate Rocks: *Journal of Geology*, v. 97, p. 421-433.
- MARTEL, A.T., and GIBLING, M.R., 1993, Clastic Dykes of the Devonian-Carboniferous Horton Bluff Formation, Nova-Scotia - Storm-Related Structures in Shallow Lakes: *Sedimentary Geology*, v. 87, p. 103-119.
- MATTES, B.W., and MORRIS, S.C., 1990, Carbonate Evaporite Deposition in the Late Precambrian - Early Cambrian Ara Formation of Southern Oman: *Geology and Tectonics of the Oman Region*, v. 49, p. 617-636.
- MATTON, G., JERBAK, M., and MAHFOUDH, A., 2002, Fractal analysis and origin of a chert megabreccia in the Richat Dome, Mauritania, Africa: *Geological Society of America, Annual Meeting, Abstracts with Programs*, v. 34, p. 555.

- MCFADDEN, K.A., HUANG, J., CHU, X.L., JIANG, G.Q., KAUFMAN, A.J., ZHOU, C.M., YUAN, X.L., and XIAO, S.H., 2008, Pulsed oxidation and biological evolution in the Ediacaran Doushantuo Formation: Proceedings of the National Academy of Sciences of the United States of America, v. 105, p. 3197-3202.
- MCLENNAN, S.M., 1989, Rare earth elements in sedimentary rocks: Influence of provenance and sedimentary processes: Reviews in Mineralogy and Geochemistry, v. 21, p. 169-200.
- MCLENNAN, S.M., BOCK, B., HEMMING, S.R., HUROWITZ, J.A., LEV, S.M., and MCDANIEL, D.K., 2003, The roles of provenance and sedimentary processes in the geochemistry of sedimentary rocks, *in* Lentz, D.R., ed., Geochemistry of Sediments and Sedimentary Rocks: Secular Evolutionary Considerations to Mineral Deposit-Forming Environments, Geological Association of Canada, p. 7-38.
- MCMANUS, J., BERELSON, W.M., KLINKHAMMER, G.P., HAMMOND, D.E., and HOLM, C., 2005, Authigenic uranium: relationship to oxygen penetration depth and organic carbon rain: *Geochimica Et Cosmochimica Acta*, v. 69, p. 95-108.
- MELLO, U.T., KARNER, G.D., and ANDERSON, R.N., 1995, Role of Salt in Restraining the Maturation of Subsalt Source Rocks: Marine and Petroleum Geology, v. 12, p. 697-716.
- MELNIK, Y.P., 1982, Precambrian Banded Iron Formation: Physiochemical Conditions of Formation: Amsterdam, Elsevier, 310 p.
- MEYERS, P.A., 1993, Origin of the Pliopleistocene Vrica Laminites - Organic Geochemical Evidence: Marine Geology, v. 115, p. 117-127.
- MILLERO, F.J., 1991, The Oxidation of H₂S in Black-Sea Waters: Deep-Sea Research Part a-Oceanographic Research Papers, v. 38, p. S1139-S1150.
- MILLERO, F.J., 1996, Chemical Oceanography: Boca Raton, CRC Press, 469 p.
- MILLIKEN, K.L., 1979, Silicified Evaporite Syndrome - 2 Aspects of Silicification History of Former Evaporite Nodules from Southern Kentucky and Northern Tennessee: Journal of Sedimentary Petrology, v. 49, p. 245-256.
- MILLS, P.C., 1983, Genesis and Diagnostic-Value of Soft-Sediment Deformation Structures - a Review: Sedimentary Geology, v. 35, p. 83-104.
- MILLSON, J.A., MERCADIER, C.G.L., LIVERA, S.E., and PETERS, J.M., 1996, The lower palaeozoic of Oman and its context in the evolution of a Gondwanan continental margin: Journal of the Geological Society, v. 153, p. 213-230.

- MORFORD, J.L., and EMERSON, S., 1999, The geochemistry of redox sensitive trace metals in sediments: *Geochimica Et Cosmochimica Acta*, v. 63, p. 1735-1750.
- MORFORD, J.L., EMERSON, S.R., BRECKEL, E.J., and KIM, S.H., 2005, Diagenesis of oxyanions (V, U, Re, and Mo) in pore waters and sediments from a continental margin: *Geochimica Et Cosmochimica Acta*, v. 69, p. 5021-5032.
- MORFORD, J.L., RUSSELL, A.D., and EMERSON, S., 2001, Trace metal evidence for changes in the redox environment associated with the transition from terrigenous clay to diatomaceous sediment, Saanich Inlet, BC: *Marine Geology*, v. 174, p. 355-369.
- MORRIS, R.C., 1993, Genetic Modeling for Banded Iron-Formation of the Hamersley Group, Pilbara Craton, Western-Australia: *Precambrian Research*, v. 60, p. 243-286.
- MURAMOTO, J.A., HONJO, S., FRY, B., HAY, B.J., HOWARTH, R.W., and CISNE, J.L., 1991, Sulfur, Iron and Organic-Carbon Fluxes in the Black-Sea - Sulfur Isotopic Evidence for Origin of Sulfur Fluxes: *Deep-Sea Research Part a-Oceanographic Research Papers*, v. 38, p. S1151-S1187.
- MURRAY, R.W., 1994, Chemical criteria to identify the depositional environment of chert: general principles and applications: *Sedimentary Geology*, v. 90, p. 213-232.
- MURRAY, R.W., JONES, D., and BUCHHOLTZ TEN BRINK, M.R., 1992, Diagenetic formation of bedded chert: evidence from chemistry of the chert-shale couplet: *Geology*, v. 20, p. 271-274.
- NEUWERTH, R., SUTER, F., GUZMAN, C.A., and GORIN, G.E., 2006, Soft-sediment deformation in a tectonically active area: The Plio-Pleistocene Zarzal Formation in the Cauca Valley (Western Colombia): *Sedimentary Geology*, v. 186, p. 67-88.
- NICHOLAS, C.J., and BRASIER, M., 2000, Outcrop equivalent of the subsurface Precambrian-Cambrian Ara Group in Oman: *Proceedings of the Fourth Middle East Geosciences Conference, GEO 2000*, p. 151-152.
- NICHOLAS, C.N., 2006, The Precambrian-Cambrian Ara Group in outcrop, Huqf region, South Oman, unpublished report: Muscat, Petroleum Development of Oman, p. 64.
- NOFFKE, N., 1998, Multidirected ripple marks rising from biological and sedimentological processes in modern lower supratidal deposits (Mellum Island, southern North Sea): *Geology*, v. 26, p. 879-882.
- NOFFKE, N., KNOLL, A.H., and GROTZINGER, J.P., 2002, Sedimentary controls on the formation and preservation of microbial mats in siliciclastic deposits: A case study from the Upper Neoproterozoic Nama Group, Namibia: *Palaios*, v. 17, p. 533-544.

- NOZAKI, Y., ZHANG, J., and AMAKAWA, H., 1997, The fractionation between Y and Ho in the marine environment: *Earth and Planetary Science Letters*, v. 148, p. 329-340.
- O'BRIEN, N.R., 1996, Shale lamination and sedimentary processes, *in* Kemp, A.E.S., ed., *Palaeoclimatology and Palaeoceanography from Laminated Sediments*, Geological Society Special Publication, p. 23-36.
- ORANGE, F., WESTALL, F., DISNAR, J.R., PRIEUR, D., BIENVENU, N., LEROMANCER, M., and DEFARGE, C., 2009, Experimental silicification of the extremophilic Archaea *Pyrococcus abyssi* and *Methanocaldococcus jannaschii*: applications in the search for evidence of life in early Earth and extraterrestrial rocks: *Geobiology*, v. 7, p. 403-418.
- PAREKH, P.P., MOLLER, P., DULSKI, P., and BAUSCH, W.M., 1977, Distribution of Trace-Elements between Carbonate and Non-Carbonate Phases of Limestone: *Earth and Planetary Science Letters*, v. 34, p. 39-50.
- PASSIER, H.F., BOTTCHEER, M.E., and DE LANGE, G.J., 1999, Sulphur enrichment in organic matter of eastern Mediterranean sapropels: A study of sulphur isotope partitioning: *Aquatic Geochemistry*, v. 5, p. 99-118.
- PERRY, E.C., and LEFTICARIU, L., 2007, Formation and geochemistry of Precambrian cherts, *in* Holland, H., Turekian, K., and MacKenzie, F.T., eds., *Sediments, Diagenesis, and Sedimentary Rocks: Treatise on Geochemistry*: Oxford, Pergamon, p. 1-21.
- PETERSON, M.N., and VON DER BORCH, C.C., 1965, Chert - Modern Inorganic Deposition in a Carbonate-Precipitating Locality: *Science*, v. 149, p. 1501-1503.
- PHOENIX, V.R., MARTINEZ, R.E., KONHAUSER, K.O., and FERRIS, F.G., 2002, Characterization and implications of the cell surface reactivity of *Calothrix sp.* strain KC97: *Applied and Environmental Microbiology*, v. 68, p. 4827-4834.
- PICARD, S., LECUYER, C., BARRAT, J.A., GARCIA, J.P., DROMART, G., and SHEPPARD, S.M.F., 2002, Rare earth element contents of Jurassic fish and reptile teeth and their potential relation to seawater composition (Anglo-Paris Basin, France and England): *Chemical Geology*, v. 186, p. 1-16.
- PISCIOTTO, K.A., 1981, Diagenetic Trends in the Siliceous Facies of the Monterey Shale in the Santa-Maria Region, California: *Sedimentology*, v. 28, p. 547-571.
- RAISWELL, R., 1982, Pyrite texture, isotopic composition, and the availability of iron: *American Journal of Science*, v. 282 p. 1244-1263.
- RAISWELL, R., BOTTRELL, S.H., ALBIATTY, H.J., and TAN, M.M., 1993, The Influence of Bottom Water Oxygenation and Reactive Iron Content on Sulfur Incorporation into Bitumens from Jurassic Marine Shales: *American Journal of Science*, v. 293, p. 569-596.

- RENAUT, R.W., JONES, B., and TIERCELIN, J.J., 1998, Rapid *in situ* silicification of microbes at Loburu hot springs, Lake Bogoria, Kenya Rift Valley: *Sedimentology*, v. 45, p. 1083-1103.
- RICKARD, D., and LUTHER, G.W., 1997, Kinetics of pyrite formation by the H₂S oxidation of iron(II) monosulfide in aqueous solutions between 25 and 125 °C: The mechanism: *Geochimica Et Cosmochimica Acta*, v. 61, p. 135-147.
- RIMMER, S.M., 2004, Geochemical paleoredox indicators in Devonian-Mississippian black shales, central Appalachian basin (USA): *Chemical Geology*, v. 206, p. 373-391.
- RODRIGUEZ-PASCUA, M.A., CALVO, J.P., DE VICENTE, G., and GOMEZ-GRAS, D., 2000, Soft-sediment deformation structures interpreted as seismites in lacustrine sediments of the Prebetic Zone, SE Spain, and their potential use as indicators of earthquake magnitudes during the Late Miocene: *Sedimentary Geology*, v. 135, p. 117-135.
- ROSELL, L., ORTI, F., KASPRZYK, A., PLAYA, E., and PERYT, T.M., 1998, Strontium geochemistry of Miocene primary gypsum: Messinian of southeastern Spain and Sicily and Badenian of Poland: *Journal of Sedimentary Research*, v. 68, p. 63-79.
- RUSSELL, A.D., and MORFORD, J.L., 2001, The behavior of redox-sensitive metals across a laminated-massive-laminated transition in Saanich Inlet, British Columbia: *Marine Geology*, v. 174, p. 341-354.
- SAYLOR, B.Z., KAUFMAN, A.J., GROTZINGER, J.P., and URBAN, F., 1998, A composite reference section for terminal Proterozoic strata of southern Namibia: *Journal of Sedimentary Research*, v. 68, p. 1223-1235.
- SCHIEBER, J., 1986, The Possible Role of Benthic Microbial Mats during the Formation of Carbonaceous Shales in Shallow Midproterozoic Basins: *Sedimentology*, v. 33, p. 521-536.
- SCHIEBER, J., BOSE, P.K., ERIKSSON, P.G., BANERJEE, S., SARKAR, S., ALTERMANN, W., and CATUNEANU, O., 2007a, Atlas of Microbial Mat Features Preserved within the Siliciclastic Rock Record: *Atlases in Geoscience*, v. 2: Amsterdam, Elsevier, 311 p.
- SCHIEBER, J., SOUTHARD, J., and THAISEN, K., 2007b, Accretion of mudstone beds from migrating floccule ripples: *Science*, v. 318, p. 1760-1763.
- SCHOENHERR, J., REUNING, L., KUKLA, P.A., LITKE, R., URAI, J.L., SIEMANN, M., and RAWAHI, Z., 2009, Halite cementation and carbonate diagenesis of intra-salt reservoirs from the Late Neoproterozoic to Early Cambrian Ara Group (South Oman Salt Basin): *Sedimentology*, v. 56, p. 567-589.
- SCHREIBER, B.C., and EL TABAKH, M., 2000, Deposition and early alteration of evaporites: *Sedimentology*, v. 47, p. 215-238.

- SCHRÖDER, S., and GROTZINGER, J.P., 2007, Evidence for anoxia at the Ediacaran-Cambrian boundary: the record of redox-sensitive trace elements and rare earth elements in Oman: *Journal of the Geological Society*, v. 164, p. 175-187.
- SCHRÖDER, S., GROTZINGER, J.P., AMTHOR, J.E., and MATTER, A., 2005, Carbonate deposition and hydrocarbon reservoir development at the Precambrian-Cambrian boundary: The Ara Group in South Oman: *Sedimentary Geology*, v. 180, p. 1-28.
- SCHRÖDER, S., SCHREIBER, B.C., AMTHOR, J.E., and MATTER, A., 2003, A depositional model for the terminal Neoproterozoic Early Cambrian Ara Group evaporites in south Oman: *Sedimentology*, v. 50, p. 879-898.
- SCHRÖDER, S., SCHREIBER, B.C., AMTHOR, J.E., and MATTER, A., 2004, Stratigraphy and environmental conditions of the terminal Neoproterozoic-Cambrian period in Oman: evidence from sulphur isotopes: *Journal of the Geological Society*, v. 161, p. 489-499.
- SCHUBEL, K.A., and SIMONSON, B.M., 1990, Petrography and Diagenesis of Cherts from Lake Magadi, Kenya: *Journal of Sedimentary Petrology*, v. 60, p. 761-776.
- SELLEY, R.C., 1998, *Elements of Petroleum Geology*: San Diego, Academic Press, 470 p.
- SHEARMAN, D.J., 1985, Syndepositional and late diagenetic alteration of primary gypsum to anhydrite, *in* Schreiber, B.C., and Harner, H.L., eds., *Sixth International Symposium on Salt*: Alexandria, The Salt Institute, p. 41-50.
- SHIELDS, G.A., and WEBB, G.E., 2004, Has the REE composition of seawater changed over geological time?: *Chemical Geology*, v. 204, p. 103-107.
- SHOLKOVITZ, E.R., LANDING, W.M., and LEWIS, B.L., 1994, Ocean Particle Chemistry - the Fractionation of Rare-Earth Elements between Suspended Particles and Seawater: *Geochimica Et Cosmochimica Acta*, v. 58, p. 1567-1579.
- SHOLKOVITZ, E.R., and SCHNEIDER, D.L., 1991, Cerium Redox Cycles and Rare-Earth Elements in the Sargasso Sea: *Geochimica Et Cosmochimica Acta*, v. 55, p. 2737-2743.
- SHOLKOVITZ, E.R., SHAW, T.J., and SCHNEIDER, D.L., 1992, The Geochemistry of Rare-Earth Elements in the Seasonally Anoxic Water Column and Porewaters of Chesapeake Bay: *Geochimica Et Cosmochimica Acta*, v. 56, p. 3389-3402.
- SIEVER, R., 1989, *The Precambrian Silica Cycle: Abstracts of Papers of the American Chemical Society*, v. 198, p. 11-Geoc.

- SIEVER, R., 1991, Silica in the oceans: Biological-geochemical interplay, *in* Schneider, S., and Boston, P.J., eds., *Scientists on Gaia*: Cambridge, Massachusetts, MIT Press, p. 287-295.
- SIEVER, R., 1992, The Silica Cycle in the Precambrian: *Geochimica Et Cosmochimica Acta*, v. 56, p. 3265-3272.
- SIMONSON, B.M., 1985, Sedimentological Constraints on the Origins of Precambrian Iron-Formations: *Geological Society of America Bulletin*, v. 96, p. 244-252.
- SIMONSON, B.M., 1987, Early Silica Cementation and Subsequent Diagenesis in Arenites from 4 Early Proterozoic Iron Formations of North-America: *Journal of Sedimentary Petrology*, v. 57, p. 494-511.
- SIMONSON, B.M., 2003, Origin and evolution of large Precambrian iron formations, *in* Chan, M.A., and Archer, A.W., eds., *Extreme depositional environments: Mega end members in geologic time*, Geological Society of America Special Paper 370, p. 231-244.
- SIMONSON, B.M., and HASSLER, S.W., 1996, Was the deposition of large precambrian iron formations linked to major marine transgressions?: *Journal of Geology*, v. 104, p. 665-676.
- SLACK, J.F., GRENNE, T., BEKKER, A., ROUXEL, O.J., and LINDBERG, P.A., 2007, Suboxic deep seawater in the late Paleoproterozoic: Evidence from hematitic chert and iron formation related to seafloor-hydrothermal sulfide deposits, central Arizona, USA: *Earth and Planetary Science Letters*, v. 255, p. 243-256.
- SLAUGHTER, M., and HILL, R.J., 1991, The Influence of Organic-Matter in Organogenic Dolomitization: *Journal of Sedimentary Petrology*, v. 61, p. 296-303.
- STIGEBRANDT, A., and MOLVAER, J., 1988, On the Water Exchange of Framvaren: *Marine Chemistry*, v. 23, p. 219-228.
- STRAUSS, H., 1993, The Sulfur Isotopic Record of Precambrian Sulfates - New Data and a Critical-Evaluation of the Existing Record: *Precambrian Research*, v. 63, p. 225-246.
- STRAUSS, H., 1997, The isotopic composition of sedimentary sulfur through time: *Palaeogeography Palaeoclimatology Palaeoecology*, v. 132, p. 97-118.
- SUGITANI, K., 1992, Geochemical Characteristics of Archean Cherts and Other Sedimentary-Rocks in the Pilbara Block, Western Australia - Evidence for Archean Seawater Enriched in Hydrothermally-Derived Iron and Silica: *Precambrian Research*, v. 57, p. 21-47.
- SUGITANI, K., YAMAMOTO, K., WADA, H., BINU-LAL, S.S., and YONESHIGE, M., 2002, Geochemistry of Archean carbonaceous cherts deposited at

- immature island-arc setting in the Pilbara Block, Western Australia: *Sedimentary Geology*, v. 151, p. 45-66.
- SUMMONS, R.E., JAHNKE, L.L., HOPE, J.M., and LOGAN, G.A., 1999, 2-Methylhopanoids as biomarkers for cyanobacterial oxygenic photosynthesis: *Nature*, v. 400, p. 554-557.
- TAYLOR, J.C., 1991, Computer Programs for Standardless Quantitative Analysis of Minerals Using the Full Powder Diffraction Profile: *Powder Diffraction*, v. 6, p. 2-9.
- TAYLOR, K.G., and MACQUAKER, J.H.S., 2000, Early diagenetic pyrite morphology in a mudstone-dominated succession: the Lower Jurassic Cleveland Ironstone Formation, eastern England: *Sedimentary Geology*, v. 131, p. 77-86.
- TAYLOR, S.R., and MCLENNAN, S.M., 1985, *The Continental Crust: its Composition and Evolution*: Oxford, Blackwell, 312 p.
- THOMSON, J., JARVIS, I., GREEN, D.R.H., and GREEN, D., 1998, Oxidation fronts in Madeira Abyssal Plain turbidites: persistence of early diagenetic trace-element enrichments during burial, Site 950, *in* Weaver, P.P.E., Schmincke, H.-U., Firth, J.V., and Duffield, W., eds., *Proceedings of the Ocean Drilling Program, Scientific Results: Texas, Ocean Drilling Program*, College Station, p. 559-572.
- TRENDALL, A.F., 1972, Revolution in earth history: *Journal of the Geological Society of Australia*, v. 19, p. 287-311.
- TRENDALL, A.F., and BLOCKLEY, J.G., 1970, The iron formations of the Precambrian Hamersley Group, Western Australia: *Western Australian Geological Survey Bulletin* 119, 366 p.
- TRIBOVILLARD, N., ALGEO, T.J., LYONS, T., and RIBOULLEAU, A., 2006, Trace metals as paleoredox and paleoproductivity proxies: An update: *Chemical Geology*, v. 232, p. 12-32.
- TUKER, M.E., 2003, *Sedimentary Rocks in the Field*, John Wiley & Sons Ltd., 234 p.
- VAN DER WAL, A., NORDE, W., ZEHNDER, A.J.B., and LYKLEMA, J., 1997, Determination of the total charge in the cell walls of Gram-positive bacteria: *Colloids and Surfaces B-Biointerfaces*, v. 9, p. 81-100.
- WALTER, M.R., VEEVERS, J.J., CALVER, C.R., GORJAN, P., and HILL, A.C., 2000, Dating the 840-544 Ma Neoproterozoic interval by isotopes of strontium, carbon, and sulfur in seawater, and some interpretative models: *Precambrian Research*, v. 100, p. 371-433.
- WANTY, R.B., and GOLDHABER, M.B., 1992, Thermodynamics and Kinetics of Reactions Involving Vanadium in Natural Systems - Accumulation of

- Vanadium in Sedimentary-Rocks: *Geochimica Et Cosmochimica Acta*, v. 56, p. 1471-1483.
- WARREN, J.K., 2006, *Evaporites: sediments, resources and hydrocarbons*: New York, Springer, 1035 p.
- WARTHMAN, R., VAN LITH, Y., VASCONCELOS, C., MCKENZIE, J.A., and KARPOFF, A.M., 2000, Bacterially induced dolomite precipitation in anoxic culture experiments: *Geology*, v. 28, p. 1091-1094.
- WEBB, G.E., and KAMBER, B.S., 2000, Rare earth elements in Holocene reefal microbialites: A new shallow seawater proxy: *Geochimica Et Cosmochimica Acta*, v. 64, p. 1557-1565.
- WEHRLI, B., and STUMM, W., 1989, Vanadyl in Natural-Waters - Adsorption and Hydrolysis Promote Oxygenation: *Geochimica Et Cosmochimica Acta*, v. 53, p. 69-77.
- WESTALL, F., BONI, L., and GUERZONI, E., 1995, The Experimental Silicification of Microorganisms: *Palaeontology*, v. 38, p. 495-528.
- WESTRICH, J.T., and BERNER, R.A., 1984, The role of sedimentary organic matter in bacterial sulfate reduction: the G model tested: *The American Society of Limnology and Oceanography*, v. 29, p. 236-249.
- WIGNALL, P.B., 1994, *Black Shales*: Oxford, Calarendon Press, 127 p.
- WIGNALL, P.B., BOND, D.P.G., KUWAHARA, K., KAKUWA, Y., NEWTON, R.J., and POULTON, S.W., 2010, An 80 million year oceanic redox history from Permian to Jurassic pelagic sediments of the Mino-Tamba terrane, SW Japan, and the origin of four mass extinctions: *Global and Planetary Change*, v. 71, p. 109-123.
- WIGNALL, P.B., and NEWTON, R., 1998, Pyrite framboid diameter as a measure of oxygen deficiency in ancient mudrocks: *American Journal of Science*, v. 298, p. 537-552.
- WIGNALL, P.B., NEWTON, R., and BROOKFIELD, M.E., 2005, Pyrite framboid evidence for oxygen-poor deposition during the Permian-Triassic crisis in Kashmir: *Palaeogeography Palaeoclimatology Palaeoecology*, v. 216, p. 183-188.
- WILKIN, R.T., and ARTHUR, M.A., 2001, Variations in pyrite texture, sulfur isotope composition, and iron systematics in the Black Sea: Evidence for Late Pleistocene to Holocene excursions of the O₂-H₂S redox transition: *Geochimica Et Cosmochimica Acta*, v. 65, p. 1399-1416.
- WILKIN, R.T., and BARNES, H.L., 1996, Pyrite formation by reactions of iron monosulfides with dissolved inorganic and organic sulfur species: *Geochimica Et Cosmochimica Acta*, v. 60, p. 4167-4179.









- WILKIN, R.T., and BARNES, H.L., 1997, Formation processes of framboidal pyrite: *Geochimica Et Cosmochimica Acta*, v. 61, p. 323-339.
- WILKIN, R.T., BARNES, H.L., and BRANTLEY, S.L., 1996, The size distribution of framboidal pyrite in modern sediments: An indicator of redox conditions: *Geochimica Et Cosmochimica Acta*, v. 60, p. 3897-3912.
- WILKINSON, M., MILLIKEN, K.L., and HASZELDINE, R.S., 2001, Systematic destruction of K-feldspar in deeply buried rift and passive margin sandstones: *Journal of the Geological Society*, v. 158, p. 675-683.
- WILLE, M., NAGLER, T.F., LEHMANN, B., SCHRÖDER, S., and KRAMERS, J.D., 2008, Hydrogen sulphide release to surface waters at the Precambrian/Cambrian boundary: *Nature*, v. 453, p. 767-769.
- WILLIAMS, L.A., 1984, Subtidal stromatolites in Monterey Formation and other organic-rich rocks as suggested contributors to petroleum formation: *American Association of Petroleum Geologists Bulletin*, v. 68, p. 1879-1893.
- WILLIAMS, L.A., and CRERAR, D.A., 1985, Silica Diagenesis .2. General Mechanisms: *Journal of Sedimentary Petrology*, v. 55, p. 312-321.
- WILLIAMS, L.A., PARKS, G.A., and CRERAR, D.A., 1985, Silica Diagenesis .1. Solubility Controls: *Journal of Sedimentary Petrology*, v. 55, p. 301-311.
- WORTHING, M.A., 2005, Petrology and geochronology of Neoproterozoic dyke swarm from Marbat, South Oman: *Journal of African Earth Sciences* v. 41, p. 248-265.
- WRIGHT, D.T., 1999, The role of sulphate-reducing bacteria and cyanobacteria in dolomite formation in distal ephemeral lakes of the Coorong region, South Australia: *Sedimentary Geology*, v. 126, p. 147-157.
- WRIGHT, D.T., and WACEY, D., 2005, Precipitation of dolomite using sulphate-reducing bacteria from the Coorong Region, South Australia: significance and implications: *Sedimentology*, v. 52, p. 987-1008.
- YEE, N., BENNING, L.G., PHOENIX, V.R., and FERRIS, F.G., 2004, Characterization of metal-cyanobacteria sorption reactions: A combined macroscopic and infrared spectroscopic investigation: *Environmental Science & Technology*, v. 38, p. 775-782.
- ZHANG, J., AMAKAWA, H., and NOZAKI, Y., 1994, The Comparative Behaviors of Yttrium and Lanthanides in the Seawater of the North Pacific: *Geophysical Research Letters*, v. 21, p. 2677-2680.
- ZHANG, J., and NOZAKI, Y., 1996, Rare earth elements and yttrium in seawater: ICP-MS determinations in the East Caroline, Coral Sea, and South Fiji basins of the western South Pacific Ocean: *Geochimica Et Cosmochimica Acta*, v. 60, p. 4631-4644.

- ZHENG, Y., ANDERSON, R.F., VAN GEEN, A., and KUWABARA, J., 2000, Authigenic molybdenum formation in marine sediments: A link to pore water sulfide in the Santa Barbara Basin: *Geochimica et Cosmochimica Acta*, v. 64, p. 4165-4178.
- ZHOU, C.M., and JIANG, S.Y., 2009, Palaeoceanographic redox environments for the lower Cambrian Hetang Formation in South China: Evidence from pyrite framboids, redox sensitive trace elements, and sponge biota occurrence: *Palaeogeography Palaeoclimatology Palaeoecology*, v. 271, p. 279-286.

Appendices

Appendix I. Wireline log interpretation

In total 12 wells were interpreted from the Athel Basin and the Birba Platform to investigate the vertical and the lateral variability. Ten wells were included in well-correlation in Chapter 5 (Fig. 5.2). This appendix presents all wells and all available logs (GR, sonic, neutron, density, porosity and oil saturation) from each well. Wells location is shown in Chapter 5 (Figs. 2.1 & 5.1).

Lithofacies key:	
	LF1: laminated microcrystalline quartz-rich mudstones
	LF2: laminated microcrystalline quartz-dominated mudstones
	LF3: Laminated microcrystalline quartz-rich, detritus-bearing mudstones
	LF4: Laminated silt-rich, clay-mineral bearing mudstones
	LF5-6: Evaporite facies (anhydrite and halite)
	LF7: Slumped mudstones
	LF8: Brecciated mudstones
	LF9: Microcrystalline quartz-, carbonate- and detritus- bearing mudstones

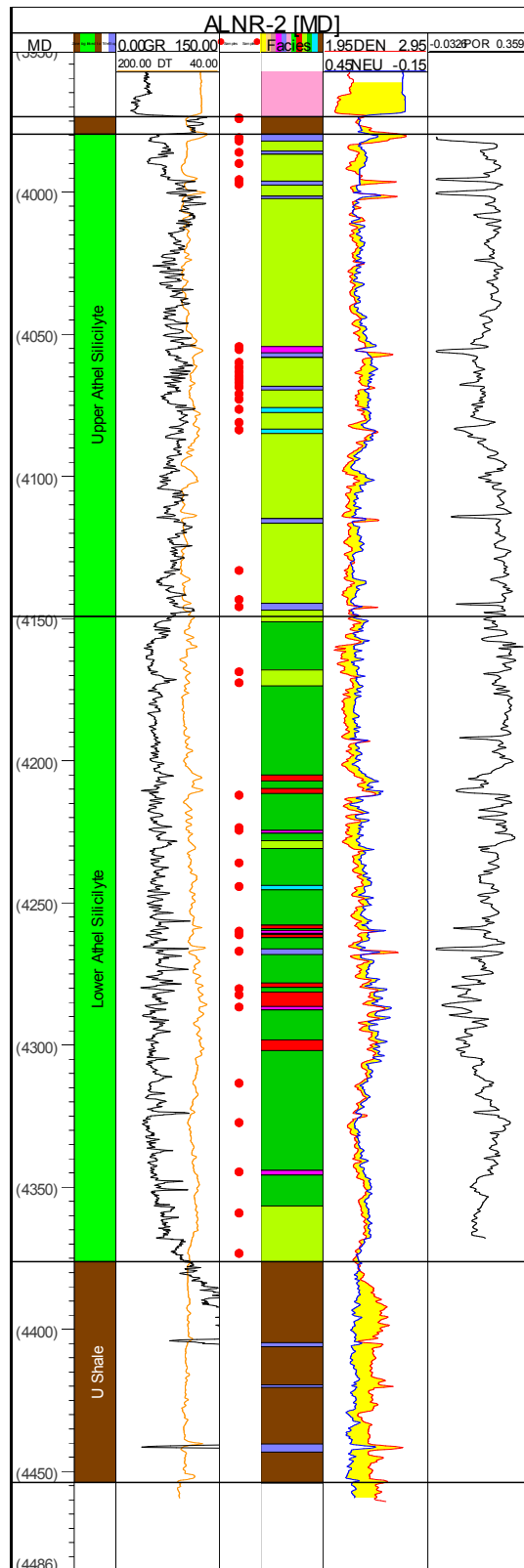


Figure 1. Showing wireline logs (GR, sonic, neutron, density and porosity) from well ALNR-2, located in the basin centre, as well as interpreted lithofacies (middle log). Most of the studied samples are obtained from this well and their depth is shown in red circles. The Thuleilat Shale encountered in this well is very thin (< 5 m) and the U Shale is around 75 m thick. Silica-dominated and silica-rich lithofacies are common in the Lower Athel Silicilyte, while silica-rich, detritus-bearing lithofacies is common in the Upper Athel Silicilyte. Carbonate-bearing lithofacies abundance increases towards the Upper Athel Silicilyte and in the bounding mudstones.

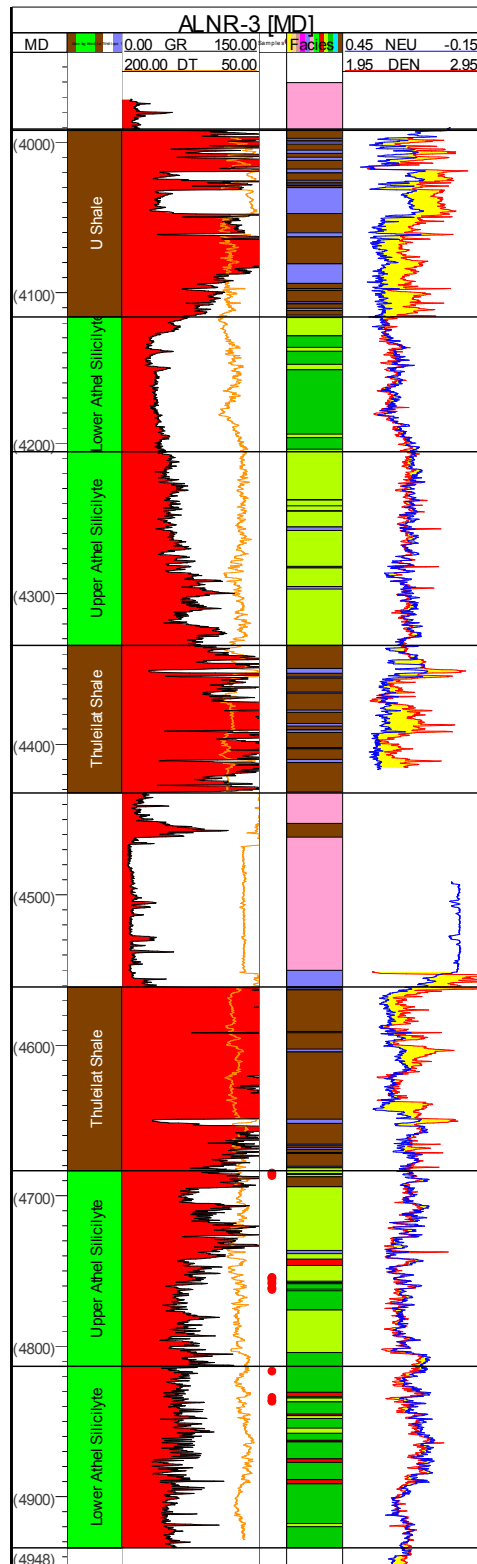


Figure 2. Showing wireline logs (GR, sonic, neutron and density) from well ALNR-3 located in the basin centre. It also shows interpreted lithofacies (middle log) from the Athel Silicilyte and the bounding mudstones. This well encountered two slabs of the Athel Silicilyte that are separated by an evaporite unit. The upper slab is upside down, which is indicated by opposite GR trend; decreasing from bottom to top section, whereas all wells show an increase in GR towards the upper Athel Silicilyte. This turning is probably caused by halokinesis. The samples obtained from this well are shown in red circles. The lower slab and the upper slab detailed interpretation are shown below in Fig. 3 and 4; respectively.

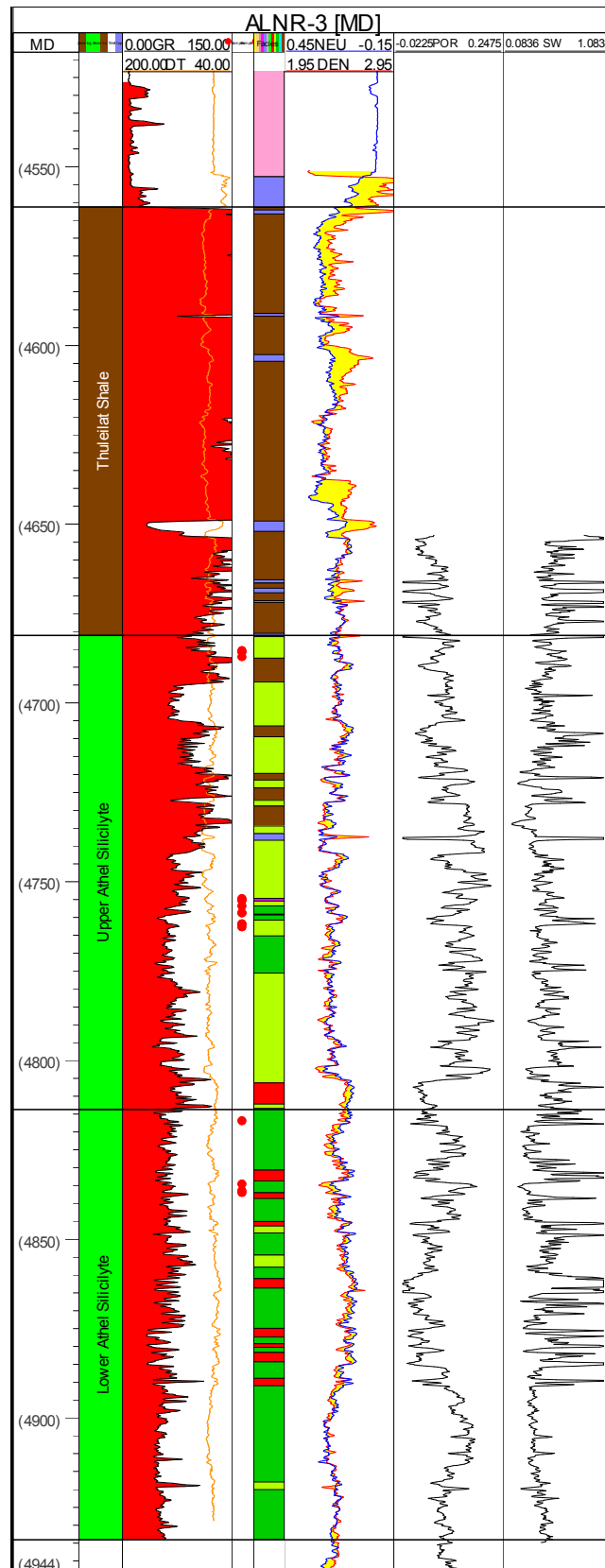


Figure 3. Showing wireline logs (GR, sonic, neutron, density, water saturation and porosity) from the lower slab of well ALNR-3 as well as interpreted lithofacies (middle log). Samples obtained from this well are shown in red circles. Silica-dominated and silica-rich lithofacies are common in the Lower Athel Silicilyte, whereas silica-rich, detritus-bearing lithofacies is common in the Upper Athel Silicilyte. The upper section of the Athel Silicilyte is interbedded with silt-rich lithofacies.

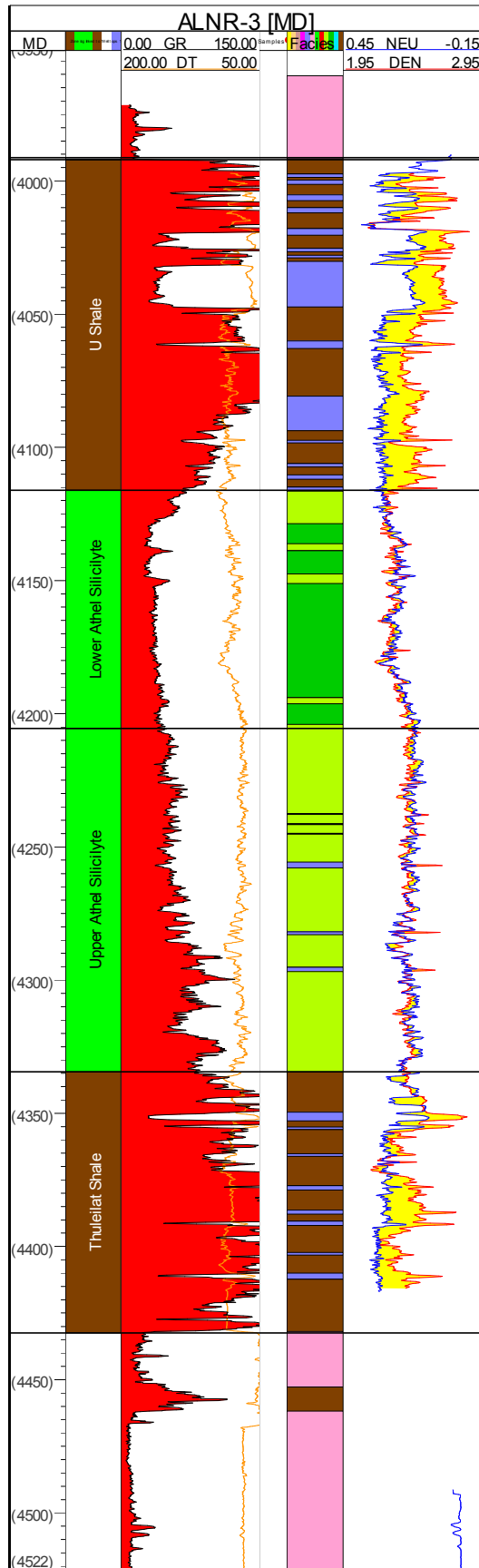


Figure 4. Showing wireline logs (GR, sonic, neutron and density) from well ALNR-3 upper slab as well as interpreted lithofacies (middle log). Silica-rich and silica-dominated lithofacies are common in the lower Athel Silicilyte, while silica-rich, detritus-bearing lithofacies is common in the upper Athel Silicilyte.

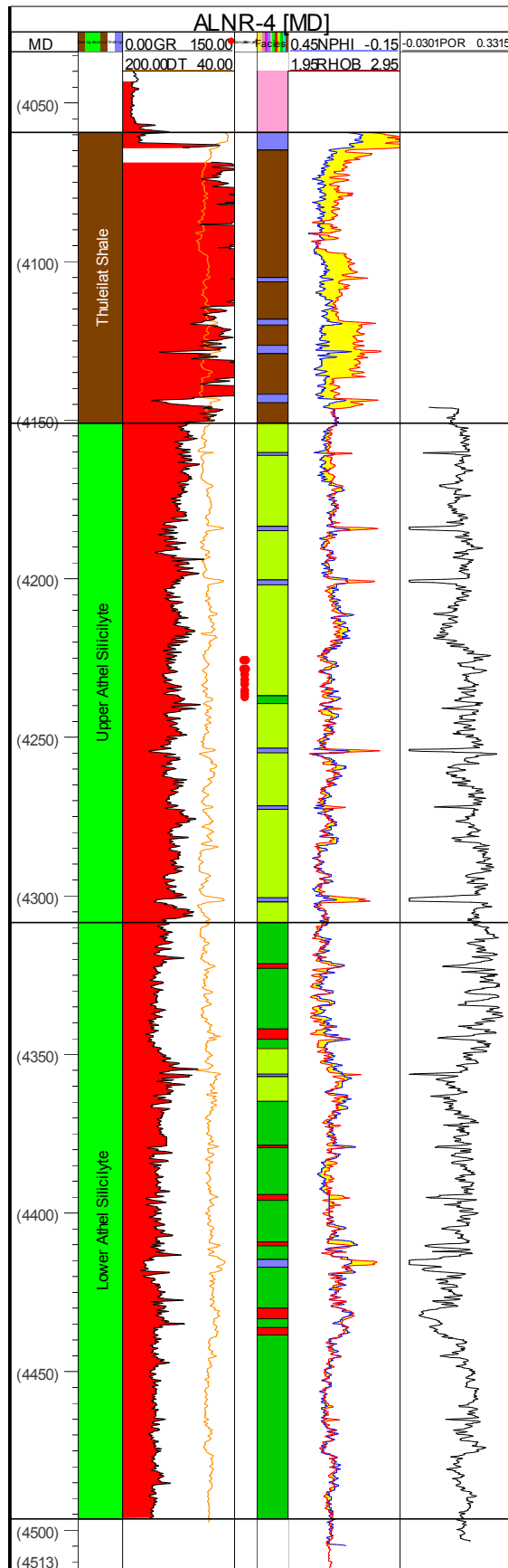


Figure 5. Showing wireline logs (GR, sonic, neutron, density and porosity) from well ALNR-4 located in the basin centre. It also shows interpreted lithofacies (middle log) from the Athel Silicilyte and the bounding mudstones. Depth of the samples obtained from this well is shown in red circle.

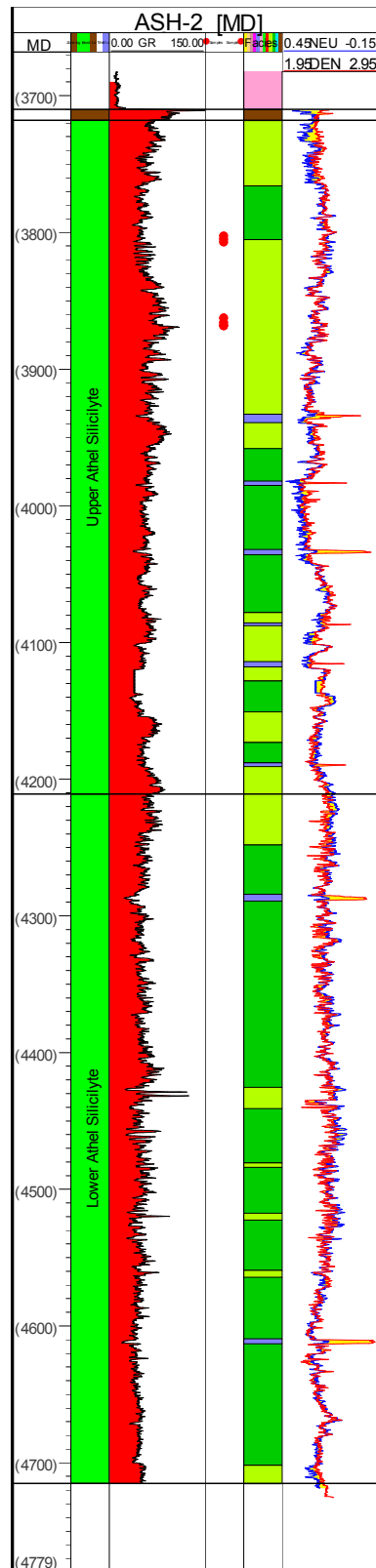


Figure 6. Showing wireline logs (GR, sonic, neutron and density) from well ASH-2 located in the basin centre. It also shows interpreted lithofacies (middle log) from the Athel Silicilyte. The depth of samples obtained from this well is shown in red circles. The total measured thickness of the Athel Silicilyte from this deviated well is 1014 m and the true stratigraphic thickness is around 430 m. The Thuleilat Shale encountered in this well is very thin (< 4 m), whereas the U Shale was not encountered (no wireline data available below the Athel Silicilyte).

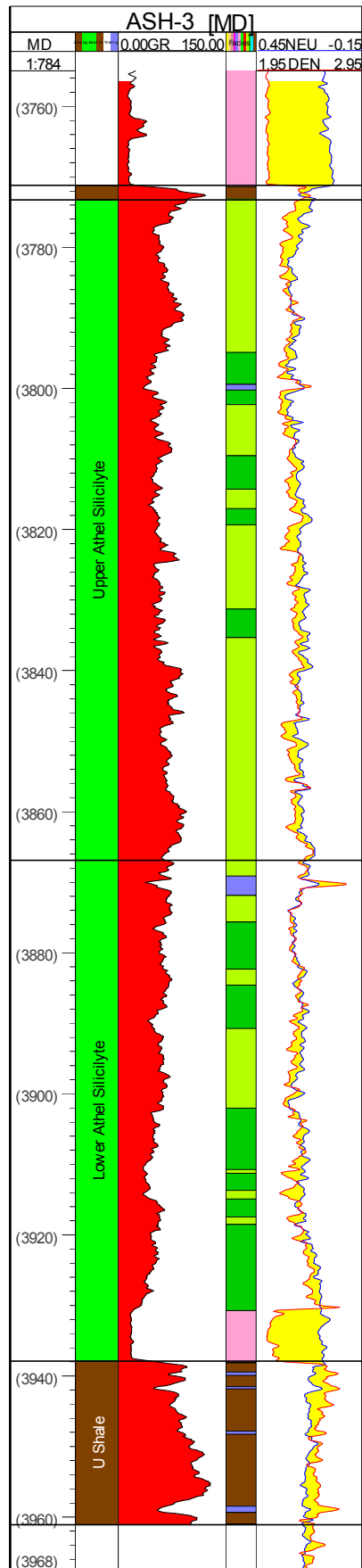


Figure 7. Showing wireline logs (GR, sonic, neutron and density) from well ASH-3 located in the basin centre. It also shows interpreted lithofacies (middle log) from the Athel Silicilyte., the Thuleilat Shale encountered in this well is very thin ($\approx 2\text{m}$ thick)

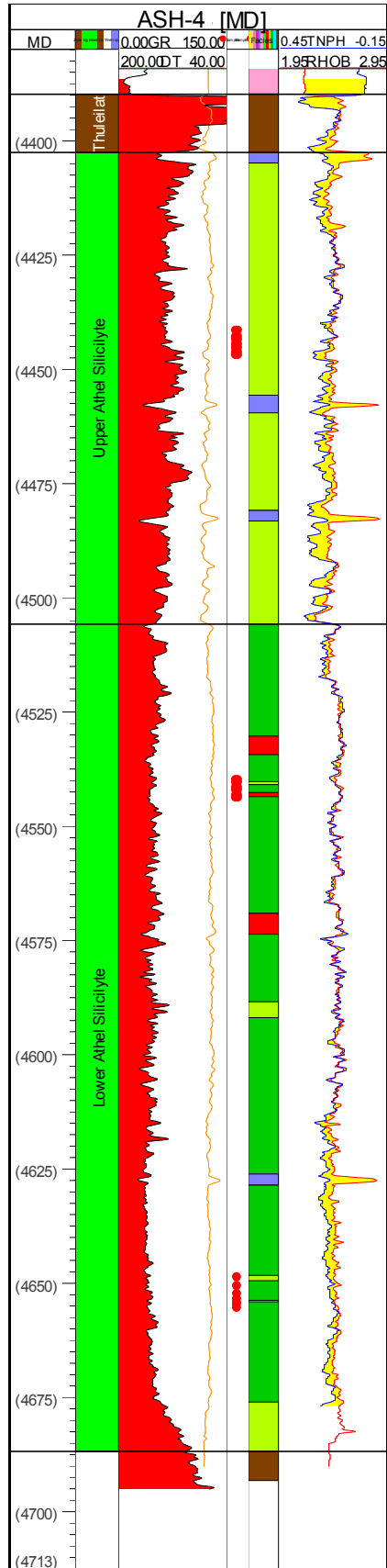


Figure 8. Showing wireline logs (GR, sonic, neutron and density) from well ASH-4 located in the basin centre. Interpreted lithofacies from the Athel Silicilyte is shown in the middle log. The depth of samples obtained from this well is shown in red circle. The Athel Silicilyte is enclosed between the Thuleilat and the U Shale. Thuleilat Shale in this well is very thin (< 14 m).

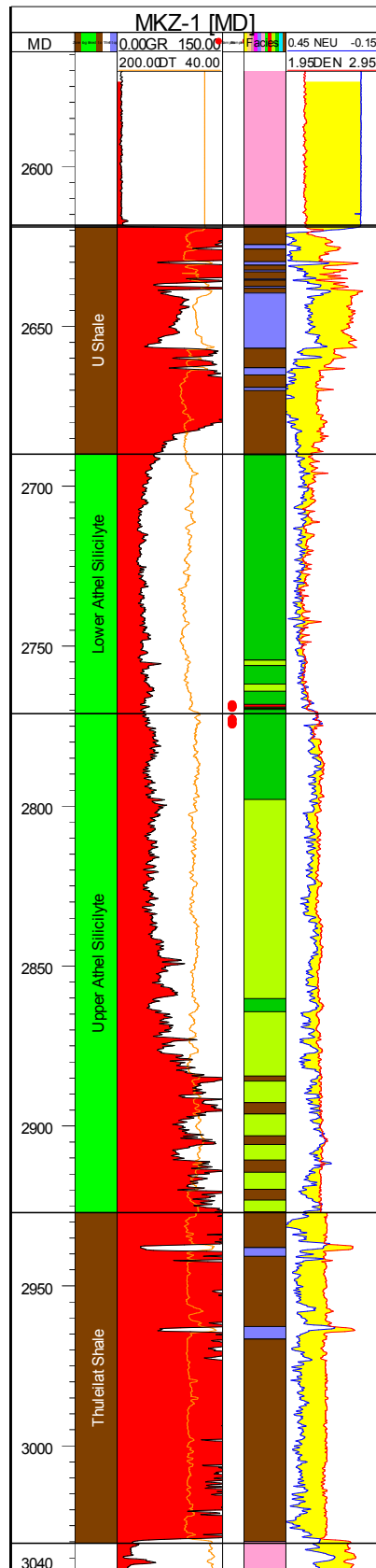


Figure 9. Showing wireline logs (GR, sonic, neutron and density) from well MKZ-1 located at the basin margin. Also it shows the interpreted lithofacies (middle log) from the Athel Silicilyte and the bounding mudstones. Note, the Athel Silicilyte is showing decrease in GR from the lower to the upper section, similar to ALNR-3 upper slab, and it is interpreted to be upside down due to the halokinesis.

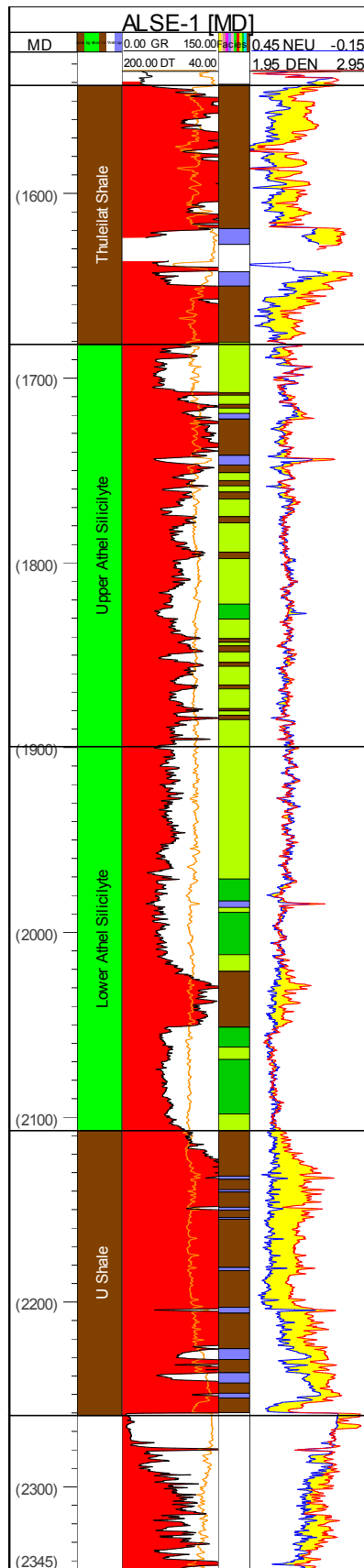


Figure 10. Showing wireline logs (GR, sonic, neutron and density) from well ALSE-1 located at the basin margin. Also it shows interpreted lithofacies (middle log) from the Athel Silicilyte and the bounding mudstones. Carbonate-bearing lithofacies (LF9) increases towards the upper Athel Silicilyte and it is common in the enclosing mudstones. The upper section of the Athel Silicilyte is interbedded with silt-rich lithofacies in a scale of 1-10s m.

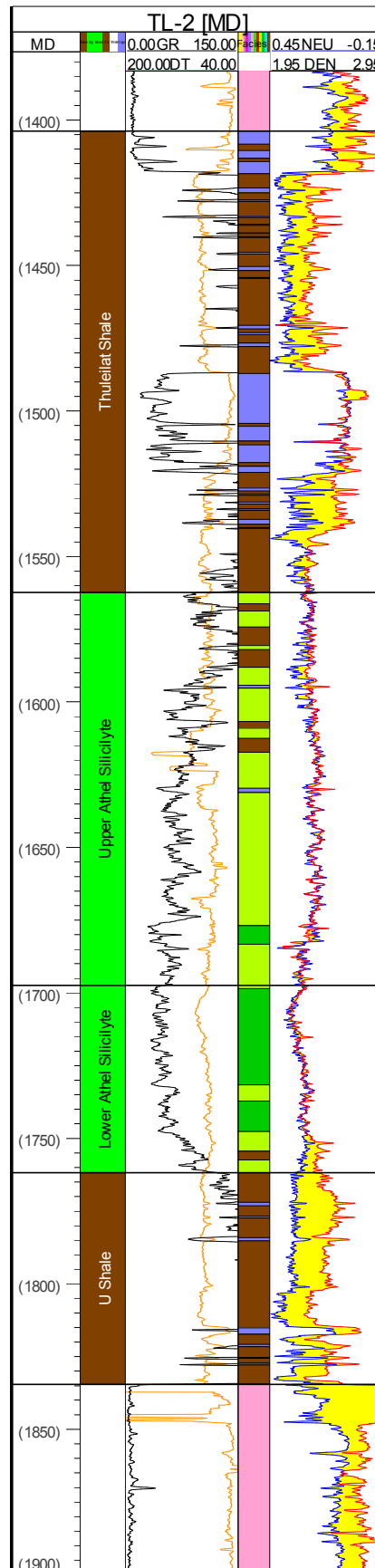


Figure 11. Showing wireline logs (GR, sonic, neutron and density) from well TL-2 drilled in the basin margin. It also shows interpreted lithofacies (middle log) of the Athel Silicilyte that is bounded by the U Shale and the Thuleilat Shale. All formations are enclosed between evaporite units of the A4 and A5 cycles.

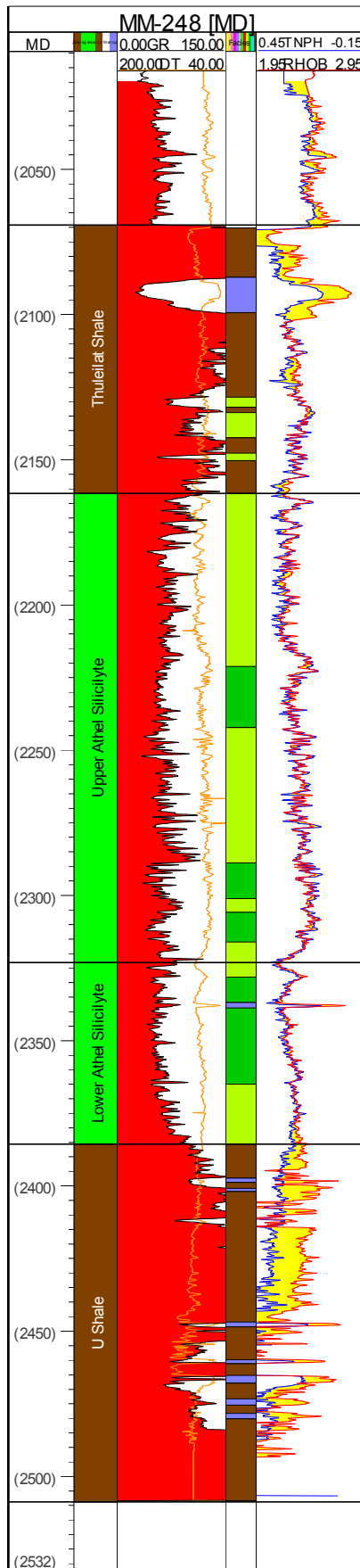


Figure 12. Showing wireline logs (GR, sonic, neutron and density) from well MM-248 located at the basin margin. Also it shows interpreted lithofacies from the Athel Silicilyte and the bounding mudstones.

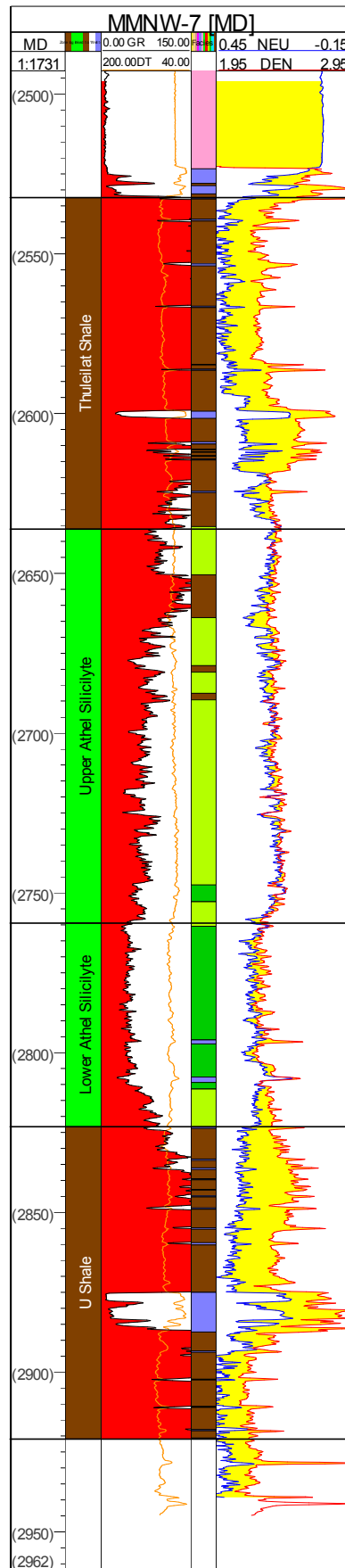


Figure 13. Showing wireline logs (GR, sonic, neutron and density) from well MMNW-7 located at the basin margin. Also it shows interpreted lithofacies from the Athel Silicilyte and the bounding mudstones.

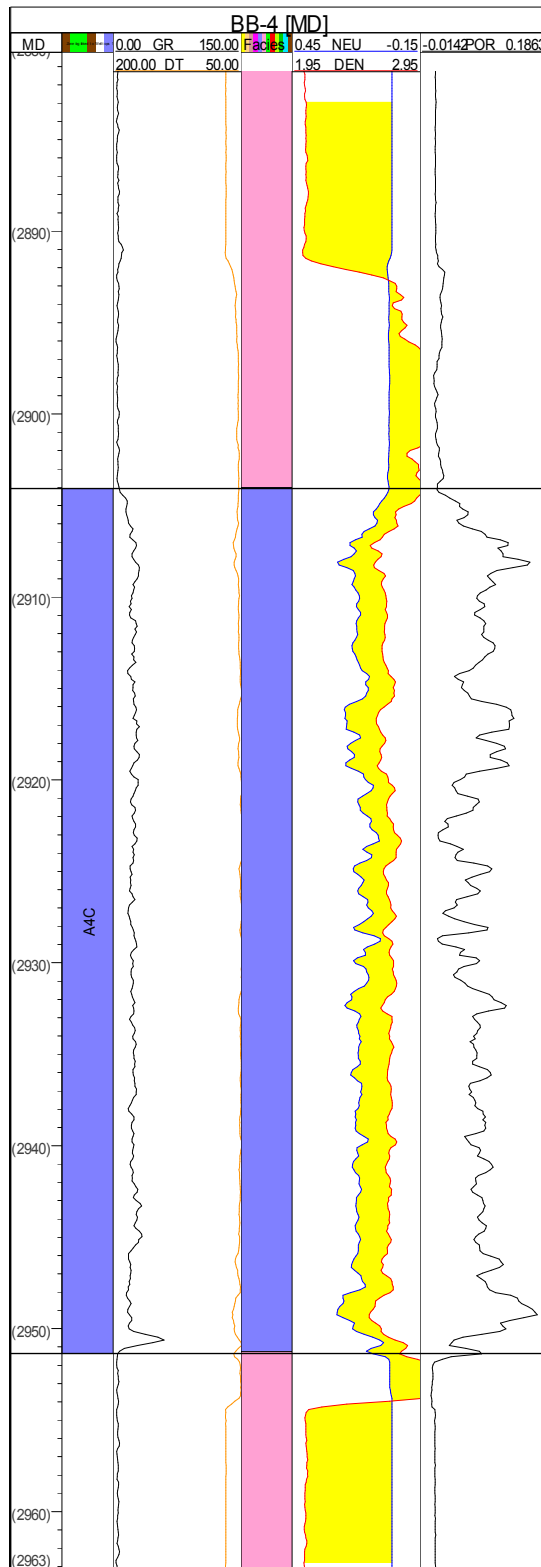


Figure 14. Showing wireline logs (GR, sonic, neutron, density and porosity) from well BB-4. This well was drilled in the Birba Platform where the Athel Silicilyte and the bounding mudstones are not encountered. Only encountered lithologies are A4 carbonates (47.5 m thick) that is enclosed between two lowstand evaporite units of the A4 (below) and A5 (above) cycles.

Appendix II. Core and thin-section photographs

This appendix show sampled cores of the Athel Silicilyte from six wells, as well as cores of the U Shale. A selection of representative thin-section microphotographs are also presented in both plane polarised light (PPL) and Backscattered electron image (BSEI) from each core. The core depth of each thin-section is indicated by a red-circle in core photographs. Core and thin-section description for each lithofacies were outlined in Chapter 5 and summarised in Table 5.1. Here lithofacies name is only indicated for each core and thin-section photograph with only a brief description.

Well ALNR-2

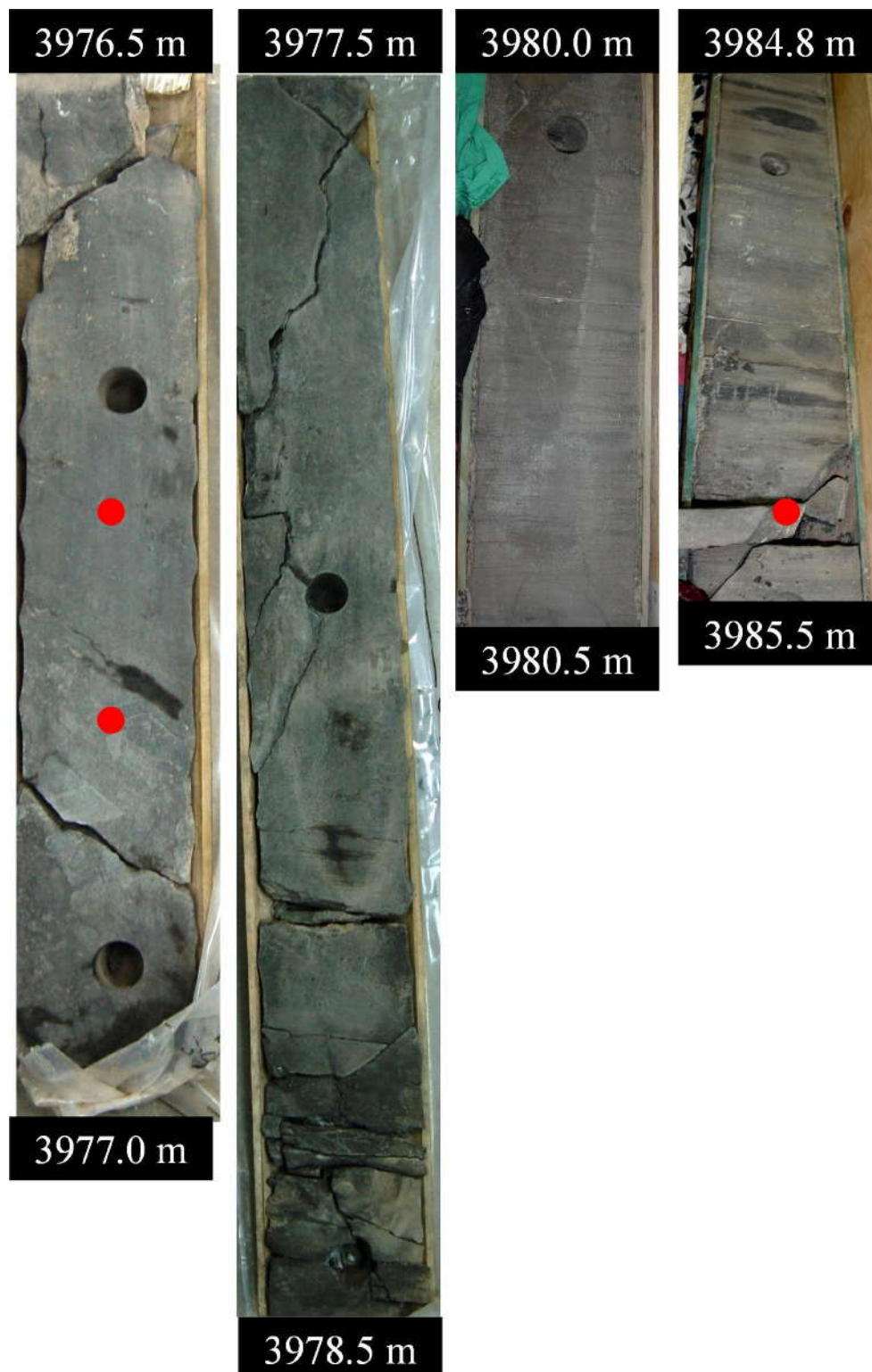


Figure 1. Depth interval from 3976.5-3976.8 m represents microcrystalline quartz-, carbonate- and detritus- bearing mudstones (LF9), from 3976.3-3976.5 m represents brecciated mudstones (LF8), from 3980.0-3980.5 m and 3984.8-3985.5 m both represent laminated microcrystalline quartz-rich, detritus-bearing mudstones (LF3). Red circles show core depth of the thin-section microphotographs presented in Figure 2. These samples are (from top to bottom): ALNR-2(4), ALNR-2(5) and ALNR-2(8).

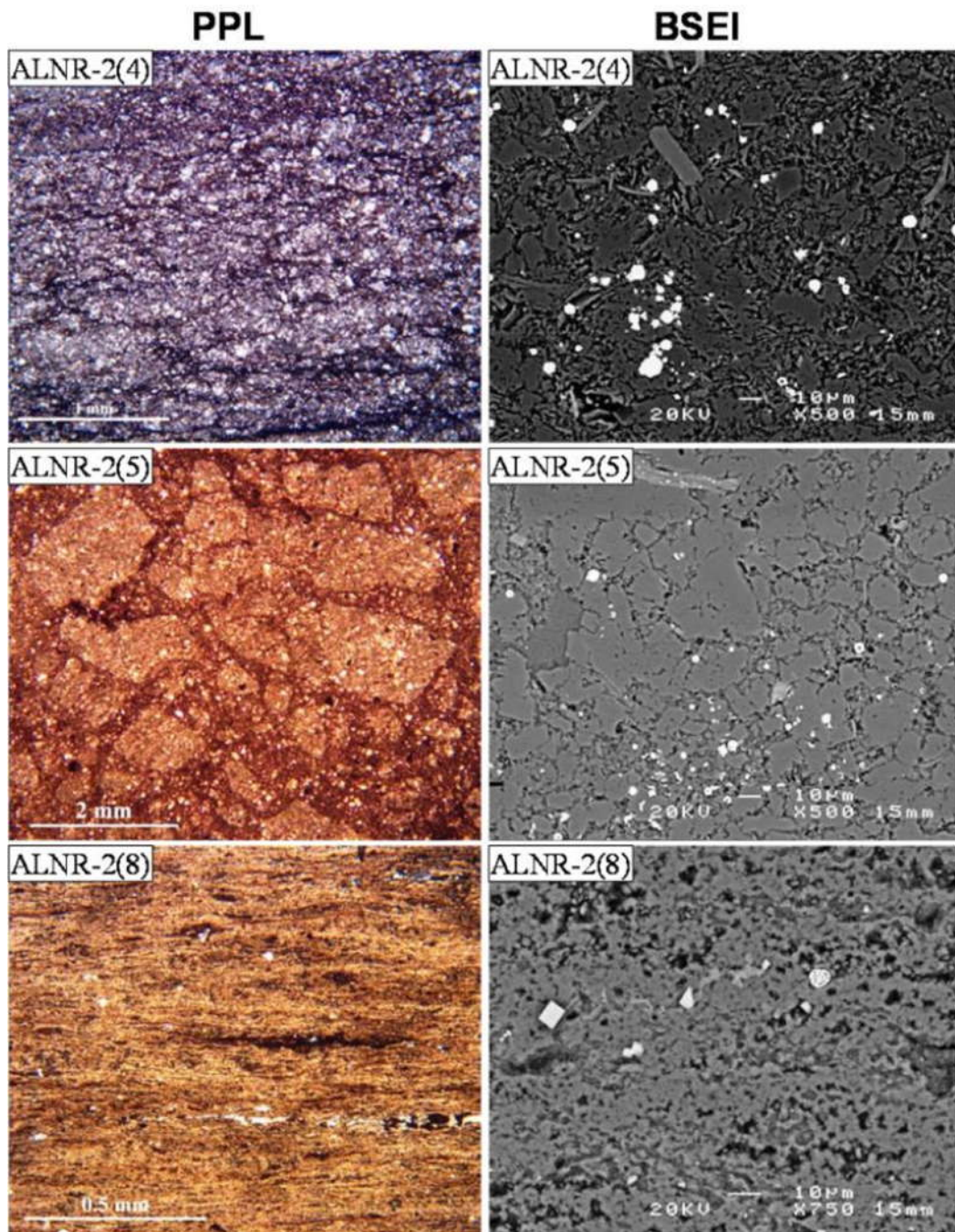


Figure 2. Sample ALNR-2(4) represents microcrystalline quartz-, carbonate- and detritus-bearing mudstones (LF9). This sample occurs very close towards the transition from Athel Silicilyte to the Thuleilat Shale. Note the abundance of detrital mica (light grey elongated shape). Sample ALNR-2(5) represents brecciated mudstones (LF8) and it is cemented by dolomite. Sample ALNR-2(8) represents laminated microcrystalline quartz-rich, detritus-bearing mudstones (LF3).

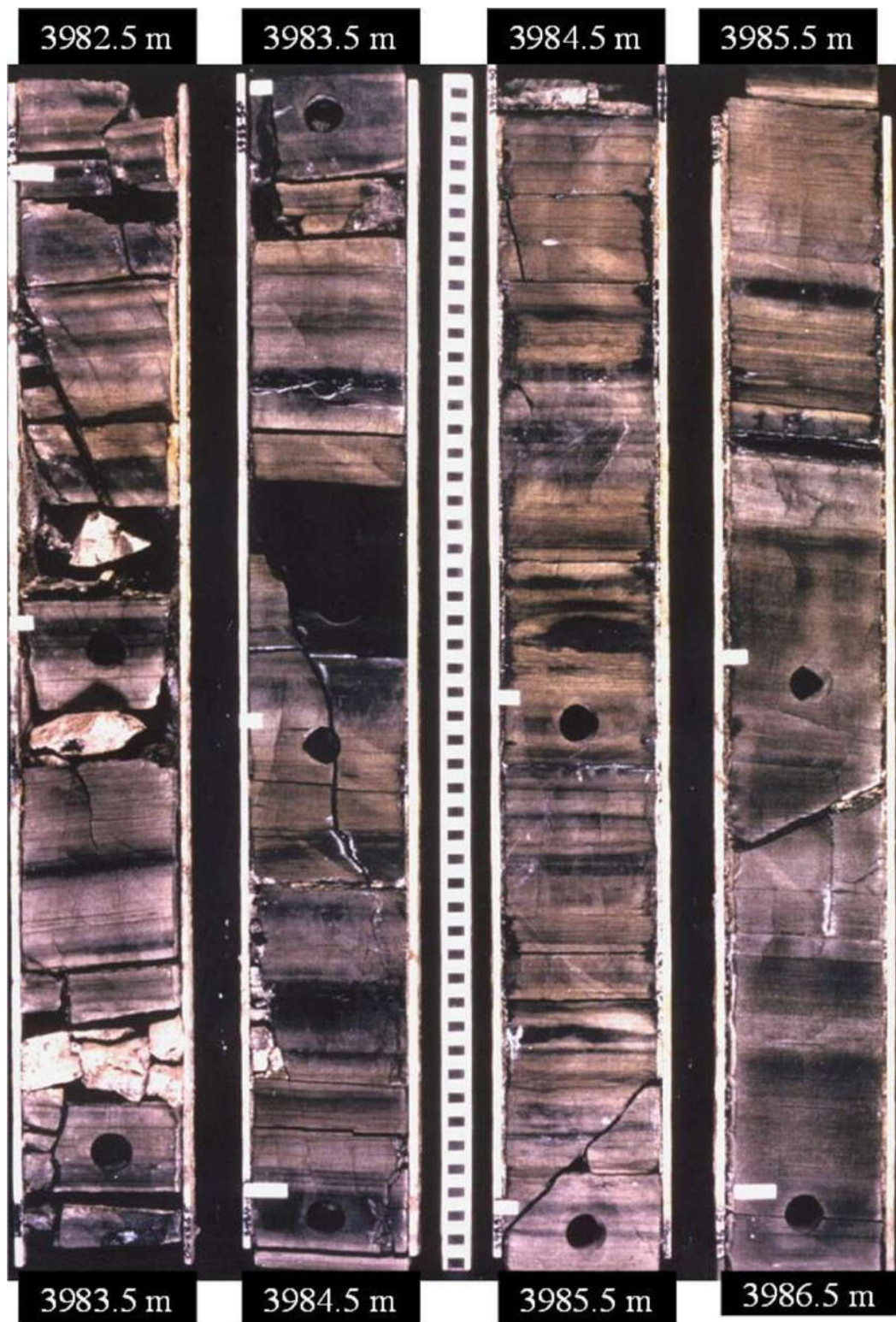


Figure 3. Depth interval from 3982.5-3986.5 m represents laminated microcrystalline quartz-rich, detritus-bearing mudstones (LF3). This lithofacies is moderately fissile and laminated



Figure 4. Depth interval from 4046.0-4048.5 m represents laminated microcrystalline quartz-rich, detritus-bearing mudstones (LF3), from 4048.5 -4049.0 m is hard to determine lithofacies since it is broken, from 4049.0- 4049.5 m represents LF3, from 4049.5-4049.75 m represents slumped mudstones (LF7), from and 4049.75-4050.0 m represents LF3, from 4050.0-4050.25 m represents microcrystalline quartz-, carbonate- and detritus- bearing mudstones (LF9), from and 4050.25-4050.75 m represents LF7 and from and 4050.75-4051.0 m represents LF3. The red circle shows core depth of the thin-section microphotographs presented in Figure 6 of sample ALNR-2(11).



Figure 5. Depth interval from 4050.0-4050.25 m represents microcrystalline quartz-, carbonate- and detritus- bearing mudstones (LF9), from and 4050.25-4050.75 m represents slumped mudstones (LF7) and from and 4050.75-4051.75 m represents laminated microcrystalline quartz-rich, detritus-bearing mudstones (LF3), from 4051.75-4052.3 m represents LF7, from 4052.3-4053.0 m is likely represents LF3. Red circles show core depth of the thin-section microphotographs presented in Figure 6. These samples are (from top to bottom): ALNR-2(12) and ALNR-2(13).

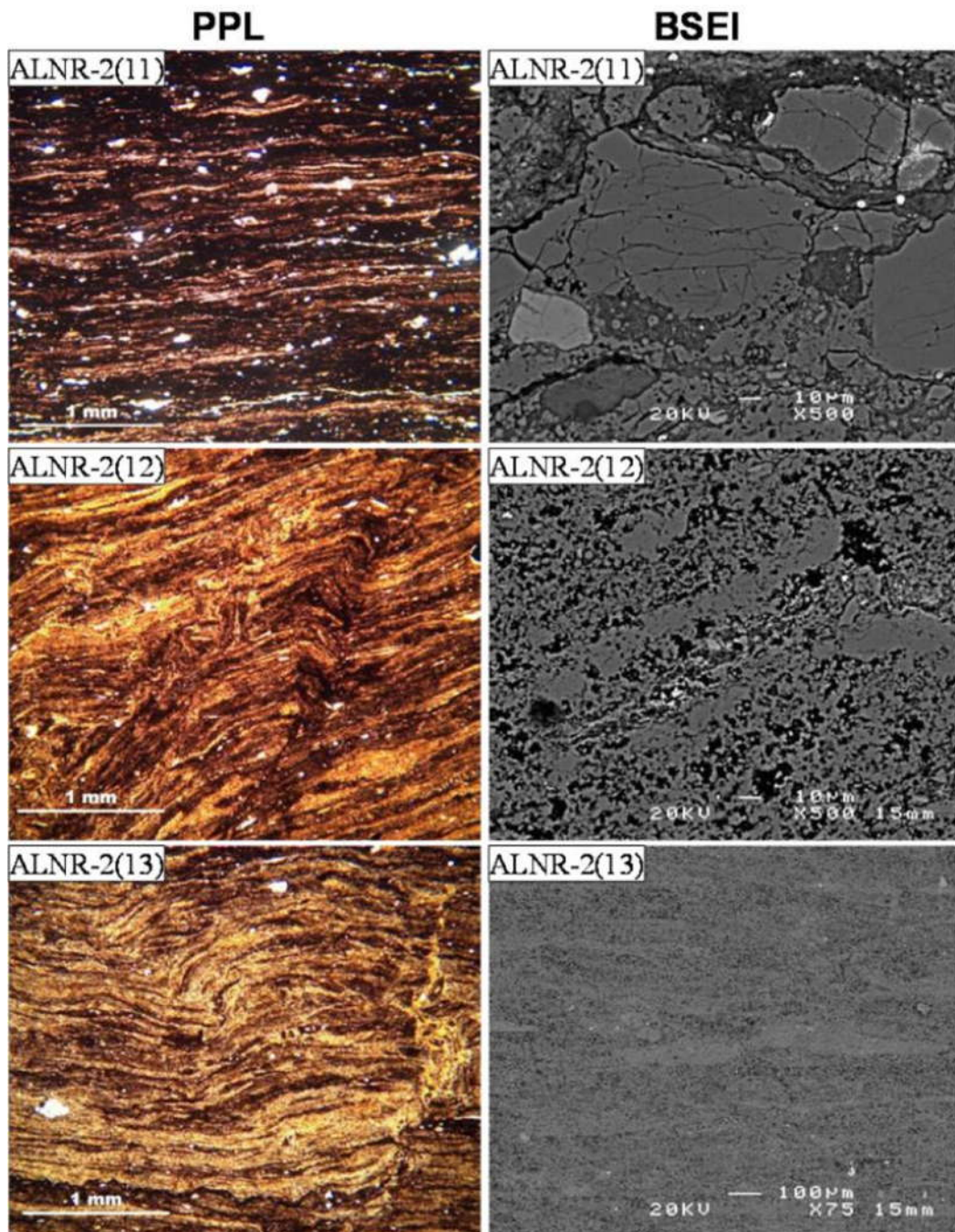


Figure 6. Sample ALNR-2(11) represents laminated microcrystalline quartz-rich, detritus-bearing mudstones (LF3). This sample contains relatively higher detrital quartz, feldspar and clay minerals. Sample ALNR-2(12) and ALNR-2(13) both represent slumped mudstones (LF7) and their mineralogical composition is similar to LF3.



Figure 7. Depth interval from 4055.0-4058.0 m represents laminated microcrystalline quartz-rich, detritus-bearing mudstones (LF3), which is moderately fissile and laminated. The red circle shows core depth of the thin-section microphotographs of sample ALNR-2(15) presented in Figure 9.



Figure 8. Depth interval from 4058.0-4060.0 m represents laminated microcrystalline quartz-rich, detritus-bearing mudstones (LF3), from 4060.0-4060.25 m represents slumped mudstones (LF7) and from 4060.25-4060.75 m represents LF3. The red circles show core depth of the thin-section microphotographs presented in Figure 9. These samples are (from top to bottom): ALNR-2(16) and ALNR-2(17).

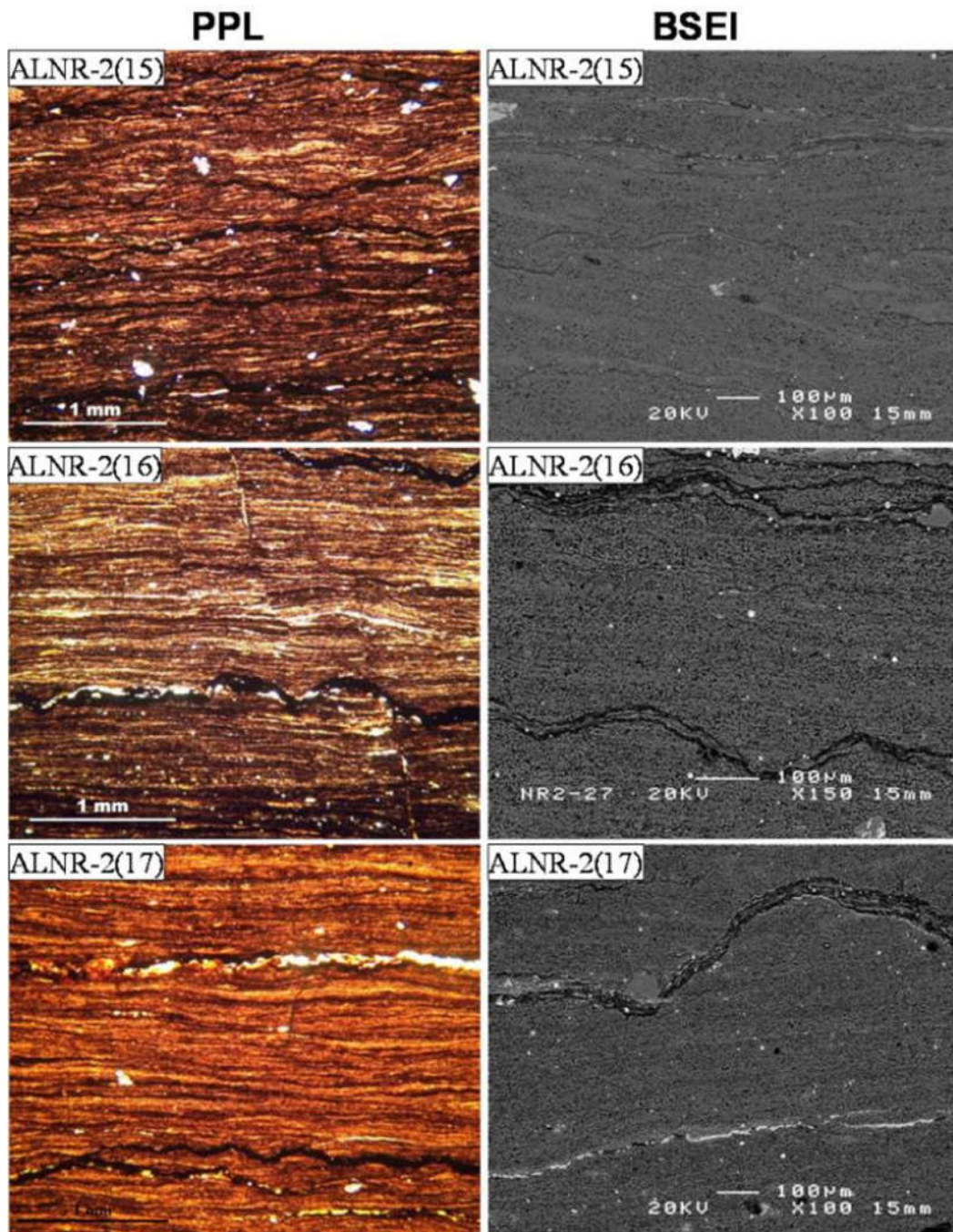


Figure 9. All samples represent laminated microcrystalline quartz-rich, detritus-bearing mudstones (LF3). These samples show wavy discontinuous lamination. These laminae alternate between silica-rich layers and more organic matter/clay mineral- rich layers. Also they show stylolites that are rich in organic matter and clay minerals.

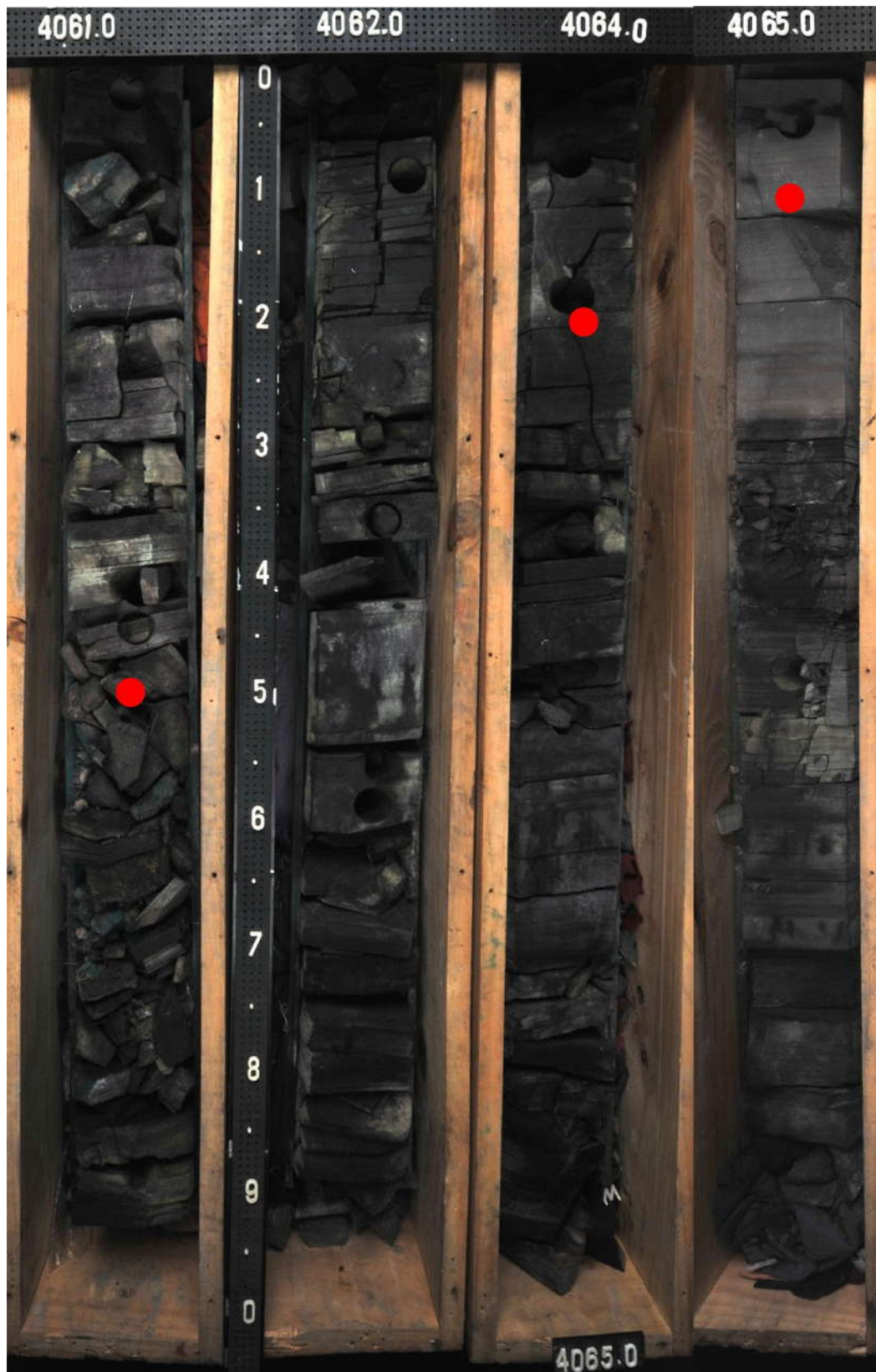


Figure 10. Depth interval from 4061.0-4065.0 m represents laminated microcrystalline quartz-rich, detritus-bearing mudstones (LF3), from 4065.0-4060.3 m represents microcrystalline quartz-, carbonate- and detritus- bearing mudstones (LF9) and from 4065.3-4066.0 m represents LF3. The red circles show core depth of the thin-section microphotographs presented in Figure 11. These samples are (from top to bottom): ALNR-2(19), ALNR-2(20) and ALNR-2(21).

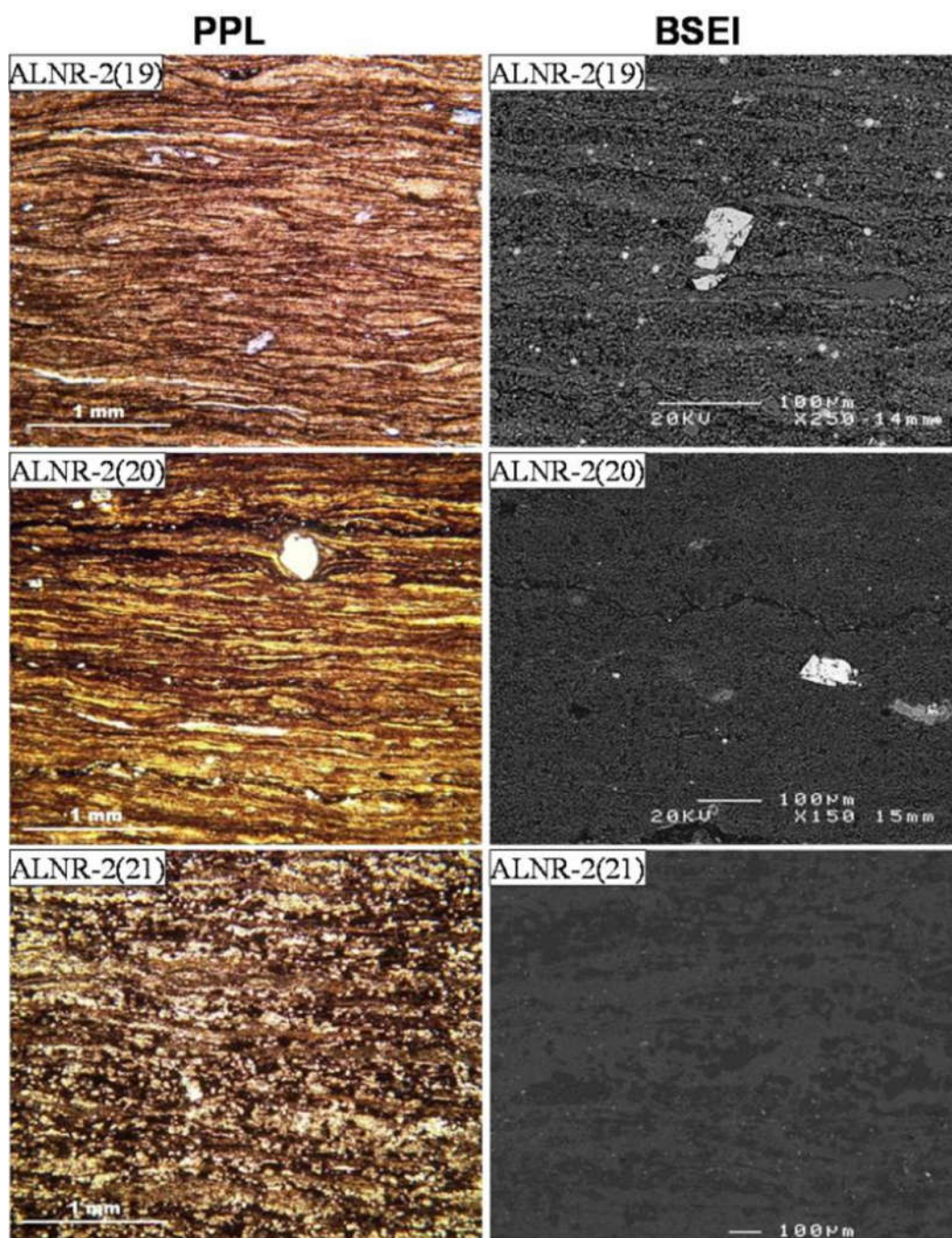


Figure 11. Samples ALNR-2(19) and ALNR-2(20) represent laminated microcrystalline quartz-rich, detritus-bearing mudstones (LF3). Sample ALNR-2(21) represents microcrystalline quartz-, carbonate- and detritus- bearing mudstones (LF9).



Figure 12. Depth interval from 4070.1-4070.2 m represents brecciated mudstones (LF8), from 4070.2-4073.1 m represents laminated microcrystalline quartz-rich, detritus-bearing mudstones (LF3). The red circle shows core depth of the thin-section microphotographs of sample ALNR-2(24) presented in Figure 14.



Figure 13. Depth interval from 4076.3-4076.5 m represents brecciated mudstones (LF8), from 4076.5.0-4077.6 m represents laminated microcrystalline quartz-rich, detritus-bearing mudstones (LF3) and from 4077.6-4080.0 m represents either slumped mudstones (LF7) or LF8. The red circles show core depth of the thin-section microphotographs presented in Figure 14. These samples are (from top to bottom): ALNR-2(25) and ALNR-2(26).

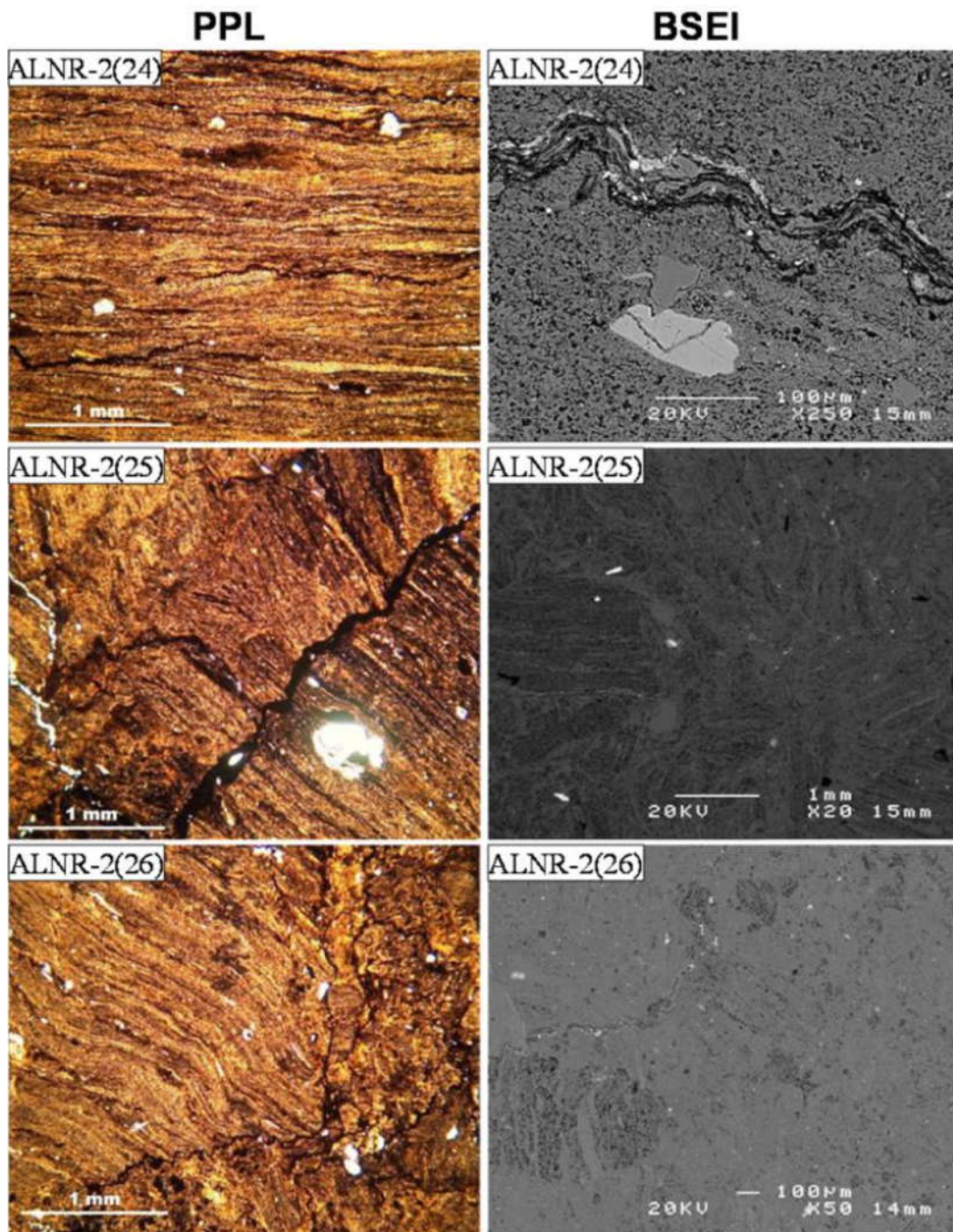


Figure 14. Sample ALNR-2(24) represents laminated microcrystalline quartz-rich, detritus-bearing mudstones (LF3). This sample shows quartz and feldspar with stylonite structure that rich in organic matter and clay minerals. Sample ALNR-2(25) and ALNR-2(26) represent brecciated mudstones (LF8) that consists of fragmented clasts of LF3.

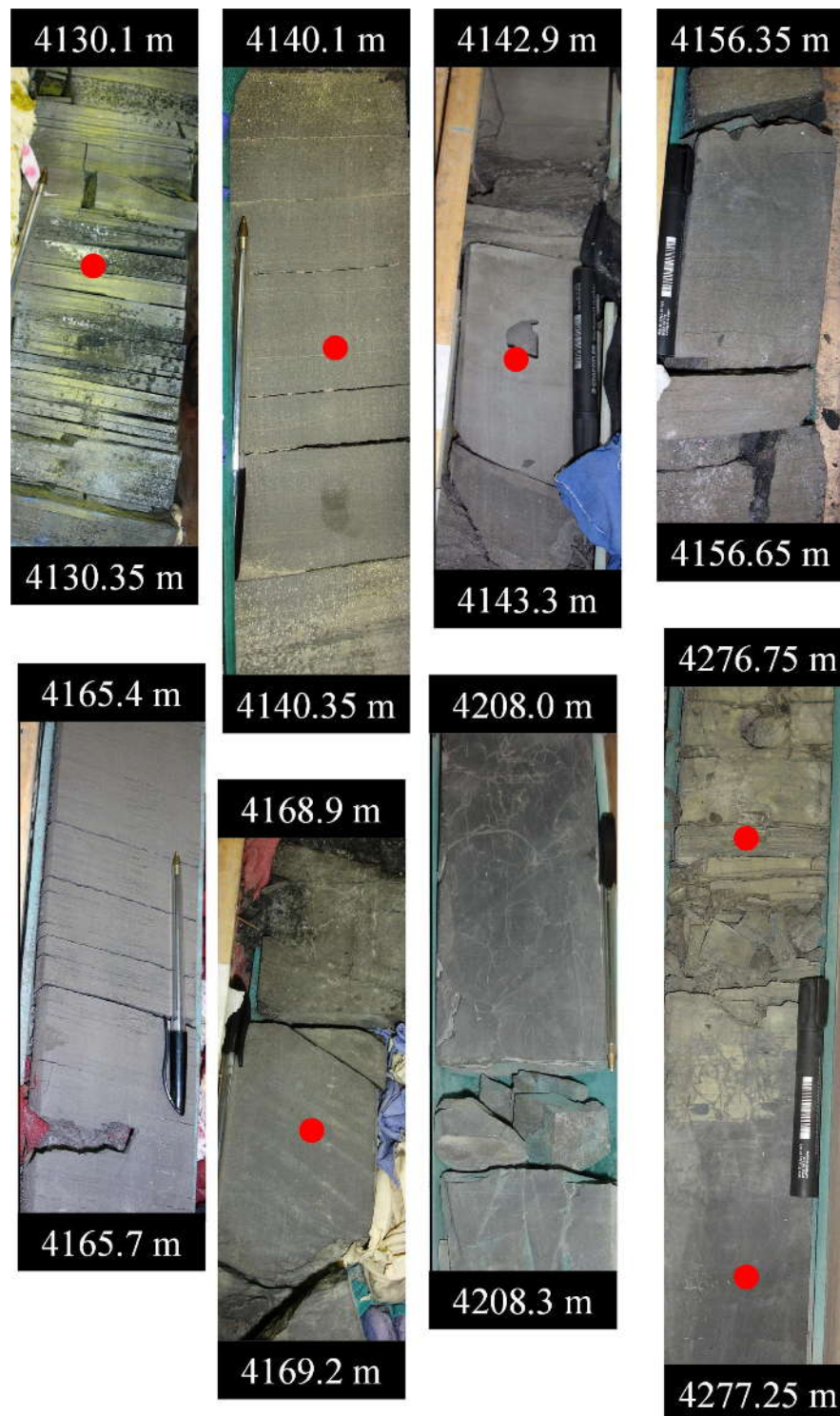


Figure 15. Depth interval from 4130.1-4130.35 m and from 4140.1-4140.35 m represent laminated microcrystalline quartz-rich, detritus-bearing mudstones (LF3), from 4142.9-4143.3 m represents in the middle microcrystalline quartz-, carbonate- and detritus-bearing mudstones (LF9; light coloured) enclosed between LF3, from 4156.35-4256.65 m represents laminated microcrystalline quartz-rich mudstones (LF1), from 4165.4-4165.7 m and from 4168.9-4169.2 m represent LF3, from 4208.0-4208.3 m represent laminated microcrystalline quartz-dominated mudstones (LF2), from 4276.75-4277.0 m represents LF1 and from 4277.0-4277.25 m represents LF2. Here LF1 and LF3 are hard to distinguish from core but microscopic analyses reveal their composition and thus their lithofacies division. The red circles show core depth of the thin-section microphotographs presented in Figures 16 & 17. These samples are (from top to bottom): ALNR-2(27), ALNR-2(28), ALNR-2(29), ALNR-2(32), ALNR-2(41), and ALNR-2(42).

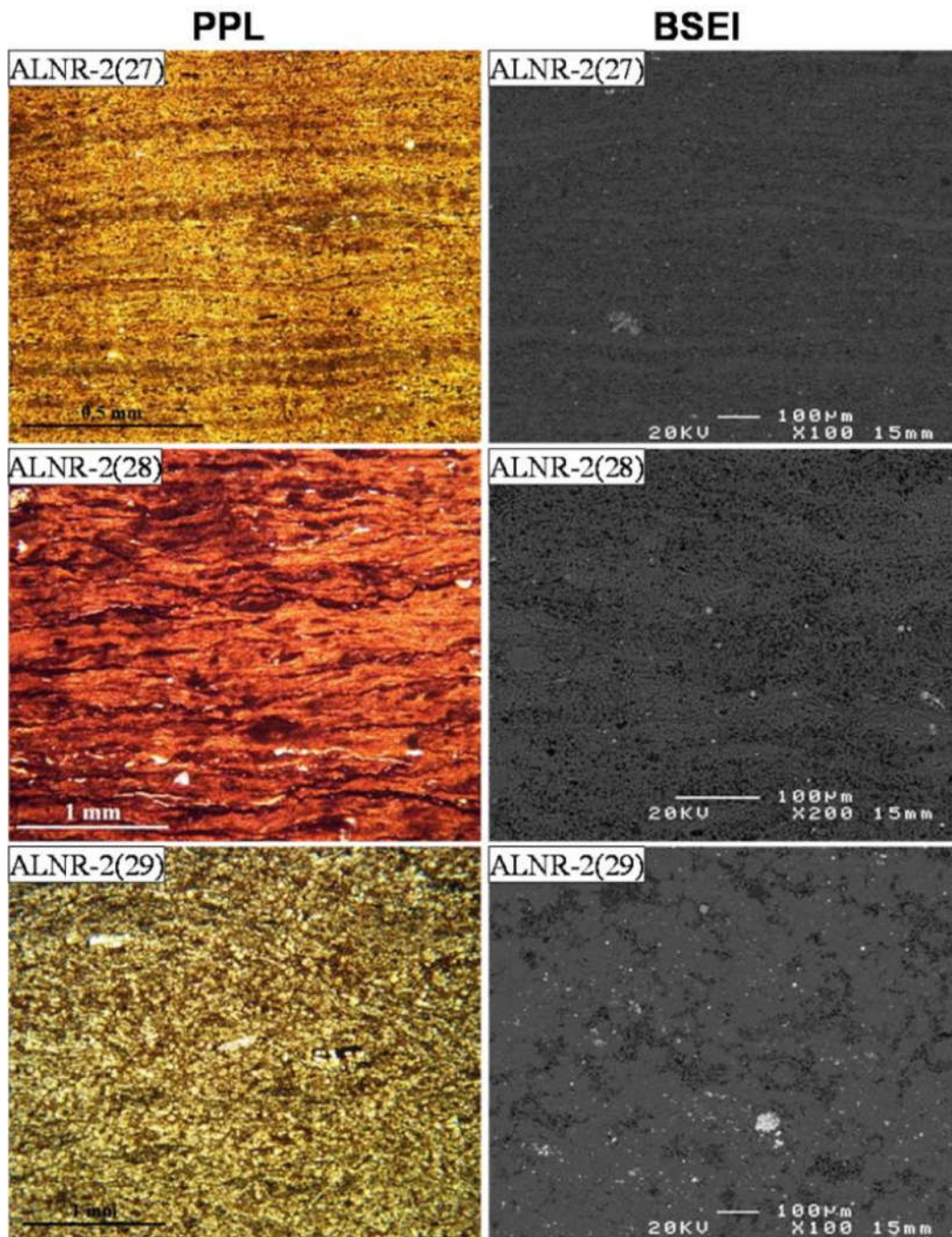


Figure 16. Sample ALNR-2(27) and ALNR-2(28) both represent laminated microcrystalline quartz-rich, detritus-bearing mudstones (LF3). This lithofacies shows wavy discontinuous lamination. These laminae alternate between silica-rich layers and more organic matter/clay mineral-rich layers. Sample ALNR-2(29) represents microcrystalline quartz-, carbonate- and detritus-bearing mudstones (LF9), which contain substantial amount of early diagenetic dolomite.

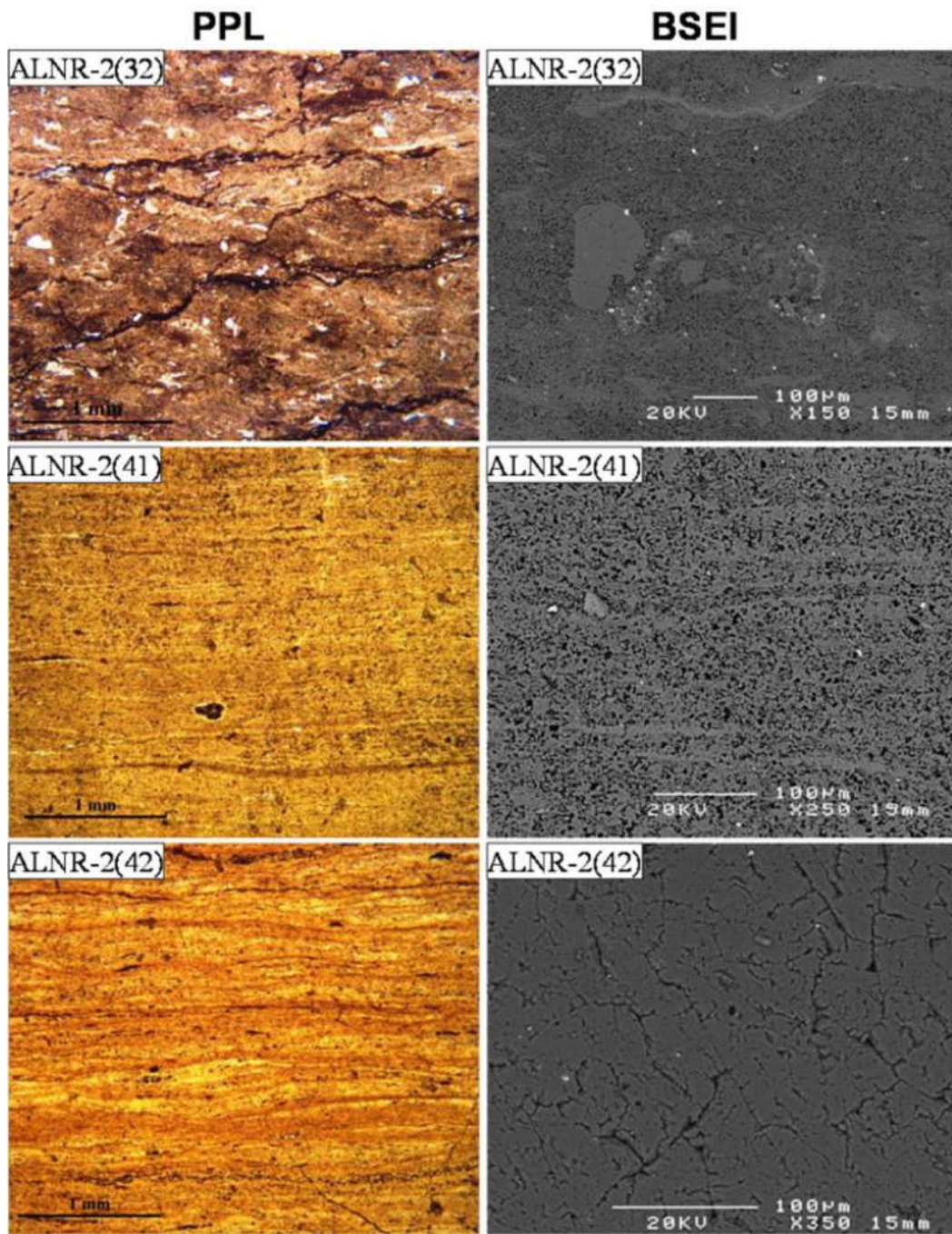


Figure 17. Sample ALNR-2(32) represents laminated microcrystalline quartz-rich, detritus-bearing mudstones (LF3), sample ALNR-2(41) represents laminated microcrystalline quartz-rich mudstones (LF1) and ALNR-2(42) represents laminated microcrystalline quartz-dominated mudstones (LF2). These samples show similar textures, only varying in the amount of microcrystalline quartz and clay mineral.

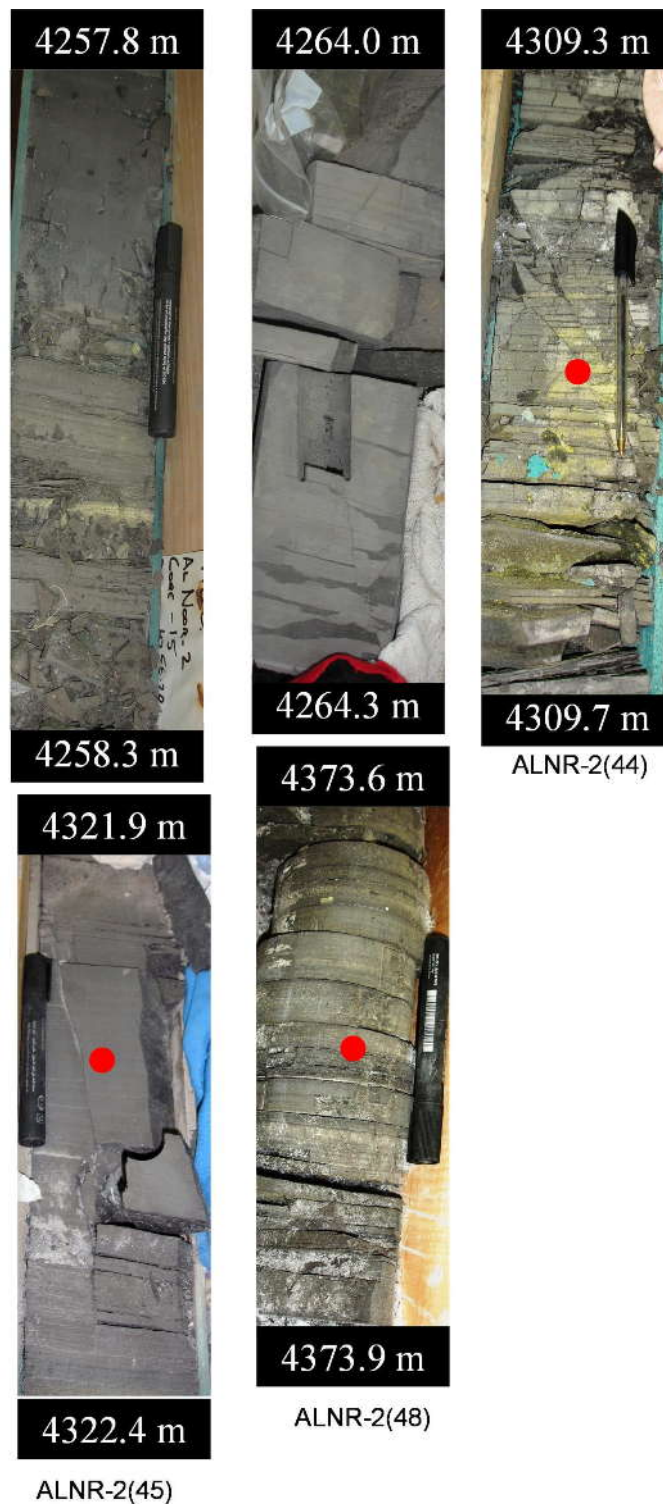


Figure 18. Depth interval from 4257.8-4258.05 m represents laminated microcrystalline quartz-dominated mudstones (LF2), from 4258.05-4258.3 m represents laminated microcrystalline quartz-rich mudstones (LF1), from 4264.0-4264.3 m represents microcrystalline quartz-, carbonate- and detritus-bearing mudstones (LF9), from 4321.9-4322.4 m represents LF9 in the middle, which is enclosed between LF1 and from 4373.6-4373.6 m represents laminated microcrystalline quartz-rich, detritus-bearing mudstones (LF3). Here LF1 is highly fissile and well laminated, LF2 is dark, not fissile and poorly laminated, LF3 is moderately fissile and laminated and LF9 is not fissile, no lamination and characterised relatively by lighter colour. The red circles show core depth of the thin-section microphotographs presented in Figures 19. These samples are (from top to bottom): ALNR-2(44), ALNR-2(45) and ALNR-2(48).

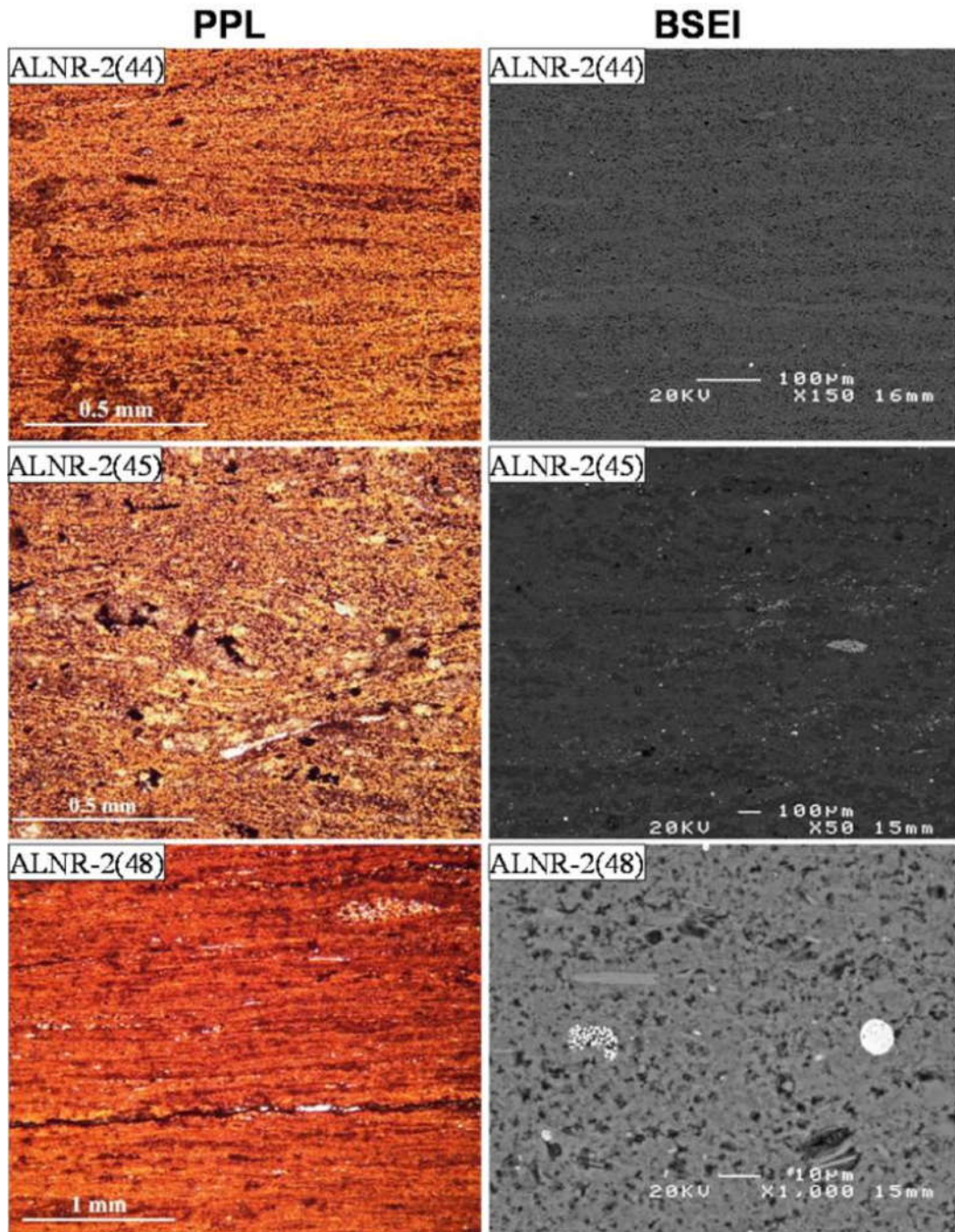


Figure 19. Sample ALNR-2(44) represents laminated microcrystalline quartz-rich mudstones (LF1), sample ALNR-2(45) represents microcrystalline quartz-, carbonate- and detritus-bearing mudstones (LF9) and sample ALNR-2(48) represents laminated microcrystalline quartz-rich, detritus-bearing mudstones (LF3). Note, the difference between sample ALNR-2(44) and ALNR-2(48) is the detrital content, while they show similar texture.

Well: ALNR-3

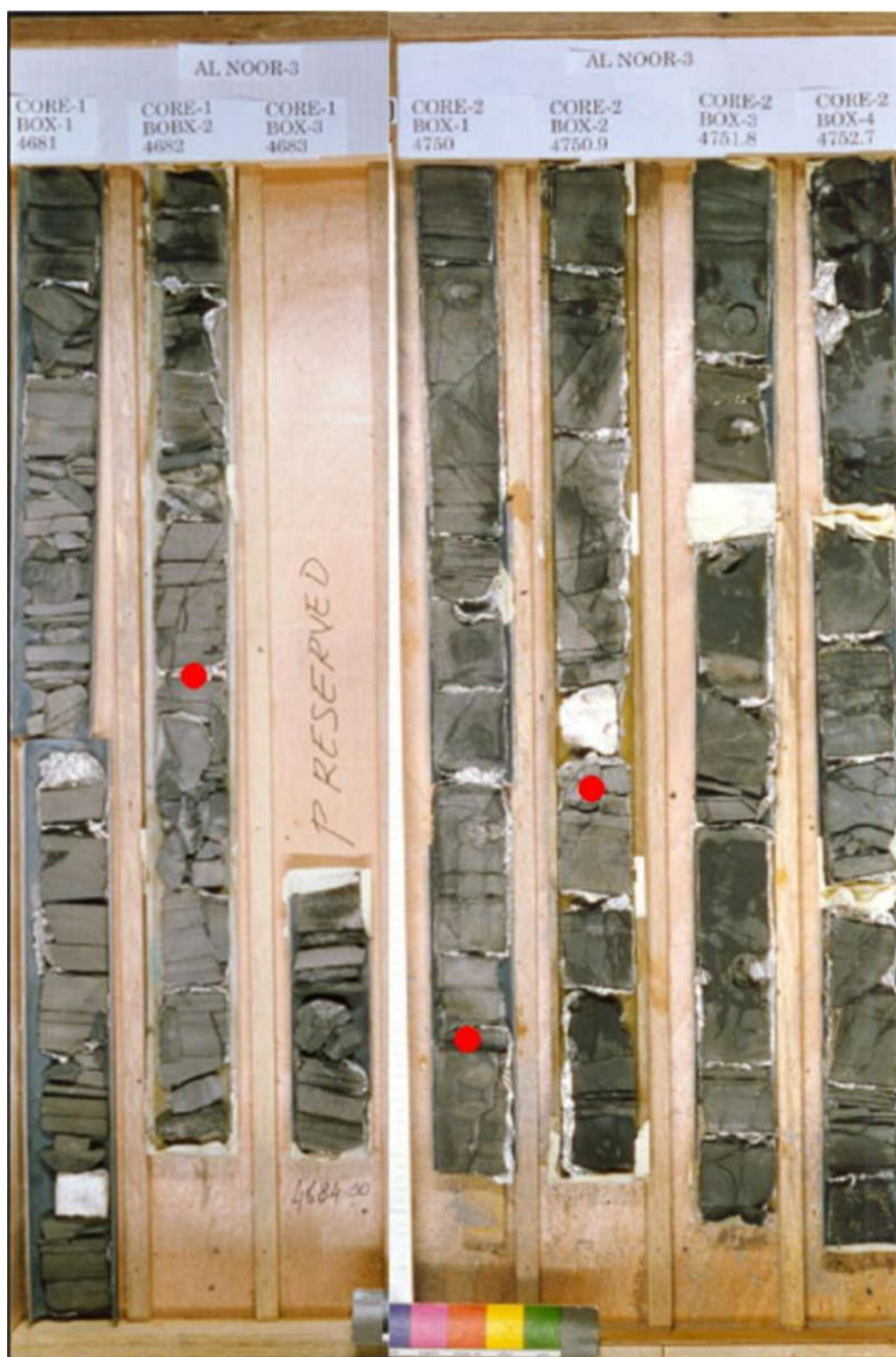


Figure 20. Depth interval from 4681.0-4684.0 m represents laminated microcrystalline quartz-rich, detritus-bearing mudstones (LF3), from 4750.0-4750.75 m represents LF3, from 4750.75-4751.05 m represents slumped mudstones (LF7), from 4751.05-4751.5 m represents LF3, from 4751.5 m to the end of the core represents alternation between LF3 and LF7 in 0.2-0.3 m scale. The red circles show core depth of the thin-section microphotographs presented in Figures 21. These samples are (from top to bottom): ALNR-3(3), ALNR-3(5) and ALNR-3(6).

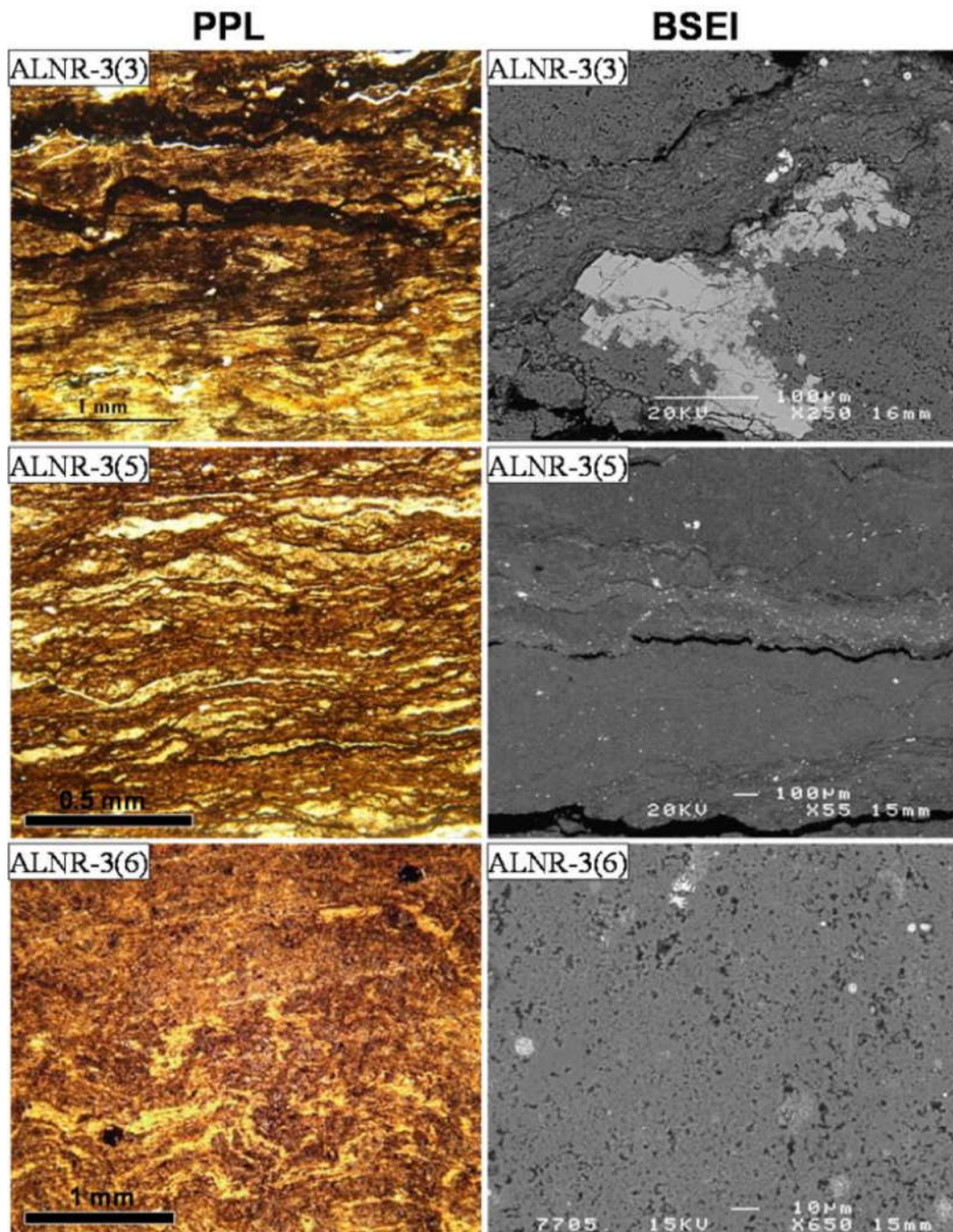


Figure 21. Sample ALNR-3(3) and ALNR-3(5) both represent laminated microcrystalline quartz-rich, detritus-bearing mudstones (LF3). These samples show wavy discontinuous lamination and contain more than 10 wt. % detrital material. Stylolite structures are cemented by clay minerals and rich in organic matter. Hydroxyfluorapatite is present in minor quantities in BSEI of ALNR-3(3). Sample ALNR-3(6) represents slumped mudstones (LF7), original lamination textures are disrupted.



Figure 22. Depth interval from 4753.6–4754.7 m represents laminated microcrystalline quartz-rich, detritus-bearing mudstones (LF3), from 4754.7–4754.9 m represents laminated microcrystalline quartz-dominated mudstones (LF2), from 4754.9–4756.0 m represents alternation between laminated microcrystalline quartz-rich mudstones (LF1; highly fissile) and LF3 (moderately fissile) in 0.1 m scale, from 4757.0 to 4758.75 m represents mainly LF3 apart from thin interval from 4757.6–4757.8 that represents LF1 (fissile and strongly laminated). The red circles show core depth of the thin-section microphotographs presented in Figures 23. These samples are (from top to bottom): ALNR-3(9), ALNR-3(11) and ALNR-3(12).

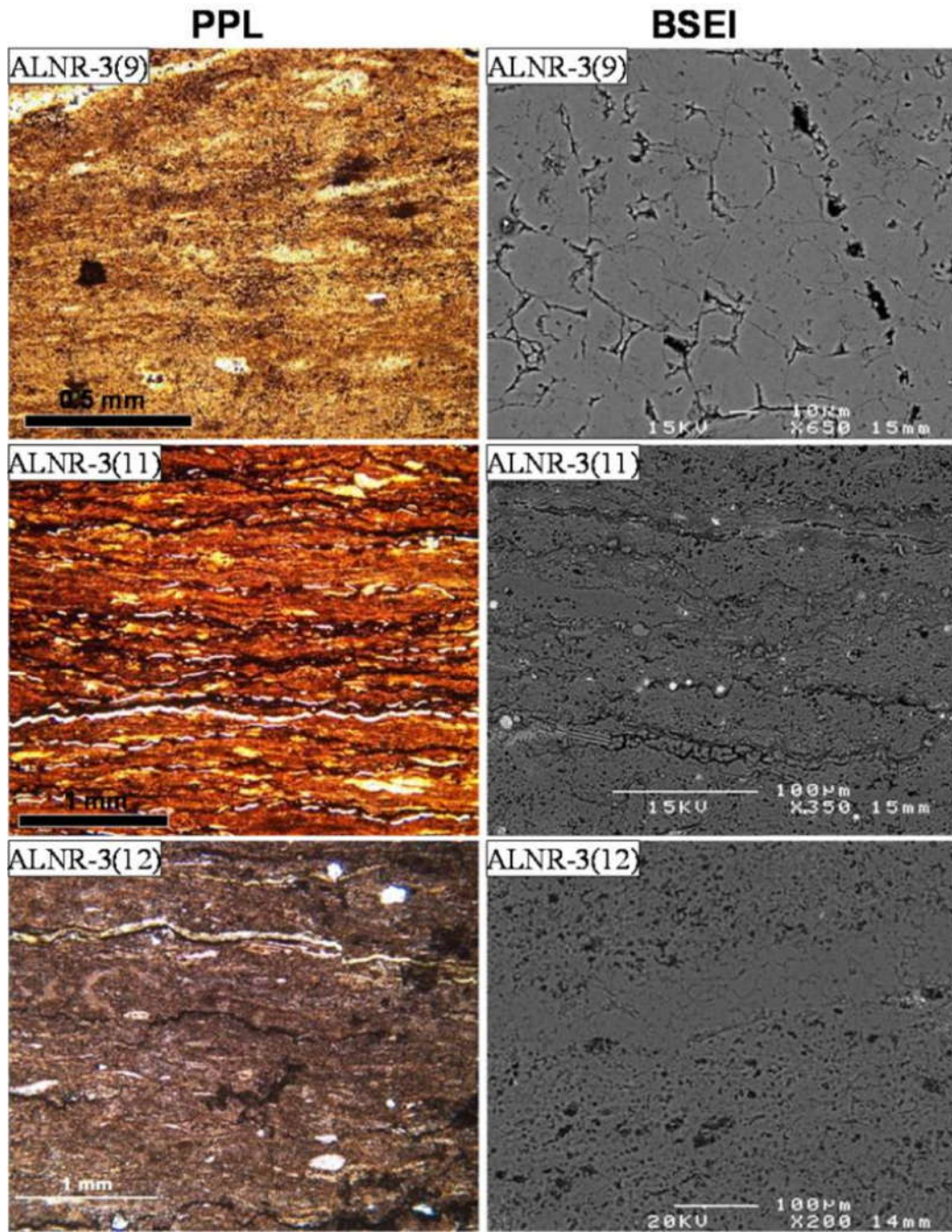


Figure 23. Sample ALNR-3(9) represents laminated microcrystalline quartz-dominated mudstones (LF2) that contains more than 90 wt. % microcrystalline quartz. Samples ALNR-3(11) and ALNR-3(12) both represent laminated microcrystalline quartz-rich, detritus-bearing mudstones (LF3).



Figure 24. Depth interval from 4812.0-4812.6 m represents either laminated microcrystalline quartz-rich mudstones (LF1) or laminated microcrystalline quartz-rich, detritus-bearing mudstones (LF3; very hard to distinguish from the core, but the sample obtained from this depth suggests that this interval represents LF1), from 4830.0-4832.3 m represents LF1, from 4832.3-4832.5 m represents laminated microcrystalline quartz-dominated mudstones (LF2). The red circles show core depth of the thin-section microphotographs presented in Figures 25. These samples are (from top to bottom): ALNR-3(13), ALNR-3(14) and ALNR-3(15).

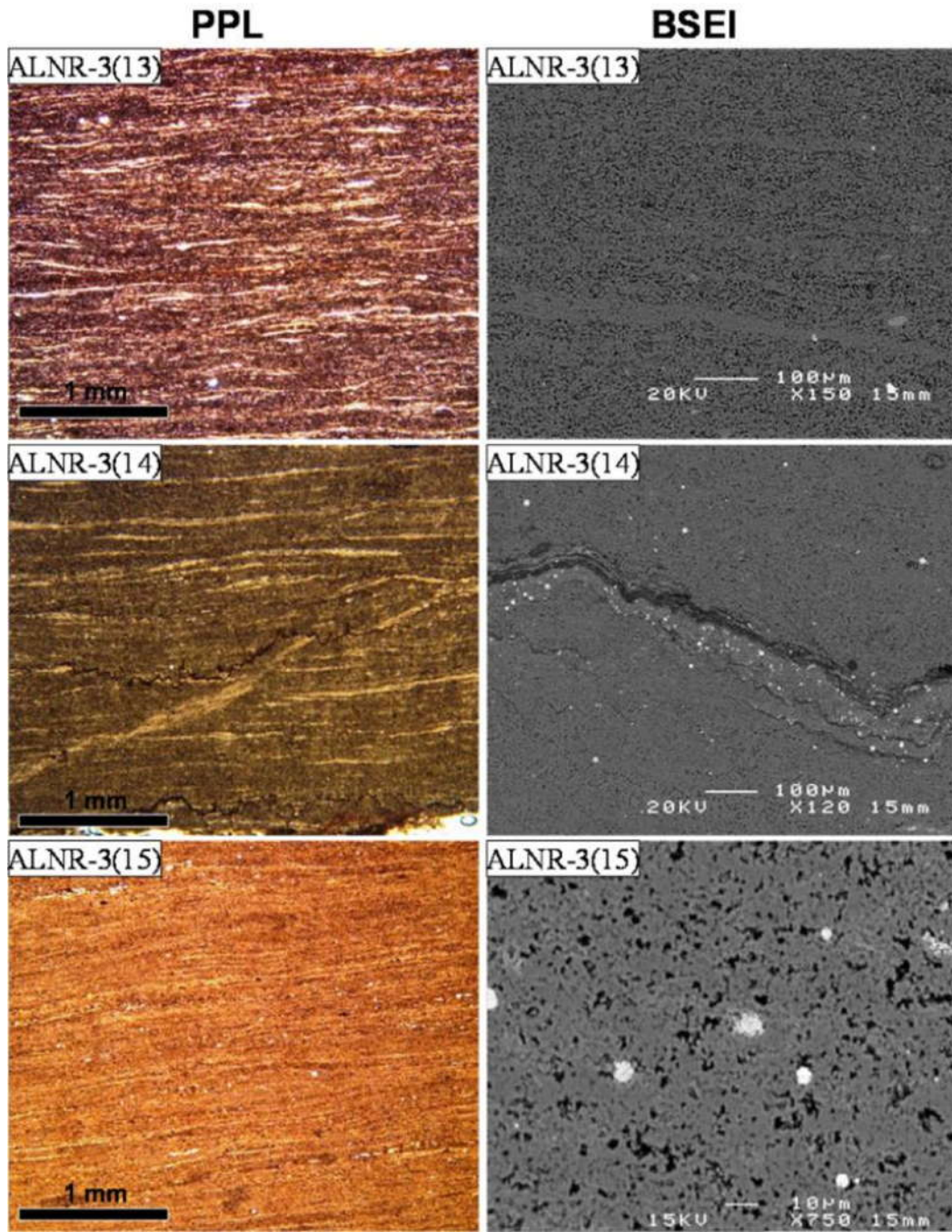


Figure 25. All samples represent laminated microcrystalline quartz-rich mudstones (LF1) that contains less than 10 wt. % detrital material (detrital quartz and clay minerals). Note the alternation between silica-rich layers and more organic matter/clay minerals-rich layers in BSEI of sample ALNR-3(13).

Well: ALNR-4



Figure 26. Depth interval from 4425.0-4433.0 m represents alternation between laminated microcrystalline quartz-rich mudstones (LF1) and laminated microcrystalline quartz-dominated mudstones (LF2). LF1 is very fissile and well-laminated, while LF2 is dark-coloured, not fissile and show very weak lamination.

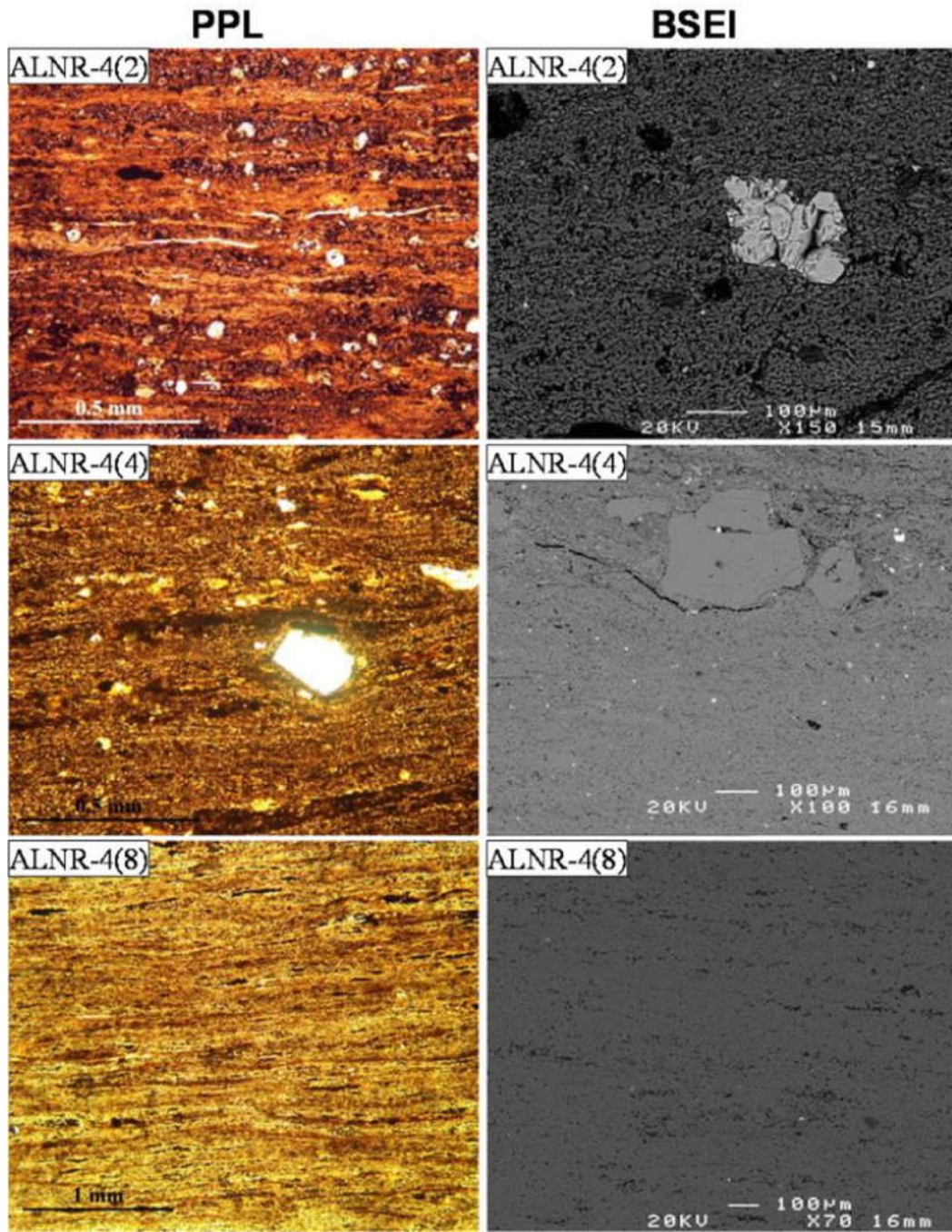


Figure 27. Samples ALNR-4(2) and ALNR-4(4) both represent laminated microcrystalline quartz-rich, detritus-bearing mudstones (LF3). Note BSEI of sample ALNR-4(2) show hydroxyfluorapatite in the middle and the black rounded shape are magnesite. Sample ALNR-4(8) represents laminated microcrystalline quartz-rich mudstones (LF1).

Well: ASH-2



Figure 28. Depth interval from 3809.5-3810.6 m and from 3866.5-3869.5 m might represent either laminated microcrystalline quartz-dominated mudstones (LF2) or laminated microcrystalline quartz-rich, detritus-bearing mudstones (LF3). Microscopic analysis of the samples obtain from these intervals suggest that interval from interval from 3809.5-3810.6 m represents laminated microcrystalline quartz-rich mudstones (LF1) and LF3 and depth interval from 3866.5-3869.5 m represents LF3. The red circles show core depth of the thin-section microphotographs presented in Figures 29. These samples are (from top to bottom): ASH-2(1), ASH-2(2) and ASH-2(4).

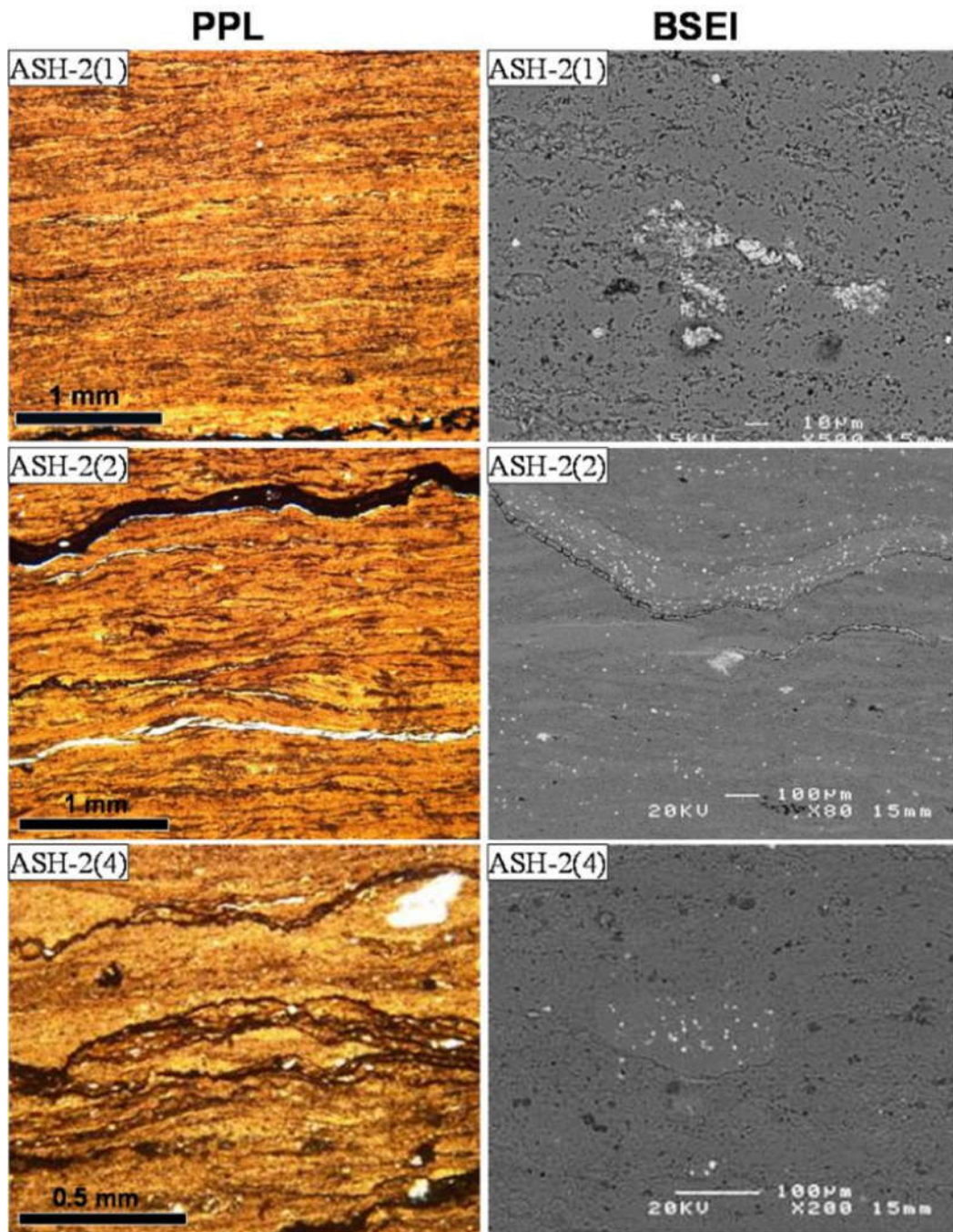


Figure 29. Samples ASH-2(1) represents laminated microcrystalline quartz-rich mudstones (LF1). Sample ASH-2(2) and ASH-2(4) both represent laminated microcrystalline quartz-rich, detritus-bearing mudstones (LF3). Note in sample AHS-2(2), stylolite structure is cemented by pyrite, clay minerals and anhydrite at the base of the structure.

Well: ASH-4

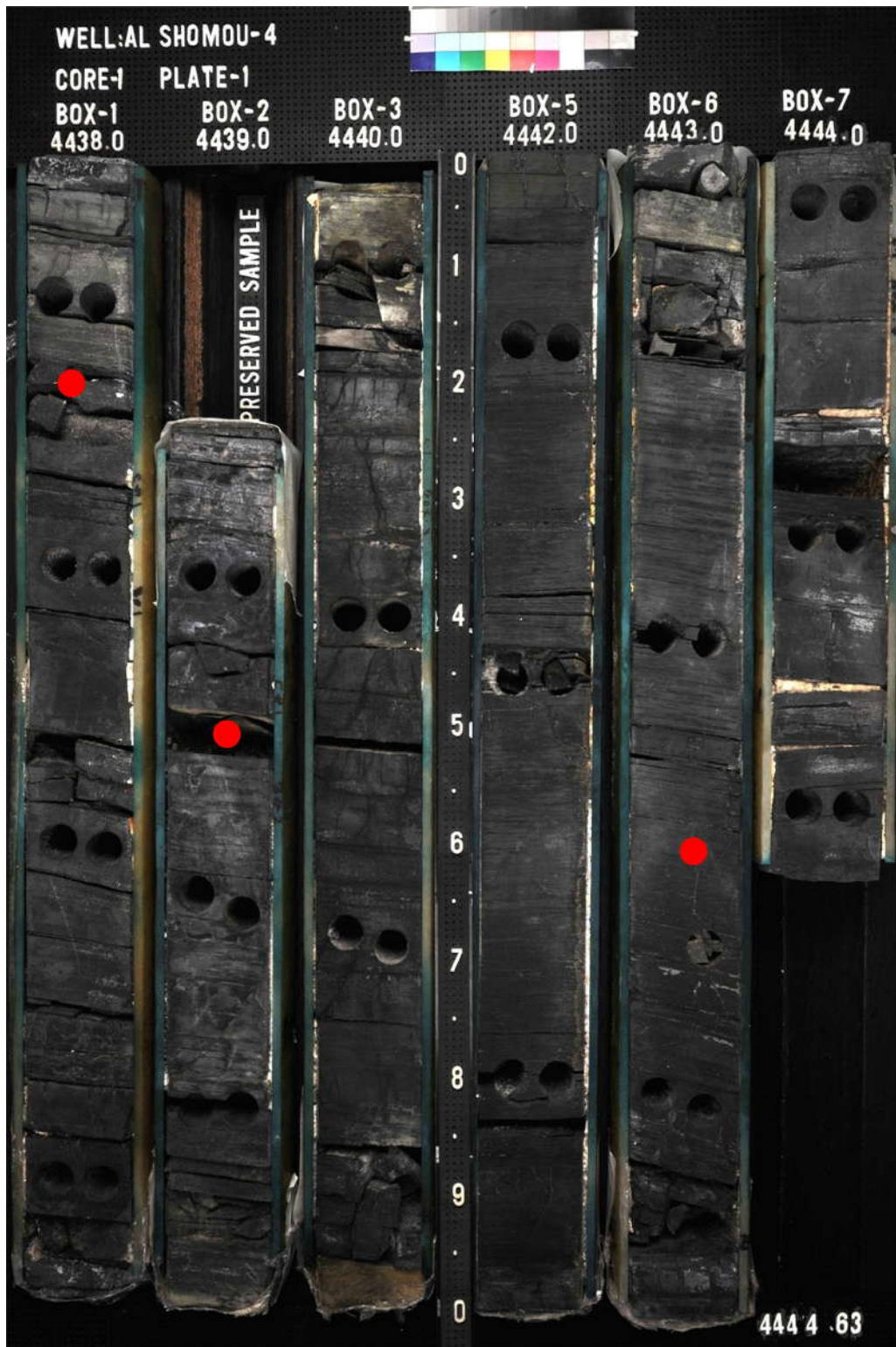


Figure 30. Depth interval from 4438.0-4444.63 m mainly represents laminated microcrystalline quartz-rich, detritus-bearing mudstones (LF3), apart from thin intervals (0.1-0.2 m) that might represent laminated microcrystalline quartz-rich mudstones (LF1) at depth 4439.9 m, 4440.1 m, 4443.2 m, 4443.9 m and 4444.3 m. The red circles show core depth of the thin-section microphotographs presented in Figures 31. These samples are (from top to bottom): ASH-4(1), ASH-4(2) and ASH-4(6).

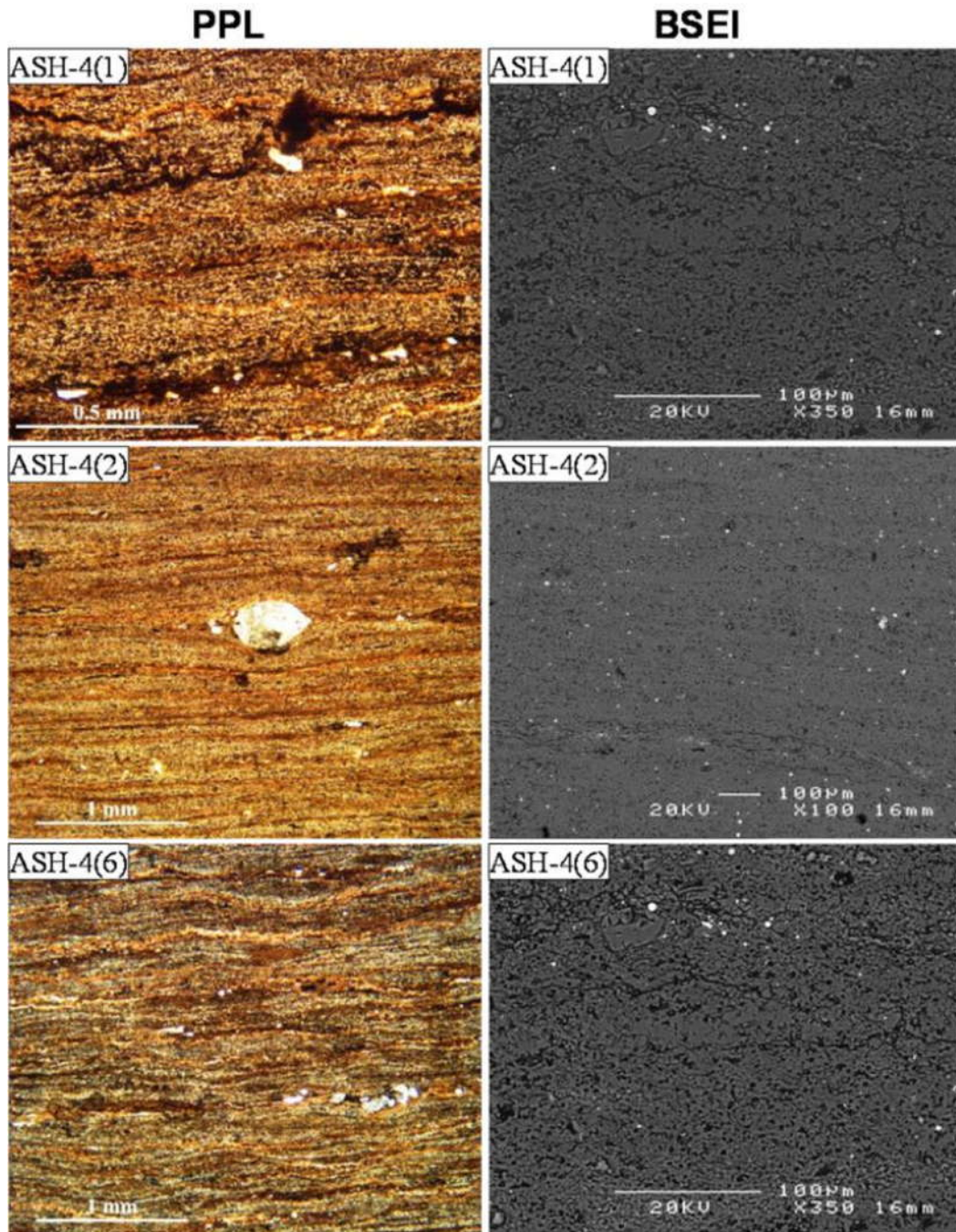


Figure 31. All samples represent laminated microcrystalline quartz-rich, detritus-bearing mudstones (LF3). Note in sample AHS-4(2) PPL image, laminae are compacted around detrital quartz grain suggesting that silica precipitation took place syndepositionally during low detrital input.

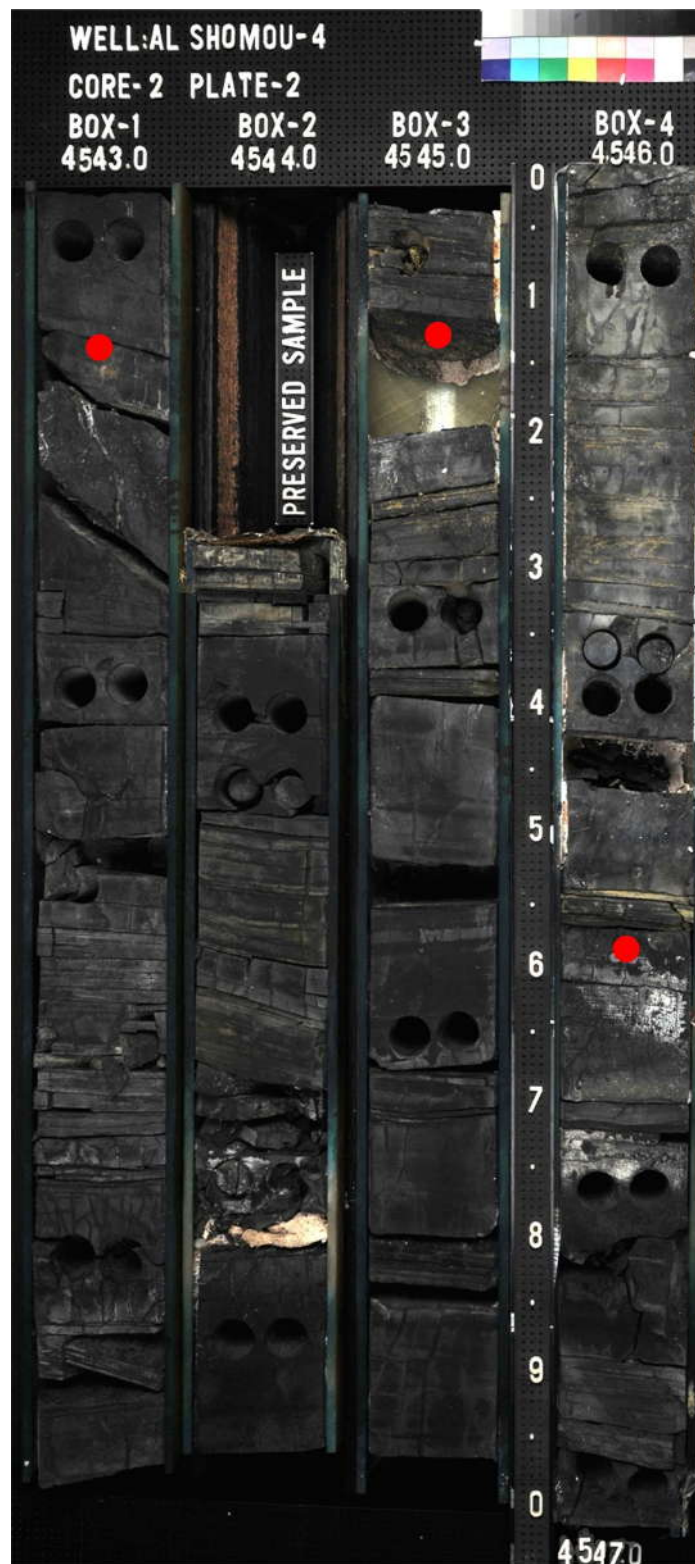


Figure 32. Depth interval from 4543.0-4543.5 m look like laminated microcrystalline quartz-rich, detritus-bearing mudstones (LF3), but microscopic analysis of the sample obtained from this interval suggests it actually represents laminated microcrystalline quartz-rich mudstones (LF1), from 4543.5-4544.3 m represents LF1, from 4544.35-4544.5 m represents laminated microcrystalline quartz-dominated mudstones (LF2), and the rest of core alternated between LF1 (fissile and laminated) and LF2 (not fissile and poorly laminated) at a scale of 0.2-.03 m. The red circles show core depth of the thin-section microphotographs presented in Figures 33. These samples are (from top to bottom): ASH-4(8), ASH-4(11) and ASH-4(12).

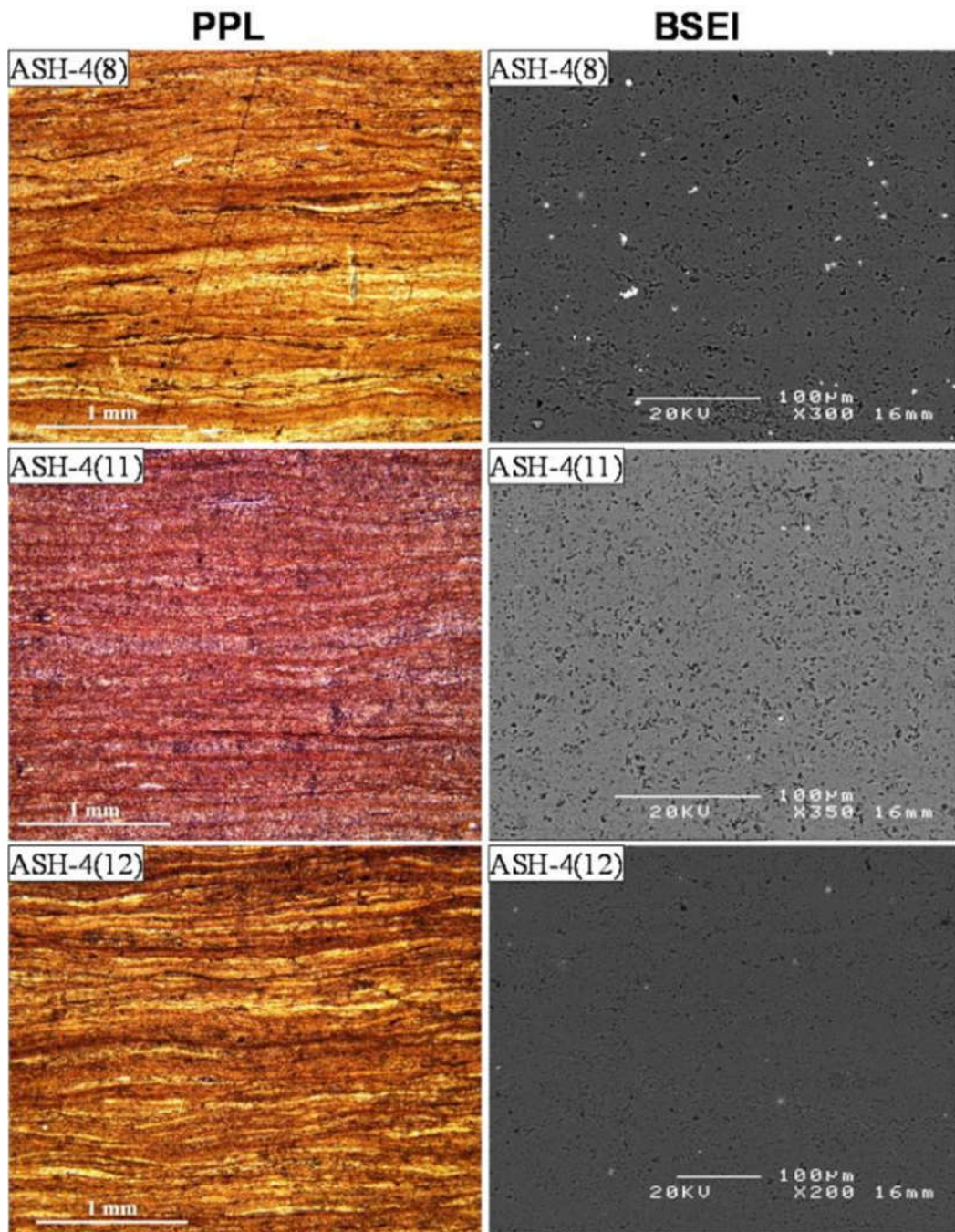


Figure 33. Samples ASH-4(8) and ASH-4(11) both represent laminated microcrystalline quartz-rich mudstones (LF1) and sample ASH-4(12) represents laminated microcrystalline quartz-dominated mudstones (LF2). Sample ASH-4(11) and ASH-4(12) look very much alike but they belong to different lithofacies category since sample ASH-4(11) contains just less than 90 wt. % microcrystalline quartz (88 wt. %), whereas sample ASH-4(12) contains just above 90 wt. % microcrystalline quartz (92 wt. %).



Figure 34. Depth interval from 4649.0-4650.45 m represents laminated microcrystalline quartz-rich mudstones (LF1), from 4650.45-4651.0 m represents laminated microcrystalline quartz-rich, detritus-bearing mudstones (LF3), from 4651.0-4651.45 m represents LF1, and from 4651.45-4653.0 m represents LF3. The red circles show core depth of the thin-section microphotographs presented in Figures 35. These samples are (from top to bottom): ASH-4(16), ASH-4(17) and ASH-4(20).

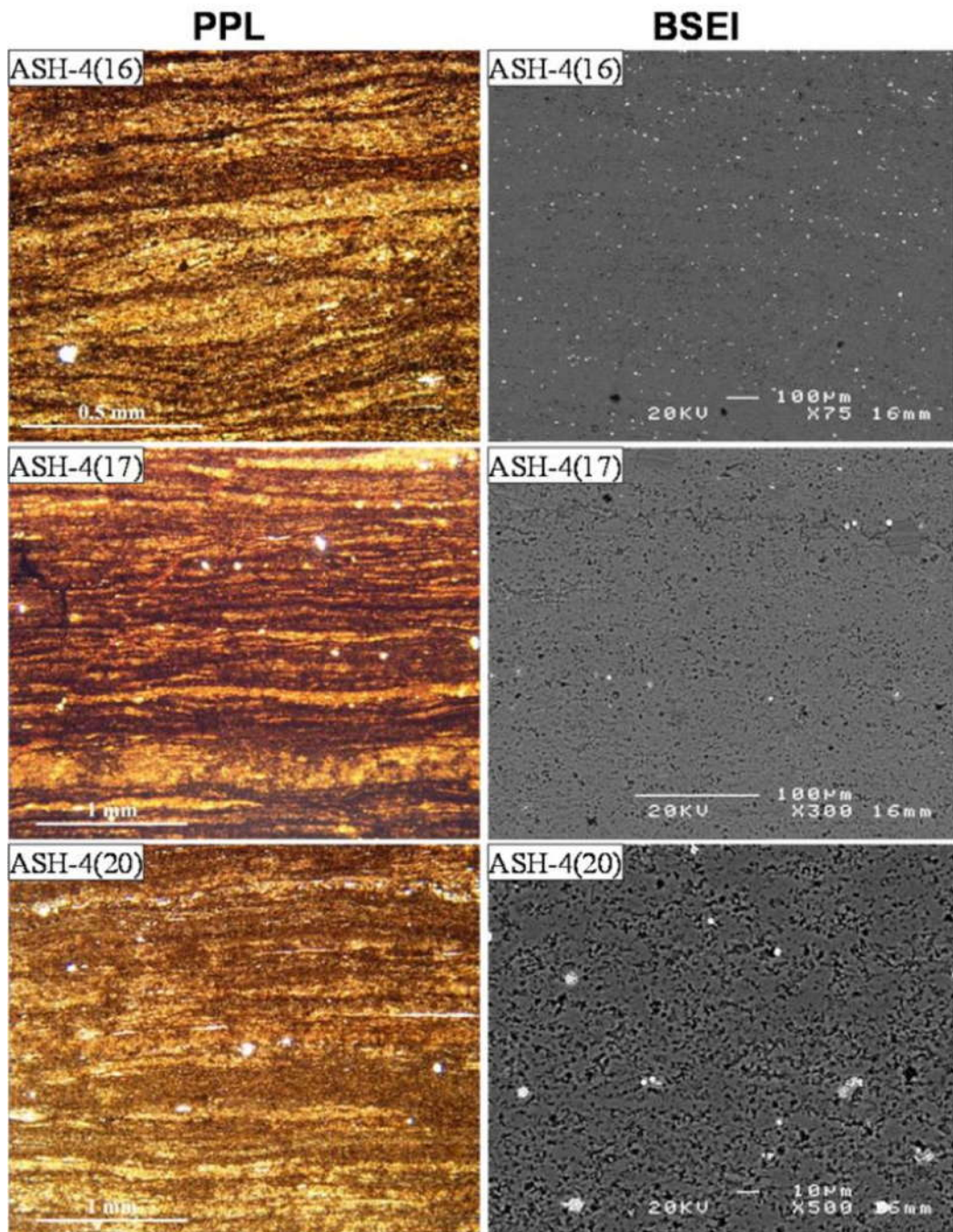


Figure 35. Samples ASH-4(168) represents laminated microcrystalline quartz-rich mudstones (LF1). Sample ASH-4(17) and ASH-4(20) both represent laminated microcrystalline quartz-rich, detritus-bearing mudstones (LF3). All samples look very similar but the variation is only in detrital material content (LF1 contains detrital material less than 10 wt. %, and LF3 more than 10 wt. %).

Well- MKZ-1

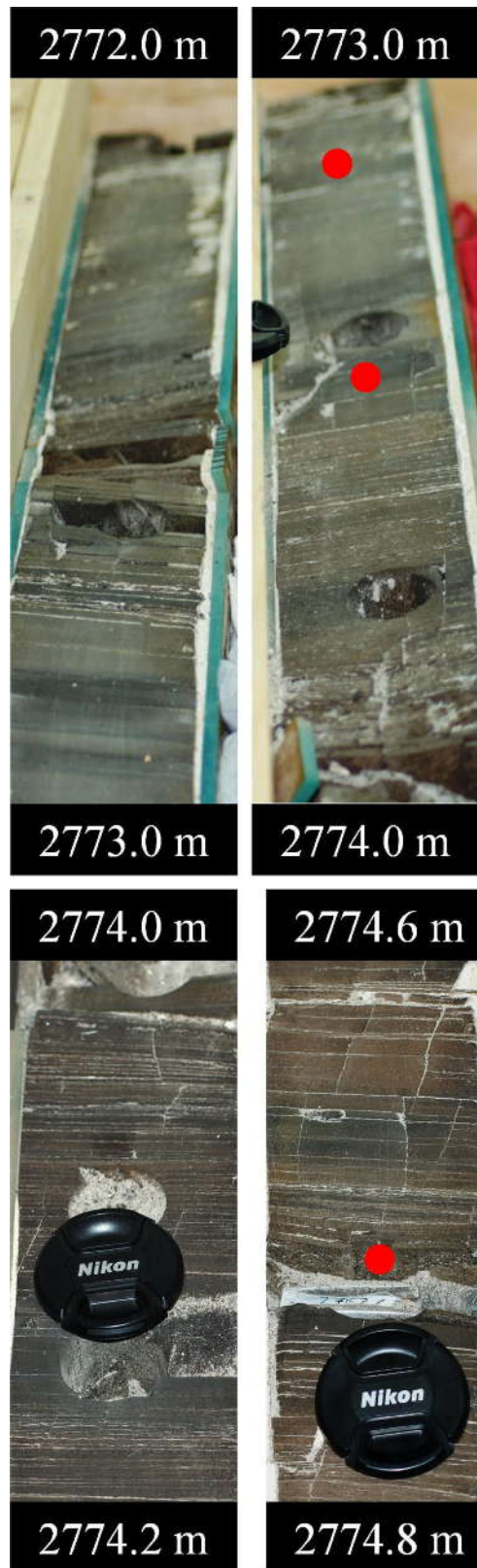


Figure 36. All core photographs represent laminated microcrystalline quartz-rich mudstones (LF1). The red circles show core depth of the thin-section microphotographs presented in Figures 37. These samples are (from top to bottom): MKZ-1(4), MKZ-1(5) and MKZ-1(7).

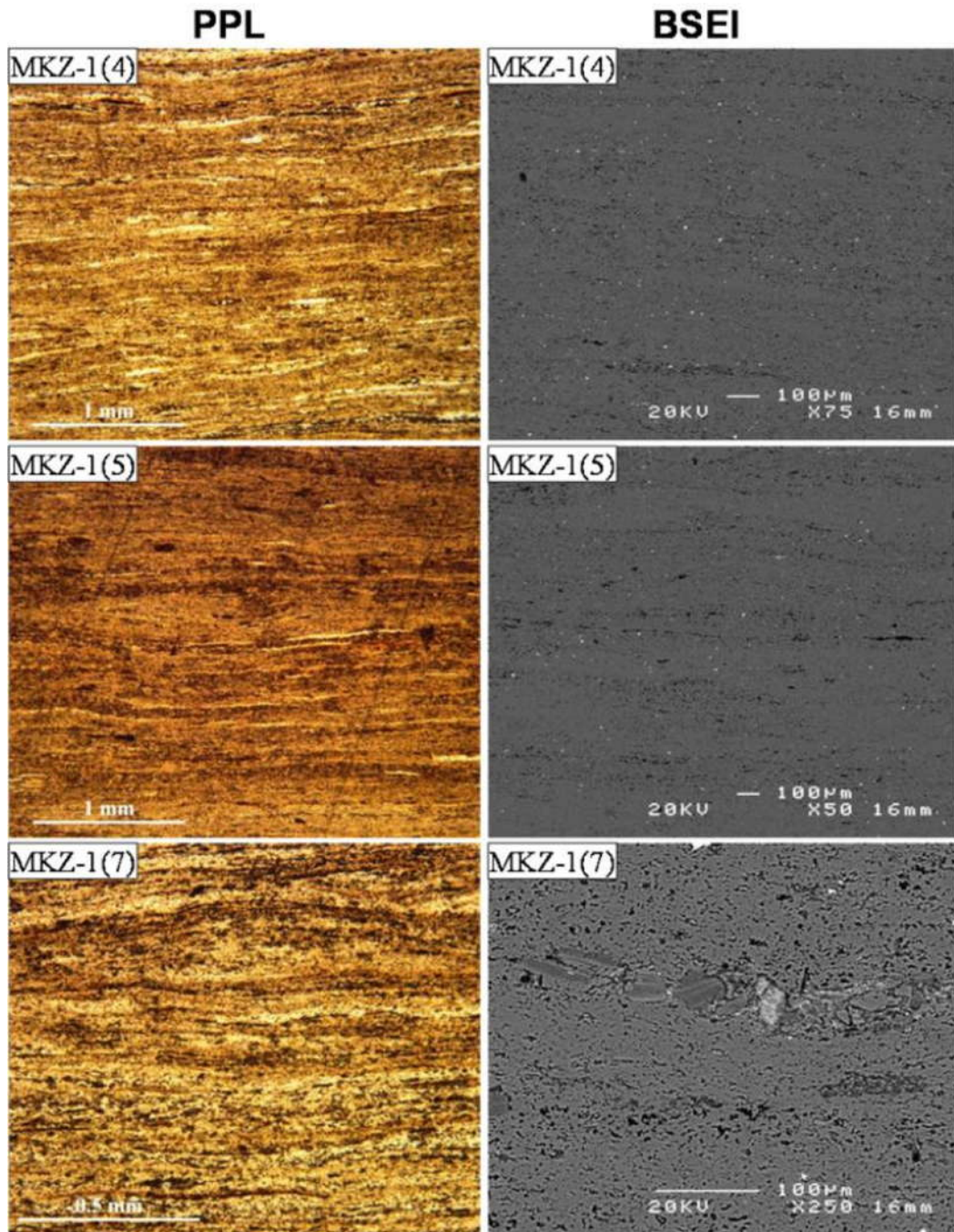


Figure 37. All sample microphotographs represent laminated microcrystalline quartz-rich mudstones (LF1). Note the alternation between silica-rich layers and more organic matter/clay minerals-rich layers.

Well: AL-9



Figure 38. All core photographs represent laminated silt-rich, clay-mineral bearing mudstones (LF4; from the U Shale), apart from thin intervals (≈ 0.1 m thick) that are dolomite cemented (LF9) at depth 1730.5 m, 1731.0 m and 1733.45 m. The red circles show core depth of the thin-section microphotographs presented in Figures 39. These samples are (from top to bottom): AL-9(1), AL-9(3) and AL-9(4).

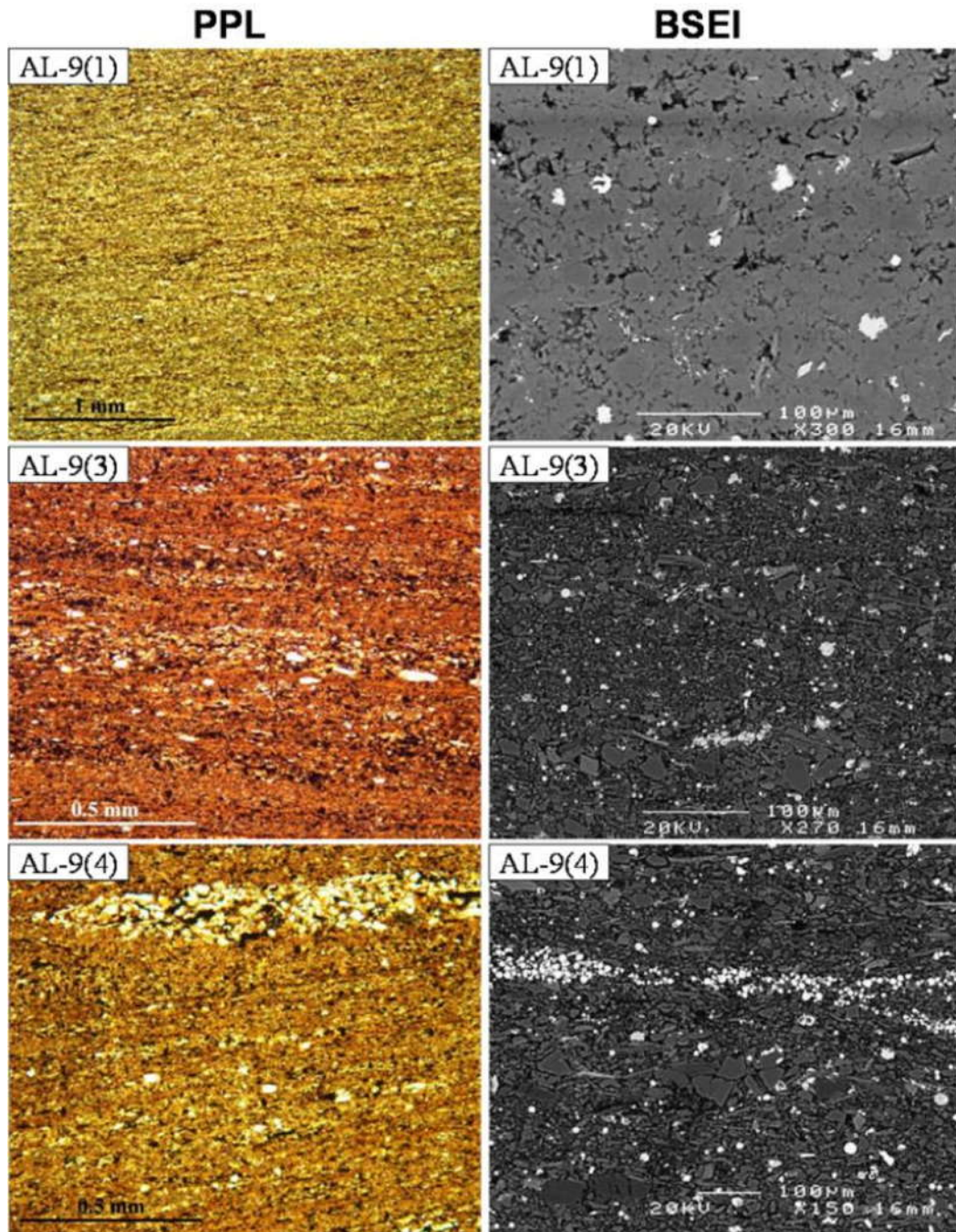


Figure 39. Samples AL-9(1) represents dolomite-cemented siltstone-rich mudstones. Samples AL-9(3) and AL-9(4) represent laminated silt-rich, clay-mineral bearing mudstones (LF4).

Appendix III: mineralogical composition and elemental concentrations of each studied sample

Appendix III outlines the following:

Table 1: mineralogical composition

Table 1: major element concentrations

Table 3: trace element concentrations

Table 4: rare earth element (REE) concentrations

Table 5: concentration of La, Ce, Nd and Y measured from XRF and LA-ICP-MS techniques

Table 1. Showing the semiquantitative estimations of each studied sample composition from all wells (wt. %). Note, samples abbreviation contain well name from which they are obtained and sample number in parentheses. In column headed “Other”, Ba stands for barite and CaP stands for hydroxyfluorapatite.

Sample abbreviation	Core depth/ m	Log depth/ m (MD)	Lithofacies	Microcrystalline quartz	Detrital quartz	Clay minerals	Pyrite	Dolomite	Magnesite	Anhydrite	Other	TOC
ALNR-2 (1)	3969.25	3974.33	LF6	0	0	0.0	1-2	0.0	0.0	95-98	0	
ALNR-2 (2)	3969.40	3974.48	LF5	4-6	10-12	15-18	5-7	0	8-10	40-43	1-2Ba	4.7
ALNR-2 (3)	3976.50	3981.53	LF9	20-22	7-8	14-16	6-8	35-38	4-5	6-8	1-2CaP	2.0
ALNR-2 (4)	3976.60	3981.63	LF9	20-21	5-7	15-17	3-4	39-42	2-3	4-6	1 CaP, 1Ba	1.8
ALNR-2 (5)	3976.80	3981.83	LF8/LF9	15-17	1-3	12-14	7-8	58-60	1-2	0	1 CaP	
ALNR-2 (6)	3977.00	3982.03	LF8/LF9	68-70	1-2	10-12	5-7	0	5-7	4-5	0	2.0
ALNR-2 (7)	3981.50	3986.53	LF9	50--55	1-2	13-15	3-4	30-32	0	0	1-2 Ba	
ALNR-2 (8)	3985.40	3990.43	LF3	75-78	7-8	9-10	2-3	0	0	3-5	0	1.4
ALNR-2 (9)	3992.20	3997.23	LF3	72-73	8-10	10-12	5-6	0	0	4-6	0	
ALNR-2 (10)	3992.40	3997.43	LF9	43-44	1-2	18-20	9-10	25-27	0	0	0	1.8
ALNR-2 (11)	4049.30	4053.94	LF3	72-75	7-8	14-16	3-5	0	0	0	0	
ALNR-2 (12)	4050.50	4055.14	LF7/LF9	66-69	6-8	7-8	2-3	0	9-11	1-3	0	4.3
ALNR-2 (13)	4052.00	4056.64	LF7	72-75	5-6	11-13	2-3	0	0	3-5	1-2 CaP	
ALNR-2 (14)	4055.60	4060.24	LF3	72-75	5--6	8-10	3-4	0	0	5	0	3.5
ALNR-2 (15)	4057.30	4061.94	LF3	70-74	4-5	16-18	3-5	0	0	0	1 CaP	
ALNR-2 (16)	4059.10	4063.74	LF3	66-70	9-11	10-12	3-5	0	0	2--3	0	5.5
ALNR-2 (17)	4060.50	4065.14	LF3	73--75	4-5	12--14	3--4	0	0	0	0	4.6
ALNR-2 (18)	4061.10	4065.74	LF3	78-80	3-4	5--8	3-4	0	0	4-6	2--3 Ba	
ALNR-2 (19)	4061.50	4066.14	LF3	71--73	2--3	13--15	4-5	0	0	4-6	1 CaP	
ALNR-2 (20)	4064.20	4068.84	LF3	77-80	3-5	8-10	2--3	0	0	2	1CaP	4.1
ALNR-2 (21)	4065.10	4069.74	LF8/LF9	38-40	0	6--8	8-10	16-18	20-22	0	1 CaP	5.6
ALNR-2 (22)	4066.70	4071.34	LF3	74-76	4-6	13--15	3-4	0	0	1-2	0	
ALNR-2 (23)	4068.60	4073.24	LF3	76-78	5-7	8-10	3-4	0	0	3-5	0	
ALNR-2 (24)	4071.70	4076.74	LF8	71-73	4-5	11-13	2-3	0	0	3-4	0	5.0

Table 1. Continued.

Sample abbreviation	Core depth/ m	Log depth/ m (MD)	Lithofacies	Microcrystalline quartz	Detrital quartz	Clay minerals	Pyrite	Dolomite	Magnesite	Anhydrite	Other	TOC
ALNR-2 (25)	4076.50	4081.56	LF3	73-75	3-4	10-12	2-3	2-3	0	2-3	0	3.2
ALNR-2 (26)	4079.00	4084.06	LF8	78-80	3-5	9-11	2-4	0	0	0	2-3 CaP	
ALNR-2 (27)	4130.40	4133.90	LF3	67-70	3-5	15-17	3-4	0	0	4-6	1 CaP	3.4
ALNR-2 (28)	4140.20	4143.70	LF3	74-76	3-4	13-15	2-3	0	0	4-5	0	
ALNR-2 (29)	4143.00	4146.50	LF9	29-32	1--2	6-8	9-11	43-45	3-5	1	1-2CaP	1.8
ALNR-2 (30)	4156.50	4160.33	LF1	79-82	2-3	5-7	2-3	0	0	5--6	0	3.3
ALNR-2 (31)	4165.60	4169.43	LF3	69-72	5-7	6-8	3-4	0	3-4	4-6	0	4.2
ALNR-2 (32)	4169.00	4172.83	LF3	70-72	6-7	13-15	3-5	0	0	4-5	1 CaP	
ALNR-2 (33)	4208.10	4212.33	LF2	90-93	1-2	2-4	1-2	0	0	1-3	0	1.3
ALNR-2 (34)	4220.00	4224.23	LF1	81-83	1-2	4-6	2-3	0	0	5-7	0	3.2
ALNR-2 (35)	4220.70	4224.93	LF8	84-86	1	4-6	2-3	0	0	4-5	0	1.1
ALNR-2 (36)	4232.40	4236.63	LF3	70-73	3-4	10-12	3-5	0	0	5-7	0	3.7
ALNR-2 (37)	4239.80	4244.06	LF8	43-45	0	2-3	4-5	0	33-36	6-8	0	7.5
ALNR-2 (38)	4256.90	4261.16	LF7	88-91	0	2-3	2-3	0	2-4	2-3	0	1.1
ALNR-2 (39)	4257.20	4261.46	LF2	89-91	1-2	3-4	2-4	0	0	3-4	0	
ALNR-2 (40)	4264.00	4267.55	LF9	28-30	0	5-7	8-9	52-54	0	0	1 CaP	1.9
ALNR-2 (41)	4276.80	4280.35	LF1	81-83	1	5-7	1-3	0	0	6-7	0	2.4
ALNR-2 (42)	4277.20	4280.75	LF2	89-92	0	2-3	1	0	0	3-4	1-2Ba	1.0
ALNR-2 (43)	4284.20	4287.63	LF7	88-91	0	3-5	2-3	0	0	4-6	0	
ALNR-2 (44)	4309.50	4313.44	LF1	84-86	0	5-7	1-2	0	0	4-6	0	2.7
ALNR-2 (45)	4322.10	4327.13	LF9	65-67	0	8-10	7-8	0	9-11	0	3Ba	4.2
ALNR-2 (46)	4339.20	4344.23	LF7	83-85	0	8-10	3-4	0	0	3-4	0	
ALNR-2 (47)	4358.80	4363.83	LF3	72-74	2-3	13-15	4-6	0	0	3-5	0	2.2
ALNR-2 (48)	4373.70	4378.73	LF3	63-65	3-5	18-20	5-6	0	0	3-5	0	2.5

Table 1. Continued

Sample abbreviation	Core depth/ m	Log depth/ m (MD)	Lithofacies	Microcrystalline quartz	Detrital quartz	Clay minerals	Pyrite	Dolomite	Magnesite	Anhydrite	Other	TOC
ALNR-3 (1)	3681.10	3685.85	LF3	80-82	4-5	5-7	2-4	0	3-5	1-2	1 CaP	
ALNR-3 (2)	3681.40	3686.15	LF3	76-77	1-2	10-12	4-5	0	0	4-5	0	1.9
ALNR-3 (3)	3682.60	3687.35	LF3	72-74	3-5	12-14	3-5	0	0	2-4	0	2.2
ALNR-3 (4)	4750.10	4754.85	LF7	77-79	0	10-12	4-5	0	0	4-6	1-2 CaP	
ALNR-3 (5)	4750.80	4755.55	LF7	79-81	1-2	9-11	3-5	0	0	3-5	0	
ALNR-3 (6)	4751.50	4756.25	LF3	53-55	1-3	28-30	6-8	0	0	6-9	0	
ALNR-3 (7)	4752.80	4757.55	LF1	87-88	0	4-6	4-5	0	1-2	1-2	0	
ALNR-3 (8)	4754.20	4758.95	LF1	86-88	0	5-7	3-5	0	0	2-4	0	
ALNR-3 (9)	4754.95	4759.70	LF2	93-95	0	2-3	1-2	0	2-3	0	0	
ALNR-3 (10)	4757.10	4761.85	LF3	77-79	3-4	8-10	2-3	0	0	3-5	0	2.5
ALNR-3 (11)	4757.80	4762.55	LF3	73-76	5-7	9-12	3-5	0	0	3-5	0	
ALNR-3 (12)	4758.30	4763.05	LF3	67-69	3-4	15-17	3-5	0	0	4-7	0	2.9
ALNR-3 (13)	4812.10	4816.85	LF1	84-86	1-2	5-7	2-3	0	0	4-6	0	
ALNR-3 (14)	4830.00	4834.75	LF1	80-83	1-2	7-9	3-5	0	0	4-6	0	
ALNR-3 (15)	4832.00	4836.75	LF1	81-82	1	7-8	3-5	0	0	2-3	0	2.5
ALNR-3 (16)	4832.6	4837.35	LF2	89--91	1-2	3-5	1-3	0		1	0	2.2
ALNR-4 (1)	4220.00	4226.00	LF3	77-79	5-7	11-13	3-5	0	0	0	1-2 CaP	
ALNR-4 (2)	4222.80	4228.80	LF3	70-74	6-8	6-8	2-3	0	4-6	2-3	2 CaP	3.1
ALNR-4 (3)	4224.50	4230.50	LF3	80-83	4-6	5-7	5-6	0	0	1-3	0	
ALNR-4 (4)	4226.10	4232.10	LF3	77-80	5-7	10-12	3-4	1	0	0	0	
ALNR-4 (5)	4228.00	4233.50	LF3	86-88	3-5	5-7	2-4	0	0	0	0	
ALNR-4 (6)	4230.00	4235.50	LF3	80-83	3-5	9-11	2-3	0	0	2-3	0	
ALNR-4 (7)	4231.00	4236.50	LF3	75-77	5-7	10-12	2-3	0	0	3-4	1 CaP	
ALNR-4 (8)	4232.00	4237.50	LF1	86-88	2-3	4-6	1-2	0	0	2-4	0	
ASH-2 (1)	3809.50	3805.50	LF1	86-87	1	7-8	2-3	0	0	2-3	1 CaP	

Table 1. Continued

Sample abbreviation	Core depth/ m	Log depth/ m (MD)	Lithofacies	Microcrystalline quartz	Detrital quartz	Clay minerals	Pyrite	Dolomite	Magnesite	Anhydrite	Other	TOC
ASH-2 (2)	3809.50	3806.50	LF3	70-73	2-3	13-15	3-6	0	0	5-7	1 CaP	1.6
ASH-2 (3)	3811.00	3807.00	LF3	76-78	2-3	10-12	2-3	0	0	5-9	0	
ASH-2 (4)	3867.20	3863.20	LF3	67-69	4-6	18-20	3-5	0	2-3	1-2	0	
ASH-2 (5)	3870.10	3866.10	LF3	63-65	5-6	16-18	3-5	0	0	5-7	0	2.9
ASH-2 (6)	3871.60	3867.60	LF3	62-64	7-9	15-16	3-5	0	1-2	5-8	1 CaP	
ASH-2 (7)	3873.70	3869.70	LF3	65-68	6-8	17-19	2-4	0	0	4-5	0	
ASH-2 (8)	3875.90	3871.90	LF3	80-82	4-6	5-7	2-3	0	0	2-3	1 Ba	2.1
ASH-4 (1)	4438.20	4441.60	LF3	66-68	3-4	14-16	6-8	0	3-4	3-5	0	
ASH-4 (2)	4439.50	4442.90	LF3	76-78	3-5	10-12	4-6	0	0	2-4	0	
ASH-4 (3)	4440.20	4443.60	LF3	73-75	3-5	13-15	6-7	0	0	3	1 CaP	
ASH-4 (4)	4441.20	4444.60	LF1	80-83	2-4	5-7	2-4	0	2-3	2-3	0	1.7
ASH-4 (5)	4442.90	4446.30	LF3	73-76	2-3	13-15	3-4	0	0	2-3	2-3 CaP	
ASH-4 (6)	4443.60	4447.00	LF3	74-76	2-4	12-14	3-5	0	0	3-4	2 CaP	
ASH-4 (7)	4444.30	4447.70	LF1	83-85	2-3	5-7	2-3	0	0	3-5	1 CaP	
ASH-4 (8)	4543.10	4539.90	LF1	84-86	0	4-6	5-7	0	0	2-4	0	1.2
ASH-4 (9)	4543.60	4540.40	LF3	68-70	2-3	17-19	5-8	0	0	3-5	0	
ASH-4 (10)	4544.80	4541.60	LF1	78-80	1-2	5-6	4-6	0	5-7	2-3	0	
ASH-4 (11)	4545.20	4542.00	LF1	87-89	1	5-7	1-2	0	0	3-4	0	
ASH-4 (12)	4546.60	4543.40	LF2	91-93	0	5-7	1-2	0	0	0	0	
ASH-4 (13)	4546.90	4543.70	LF1	87-89	0	5-6	3-4	0	2-4	0	0	
ASH-4 (14)	4646.3	4648.9	LF3	71-74	3-5	14-16	3-6	0	0	3-5	0	
ASH-4 (15)	4648.2	4650.8	LF1	83-85	3-4	6-8	2-3	0	0	2-4	0	
ASH-4 (16)	4649.8	4652.4	LF1	82-85	2-3	6-8	4-6	0	0	2-3	0	
ASH-4 (17)	4650.9	4653.5	LF3	74-76	2-3	12-13	3-4	0	0	2-4	0	2.8
ASH-4 (18)	4651.7	4654.3	LF1	83-86	2-3	6-7	2-3	0	1-2	2-3	0	

Table 1. Continued

Sample abbreviation	Core depth/ m	Log depth/ m (MD)	Lithofacies	Microcrystalline quartz	Detrital quartz	Clay minerals	Pyrite	Dolomite	Magnesite	Anhydrite	Other	TOC
ASH-4 (19)	4652.1	4654.7	LF3	81-83	1-2	9-11	2-3	0	0	3-5	0	
ASH-4 (20)	4652.9	4655.5	LF3	75-77	1-2	9-11	3-5	0	2-3	4-6	0	
MKZ-1 (1)	2768.50	2770.50	LF2	90-92	0	3-5	2-3	0	0	0	0	2.4
MKZ-1 (2)	2769.10	2771.10	LF1	86-88	2-3	5-6	4-6	0	0	0	0	
MKZ-1 (3)	2769.40	2771.40	LF2	93-95	0	3-5	2-3	0	0	0	0	
MKZ-1 (4)	2773.10	2775.10	LF1	85-87	1-2	5-7	3-5	0	0	2-3	0	
MKZ-1 (5)	2773.50	2775.50	LF1	86-88	1-2	4-5	3-4	0	0	3-4	0	
MKZ-1 (6)	2774.20	2776.20	LF1	85-87	0	4-6	3-4	0	0	4-5	0	
MKZ-1 (7)	2774.70	2776.70	LF1	81-83	2-3	4-6	3-5	0	0	3-5	0	1.8
AL-9 (1)	1730.20	na	LF9	0	11-13	6-8	6-7	72-75	0	0	1-2 Ba	
AL-9 (2)	1730.93	na	LF9	0	10-12	7-9	7-8	70-73	0	0	1-2Ba	
AL-9 (3)	1731.66	na	LF4	0	54-57	27-29	7-9	1-2	0	0	0	8.0
AL-9 (4)	1733.43	na	LF4	0	55-57	32-35	9-11	0	0	0	1 CaP	
AL-9 (5)	1735.23	na	LF4	0	60-63	27-30	6-7	2-3	0	0	1 CaP	
AL-9 (6)	1736.81	na	LF4	0	54-56	34-36	5-7	2-3	0	0	1 CaP	
AL-9 (7)	1737.21	na	LF4	0	72-75	20-24	4-5	0	0	0	0	
AL-9 (8)	1737.30	na	LF4	0	58-60	33-35	5-6	1-2	0	0	0	
AL-9 (9)	1738.15	na	LF4	0	58-62	29-32	7-9	1-2	0	0	0	
AL-9 (10)	1739.43	na	LF4	0	55-58	25-27	7-9	1-3	0	1-2	0	6.2

Table 2. Shows major element concentrations (%) of each studied sample. LOI stands for the loss on ignition.

Sample abbreviation	Core depth/ m	Lithofacies	LOI	Na ₂ O	MgO	Al ₂ O ₃	SiO ₂	P ₂ O ₅	SO ₃	Cl	K ₂ O	CaO	Fe ₂ O ₃	TiO ₃	Total	SiO ₂ /Al ₂ O ₃	Fe ₂ O ₃ /TiO ₂	Fe/Fe+Al+Mn
ALNR-2 (1)	3969.25	LF6	8.9	37.2	0.3	0.0	0.4		1.0	51.5	0.4	0.3	0.0	0	99.9	8.5	-	0.67
ALNR-2 (2)	3969.40	LF5	18.5	0.2	5.7	5.9	21.1	0.5	25.3	0.3	1.5	16.2	2.2	0.55	97.9	3.6	3.94	0.73
ALNR-2 (3)	3976.50	LF9	26.8	0.4	7.0	5.2	38.9	1.1	1.8	0.5	1.3	14.7	1.7	0.4	99.8	7.5	4.29	0.75
ALNR-2 (4)	3976.60	LF9	27.9	1.1	6.8	5.5	35.7	0.7	2.2	1.2	1.4	14.5	1.8	0.43	99.1	6.5	4.24	0.74
ALNR-2 (5)	3976.80	LF9	32.3	0.3	9.9	4.0	27.8	0.6	1.4	0.4	1.0	20.3	1.4	0.36	99.7	7.0	3.90	0.73
ALNR-2 (6)	3977.00	LF9	7.1	2.5	0.6	2.4	74.2	0.1	3.6	3.3	0.8	0.6	1.2	0.3	97.0	30.4	4.13	0.66
ALNR-2 (7)	3981.50	LF9	24.2	0.5	4.1	7.0	45.0	1.0	3.2	0.6	1.9	8.8	2.9	0.63	99.9	6.4	4.62	0.70
ALNR-2 (8)	3985.40	LF3	4.9	0.5	0.4	2.2	86.1	0.1	2.3	0.8	0.7	0.3	1.1	0.24	99.7	38.5	4.42	0.68
ALNR-2 (9)	3992.20	LF3	8.8	1.3	8.1	6.6	44.0	0.9	2.9	1.5	1.8	19.6	2.6	0.53	98.7	6.7	4.95	0.71
ALNR-2 (10)	3992.40	LF9	17.7	0.3	4.2	5.5	53.4	0.8	3.2	0.5	1.5	9.9	2.4	0.45	99.9	9.6	5.41	0.69
ALNR-2 (11)	4049.30	LF3	9.2	0.4	0.4	3.6	76.7	0.1	4.9	0.8	1.2	0.5	1.8	0.45	100.0	21.5	4.09	0.66
ALNR-2 (12)	4050.50	LF7	14.6	0.2	4.7	2.4	73.7	0.0	2.2	0.4	0.6	0.2	0.8	0.21	100.0	31.3	3.89	0.74
ALNR-2 (13)	4052.00	LF7	13.0	0.3	0.3	2.9	76.8	0.1	3.3	0.6	0.9	0.3	1.3	0.32	100.1	26.7	4.09	0.69
ALNR-2 (14)	4055.60	LF3	7.2	0.4	0.3	2.2	83.9	0.1	2.9	0.7	0.7	0.4	1.0	0.22	100.0	37.7	4.41	0.70
ALNR-2 (15)	4057.30	LF3	11.2	0.4	0.5	4.9	72.9	0.3	4.8	0.6	1.4	0.4	2.1	0.34	99.9	14.8	6.11	0.70
ALNR-2 (16)	4059.10	LF3	13.3	0.3	0.3	2.8	71.5	0.1	6.9	0.5	0.9	0.2	2.3	0.16	99.4	25.2	14.6	0.55
ALNR-2 (17)	4060.50	LF3	9.9	0.5	0.3	3.6	76.3	0.1	5.3	0.6	0.9	0.2	1.9	0.27	99.9	21.4	7.07	0.65
ALNR-2 (18)	4061.10	LF3	9.3	0.3	0.2	2.1	83.7		2.4	0.4	0.5	0.1	0.8	0.23	100.0	39.9	3.35	0.73
ALNR-2 (19)	4061.50	LF3	12.1	0.4	0.3	3.6	72.8	0.3	5.5	0.5	1.1	0.4	2.7	0.24	100.0	20.0	11.1	0.58
ALNR-2 (20)	4064.20	LF3	10.8	0.3	0.3	2.6	69.9	0.1	2.7	0.5	0.7	0.2	1.1	0.26	89.5	26.5	4.30	0.70
ALNR-2 (21)	4065.10	LF8	30.4	0.2	12.9	2.4	44.6	0.1	1.7	0.4	0.6	5.4	1.1	0.15	99.8	18.7	7.35	0.67
ALNR-2 (22)	4066.70	LF3	14.5	0.4	0.4	4.0	70.6	0.1	5.7	0.6	1.1	0.2	2.0	0.33	100.0	17.5	6.08	0.67
ALNR-2 (23)	4068.60	LF3	11.9	0.2	0.3	2.7	79.9	0.0	2.7	0.4	0.6	0.2	0.9	0.25	100.0	29.7	3.48	0.75
ALNR-2 (24)	4071.70	LF8	0.0	0.5	0.3	3.2	86.7	0.0	5.3	0.6	1.0	0.2	1.7	0.34	99.8	26.9	4.92	0.66

Table 2. Continued.

Sample abbreviation	Core depth/ m	Lithofacies	LOI	Na ₂ O	MgO	Al ₂ O ₃	SiO ₂	P ₂ O ₅	SO ₃	Cl	K ₂ O	CaO	Fe ₂ O ₃	TiO ₃	Total	SiO ₂ /Al ₂ O ₃	Fe ₂ O ₃ /TiO ₂	Fe/Fe+Al+Mn
ALNR-2 (25)	4076.50	LF3	8.6	0.5	0.3	3.0	78.5	0.1	5.0	0.6	0.9	0.3	1.7	0.32	99.8	26.5	5.16	0.64
ALNR-2 (26)	4079.00	LF8	-	-	-	-	-	-	-	-	-	-	-	-	-	-	-	-
ALNR-2 (27)	4130.40	LF3	8.7	0.6	0.5	4.6	73.8	0.4	5.5	0.8	1.4	0.2	3.2	0.23	99.9	16.1	13.9	0.59
ALNR-2 (28)	4140.20	LF3	9.9	0.4	0.6	4.8	76.7	0.1	3.3	0.7	1.2	0.3	1.7	0.42	100.1	16.1	4.03	0.74
ALNR-2 (29)	4143.00	LF9	31.7	0.1	9.3	2.8	35.2	0.9	1.6	0.3	0.6	16.1	1.0	0.19	99.8	12.4	5.51	0.72
ALNR-2 (30)	4156.50	LF1	7.7	0.4	0.3	2.3	84.3	0.1	2.4	0.6	0.6	0.2	1.0	0.21	100.0	37.2	4.60	0.70
ALNR-2 (31)	4165.60	LF3	20.5	0.4	0.9	3.1	70.3	0.1	2.2	0.6	0.7	0.1	0.8	0.33	100.1	22.7	2.52	0.79
ALNR-2 (32)	4169.00	LF3	9.9	0.5	0.8	4.5	75.1	0.5	4.1	0.8	1.2	0.4	2.0	0.47	100.1	16.8	4.17	0.69
ALNR-2 (33)	4208.10	LF2	3.2	0.5	0.1	1.0	90.8		2.1	0.8	0.3	0.1	0.7	0.07	99.7	95.4	10.5	0.56
ALNR-2 (34)	4220.00	LF1	6.6	0.5	0.2	2.7	84.7	0.2	2.2	0.8	0.6	0.1	0.9	0.17	99.8	31.8	5.30	0.75
ALNR-2 (35)	4220.70	LF8	3.3	0.7	0.6	1.1	90.4		1.5	1.2	0.3	0.1	0.6	0.06	99.9	80.2	10.1	0.65
ALNR-2 (36)	4232.40	LF3	9.4	0.5	0.4	3.8	78.0	0.3	3.9	0.7	0.9	0.2	1.8	0.25	100.0	20.7	7.16	0.68
ALNR-2 (37)	4239.80	LF8	33.3	0.8	23.0	1.3	38.2	0.0	1.1	0.9	0.2	0.3	0.4	0.04	99.6	28.7	10.5	0.69
ALNR-2 (38)	4256.90	LF7	2.6	0.5	0.1	0.7	93.7		0.9	0.7	0.2	0.0	0.3	0.05	99.8	128.1	6.33	0.70
ALNR-2 (39)	4257.20	LF2	8.0	0.8	0.1	1.6	84.3	0.1	2.1	1.2	0.4	0.1	0.6	0.1	99.5	52.0	6.36	0.72
ALNR-2 (40)	4264.00	LF9	32.0	9.1	0.0	2.5	30.4	0.5	1.6	0.1	0.5	21.5	1.0	0.14	99.4	11.9	7.43	0.70
ALNR-2 (41)	4276.80	LF1	5.4	0.5	0.2	1.8	87.5	0.1	2.2	0.8	0.5	0.1	0.8	0.11	99.8	48.3	7.47	0.69
ALNR-2 (42)	4277.20	LF2	2.2	0.3	0.1	0.7	94.6		0.9	0.5	0.2	0.0	0.3	0.05	99.9	133.5	6.67	0.68
ALNR-2 (43)	4284.20	LF7	2.7	0.2	0.2	1.0	93.4		1.1	0.4	0.3	0.1	0.5	0.07	99.9	93.1	7.02	0.67
ALNR-2 (44)	4309.50	LF1	6.4	0.8	0.2	2.0	83.4		3.7	1.2	0.5	0.1	1.4	0.12	99.8	42.5	11.3	0.59
ALNR-2 (45)	4322.10	LF9	14.5	0.6	5.9	2.8	69.0	0.9	1.9	1.0	0.7	0.4	1.7	0.16	99.6	24.6	10.6	0.62
ALNR-2 (46)	4339.20	LF7	4.6	1.0	0.2	2.6	85.8	0.1	2.3	1.3	0.7	0.1	1.1	0.14	99.9	33.1	7.81	0.70
ALNR-2 (47)	4358.80	LF3	5.6	1.2	0.5	3.6	81.0	0.2	3.0	2.0	1.0	0.1	1.5	0.21	99.9	22.4	6.99	0.71
ALNR-2 (48)	4373.70	LF3	7.0	0.5	0.6	5.4	78.5	0.2	3.0	1.0	1.5	0.1	1.8	0.31	99.8	14.6	5.81	0.75
ALNR-3 (1)	3681.10	LF3	5.5	0.3	1.1	2.7	86.0	0.1	1.6	0.5	0.5	0.6	0.9	0.25	100.0	32.1	3.53	0.75
ALNR-3 (2)	3681.40	LF3	7.7	0.7	0.9	-	80.8	0.1	3.9	1.3	1.1	1.3	1.8	0.42	100.1	-	-	-

Table 2. Continued.

Sample abbreviation	Core depth/ m	Lithofacies	LOI	Na ₂ O	MgO	Al ₂ O ₃	SiO ₂	P ₂ O ₅	SO ₃	Cl	K ₂ O	CaO	Fe ₂ O ₃	TiO ₃	Total	SiO ₂ /Al ₂ O ₃	Fe ₂ O ₃ /TiO ₂	Fe/Fe+Al+Mn
ALNR-3 (3)	3682.60	LF3	7.7	0.7	0.9	-	80.8	0.1	3.9	1.3	1.1	1.3	1.8	0.63	100.3	-	-	-
ALNR-3 (4)	4750.10	LF7	9.7	0.6	0.4	3.2	76.2	0.1	4.9	1.0	0.8	0.4	2.4	0.26	100.0	23.5	9.09	0.58
ALNR-3 (5)	4750.80	LF7	9.7	0.3	0.3	3.1	76.2	0.0	5.3	0.5	0.8	0.3	3.1	0.21	100.0	24.5	14.6	0.50
ALNR-3 (6)	4751.50	LF3	13.9	0.5	0.9	11.0	59.8	0.0	5.7	0.5	2.6	0.2	4.0	0.88	100.1	5.4	4.52	0.73
ALNR-3 (7)	4752.80	LF1	4.1	0.3	0.3	1.7	90.0	0.0	1.5	0.4	0.4	0.2	0.9	0.11	99.9	53.8	8.39	0.64
ALNR-3 (8)	4754.20	LF1	5.4	0.4	0.2	2.2	87.1	0.0	2.5	0.5	0.5	0.1	1.0	0.12	99.9	39.8	8.68	0.68
ALNR-3 (9)	4754.95	LF2	3.7	0.3	1.1	0.7	92.1	0.0	0.8	0.5	0.1	0.1	0.3	0.05	99.7	124.3	6.08	0.70
ALNR-3 (10)	4757.10	LF3	7.7	0.5	0.3	4.0	81.5	0.1	2.9	0.4	0.8	0.2	1.4	0.23	100.0	20.4	6.03	0.74
ALNR-3 (11)	4757.80	LF3	6.0	0.6	0.4	3.9	83.0	0.1	2.4	1.0	0.8	0.3	1.1	0.29	100.0	21.2	3.67	0.79
ALNR-3 (12)	4758.30	LF3	8.3	0.7	0.5	5.4	74.8	0.1	4.4	1.3	1.3	0.5	2.0	0.5	99.7	14.0	3.91	0.73
ALNR-3 (13)	4812.10	LF1	10.5	0.2	0.2	1.8	83.0	0.0	2.5	0.2	0.4	0.1	0.8	0.12	99.8	45.0	7.03	0.69
ALNR-3 (14)	4830.00	LF1	9.0	0.3	0.3	3.7	80.8	0.0	2.9	0.4	0.9	0.1	1.4	0.25	100.0	21.9	5.55	0.73
ALNR-3 (15)	4832.00	LF1	6.2	0.4	0.2	2.7	83.2	0.1	4.1	0.5	0.7	0.1	1.6	0.17	99.9	30.3	9.69	0.62
ALNR-3 (16)	4832.6	LF2	4.6	0.2	0.3	1.8	90.3		1.1	0.4	0.4	0.0	0.6	0.1	100.0	49.0	5.93	0.76
ALNR-4 (1)	4220.00	LF3	6.4	0.5	0.6	3.5	81.0	0.2	3.7	0.9	0.8	0.6	1.5	0.4	100.1	23.4	3.82	0.69
ALNR-4 (2)	4222.80	LF3	10.3	0.4	1.5	2.9	79.1	0.1	2.4	0.8	0.6	0.5	1.1	0.29	99.9	27.6	3.78	0.72
ALNR-4 (3)	4224.50	LF3	6.7	0.3	0.4	2.4	85.3	0.1	2.2	0.3	0.5	0.4	1.0	0.28	100.0	35.4	3.43	0.71
ALNR-4 (4)	4226.10	LF3	5.6	0.6	0.5	2.2	84.6	0.0	2.4	1.4	0.6	0.7	1.0	0.26	100.0	37.6	3.94	0.69
ALNR-4 (5)	4228.00	LF3	4.8	0.2	0.3	2.2	87.7	0.1	2.4	0.4	0.5	0.3	1.0	0.18	99.9	40.5	5.37	0.69
ALNR-4 (6)	4230.00	LF3	6.5	0.4	0.6	3.3	81.5	0.2	3.5	0.8	0.8	0.5	1.5	0.32	100.0	24.6	4.65	0.69
ALNR-4 (7)	4231.00	LF3	9.1	0.3	0.6	4.4	76.1	0.2	4.5	0.8	1.0	0.9	1.6	0.38	100.0	17.3	4.26	0.73
ALNR-4 (8)	4232.00	LF1	3.4	0.2	0.2	1.6	90.3	0.0	2.4	0.4	0.3	0.2	0.7	0.13	100.0	58.0	5.61	0.68
ASH-2 (1)	3809.50	LF1	5.7	0.4	0.4	2.9	65.1	0.2	2.7	0.8	1.1	0.3	1.9	0.2	99.8	28.6	9.54	0.60
ASH-2 (2)	3810.50	LF3	6.9	0.3	0.9	4.0	79.3	0.1	4.3	0.3	1.1	0.2	2.2	0.24	100.0	20.0	9.37	0.64
ASH-2 (3)	3811.00	LF3	10.5	0.3	1.1	4.1	77.0	0.1	3.3	0.4	0.9	0.1	2.0	0.29	100.0	18.9	7.02	0.67
ASH-2 (4)	3867.20	LF3	8.8	0.3	2.2	5.6	73.4	0.1	4.6	0.8	1.5	0.1	2.1	0.62	100.2	13.0	3.41	0.73

Table 2. Continued.

Sample abbreviation	Core depth/ m	Lithofacies	LOI	Na ₂ O	MgO	Al ₂ O ₃	SiO ₂	P ₂ O ₅	SO ₃	Cl	K ₂ O	CaO	Fe ₂ O ₃	TiO ₃	Total	SiO ₂ /Al ₂ O ₃	Fe ₂ O ₃ /TiO ₂	Fe/Fe+Al+Mn
ASH-2 (5)	3870.10	LF3	9.9	0.3	0.8	5.6	75.4	0.2	3.6	0.5	1.3	0.3	1.8	0.55	100.2	13.5	3.19	0.76
ASH-2 (6)	3871.60	LF3	7.9	0.4	1.2	5.2	76.4	0.1	4.4	0.8	1.3	0.2	1.7	0.47	100.1	14.8	3.66	0.75
ASH-2 (7)	3873.70	LF3	7.6	0.4	1.9	5.3	75.8	0.1	4.6	0.9	1.3	0.1	1.8	0.52	100.1	14.2	3.43	0.75
ASH-2 (8)	3873.90	LF3	4.4	0.4	0.3	2.2	89.9	0.0	1.1	0.6	0.4	0.1	0.5	0.12	99.9	41.5	4.47	0.80
ASH-4 (1)	4438.20	LF3	5.5	0.3	0.7	5.0	82.0	0.0	2.6	0.6	1.1	0.1	1.7	0.36	100.0	16.5	4.59	0.75
ASH-4 (2)	4439.50	LF3	6.4	0.6	0.7	3.7	80.6	0.0	3.8	1.0	0.8	0.3	1.5	0.24	99.7	21.8	6.21	0.71
ASH-4 (3)	4440.20	LF3	7.4	0.6	1.0	4.9	77.1	0.1	3.8	1.2	1.1	0.3	2.1	0.36	99.9	15.6	5.76	0.70
ASH-4 (4)	4441.20	LF1	4.3	0.4	0.5	2.5	87.7	0.0	2.0	0.7	0.5	0.3	0.8	0.2	99.8	35.7	4.13	0.75
ASH-4 (5)	4442.90	LF3	7.0	0.8	0.7	5.1	78.5	0.3	2.8	1.3	1.0	0.4	1.5	0.39	100.0	15.3	3.82	0.77
ASH-4 (6)	4443.60	LF3	6.7	0.8	0.5		82.3	0.5	3.4	1.5	1.1	0.9	1.6	0.3	99.8		5.43	
ASH-4 (7)	4444.30	LF1	5.1	0.3	0.8	2.6	85.9	0.0	2.6	0.6	0.5	0.3	1.0	0.22	99.9	33.0	4.64	0.72
ASH-4 (8)	4543.10	LF1	3.5	0.3	0.9	1.9	90.0	0.0	1.3	0.5	0.4	0.2	0.7	0.08	99.8	48.2	8.23	0.74
ASH-4 (9)	4543.60	LF3	8.8	0.5	0.8	6.9	71.3	0.1	5.7	0.6	1.5	0.3	2.9	0.49	100.0	10.3	5.93	0.70
ASH-4 (10)	4544.80	LF1	6.6	0.9	2.3	2.1	82.4		2.2	1.5	0.4	0.2	0.8	0.11	99.6	38.4	6.89	0.74
ASH-4 (11)	4545.20	LF1	4.9	0.5	0.3	2.3	87.5	0.0	1.9	0.9	0.5	0.2	0.7	0.11	99.9	37.7	6.49	0.76
ASH-4 (12)	4546.60	LF2	3.4	0.3	0.2	2.0	90.0	0.1	1.8	0.6	0.4	0.2	0.8	0.09	99.7	45.9	8.73	0.71
ASH-4 (13)	4546.90	LF1	3.7	0.2	0.9	2.0	89.1	0.1	1.7	0.4	0.5	0.1	1.0	0.09	99.9	44.8	10.96	0.67
ASH-4 (14)	4646.3	LF3	6.3	0.4	0.7	5.7	79.1	0.0	3.6	0.6	1.3	0.3	1.5	0.33	99.8	13.8	4.65	0.79
ASH-4 (15)	4648.2	LF1	4.6	0.6	0.4	3.0	85.8	0.0	2.4	0.9	0.6	0.2	1.3	0.13	99.9	28.5	10.08	0.70
ASH-4 (16)	4649.8	LF1	5.0	0.4	0.4	3.3	85.3	0.0	2.3	0.9	0.6	0.2	1.2	0.13	99.9	25.9	9.58	0.72
ASH-4 (17)	4650.9	LF3	7.6	0.4	0.5	5.8	75.7	0.0	5.4	0.6	1.1	0.2	2.3	0.33	100.0	13.1	6.88	0.72
ASH-4 (18)	4651.7	LF1	4.4	0.2	0.3	3.0	88.4	0.0	1.6	0.3	0.6	0.0	0.9	0.18	99.8	29.4	5.17	0.76
ASH-4 (19)	4652.1	LF3	4.9	0.5	0.3	4.3	84.2	0.0	2.5	0.8	0.8	0.2	1.2	0.19	99.9	19.7	6.27	0.78
ASH-4 (20)	4652.9	LF3	6.0	0.3	0.4	4.3	81.7	0.0	3.7	0.6	0.8	0.1	1.9	0.19	99.9	19.1	10.0	0.69
MKZ-1 (1)	2768.50	LF2	6.9	0.1	0.4	1.9	86.5	0.0	1.5	1.2	0.4	0.1	0.7	0.09	99.9	45.9	7.68	0.73
MKZ-1 (2)	2769.10	LF1	7.1	0.3	0.6	2.7	84.2	0.1	2.1	1.0	0.5	0.2	1.0	0.16	99.8	31.6	6.00	0.73

Table 2. Continued.

Sample abbreviation	Core depth/ m	Lithofacies	LOI	Na ₂ O	MgO	Al ₂ O ₃	SiO ₂	P ₂ O ₅	SO ₃	Cl	K ₂ O	CaO	Fe ₂ O ₃	TiO ₃	Total	SiO ₂ /Al ₂ O ₃	Fe ₂ O ₃ /TiO ₂	Fe/Fe+Al+Mn
MKZ-1 (3)	2769.40	LF2	4.6	0.3	0.3	1.2	90.3		1.1	1.1	0.3	0.2	0.4	0.06	99.9	77.4	7.00	0.73
MKZ-1 (4)	2773.10	LF1	6.9	0.4	0.8	1.6	85.5	0.0	1.5	1.9	0.4	0.2	0.5	0.1	99.9	53.0	5.03	0.76
MKZ-1 (5)	2773.50	LF1	5.3	0.2	0.3	1.2	90.1	0.0	1.3	0.7	0.3	0.1	0.5	0.08	99.9	77.9	5.84	0.71
MKZ-1 (6)	2774.20	LF1	5.1	0.4	0.4	1.2	89.1	0.0	1.4	1.2	0.3	0.1	0.6	0.07	99.9	72.5	9.21	0.65
MKZ-1 (7)	2774.70	LF1	5.1	0.3	0.5	1.5	89.0		1.1	1.3	0.3	0.1	0.5	0.08	99.9	58.3	5.99	0.76
AL-9 (1)	1730.20	LF9	40.2	0.2	13.4	3.2	13.7	0.2	1.3	0.0	0.7	24.2	1.5	0.25	98.9	4.3	6.06	
AL-9 (2)	1730.93	LF9	40.7	0.2	13.9	3.1	12.1	0.2	1.1	0.0	0.6	25.2	1.4	0.25	98.8	4.0	5.53	
AL-9 (3)	1731.66	LF4	17.8	0.5	0.9	10.4	56.4	0.1	5.2	0.0	2.6	0.5	4.8	0.91	100.2	5.4	5.29	0.58
AL-9 (4)	1733.43	LF4	16.8	0.5	1.4	11.5	54.8	0.2	4.7	0.0	3.0	1.1	5.0	1.01	100.0	4.8	4.96	0.50
AL-9 (5)	1735.23	LF4	20.2	0.5	1.6	9.0	53.0	0.1	5.3	0.0	2.3	2.4	4.7	0.82	100.0	5.9	5.70	0.73
AL-9 (6)	1736.81	LF4	20.5	0.5	1.2	10.2	52.9	0.5	4.8	0.0	2.4	0.9	4.1	0.93	98.9	5.2	4.36	0.64
AL-9 (7)	1737.21	LF4	-	-	-	-	-	-	-	-	-	-	-	-	-	-	-	-
AL-9 (8)	1737.30	LF4	17.1	0.5	1.5	10.8	55.1	0.2	4.5	0.0	3.0	1.4	5.0	1	100.1	5.1	5.03	0.70
AL-9 (9)	1738.15	LF4	17.4	0.5	1.0	10.7	56.3	0.2	5.0	0.0	2.7	0.4	4.9	0.94	100.1	5.3	5.25	0.74
AL-9 (10)	1739.43	LF4	17.9	0.4	1.1	9.3	54.6	0.1	6.7	0.0	2.3	0.8	6.0	0.83	100.1	5.9	7.22	0.79

Table 3. Shows redox-sensitive element concentrations (ppm) and their enrichment factor (EF) values relative to PAAS of each studied sample. It also shows Mo/TOC ratios (TOC values presented in Table 1) that used in seawater renewal time estimation.

Sample abbreviation	Core depth/ m	Lithofacies	Zr	V	Mn	Mo	U	U (EF)	V (EF)	Mo (EF)	Mn (EF)	Mo/TOC × 10 ⁻⁴
ALNR-2 (1)	3969.25	LF6	-		6.8		0.7	85.0			1.83	
ALNR-2 (2)	3969.40	LF5	39.1	1001.9	153.4	121.2	20.3	20.8	21.21	256.63	0.35	25.53
ALNR-2 (3)	3976.50	LF9	103.8	194.3	634.1	4.5	5.2	6.1	4.68	10.85	1.64	2.24
ALNR-2 (4)	3976.60	LF9	108.9	162.8	638.5	5.3	3.4	3.8	3.74	12.16	1.57	2.90
ALNR-2 (5)	3976.80	LF9	176.2	283.8	685.5	3.6	4.9	7.4	8.89	11.27	2.30	
ALNR-2 (6)	3977.00	LF9	39.9	321	50.9	12.2	13.9	34.4	16.44	62.47	0.28	6.13
ALNR-2 (7)	3981.50	LF9	134	356.6	364.9	9.5	10.5	9.1	6.35	16.93	0.70	
ALNR-2 (8)	3985.40	LF3	33.2	259.7	33.5	14	8.2	22.2	14.52	78.28	0.20	10.07
ALNR-2 (9)	3992.20	LF3	75.7	281.5	88.6	14.7	8.6	7.9	5.34	27.89	0.18	
ALNR-2 (10)	3992.40	LF9	136	422.8	234.6	7.9	14.8	16.2	9.55	17.85	0.57	4.33
ALNR-2 (11)	4049.30	LF3	59.5	267	62.8	20.6	15.0	25.5	9.37	72.33	0.24	
ALNR-2 (12)	4050.50	LF7	31.9	148.5	240.4	15.4	10.9	28.0	7.88	81.73	1.37	3.60
ALNR-2 (13)	4052.00	LF7	50.3	200.8	43.3	21.5	5.9	12.4	8.73	93.47	0.20	
ALNR-2 (14)	4055.60	LF3	31.1	156.5	37.9	16.4	8.3	22.6	8.79	92.16	0.23	4.74
ALNR-2 (15)	4057.30	LF3	49.9	576.2	77.1	25.6	18.8	23.2	14.69	65.25	0.21	
ALNR-2 (16)	4059.10	LF3	27.3	182	34.6	18.9	13.0	27.8	8.04	83.53	0.16	3.43
ALNR-2 (17)	4060.50	LF3	36.3	354.9	74.8	21.7	15.3	26.0	12.46	76.17	0.28	4.71
ALNR-2 (18)	4061.10	LF3	50.5	133	33.9	20.9	16.3	47.0	7.93	124.66	0.22	
ALNR-2 (19)	4061.50	LF3	42.0	406.8	87.2	28.9	30.5	50.7	13.98	99.35	0.32	
ALNR-2 (20)	4064.20	LF3	36.4	269.9	56.7	27.6	12.8	29.4	12.79	130.84	0.29	6.67
ALNR-2 (21)	4065.10	LF8	49.1	496.1	810.3	11.4	9.2	23.3	25.99	59.72	4.55	2.03
ALNR-2 (22)	4066.70	LF3	45.8	381.2	74	36.3	11.1	16.7	11.85	112.80	0.25	
ALNR-2 (23)	4068.60	LF3	39.1	252.6	36.2	30.7	6.8	15.3	11.77	142.99	0.18	
ALNR-2 (24)	4071.70	LF8	42.9	331.1	46.8	33.6	8.8	16.5	12.84	130.28	0.19	6.73

Table 3. Continued.

Sample abbreviation	Core depth/ m	Lithofacies	Zr	V	Mn	Mo	U	U (EF)	V (EF)	Mo (EF)	Mn (EF)	Mo/TOC × 10 ⁻⁴
ALNR-2 (25)	4076.50	LF3	37.1	261.9	55.1	15.9	12.2	24.9	11.05	67.09	0.25	4.92
ALNR-2 (26)	4079.00	LF8	-	-	-	-	-	-	-	-	-	-
ALNR-2 (27)	4130.40	LF3	39.3	161.6	47.8	26.6	8.0	10.6	4.42	72.68	0.14	7.93
ALNR-2 (28)	4140.20	LF3	56.5	283.7	80.2	36.4	9.3	11.8	7.45	95.64	0.23	
ALNR-2 (29)	4143.00	LF9	83.3	797.9	502.8	19.5	8.1	17.3	35.31	86.30	2.38	10.82
ALNR-2 (30)	4156.50	LF1	28.4	137.4	39.5	21.3	3.5	9.4	7.59	117.69	0.23	6.55
ALNR-2 (31)	4165.60	LF3	42.1	223.8	58.6	38.8	5.4	10.6	9.04	156.70	0.25	9.21
ALNR-2 (32)	4169.00	LF3	63.4	323.4	69	28.6	6.8	9.2	9.08	80.32	0.21	
ALNR-2 (33)	4208.10	LF2	52.7	42.2	24.8	16.7	3.8	24.2	5.55	219.53	0.35	12.91
ALNR-2 (34)	4220.00	LF1	22.7	154.8	30.3	25.7	5.8	13.2	7.28	120.83	0.15	8.14
ALNR-2 (35)	4220.70	LF8	43.3	40.3	37.2	8.7	2.3	12.4	4.47	96.56	0.44	7.92
ALNR-2 (36)	4232.40	LF3	34.3	210.7	49.8	48.9	7.0	11.3	7.01	162.65	0.18	13.32
ALNR-2 (37)	4239.80	LF8	11.0	55.5	1664.8	9.4	1.4	6.4	5.22	88.35	16.8	1.25
ALNR-2 (38)	4256.90	LF7	27.2	57.9	9	19.7	3.6	29.8	9.91	337.13	0.17	17.14
ALNR-2 (39)	4257.20	LF2	14.1	151.2	15.7	27.1	3.7	13.8	11.68	209.31	0.13	
ALNR-2 (40)	4264.00	LF9	75.1	665.2	677.6	30.9	9.2	21.9	32.74	152.07	3.57	15.88
ALNR-2 (41)	4276.80	LF1	17.0	179.5	25.3	29.3	5.1	17.0	12.40	202.34	0.19	12.11
ALNR-2 (42)	4277.20	LF2	42.3	33.2	8.3	14	3.7	31.6	5.87	247.43	0.16	13.43
ALNR-2 (43)	4284.20	LF7	23.6	72.3	20	21	1.5	9.1	9.02	262.13	0.27	
ALNR-2 (44)	4309.50	LF1	19.9	163.6	25.8	26.1	5.4	16.7	10.43	166.47	0.18	9.57
ALNR-2 (45)	4322.10	LF9	30.6	137	576.8	16.3	9.5	20.5	6.12	72.78	2.76	3.90
ALNR-2 (46)	4339.20	LF7	19.5	64.7	31.9	14.9	5.8	13.6	3.13	71.97	0.17	
ALNR-2 (47)	4358.80	LF3	27.9	200.6	45.6	35.9	3.3	5.5	6.94	124.27	0.17	16.22
ALNR-2 (48)	4373.70	LF3	45.4	292.6	53	54.9	5.4	6.1	6.81	127.83	0.13	21.92
ALNR-3 (1)	3681.10	LF3	35.5	121.3	68	9.5	6.6	14.9	5.67	44.40	0.34	
ALNR-3 (2)	3681.40	LF3	54.3	289.4	67.1	20.5	14.6	-	-	-	-	10.60

Table 3. Continued.

Sample abbreviation	Core depth/ m	Lithofacies	Zr	V	Mn	Mo	U	U (EF)	V (EF)	Mo (EF)	Mn (EF)	Mo/TOC × 10 ⁻⁴
ALNR-3 (3)	3682.60	LF3	85.6	517.1	114.4	36.2	20.0	-	-	-	-	16.10
ALNR-3 (4)	4750.10	LF7	38.8	239	50.1	56.9	7.9	14.8	9.24	219.94	0.21	
ALNR-3 (5)	4750.80	LF7	33.7	200.6	47.3	50.7	7.5	14.6	8.09	204.37	0.20	
ALNR-3 (6)	4751.50	LF3	131.2	793.2	119.4	215.6	25.2	13.9	9.04	245.84	0.15	
ALNR-3 (7)	4752.80	LF1	19.7	87	36.3	25.5	3.5	12.7	6.51	190.83	0.29	
ALNR-3 (8)	4754.20	LF1	19.6	140.9	23.5	53.5	4.2	11.6	8.06	306.13	0.14	
ALNR-3 (9)	4754.95	LF2	16.7	32.5	62.7	15.1	1.4	11.4	5.49	255.06	-	
ALNR-3 (10)	4757.10	LF3	38.1	239.9	45.4	51.6	7.4	11.2	7.51	161.63	0.15	20.92
ALNR-3 (11)	4757.80	LF3	44.3	289	40.5	24.6	6.1	9.4	9.24	78.67	0.14	
ALNR-3 (12)	4758.30	LF3	66.8	413	73	25.4	7.6	8.6	9.65	59.37	0.18	8.87
ALNR-3 (13)	4812.10	LF1	19.6	154.3	23.6	37.3	4.7	15.5	10.49	253.53	0.17	
ALNR-3 (14)	4830.00	LF1	37.6	237.3	64.7	53.6	9.3	15.3	8.05	181.76	0.24	
ALNR-3 (15)	4832.00	LF1	27.3	180.7	42.1	33.2	5.9	13.0	8.24	151.43	0.21	13.47
ALNR-3 (16)	4832.6	LF2	15.0	129.2	20.3	31.8	3.8	12.5	8.78	216.03	0.15	14.75
ALNR-4 (1)	4220.00	LF3	52.8	189.7	50.4	14.2	8.2	14.4	6.87	51.46	0.20	
ALNR-4 (2)	4222.80	LF3	37.2	186.4	85.1	20.6	12.0	25.4	8.14	89.96	0.40	6.69
ALNR-4 (3)	4224.50	LF3	33.0	169.1	38.8	21.7	9.8	24.6	8.79	112.78	0.22	
ALNR-4 (4)	4226.10	LF3	32.6	157.9	36.1	20.9	9.6	25.9	8.80	116.50	0.22	
ALNR-4 (5)	4228.00	LF3	33.1	122.5	35.2	11.9	9.6	26.9	7.09	68.91	0.22	
ALNR-4 (6)	4230.00	LF3	36.7	289.1	61	24.9	13.4	24.5	10.92	94.01	0.25	
ALNR-4 (7)	4231.00	LF3	48.6	416	69.4	29.8	12.3	16.9	11.83	84.78	0.21	
ALNR-4 (8)	4232.00	LF1	18.0	88.2	25.5	12.4	7.0	27.2	7.09	99.71	0.22	
ASH-2 (1)	3809.50	LF1	30.4	241.4	50.5	25.9	9.4	19.5	10.38	111.32	0.23	
ASH-2 (2)	3810.50	LF3	38.9	320.6	74.9	31	11.9	18.2	10.12	97.89	0.25	19.90
ASH-2 (3)	3811.00	LF3	48.3	253.2	64.9	33.6	7.5	11.2	7.80	103.46	0.21	
ASH-2 (4)	3867.20	LF3	65.4	390.2	81.7	21.1	14.0	15.1	8.68	46.92	0.19	

Table 3. Continued.

Sample abbreviation	Core depth/ m	Lithofacies	Zr	V	Mn	Mo	U	U (EF)	V (EF)	Mo (EF)	Mn (EF)	Mo/TOC × 10 ⁻⁴
ASH-2 (5)	3870.10	LF3	81.2	369.4	59.7	30.4	15.2	16.4	8.26	67.98	0.14	10.53
ASH-2 (6)	3871.60	LF3	60.9	318.8	63.5	26.4	13.2	15.5	7.74	64.09	0.17	
ASH-2 (7)	3873.70	LF3	56.8	302.9	83	23.3	15.2	17.2	7.10	54.62	0.21	
ASH-2 (8)	3873.90	LF3	18.7	88.7	20.1	13.8	3.5	9.8	5.13	79.84	0.12	6.71
ASH-4 (1)	4438.20	LF3	58.8	419.4	58.9	68.7	15.9	19.3	10.53	172.54	0.16	
ASH-4 (2)	4439.50	LF3	34.2	265.1	40	54	11.9	19.5	8.99	183.17	0.15	
ASH-4 (3)	4440.20	LF3	55.6	357.5	58.1	51.5	10.5	12.9	9.04	130.28	0.16	
ASH-4 (4)	4441.20	LF1	30.2	181	35.1	23.8	6.0	14.8	9.22	121.18	0.19	13.84
ASH-4 (5)	4442.90	LF3	58.4	359.4	69.5	43.6	9.8	11.5	8.74	106.08	0.18	
ASH-4 (6)	4443.60	LF3	48.0	307.2	50.8	32	12.2	-	-	-	-	
ASH-4 (7)	4444.30	LF1	32.9	172.7	39.9	20.9	9.2	21.4	8.30	100.41	0.21	
ASH-4 (8)	4543.10	LF1	17.4	60.5	48.6	15.5	4.0	13.0	4.06	104.00	0.35	13.39
ASH-4 (9)	4543.60	LF3	60.0	357.8	94.8	73.9	11.1	9.7	6.48	133.76	0.18	
ASH-4 (10)	4544.80	LF1	15.2	103.3	61.3	26.1	5.5	15.5	6.03	152.27	0.38	
ASH-4 (11)	4545.20	LF1	15.7	101.9	19.2	23.9	3.8	9.9	5.50	128.92	0.11	
ASH-4 (12)	4546.60	LF2	18.1	66.1	24.2	18.8	3.8	11.7	4.22	120.09	0.17	
ASH-4 (13)	4546.90	LF1	16.0	64.2	32.1	17.6	3.8	11.6	4.04	110.79	0.22	
ASH-4 (14)	4646.3	LF3	40.6	185.8	39.3	34	6.4	6.7	4.05	74.10	0.09	
ASH-4 (15)	4648.2	LF1	17.8	96.7	22.2	15.7	3.0	6.0	4.02	65.26	0.10	
ASH-4 (16)	4649.8	LF1	20.7	106.9	27.3	16.4	3.9	7.2	4.07	62.45	0.11	
ASH-4 (17)	4650.9	LF3	43.3	211.7	39.1	43.2	8.0	8.4	4.58	93.48	0.09	15.66
ASH-4 (18)	4651.7	LF1	27.1	157	23.3	32.5	4.8	9.7	6.53	135.27	0.10	
ASH-4 (19)	4652.1	LF3	28.1	162.4	28.9	28.1	6.0	8.5	4.76	82.41	0.09	
ASH-4 (20)	4652.9	LF3	30.2	221.8	27.3	34.8	6.4	9.0	6.48	101.68	0.09	
MKZ-1 (1)	2768.50	LF2	17.9	109.3	26.8	16.6	3.7	11.9	7.26	110.31	0.19	6.89
MKZ-1 (2)	2769.10	LF1	25.4	202.3	40.5	26.4	5.2	11.8	9.50	123.93	0.20	

Table 3. Continued.

Sample abbreviation	Core depth/ m	Lithofacies	Zr	V	Mn	Mo	U	U (EF)	V (EF)	Mo (EF)	Mn (EF)	Mo/TOC × 10 ⁻⁴
MKZ-1 (3)	2769.40	LF2	12.0	55.4	18.2	11.6	1.7	8.8	5.94	124.45	0.21	
MKZ-1 (4)	2773.10	LF1	18.2	180.3	20.9	19.9	4.3	16.1	13.98	154.27	0.17	
MKZ-1 (5)	2773.50	LF1	18.3	92.4	16	17.6	5.0	26.2	10.00	190.45	0.19	
MKZ-1 (6)	2774.20	LF1	15.5	95.4	22.8	15.9	3.5	17.3	9.73	162.11	0.25	
MKZ-1 (7)	2774.70	LF1	17.2	97.2	18	14.2	3.3	13.1	7.97	116.50	0.16	7.96
AL-9 (1)	1730.20	LF9	27.0	259.7	1990.9	26.2	5.9	11.3	10.32	104.13	8.48	
AL-9 (2)	1730.93	LF9	29.4	297.7	1918.9	26.3	6.6	13.1	12.18	107.64	8.41	
AL-9 (3)	1731.66	LF4	113.9	886.2	145.2	121.4	19.5	11.4	10.69	146.43	0.19	15.21
AL-9 (4)	1733.43	LF4	119.3	1273.3	171.3	115	21.9	11.6	13.91	125.64	0.20	
AL-9 (5)	1735.23	LF4	95.9	1095	280.3	142.6	29.1	19.7	15.30	199.19	0.42	
AL-9 (6)	1736.81	LF4	136	1449.5	158.1	140.7	34.0	20.2	17.83	173.04	0.21	
AL-9 (7)	1737.21	LF4	-	-	-	-	-	-	-	-	-	
AL-9 (8)	1737.30	LF4	120.7	1032	176.6	108.6	21.0	11.8	11.99	126.13	0.22	
AL-9 (9)	1738.15	LF4	118.3	936.3	145.9	123.1	21.5	12.2	10.95	143.90	0.18	
AL-9 (10)	1739.43	LF4	102.9	720.7	149.3	105.3	13.0	8.5	9.73	142.20	0.22	16.87

Table 4. Corrected rare earth element concentrations (ppm) and calculated anomalies of each studies sample.

	Lithofacies	La	Ce	Pr	Nd	Sm	Eu	Gd	Tb	Dy	Y	Ho	Er	Tm	Yb	Lu	∑ REE	Pr/Yb	La _{anom.}	Ce _{anom.}	Eu _{anom.}	Y/Ho
ALNR-2(5)	LF9	23.04	46.11	5.58	22.74	6.23	1.54	4.07	0.63	4.29	30.09	1.36	2.82	0.38	2.47	0.36	151.70	0.72	1.09	0.98	1.40	22.14
ALNR-2(9)	LF3	32.68	64.06	6.38	24.83	4.11	0.84	2.77	0.38	2.30	17.70	0.53	1.55	0.22	1.67	0.23	160.26	1.22	1.22	1.13	1.18	33.45
ALNR-2(11)	LF3	23.02	41.85	5.11	21.27	3.24	0.79	2.02	0.35	2.16	21.37	0.57	1.62	0.31	1.93	0.28	125.89	0.84	1.25	0.99	1.34	37.63
ALNR-2(14)	LF3	5.42	10.17	1.09	4.76	0.94	0.18	0.51	0.08	0.44	3.53	0.10	0.27	0.05	0.32	0.04	27.89	1.09	1.57	1.19	1.14	36.77
ALNR-2(21)	LF9	10.92	20.26	2.34	13.44	3.46	1.06	2.99	0.48	3.19	29.07	0.80	2.51	0.40	3.03	0.44	94.37	0.25	1.50	1.91	1.57	36.44
ALNR-2(24)	LF3	9.62	14.84	1.58	5.74	1.01	0.22	0.79	0.14	1.00	10.87	0.23	0.85	0.13	0.80	0.12	47.95	0.63	1.28	0.99	1.10	46.86
ALNR-2(27)	LF3	14.63	29.49	3.33	13.40	3.02	0.58	1.57	0.24	1.13	8.36	0.29	0.84	0.12	0.98	0.18	78.17	1.08	1.13	1.04	1.16	28.60
ALNR-2(28)	LF3	20.72	33.51	3.69	13.74	2.20	0.48	1.43	0.27	1.84	17.90	0.45	1.32	0.19	1.82	0.21	99.77	0.65	1.23	0.98	1.15	39.36
ALNR-2(29)	LF9	8.00	16.00	1.67	6.73	2.31	0.53	2.27	0.73	6.04	53.03	1.54	4.76	0.76	5.85	0.88	111.09	0.09	1.22	1.12	0.82	34.36
ALNR-2(30)	LF1	4.15	5.22	0.53	3.08	0.53	0.12	0.42	0.11	0.66	4.62	0.15	0.41	0.08	0.51	0.07	20.65	0.33	0.90	2.26	1.00	30.45
ALNR-2(39)	LF2	8.60	14.84	1.52	7.79	1.17	0.24	0.82	0.14	1.07	7.85	0.22	0.72	0.10	0.70	0.10	45.86	0.69	4.03	1.64	1.08	35.61
ALNR-2(44)	LF1	5.37	9.53	1.01	4.09	0.85	0.17	0.48	0.07	0.54	4.51	0.13	0.37	0.05	0.40	0.07	27.65	0.81	1.36	1.10	1.18	34.81
ALNR-2(47)	LF3	5.80	10.29	1.10	4.61	1.07	0.44	0.75	0.10	0.69	4.79	0.17	0.44	0.09	0.52	0.08	30.93	0.67	1.50	1.14	2.33	28.67
ALNR-3(3)	LF3	9.30	20.18	1.92	8.51	1.73	0.29	1.09	0.21	1.23	9.71	0.27	1.64	0.11	0.88	0.16	57.23	0.70	1.61	1.37	0.89	35.44
ALNR-3(6)	LF3	43.64	66.49	7.22	30.99	6.37	1.69	4.61	0.74	6.04	29.05	0.95	2.85	0.43	3.27	0.49	204.85	0.70	1.83	1.16	1.44	30.44
ALNR-3(7)	LF1	16.67	27.55	3.10	12.47	2.54	0.50	1.70	0.21	1.33	9.11	0.28	0.77	0.10	0.86	0.11	77.31	1.15	1.38	1.04	1.16	32.28
AL-9(4)	LF4	30.51	50.03	6.95	23.40	5.04	1.02	3.73	0.50	3.21	20.45	0.69	2.00	0.36	2.34	0.33	150.57	0.95	0.81	0.71	1.15	29.83
AL-9(5)	LF4	25.25	50.45	5.75	25.73	5.30	1.12	3.51	0.67	3.42	29.18	1.44	2.39	0.70	2.35	0.35	157.59	0.78	1.51	1.16	1.12	20.28
AL-9(8)	LF4	45.41	73.28	8.52	35.45	7.60	1.45	5.12	1.03	6.33	38.94	1.70	4.17	0.57	3.79	0.55	233.90	0.72	1.48	1.04	0.99	22.95
AL-9(9)	LF4	45.25	85.68	9.89	38.50	8.37	1.95	6.47	0.97	5.53	32.40	1.38	3.51	0.70	3.81	0.52	244.95	0.83	1.09	0.97	1.26	23.52
AL-9(10)	LF4	38.03	69.18	7.75	31.64	6.67	1.44	5.47	0.97	5.31	36.98	1.21	3.63	0.50	3.74	0.47	212.99	0.66	1.30	1.06	1.09	30.46

Table 5. Show mutual rare earth element (La, Ce, Nd and Y) concentrations that measured from XRF and LA-ICP-MS technique. XRF data were used to correct LA-ICO-MS (by dividing LA-ICP-MS concentration by a factor of 5.0).

Sample	Lithofacies	Concentrations from LA-ICP-MS				Concentrations from XRF			
		La ppm	Ce ppm	Nd ppm	Y ppm	La ppm	Ce ppm	Nd ppm	Y ppm
ALNR-2(5)	LF9	115.2	230.6	113.7	150.47	13.7	28.5	11.9	21.9
ALNR-2(9)	LF3	163.4	320.4	124.2	88.53	20.0	34.4	14.2	13.4
ALNR-2(11)	LF3	115.1	209.3	106.4	106.89	17.4	24.7	12.4	11.1
ALNR-2(14)	LF3	27.1	50.9	23.8	17.65	8.9	9.1	5.2	7.4
ALNR-2(21)	LF9	54.6	101.3	67.2	145.38	10.1	11.3	5.9	26.3
ALNR-2(24)	LF3	48.1	74.2	28.7	54.38	9.5	10.1	5.9	11.1
ALNR-2(27)	LF3	73.2	147.5	67.0	41.83	12.8	19.4	13.4	9.2
ALNR-2(28)	LF3	103.6	167.6	68.7	89.54	14.2	21.5	9.9	11.5
ALNR-2(29)	LF9	40.0	80.0	33.6	265.23	10.9	11.5	8.4	37.3
ALNR-2(30)	LF1	20.8	26.1	15.4	23.12	7.7	8.2	3.5	6.3
ALNR-2(39)	LF2	43.0	74.2	38.9	39.24	5.6	7.4	6.6	4.3
ALNR-2(44)	LF1	26.9	47.7	20.4	22.54	7.2	11.4	6.7	5.6
ALNR-2(47)	LF3	29.0	51.4	23.1	23.94	11.0	13.7	7.2	7.7
ALNR-3(3)	LF3	17.21	37.34	15.74	17.96	14.10	25.10	14.40	23.80
ALNR-3(6)	LF3	80.75	123.03	57.34	53.74	28.60	48.40	20.00	32.80
ALNR-3(7)	LF1	30.84	50.97	23.07	16.86	6.10	4.80	2.70	5.50
AL-9(4)	LF4	152.6	250.2	117.0	102.26	35.4	69.4	35.1	37.8
AL-9(5)	LF4	126.3	252.3	128.7	145.91	32.6	63.4	29.8	40.9
AL-9(8)	LF4	227.1	366.5	177.3	194.73	37.7	69.2	31.7	36.6
AL-9(9)	LF4	226.3	428.5	192.5	162.05	41.7	64.8	28.4	32.8
AL-9(10)	LF4	190.2	346.0	158.2	184.92	35.8	58.8	25.8	34.4

Appendix IV: Reaction-path modelling

Constraints on initial system				
H2O		1	free kg	solvent
CO3--	u	150	mg/kg	
HCO3-	u			
SiO2(aq)	u	100	mg/kg	
H+	u	8.1	pH	
SO4--	u	2500	mg/kg	
O2(aq)	u	.1	mg/kg	
Mg++	u	1290	mg/kg	
Ca++	u	420	mg/kg	
K+	u	399	mg/kg	
Cl-	u	19350	mg/kg	
Fe++	u	.1	mg/kg	
Na+	u	10752	mg/kg	

add

Time start days end days

T constant 25 °C

Figure 1. shows the composition for the initial system used during the reaction-path modelling. The composition represents 1 kg of seawater. Only sulphate reduction reaction allowed to take place (by reducing oxygen and Fe(III) concentration) in order to test its effect on pH. pH value drop from 8.1 to less than 7 as the reaction takes place (Chapter 7; Fig. 7.5).